DISSERTATION

MICROGLIAL INNATE AND ADAPTIVE IMMUNE FUNCTION MODULATES DISEASE PATHOLOGY IN AN ENVIRONMENTAL PESTICIDE MODEL OF PARKINSON'S DISEASE

Submitted by

Savannah M. Rocha

Department of Microbiology, Immunology and Pathology

In partial fulfillment of the requirements

For the Degree of Doctor of Philosophy

Colorado State University

Fort Collins, Colorado

Summer 2022

Doctoral Committee:

Advisor: Mark Zabel
Co-Advisor: Ronald B. Tjalkens

Jerry Bouma
Rebakah Kading
Julie Moreno

ABSTRACT

MICROGLIAL INNATE AND ADAPTIVE IMMUNE FUNCTION MODULATES DISEASE PATHOLOGY IN AN ENVIRONMENTAL PESTICIDE MODEL OF PARKINSON'S DISEASE

Parkinson's Disease (PD) is the world's foremost movement disorder with pathological features including loss of dopaminergic neurons (DAn) within the substantia nigra pars compacta (SNpc), chronic activation of glial cells, and the misfolding and aggregation of α-synuclein (α-syn). Compounding evidence gathered over the past two centuries suggests environmental exposures, genetics, and aging can induce complicated cell-to-cell interactions that evoke and facilitate chronic inflammatory states; but the role that individual glial cells, in particular microglia, have in the progression of disease remains unknown. Difficulties in recapitulating the three pathological hallmarks of PD underscore the need for better animal models. To address this gap in functional investigation, the studies herein provide, for the first time, an optimized environmental exposure model with the pesticide rotenone (2.5mg/kg/day) in murine, which has proven effective at mirroring DAn degeneration, gliosis and misfolded α-syn accumulation. The pathology observed was region-, time- and dose-dependent, emphasizing the importance of environmental exposure and associated PD diagnosis. The successful optimization of this exposure model has allowed for its implementation in transgenic mice, which was previously unfeasible. To determine microglial specific innate inflammatory reactions in the progression of PD, we targeted the inflammatory transcriptional regulator NF-κB by use of transgenic CX3CR1-Cre::IKK2$^{fl/fl}$ mice. Genetic inhibition of the canonical NF-κB pathway in microglia revealed neuroprotective

effects post-exposure to rotenone. Interestingly, despite the reduction in neurodegeneration of DAn, there were increased levels of misfolded α-syn in surviving DAn and microglia. This finding alone indicates that misfolding and aggregation of α-syn, astrocytic responses, and neuronal interactions, in concert, are not enough to elicit the extensive pathology observed in idiopathic PD; rather, the misfolding may occur from microenvironment changes and serve as an inflammatory catalyst in microglia. Further investigation into the capacity of immune functionality of microglial cells revealed that these cells can be primed/trained by one exposure and, upon second exposure, become hyper-activated exacerbating neurodegenerative effects. Dual exposure was accomplished by exposing juvenile animals to Mn in drinking water (50mg/kg/day) for the duration of 30 days, followed by adult exposure to rotenone for 14 days with a successive 14-day lesioning period. Juvenile Mn exposure alone was not sufficient enough to induce neurodegeneration, however, the combined effects of Mn and rotenone exposure showed DAn degeneration, gliosis, and α-syn misfolding. Dually exposed microglial NF-κB knockout (KO) animals retained high levels of misfolded α-syn in DAn and microglia, as previously observed with rotenone exposure alone. Remarkably, the neuroprotection previously observed in KO animals exposed to rotenone was no longer present in dual-exposure KO animals. This finding emphasizes that neurotoxic signals and products generated from the activation of primed/trained immunity in microglia is independent of canonical NF-κB. The breadth of this research provides pivotal evidence towards a new frontier of PD research by the establishment of a novel environmental model in mice that mirrors the pathology observed in idiopathic PD patients. In addition, these studies positively identify microglial canonical NF-κB as a potential therapeutic target in single toxin exposure instances, whereas it becomes inappropriate for dual or multi-exposure circumstances.

ACKNOWLEDGEMENTS

The process of earning a Doctor of Philosophy is shaped by the research conducted, the connections made, and the time invested to become an expert in ones regarded field. The culmination of these aspects, ultimately, is not the entirety of the data produced (although the degree depends upon this) but rather is the successful development of a skilled scientist. Through the course of a PhD, I believe that the mentorship received by a student is the most valuable. Given this, I would like to wholeheartedly thank Dr. Ron Tjalkens for trusting in my technical abilities and giving me the opportunity to conduct research in his laboratory. The overwhelming amount of advice and lessons I have learned from Dr. Tjalkens has been a cornerstone that will serve as such throughout the entirety of my career. I would also like to thank him for the creative freedom he has allowed me to have over the course of my degree, which has allowed me to express and showcase my ideas in ways I never imagined possible. It has been a pleasure and an honor to work in his laboratory and conduct groundbreaking research in the field I love. I would also like to thank Dr. Mark Zabel for sparking the initial research flame that has led me to this point. His patient mentorship, guidance, and leadership throughout my undergraduate and graduate degrees has taught me the kindness, integrity, humbleness, and inclusivity I aspire to have in my future endeavors. Next, I would like to thank my committee composed of Dr. Rebekah Kading, Dr. Jerry Bouma, and Dr. Julie Moreno for taking time to listen to my ideas and lend expertise over the last five years. Research questions posed and advice given by each has broadened the scope of my studies and always fostered my growth towards becoming a well-rounded scientist. I would like to extend a very special thank you to my parents, Gilbert and Kelly Rocha, for always supporting me, believing in me, and pushing me to achieve my dreams. Witnessing my dad go through

chemotherapy and radiation treatment in high school opened my eyes to the heartbreak and struggle diseases pose. However, it also allowed me to see the beauty of science and technology in treatment regimens. It inspired me to pursue science as a career and has remained the driving force behind my research. In this moment, I would like to rejoice with you, Dad, for being cancer free for a decade and putting up the hard fight that was necessary all those years ago to be able to be here today; and Mom, for the hours you spent caring for Dad when he was ill and the fortitude you had then and continually show each and every day. I love you both more than you will ever know. To my fiancé, Scott, thank you for supporting me daily on this journey, through all of the failures and triumphs. Without his unconditional love, I would not have been able to accomplish the extent of what I have. I would also like to thank my friends, family, past and present laboratory members, teachers, mentors, and professors that have shaped me into the individual I am today. Finally, I would like to acknowledge the patients and families that are currently affected by the vast array of neurodegenerative diseases. I am grateful each and every day to have the ability and opportunity to add to the growing field of knowledge regarding these diseases and I hope nothing more than for a treatment/cure to be discovered.

DEDICATION

The research herein is dedicated to individuals and their families who have suffered and are currently suffering from neurodegenerative diseases. May this serve as one step closer to a treatment/cure.

TABLE OF CONTENTS

LIST OF TABLES

LIST OF FIGURES

CHAPTER 2

CHAPTER 3

APPENDIX I

APPENDIX II

APPENDIX IV

CHAPTER 1

LITERATURE REVIEW

1.1. The History of Parkinson's Disease

Parkinson's Disease (PD) is the second most common neurodegenerative disease worldwide, affecting 1-2 individuals per 1000 at any given time (Tysnes and Storstein, 2017) and is the most prevalent movement disorder in the aging population (Billingsley et al., 2018). Disease onset typically occurs as aging progresses, where 1% of diagnosis are made in individuals at or above the age of 60 and 4-5% in individuals over the age of 85. The incidence of PD is twice as high in men than in women (Castellani and Perry, 2012; Billingsley et al., 2018; Cerri et al., 2019). Clinical symptoms of PD are characterized by progressive motor dysfunction in initiating voluntary movement, however non-motor symptoms can occur prior to and in concert with motor manifestations. The prodromal phase of PD, occurring up to two decades before diagnosis, includes non-motor symptoms ranging from depression, anxiety, behavioral changes, sleep disturbances, and anosmia to gastrointestinal dysfunction (Kouli et al., 2018). Motor disturbances include bradykinesia, masked facial expressions, rigidity and postural instability, tremor, gait difficulties, dystonia, speech deficits, and impaired handwriting and grip force (Mazzoni et al., 2012; Moustafa et al., 2016).

The pathological basis resulting in clinical symptomology has been investigated for over 200 years beginning with 'Shaking Palsy,' an early description of the disease by James Parkinson in 1817; however, little progress has been made to uncover the complex mechanisms associated with disease etiology. Pathologically, PD is characterized by a loss of dopaminergic neurons

(DAn) within the substantia nigra pars compacta (SNpc) and accumulation of proteinaceous aggregates of α-synuclein (α-syn) in surviving neurons form what is known as a Lewy body. PD represents the most common synucleinopathy although there are others such as multiple systems atrophy and dementia with Lewy bodies, of which are clinically similar in manifestation, and may have overlapping genetic mutation associations.

Challenges in conducting research into the causes of PD arise in part from the lack of experimental models recapitulating the majority of neuropathological features that occur within the idiopathic disease. Current treatments for PD are limited to symptomatic therapies and include leva-dopa (L-Dopa), monoamine oxidase B (MAO-B) inhibitors, dopamine (DA) agonists, catechol-O-methyltransferase (COMT) inhibitors, N-methyl-D-aspartate (NMDA) receptor inhibitors, and anti-cholinergic that lose efficacy over time. Late-stage disease treatments involve invasive deep-brain stimulation where there is no guarantee of symptom reduction. Ultimately, there is no cure for this disease.

1.2. Etiology

1.2.1 Genetics

To date, the etiology of PD is not well understood despite modern experimental models attempting to detail the complex pathology. The greatest risk factor for PD is increasing age, but there is evidence indicating biological sex, environmental exposures, genetics, ageing, and a combination therein as factors that contribute to disease onset and progression, making this disease one of the most common polygenic diseases worldwide. Although PD is generally defined as a sporadic or idiopathic disorder, there are a minority of cases (10-15%) that report a family history, and 5% of those represent Mendelian inheritance (Castellani and Perry, 2012; Deng et al., 2018).

The past two decades have served as pillars in the advancement of PD genetics research. The year 1997 marked the first year in which a genetic mutation in the *Snca* (encoding α-syn) gene was identified, relating that there was a possible heritable component of PD. Subsequent identification of gene mutations leading to early-disease onset were identified in *Prkn* (*Park2*)*, Pink1,* and *Dj-1* (*Park7*). To date, 90 independent risk signals have been identified using genome-wide association studies (GWAS) and 23 of those make up *Park* genes, demonstrating either autosomal dominant (*Snca, Lrrk2, Vsp32*), or autosomal recessive inheritance (*Park2, Pink1, and Park7*) (Kouli et al., 2018; Blauwendraat et al., 2020). Point mutations and multiplications in *Snca* result in pleiomorphic risk, where association with the locus can induce severe early-onset disease and/or the non-coding variability within the locus confers risk and predisposes to genetically complex PD (Billingsley et al., 2018). Interestingly, N370S and L444P mutations in the glucocerebrosidase (*GBA*) gene that participates in lysosomal function have also been linked to familial PD, accounting for 6-7% of PD diagnosis before the age of 51 (Alcalay et al., 2010; Sidransky and Lopez, 2012). The most frequent autosomal dominant mutation resulting in monogenic PD was discovered in 2004 in the gene encoding leucine-rich repeat kinase 2 (*Lrrk2*) where 6 mutations in this gene have been validated as pathogenic. The most common mutation is p.G2019S, which is estimated to account for 1% of sporadic and 4% of familial cases worldwide (Healy et al., 2008; Billingsley et al., 2018; Kouli et al., 2018). Autosomal recessive mutations that lead to PD often occur earlier than classical PD and have been linked to mitochondrial homeostasis (*Park2*, *Pink1*, and *Park7*).

1.2.1.1 Mitochondrial Involvement in Parkinson's Disease

Many of the genes identified as risk factors for PD encoded proteins that participate in the maintenance of protease, lysosomal or mitochondrial homeostasis and physiological functionality (Nandipati and Litvan, 2016). Studies investigating familial PD show that there are mitochondrial deficits along with autophagy impairments, highlighting the importance of these two mechanisms in the progression of PD pathology (Barazzuol et al., 2020). Two highly characterized proteins involved in PD are PARK2 (an E3 ubiquitin ligase) and PINK1 (a serine/threonine kinase with a mitochondrial targeting sequence), both of which are involved in clearance of defective mitochondria via autophagy; this process is referred to as mitophagy. This form of selective autophagy requires ubiquitination signaling to direct recruitment of the autophagosome for subsequent degradation of the mitochondria. PINK1 and PARK2 have been shown to localize within the endoplasmic reticulum, an important site for mitochondrial association. Mitochondrial contact with these sites modulates numerous cellular functions such as Ca^{2+} homeostasis, lipid transfer, mitochondrial metabolism and dynamics, apoptosis and mitophagy, indicating the importance of the PINK1/PARK2 quality control pathway (Matsuda et al., 2010; Csordas et al., 2018; Barazzuol et al., 2020).

An inherent characteristic of mitochondria is the presence of an electrochemical gradient between the inner and outer membrane. This proton gradient modulates the intake and export of charged ions and proteins and drives the production of adenosine-triphosphate (ATP) through oxidative phosphorylation. The transmembrane electrochemical gradient is also used to facilitate active transport of selective metabolites across the inner membrane, resulting in high ratios of ATP to its hydrolysis products driving a large number of the cell's energy requiring processes (Alberts et al., 2002).

Loss of the electrochemical gradient and subsequent depolarization of mitochondria can occur through numerous processes however when depolarization takes place, PINK1 binds and is sequestered to the translocase of the outer membrane (TOM) where a super-complex is then formed (Sekine and Youle, 2018). This results in the activation and autophosphorylation of PINK1 which then phosphorylates ubiquitinated substrates on the outer mitochondrial membrane (OMM) thus recruiting and activating PARK2 (Barazzuol et al., 2020). PARK2 further ubiquitinates proteins on the damaged mitochondria, serving as continued substrates of PINK1 in a positive-feedback loop manor resulting in coating of the OMM in ubiquitin. This combination of signaling and marking events recruits autophagosomes allowing for the engulfment and degradation of the dysfunctional mitochondria. Genetic mutations in either PINK1 or PARK2 leading to the accumulation of dysfunctional mitochondria within DAn and glial cells increase accumulation of reactive oxygen species (ROS), inflammatory signaling cascades, and ultimately neurodegeneration.

1.2.2 Environmental Exposures

The complexity of lifelong exposures in the general population continues to add variability and pose challenges in epigenetic analysis. It remains unknown if single, dual, or multiple exposures act independently of one another or if multiple lifelong exposures act synergistically to promote the onset of idiopathic PD and Parkinsonism. There have been several causative agents found to induce neurological and neuropathological features similar to that observed in idiopathic PD. Of these, are neuroleptic drugs (risperidone, olanzapine, aripiprazole), manganese (Mn), organophosphates, rotenone, maneb, paraquat and infectious biological agents are the most widely characterized (Brown et al., 2006; Shin and Chung, 2012; Bantle et al., 2019). Excess

accumulation of trace metals such as iron, selenium, copper, and manganese through dietary intake, drinking water, or inhalation from industrial welding and machining have also been linked to parkinsonian-like deficits (Nandipati and Litvan, 2016).

1.2.2.1 Manganese

Mn is an essential trace element to life and is tightly regulated in humans with tissue concentrations ranging from 0.3 to 2.9 μg Mn/g wet weight (Mezzaroba et al., 2019). Found in the liver, kidneys, pancreas, bone, and basal ganglia of the brain, this metal participates as a cofactor in a wide array of enzymatic processes that are physiologically relevant to maintaining cellular homeostasis and survival, in addition to aiding in organ and tissue development (Erikson et al., 2005; Hsu et al., 2018; Mezzaroba et al., 2019; Zoroddu et al., 2019). Mn is involved in amino acid, lipid, protein, and carbohydrate metabolism; moreover, it is an important element for protein glycosylation, immune function, regulation of blood sugar, ATP production, reproduction, digestion, bone growth, and blood clotting (Aschner and Aschner, 2005; Aschner et al., 2005; Roth, 2006; Tuschl et al., 2013). Importantly, Mn is required in metalloenzymes, such as those located in the mitochondria, that facilitate detoxification of superoxide free radicals (Martinez-Finley et al., 2013).

Dietary intake is the main source of Mn acquisition and is rich in a variety of foods including grains, green vegetables, fruits, nuts, pineapple, beans, spices and tea (Aschner and Aschner, 2005). Mn is also naturally occurring in groundwater, with concentrations varying with geographical location and geochemical conditions (Schullehner et al., 2020). In regions where ground water is typically consumed as drinking water, or episodic water treatment failure occurs, Mn exposure of individuals is increased. Molecular mechanisms of Mn uptake are not well

characterized, but it is thought that the gut tightly controls the amount of body Mn through passive diffusion or through active transport mediated by divalent metal transporter 1 (DMT-1) where only 1-5% is absorbed and the remainder is promptly excreted into the bile by the liver (Davidsson et al., 1991; Aschner et al., 2007). However, impaired hepatobiliary excretion can lead to increased levels of Mn in the body, and ultimately the brain. Children appear to be especially vulnerable to Mn overexposure due to increased concentrations of the metal in infant formula in concert with drinking water. This subpopulation has the highest drinking water intake per kilogram of body weight and, unlike adults, do not have developed biliary excretion and intestinal absorption systems (Aschner and Aschner, 2005; Erikson et al., 2007; Ljung and Vahter, 2007). Other predominant exposures of Mn occurs in occupational settings where Mn-laden dust is inhaled during mining, welding, smelting, or battery manufacturing (Tuschl et al., 2013). Inhalation of Mn can also occur in individuals that work or reside close to ferroalloy industries or in areas with high use of methylcyclopentadienyl Mn tricarbonyl (MMT), a gasoline fuel additive.

Despite the essential role of this metal in cellular homeostasis and physiological function, Mn is toxic to the central nervous system (CNS) at excessive levels. A growing body of literature indicates Mn exposure and excessive accumulation as a driving factor in neurodegenerative disorders (Bowman et al., 2011). Prolonged exposure and excessive accumulation through occupational means can result in a condition known as Manganism that resembles symptomology seen in PD. Neurological deficits have also been reported in children exposed to increased levels of Mn, ranging from increased prevalence of attention deficit hyperactivity disorder (ADHD) and overall decreased Intelligence Quotient (IQ) (Roels et al., 2012; Schullehner et al., 2020). Subpopulations of glial cells in the brain are known to uptake Mn readily through ZIP8/14, glutamate receptors, manganese citrate transporters, DMT-1 and Ca^{2+} channels (Harischandra et

al., 2019). Once in the cell, Mn preferentially accumulates within mitochondria via the Ca^{2+} uniporter where it mainly binds to the mitochondrial membrane or matrix proteins (Harischandra et al., 2019). At high concentrations, Mn binds to succinate, malate and glutamate which are important substrates in mitochondrial respiration, ultimately rendering the mitochondrion incapable of performing oxidative phosphorylation and leading to an accumulation of ROS (Gavin et al., 1999; Martinez-Finley et al., 2013; Harischandra et al., 2019). As a result, cellular viability is compromised, neuroinflammation is induced and neurotransmitters fluctuate. All of these features contribute to the complexity of the pathological progression of idiopathic PD.

1.2.2.2 Pesticides and Parkinsonism

Pesticides are used globally in public health to control disease vectors and in the agricultural industry to control pests that are damaging to crops (Garcia-Garcia et al., 2016). These chemicals have been scrutinized for their ability to induce neurological changes in the brain leading to the destruction of DAn within the SNpc (Kouli et al., 2018; Ball et al., 2019). In the 1980s, intravenous exposure to the toxicant 1-methyl-4-phenyl-1,2,3,6-tetrahyrdopyridine (MPTP) resulted in clinical, pathological, and biochemical features that resembled those of textbook advanced stage PD. Metabolism of MPTP by astrocytes in the brain to 1-methyl-4-phenylpyridium (MPP^+), structurally resembled a popular pesticide, paraquat. Thus, this finding among others, rekindled research driven towards investigating pesticides exposure and PD pathogenesis (Brown et al., 2006; Ball et al., 2019). Common pesticides under investigation for increasing PD risk include paraquat, permethrin, dieldrin, and rotenone. The major classification breakdowns of these pesticides are organophosphates, organochlorines, pyrethroids, and rotenoids (Hatcher et al., 2008). Recent studies have confirmed preferential targeting of DAn by the organochlorine dieldrin

where the severity if impact was dose-dependent (Kanthasamy et al., 2005; Richardson et al., 2006; Hatcher et al., 2007). Rotenone is the major pesticide within the rotenoid subclassification that has raised concerns for PD risk, despite this, it is still utilized worldwide.

1.2.2.2.1 Rotenone

Rotenone is a naturally occurring insecticide, pesticide and piscicide that is found within the stems and roots of *Lonchocarpus*, *Derris*, *Tephrasia* and *Munduela* plant species native to the East Indies, North America, and South America (1933; Gupta, 2012). This compound was originally isolated from the roots of plants by indigenous tribes in Southeast Asia and South America where it was introduced to bodies of water for harvesting fish for consumption. Since, worldwide usage of rotenone has been implemented and used continuously to control noxious fish populations, food-web manipulation, control of fish diseases, restoring bodies of water to endangered species, control of insects in commercial and industrial crop production, management of household insects and pests, and extermination of ticks, fleas and flies in veterinary medicine (McClay, 2000; Ling, 2003; Gupta, 2012).

When applied to freshwater bodies of water, rotenone can persist for days to months, where temperature, water depth, light exposure, presence of organic debris, initial dose amount and seasons contribute to the half-life of the molecule (Ling, 2003). Rotenone is highly lipophilic and readily crosses biological membranes where it acts as a high-affinity inhibitor of complex 1 (nicotinamide adenine dinucleotide-dehydrogenase; NADH) in the mitochondrial electron transport chain (ETC), leading to increases in the amount of superoxide and free radical oxygen species (Henchcliffe and Beal, 2008).

1.2.2.3 Infectious Agents

The possibility of infectious agents inducing Parkinson's pathology has gained significant support within the last several decades. Observation of clusters of individuals that presented with Parkinsonism following historical infectious outbreaks provide foundational knowledge to the hypothesis that acquired infections may lead to chronic neurological disease. Increased plausibility was put forth with Braak staging where pathological spread may originate through olfactory nerve (CNII) and vagus nerve (CNX)(Braak et al., 2004). These extensive peripheral nerve pathways may serve as neural highways for the spread of infectious neurotropic agents, ultimately allowing access to the brain.

The complex and interconnected pathology underlying infections and PD may extend far beyond an initial triggering event. PD is ultimately the result of the aging nervous system which becomes more vulnerable to the direct and indirect effects of infections. Biochemical and biomechanical changes resulting from aging render neuronal cells susceptible to oxidative damage and increase metabolic stress. This in combination with infectious agents worsen PD and other neurodegenerative disease symptoms that often progress and may never return to baseline.

1.2.2.3.1 Bacterial Infections and Parkinson's Disease

Bacterial production of pro-inflammatory molecules and neurotoxins that are able to penetrate the blood-brain barrier (BBB) may play a major role in the development and/or continued progressive pathology of PD. A known inducer of inflammation is the bacterial endotoxin lipopolysaccharide (LPS), which is produced exclusively in gram-negative bacteria. In theory, an increase in the abundance of gram-negative bacterial populations within an individual could induce the inflammatory cascade that is reported in PD (Smeyne et al., 2021).

Increased presence of gastric and duodenal ulcers in patients with PD have been described as early as the 1960s, where the gram-negative bacterium *Helicobacter pylori* is the causative agent (Schwab, 1961). Preceding antibiotic administration, vagotomies (CNX) were performed and this was associated with a reduction in the risk of PD, which has also been shown in modern animal models of PD (Svensson et al., 2015; Liu et al., 2017a; Kim et al., 2019). Meta-analysis and case control studies have reported 1.5-3 fold increases in development of PD post *H. pylori* infection, indicating this as a potential biological agent associated with the onset and progression of PD. *H. pylori* also plays a role in the adsorption of L-Dopa, an important downstream metabolite of DA, of which PD patients lack. The adsorption of this metabolite due to infection is an important factor in clinical cases when assessing metabolite levels and subsequent treatment determination (Smeyne et al., 2021).

Determination of the role of bacterial infections and increased likelihood of PD is not limited to single bacterial species, rather that of bacterial populational dynamics. The gut microbiome has become an active area of study within the last decade due to rising evidence coupling the gut-brain axis with chronic neurodegenerative disease states. One of the earliest symptoms in the prodromal phase of PD is intestinal dysfunction, which may be associated with resident gut microbiome populations. There are over 1,000 different bacterial species that cultivate the gastrointestinal tract and a number of metagenomic studies have shown that there are populational differences between the microbiota found within individuals with and without PD (Zhernakova et al., 2016). Dysbiosis in the gut microbiome has shown a higher prevalence of *Bifidobacteriaceae*, *Christensenellaceae*, *Lachno-spiraceae*, *Lactobacillaceae*, *Pasteurellaceae* and *Verrucomicrobiaceae* (Hasegawa et al., 2015; Smeyne et al., 2021). Microbial changes in the gut microbiome heavily affect metabolism of toxic compounds, such as pesticides, where

excessive accumulation of environmental toxins would occur due to the decreases in ability of the microbiome to properly metabolize these molecules.

1.2.2.3.2 Viral Infections and Parkinson's Disease

Neurological complications as sequelae of viral infections, although rare, have been documented for over a century beginning with the 1918 influenza (H1N1) pandemic, also known as the Spanish Flu. Historical records show that neurological manifestations following influenza infection include delirium, cycloplegia, encephalitis lethargica (EL), seizures, encephalopathy, myelopathy, bulbar paralysis, parathesis, and ataxia (Henry et al., 2010). Out of those who experienced EL, 80% of them went on to develop Parkinson's-like disease and presented with tremor, bradykinesia, and masked facies- the resulting disease was then termed post-encephalitic Parkinson's disease (PEP) (Cunha, 2004; Jang et al., 2009b; Maurizi, 2010). Extensive supporting evidence suggests that viral infection induces the encephalopathy that results in long standing disease state. Studies have further characterized the neurotropic nature of the virus showing extensive neuroaxis involvement beginning in the enteric and peripheral nervous system and progressing to CNS invasion (Tanaka et al., 2003; Klopfleisch et al., 2006; Jang et al., 2009a).

A number of other viruses have also been associated with both acute and chronic parkinsonism, including Epstein-Barr virus (EBV), cytomegalovirus, varicella zoster virus (VZV), measles, polio, coxsackie, West Nile virus, Japanese Encephalitis B, herpes, acquired immunodeficiency disorders (HIV), and Western Equine Encephalitis (WEEV) (Sasco and Paffenbarger, 1985; Woulfe et al., 2000; Ball, 2003; Hemling et al., 2003; Jang et al., 2009b; Bantle et al., 2019). More recently, there has been concern with SARS-CoV-2 virus, the causative agent of CoVID-19, and the potential for neuro-invasion and subsequent Parkinson's-like pathology.

Due to the gastrointestinal dysfunction, 'brain fog', anosmia and ageusia (CNI, VII, IX, X), vision impairment (CNII), memory decline, sleep disturbances and seizures post-acute neurological deficits are probable. Numerous case reports have documented the presence of encephalopathy, neurotransmitter alterations relating to serotonin and DA, neuropathy, abnormal movements, meningoencephalitis, and vascular abnormalities in the post-acute phases of the disease (Nolen et al., 2022). Furthermore, SARS-CoV-2 co-localization with microtubule associated protein 2 relating to the trigeminal nerve (CNV) and marked neuronal infection in humanized-ACE2 transgenic animals enhances the hypothesis that SARS-CoV-2 may be a virus that can induce Parkinson's-like pathology (Fagre et al., 2021; Kumari et al., 2021; Zhang et al., 2021).

Interestingly, samples of cerebral spinal fluid (CSF) and blood from patients presenting with clinical manifestations of PD post viral infection, and *postmortem* brain samples, reveal little to no biochemical or biological markers indicative of persistent viral infection (Kapila et al., 1958). There are two current standing hypotheses within the PD field regarding viral infection and the ensuing pathology. 1) Direct viral invasion of central nervous tissue predisposes patients to the development of PD (less likely), 2) a CNS cytokine storm caused by the virus (more likely) primes glial cells to generate a more robust immune response to a secondary exposure later in life. The latter hypothesis would not require virus to be present at the time when patient develops EL or PEP (Henry et al., 2010).

1.3 Glial Reactivity and the Function of Innate and Adaptive Immunity

1.3.1 Astrocytes

Astrocytes are the most abundant sub-population of the neurovascular unit that continuously tile the mammalian CNS (Fan and Huo, 2021). These cells are long-lived and provide

a crucial role in physical interaction and communicating with neurons, oligodendrocytes, microglia, and vascular endothelium which will further be referred to as the vascular unit. Astrocytes provide extensive support through homeostasis of extracellular fluid, ions and neurotransmitters, provide glucose metabolites to neurons for energy, modulate local blood flow, regulate drainage of interstitial fluid, play essential roles in synapse formation and plasticity, and exhibit dynamic functions in neural circuit formation, neurological function and behavior (Matias et al., 2019; Sofroniew, 2020).

These cells demonstrate an evolutionarily ancient response to disease and injury commonly referred to as astrocyte activation states (Sofroniew, 2020). Over the past three decades, experimental studies investigating the dynamic nature of these cells have elucidated morphological, transcriptional, and physiological changes that can occur. These changes are known to powerfully influence outcomes in all types of CNS disorders, demonstrating the ability of these cells to respond to a repertoire of diverse molecular signals arising from any given number of cell types.

Initially, it was believed that astrocytes represented a homogenous population, however, careful investigation of these cells has revealed heterogenicity both morphologically and functionally, within singular brain regions as well as across multiple brain regions (Matias et al., 2019). Recently conducted regional single cell sequencing of astrocytes highlighted the extent of diversity where 70% of enriched sequences were specific to a single subtype (Batiuk et al., 2020). The recognition of spatial distinct astrocytic subpopulations enhanced the need for a commonly recognized nomenclature within the field. Hence, the capacity of these cells to adapt and respond has further been broken down into what is known as astrocyte ‘states’ and it is important to note that the state of an individual astrocyte can progressively change and revert to the original state

rendering each individual cell as dynamic and continually adapting to the surrounding environment. Of these, there are two reactive opposing states that an A0, resting ramified, astrocyte may dynamically adopt and are as follows: neurotoxic astrocytes (A1; pro-inflammatory) or neuroprotective astrocytes (A2; anti-inflammatory). However, it is important to note that because of the immense complexity of astrocytic responses, there is no prototypical neurotoxic or neuroprotective astrocyte nor is there a strictly binary phenotyping system available; rather, reactive astrocytes may adopt multiple states depending upon the stimulus, individual, previous exposures, biological sex, brain region, and genetic factors resulting in only a minute fraction of common changes between different states (Liddelow et al., 2017; Guttenplan et al., 2020; Escartin et al., 2021). This only adds to the complexity of the characterization of the cellular responses in the investigation of neurodegeneration. For the purposes of these studies and ease of condensed descriptions, neurotoxic astrocytes will be further referred to as A1 and neuroprotective astrocytes will be further referred to as A2.

1.3.1.1 Detection of A1 Neurotoxic Astrocytes

Reactive astrocytes are among those that have undergone morphologic, molecular, and functional changes in response to a pathological stimulation (Escartin et al., 2021). The first description of a 'reactive astrocyte' occurred in the 1970s with the discovery of glial fibrillary acidic protein (GFAP) (Eng et al., 1971; Eng et al., 2000). This quickly became the standard marker utilized to identify 'activated' astrocytes, despite cell-cycle dependent expression and evidence of regulation by a large number of inter- and intra-cellular signaling molecules functioning at regional and local capacities (Malatesta et al., 2003; Sofroniew and Vinters, 2010). It is important to realize that previous morphometric characterization of astrocytes based on GFAP

expression is insufficient in and of itself, being that the volume accessed by reactive astrocytes does not change, as they remain in their respective territorial domains (Wilhelmsson et al., 2006). Updated detection methods accounting for proliferation and cell cycle state have allowed for more sensitive detection of the continuum of activation profiles these cells may possess. Identification now include proteins and genes associated with the cytoskeleton (GFAP, Nestin, Synemin, Vimentin), cellular metabolism (ALDOC, BLBP/FABP7, MAO-B, TSPO), chaperone proteins (CRYAB/HSPB1/HSP27), secreted proteins (Serping1, C3, CHI3l1/YKL40, Lcn2, Serpina3n/ACT, MT, THBS-1), cell signaling/transcription factors (NFAT, NTRK2/TrkB IL17R, S100β, SOX9, STAT3), and channels/transporters (Glutamate transporter, K^+ channel) (Escartin et al., 2021; Fan and Huo, 2021). It has become apparent that precise detection of activated astrocytes in disease associated regions requires multifactorial analysis of hundreds of variables, which is unrealistic in individual experiment cases where time constraints and experimental cost are limiting factors. However, accurate quantification of at least two-three parameters has become common place to further understand the implications of activated astrocytes in neurodegenerative diseases (Escartin et al., 2021).

1.3.1.2 Detection of A2 Neuroprotective Astrocytes

A2 astrocytes are believed to provide trophic support promoting reparative functions, survival, and growth of neurons (Fan and Huo, 2021). Importantly, these astrocytes have increased abilities to uptake glutamate and decrease inflammatory factors through cell-cell communication with adjacent astrocytes and microglia. Identification of this subtype of cell is possible through morphometric, transcriptional, and proteomic analysis. Astrocytes are capable of rapid and reversible structural remodeling. These changes can occur in a matter of hours and hold importance

in the ability of the astrocyte to switch in tandem with brain state switch. Interestingly, A2 morphometric remodeling has been observed in states of natural sleep and general anesthesia (Zhou et al., 2019; Pandey et al., 2022). Typical A2 astrocytes have extensive connectivity territories that are highly complex with diameters of ~40-60μm and volumes on the order of 10^4μm (Bushong et al., 2002; Ogata and Kosaka, 2002; Chai et al., 2017; Zhou et al., 2019). Morphometric and structural determination of astrocytes, however, remains highly brain region specific and time intensive. Due to the complexity, and regional variability in astrocyte phenotype, transcriptional and proteomic advancements have helped to identify distinct transcriptomic signatures associated with an A2 phenotype. Upregulation of several protein and transcriptional markers have been attributed to A2 astrocytes including transforming growth factor β (TGFβ), vascular endothelial growth factor (VEGF), pentraxin 3 (PTX3), atypical chemokine receptor 7 (CXCR7), signal transducer and activator of transcription 3 (STAT3), prostaglandin E2 (PGE2), S100 calcium binding protein A10 (S100A10), sphingosine 1-phosphate receptor 3 (S1PR3), tumor necrosis factor (TNF) related weak inducer of apoptosis (TWEAK), interleukin 6 (IL-6), and interleukin 10 (IL-10) (King et al., 2020; Zong et al., 2020; Fan and Huo, 2021). Successful identification of this sub-type of cell will only aid in the overall understanding of neurodegenerative diseases and may potentially allow for therapeutic targeting to ameliorate pathology associated with activated, neuroinflammatory astrocytes.

1.3.2 Microglia

Microglia make up another sub-population of the neurovascular unit and arise from embryonic yolk-sac macrophages (Tay et al., 2017). These cells are unique in that they are capable of performing context dependent self-renewal to ensure population maintenance; unlike short-

lived peripheral macrophages that arise from the bone marrow (Ginhoux and Prinz, 2015). Like astrocytes, binary naming strategies have been implemented to identify different states that microglia can dynamically adopt, where M1 identifies inflammatory ameboid microglia and M2 identifies ramified resting microglia. Recent studies have demonstrated that during ontogeny the brain is permanently organized as male- or female-typical in a process known as sexual differentiation (Lenz and Nelson, 2018). These states are induced by steroid hormones where male total microglial populations are increased compared to females and the microglia adopted more ameboid morphologies. Female microglia have been observed to be more ramified in state and express the purinergic receptor P2YR4 (Nelson and Lenz, 2017). Female microglia are also known to have functionally higher levels of phagocytic gene expression and overall increased abilities to perform phagocytosis (Lenz and Nelson, 2018). Importantly, these sex-differences may very well predetermine exposure- and age- dependent innate and adaptive immune responses in the brain.

Microglial cells have been traditionally regarded as macrophages of the CNS; however, compounding research suggests that these cells are distinct in their function and have some, but not full, resemblance to their peripheral counterpart, the macrophage. Similar to the macrophage, microglia retain the responsibility of being the primary respondent to environmental changes and subsequently orchestrating the appropriate responses to resolve the perceived danger. These glial cells have been shown to express a wide variety of functional toll-like receptors (TLRs) that recognizing pathogen associated molecular patterns (PAMPs) that induce the hallmark innate immune function of phagocytosis (Olson and Miller, 2004). TLR associated stimulation also recapitulated the production and secretion of pro-inflammatory innate cytokines like TNFα and IL-6 (Town et al., 2005). Several studies have demonstrated that LPS induced TLR4 signaling and

was capable of activating nuclear factor kappa B (NF-κB) pro-inflammatory cascades, much like responses initiated by macrophages in the periphery (Papageorgiou et al., 2016).

Sizable contributions to literature within the last decade have implicated that microglial cells may not only have a function as innate surveyors, but may retain some form of 'memory' through inflammatory priming events that allows them to function as an adaptive immune cells. A primed microglial profile is determined by 1) increased basal expression of inflammatory markers and mediators, 2) a lower threshold required to become activated and adopted M1 inflammatory state, and 3) an exaggerated inflammatory response upon stimulus (Norden et al., 2015). Primed microglial cells are thought to function in parallel to what an antigen presenting (APC) in the periphery would, with increased phagocytic ability and upregulated presentation of pathogenic peptides on major histocompatibility complex II (MHCII) domains. In addition to this, revolutionary experimentation has demonstrated that as a population, microglia are long-live cells, however, at an individual cellular level, they are not. Microglial cells die and regenerate as rapidly as every week, where the dynamics and the positions of the individual cells change. This observation, in part with the ideology of priming occurring through exposures that are separated by substantial amounts of time, has indicated that microglial 'memory' acquisition must happen through epigenetic (inheritable) changes that alter the responsive capability of these cells or that the 'memory' is held elsewhere within the neurovascular unit (Askew et al., 2017; Zhang et al., 2022). Substantial evidence has been put forth to support the former, indicating that a combination of exposure induced epigenetic changes acquired throughout the lifespan may be responsible for the aberrant activation of primed microglia (Zhang et al., 2022). It has also been shown that microglia can facilitate neuron-T-cell interaction and can directly interact with T-cells via cluster

of differentiation molecule 40 ligand and cluster of differentiation molecule 40 (CD40l/CD40) stimulation, which is believed to further induce a state of adaptive or trained immunity.

1.3.3 T-cells and Peripheral Macrophages

Although concerted efforts have focused on elucidating microglial innate and trained immunological responses, the direct interactions between peripherally invading immune cells and microglial cells remains less established (Subbarayan et al., 2020). Typically, peripheral immune cells are restricted from accessing the CNS by implementation of the BBB. However, upon toxic stimulus, glial cells produce molecules capable of increasing the permeability of the tight junctions of the BBB, allowing peripheral immune cells to infiltrate into the brain. Of concern, these cells are adapted to mounting widespread inflammation that is not conducive to maintaining the homeostatic environment of the brain. *Postmortem* examination of PD patients has revealed the presence of non-microglial myeloid derived cells, most likely invading monocytes (Harms et al., 2021). Recognition of brain derived chemokine C-C motif ligand 2 (CCL2) is recognized by C-C chemokine receptor type 2 (CCR2) expressing monocytes, encouraging extravasation into the brain (Harms et al., 2018), where inhibition of this signaling access was neuroprotective (Harms et al., 2021). *Postmortem* analysis also confirmed the presence of both cluster of differentiation molecule 8 positive ($CD8^+$) cytotoxic T-cells and cluster of differentiation molecule 4 positive ($CD4^+$) helper T-cells, indicating that pathophysiological environments created by glial-glial and glial-neuronal interactions may assist in extravasation from vessels into the brain (Brochard et al., 2009). Moreover, increased monocyte and T-cell infiltration correspond with disease severity, suggesting that antigen presentation and MHCII upregulation through adaptive immunity are critical factors in the

modulation of overarching disease pathology. Recent research has shown the prevalence of $CD4^+$ T-cells that are capable of recognizing and responding to MHCII epitopes derived from α-syn, the protein that is known to misfold in PD (Schetters et al., 2017; Sulzer et al., 2017). The combined, complex, and admittedly enigmatic interactions of the multiple cell types, native and foreign, innate and adaptive, in the brain compound the effects of PD and unequivocally lead to microenvironment shifts that foster progressive pathology.

1.4 Protein Misfolding and Aggregation

Proper protein production and sequential coordinated interactions determine outcomes of numerous cellular processes. To date, there are approximately 30,000 different proteins encoded by the human genome which function individually and in concert to effectively carry-out complex physiologic functions that allow for survival (Kumar et al., 2016). Production of proteins begins from generation of coding messenger RNA (mRNA) sequences that are recognized by ribosomes. Ribosomes in effect act as the translators of the cell; they identify the coding mRNA sequences and generate linear amino acid chains, in a process appropriately known as translation. Post-translational modifications aid in the folding of the linear sequence into a three-dimensional physiologically active conformation. Some proteins undergo spontaneous folding while others rely on post-translational modifications and secondary molecular interactions to ultimately determine the tertiary state. In any case, the possibility of protein misfolding can occur.

There are inherent mechanisms within cells that combat the misfolding of proteins. These processes are highly regulated and sophisticated and include two major branches, autophagy and the ubiquitin proteosome system (UPS). Alterations in these systems along with somatic mutations, transcriptional and/or translational errors, breakdown of the protein folding and

chaperone machinery, erroneous post-translational modifications, and structural modifications driven by microenvironment changes are largely implicated in neurodegenerative diseases including PD, Alzheimer's Disease (AD), Huntington's Disease, prion diseases, and frontotemporal dementia, to name a few (Kelly, 1996; Soto, 2001; McNaught et al., 2003; Nixon et al., 2005; Wang et al., 2008; Yen, 2011; Thibaudeau et al., 2018). In each of these diseases, aggregation of misfolded proteins occurs when natively buried hydrophobic amino acid residues are exposed due to intermediate state or partial folding of the protein. Hydrophobic forces propel misfolding and ultimately result in the formation of structurally diverse aggregates, oligomers, and amyloid fibrils (Jahn and Radford, 2008; Tartaglia et al., 2008). Thus, highly soluble proteins containing α-helical structures are converted into insoluble, filamentous polymers that are cross-β-pleated sheet rich (Kumar et al., 2016). Recent hypotheses in the field suggest that misfolded proteins propagate in a prion-like fashion where the initial misfolded protein acts as a 'seed' (Soto, 2012; Goedert, 2015; Walker and Jucker, 2015; Stopschinski and Diamond, 2017). The seed then sporadically induces conformational misfolding of native proteins that are identical to or share high homology with the originally misfolded isoform. The resulting misfolding kinetics and aggregation state is believed to proceed through nucleation-dependent polymerization (Jarrett and Lansbury, 1993). Formation of bona fide aggregate nuclei is widely accepted as the rate-limiting step (Kelly, 1998), followed by intermediate species formation. The intermediate species can be composed of oligomers or protofibrils that intrinsically favor pore-like and tubular structures (Lashuel et al., 2002; Poirier et al., 2002). Progressive aggregate assembly occurs exponentially post-nuclear formation and involves the association and incorporation of monomers and/or oligomers (Moreno-Gonzalez and Soto, 2011; Cohen et al., 2012) which sequentially spread cell-to-cell, supporting the regional pathological progression of neurodegenerative diseases.

Although misfolded protein aggregation and dissemination is prevalent in numerous neurodegenerative diseases, structural and strain identification through biochemical testing modalities remains difficult due to the inherent insoluble nature of these protein formations. Recently, several studies have identified structurally unique conformational strains of misfolded aggregates composed of amyloid-β, tau, and α-syn, the misfolded proteins commonly observed in AD and PD (Bousset et al., 2013; Guo et al., 2013; Lesne, 2014; Watts et al., 2014; Kaufman et al., 2016; Narasimhan et al., 2017; Soto and Pritzkow, 2018; Shahnawaz et al., 2020). These findings provide critical evidence supporting the heterogeneity of aggregate strains and suggest a protein conformation specific molecular explanation for clinically distinct presentations in neurodegenerative diseases (Melki, 2015; Narasimhan et al., 2017).

It was previously accepted that the misfolding of an individual protein had unique pathological implications in singular neurodegenerative diseases. However, recent additions to the body of literature suggest that multiple neurodegenerative diseases may share significant overlap, where the misfolding of individual proteins is regionally distinct and dependent upon the initial insult. Yet, the ensuing changes in the microenvironment of the brain may facilitate structural remodeling of other disease related proteins with the capacity to form amyloid-like aggregates (Clinton et al., 2010; Frost and Diamond, 2010; Westermark and Westermark, 2010). The exact pathophysiological association between a misfolded protein(s) and the process of neurodegeneration remains unclear. Nonetheless, studies aimed at identification of proteinaceous components have implicated α-syn as a protein of interest in sporadic PD, Lewy-body dementia, Lewy body variant of AD, Down syndrome, Multiple System Atrophy, neurodegeneration with brain iron accumulation, traumatic brain injury (TBI), Pick disease, and Amyotrophic lateral sclerosis (ALS) (Galvin et al., 2001; Hardenberg et al., 2021).

1.4.1 α-Synuclein

α-Syn is a highly conserved 140-amino-acid protein that is abundantly expressed in neurons and is localized to the pre-synaptic terminal, nucleus (Maroteaux et al., 1988), mitochondria (Li et al., 2007), endoplasmic reticulum (Hoozemans et al., 2007), Golgi apparatus (Gosavi et al., 2002; Mori et al., 2002), and endolysosome (Goedert, 2001; Lee et al., 2004; Bernal-Conde et al., 2019). This protein is encoded by the *SNCA* gene and accounts for 1% of cytosolic protein in the brain, yet the precise physiological role is unknown. Initially, biochemical studies conducted *in vitro* proposed the main physiological function of α-syn was based on association of the protein with the high curvature membranes of synaptic vesicles, of which has become highly controversial due to the lack of *in vivo* replicability, non-uniform expression on neuronal boutons, weak membrane-interaction patterns with synaptic vesicles, and apparent dispersion of α-syn into axons (Burre et al., 2018; Huang et al., 2019; Sulzer and Edwards, 2019). Because ultimate functionality relates to sequence and structure, concerted efforts have been mounted to better characterize α-syn. This protein contains an amphipathic lysine-rich amino terminus, that facilitates membrane association, and an inherently disordered acidic carboxyl-terminal tail. The apparent multi-functional properties of α-syn may be in part due to the flexibility of this tail, allowing the protein to adopt numerous conformations upon interaction with biologically unique membranes, proteins, protein complexes, small molecules, metals, or pathogens (Eliezer et al., 2001; Ulmer et al., 2005; Ramakrishnan et al., 2006; Ullman et al., 2011; Lashuel et al., 2013; Massey and Beckham, 2016). Under physiologic conditions, α-syn can exist dynamically as unfolded cytosolic monomers, membrane bound monomers or tetramers. When the delicate

equilibrium between these forms is disrupted and levels of unfolded α-syn monomers increase, oligomer formation and aggregation is favored (Gomez-Benito et al., 2020).

Although there is lingering controversy regarding the exact biological function of native α-syn, it is widely acknowledged that accumulation of fibrillar forms of this protein is one of the primary constituents of Lewy bodies (Gibb and Lees, 1988; Burre et al., 2015). Lewy bodies are spherical inclusions located in the cytoplasm of surviving DAn of the SNpc that are present in late-stage PD *postmortem* samples. Often, there are multiple Lewy bodies present within a single neuron, where aggregated fibrillar α-syn is localized to the 'halo' of the Lewy body and the focal center consists of PARK2 and ubiquitin-positive domains (Riederer et al., 2019). There is intense debate as to the cytotoxic effects of α-syn species, despite research supporting the toxic capacity of both oligomers and fibrils (Peelaerts et al., 2015; Miraglia et al., 2018), however, recent investigation suggest that oligomers and protofibrils formed in the early stages of misfolding are highly neurotoxic and cause the cell death that is observed in PD. Yet, fibril species appear to be the most effective at propagating and inducing prion-like cell-to-cell and tissue-to-tissue spread and progression of the disease (Alam et al., 2019; Mehra et al., 2019).

Although there are numerous study results that support prion-like propagation and spread of α-syn, modern observations have challenged this hypothesis. Early characterization and gross examination that led to the birth of Braak staging only accounts for specific target neuronal sub-populations. As previously stated, protein misfolding in neurodegenerative diseases may very well be a multi-facetted time sensitive disease involving more than one misfolded type of protein, where initial characterization relied solely on *postmortem* patient samples which in effect added timepoint bias. Therefore, it remains unclear if the biochemical process and result of α-syn misfolding is a cause of or a mere result of disease. Aiming to address this centuries-long question,

a new functional hypothesis has taken the forefront of PD research. This idea proposed that selective vulnerability of DAn populations and the misfolding of α-syn was due to adverse stimuli receive from surrounding glial cells in the process of neuroinflammation.

1.5 Neuroinflammation

Although the exact impact that glial cells have in PD remains largely unknown, tremendous advancements in technology within the past decade have aided in the production of evidence suggesting that neurodegeneration of DAn within the SNpc is due to the pathophysiological response mounted by resident glial cells. Traditional immunology has long considered the brain and CNS an immune privileged site, however, cellular responses specialized to the delicate environment of the brain can be initiated in response to pathogens or disease associated signals. Chronic inflammation produced by microglia and astrocytes remains consistently associated with the severity and progressive pathological states of PD. Studies utilizing 6-hydroxy-dopamine (6-OHDA) and MPTP exemplify induction of dopaminergic neurodegeneration through increases of the pro-inflammatory cytokines TNF-α, interferon γ (INF- γ), interleukin 1 β (IL-1β), interleukin 2 (IL-2), IL-6, inducible nitric oxide synthase (NOS2), and NF-κB (Goes et al., 2018; Troncoso-Escudero et al., 2018).

One glial cell that is capable of producing NOS2, chemokine C-C motif ligand 5 (CCL5), CCL2, TNF-α and IL-1β are astrocytes. Chronologically, it has yet to be understood if astrocytes trigger the inflammatory cascade achieved through cell-cell communication, that leads to neurodegeneration. Curiously, astrocyte changes are observed in PD relevant brain regions in human patients during the onset of symptomology, indicating that these cell may play an important role in the initiation of the disease process (Wakabayashi et al., 2000). These cells have intimate

proximity to neurons and, in diseased state, are observed to down-regulate glutamate receptors and increase α-syn up-take, both of which may contribute to the progressive pathology that is observed in PD (Gu et al., 2010). Severity of neuronal loss has been positively correlated with α-syn accumulation within astrocytes of the SN and extra nigral regions in PD patients (Wakabayashi et al., 2000). Furthermore, immunoreactive astrocytes harboring misfolded α-syn aggregates appear to accompany the formation of Lewy bodies and neurites. Compelling evidence from our lab has shown that when IκB kinase 2 (IKK2) is inhibited in astrocytes and animals are challenged with chemical or pathogenic initiators of PD, neuroprotection is achieved (Hammond et al., 2020; Bantle et al., 2021b). These recent findings support the idea that astrocytes, in some capacity, are modulating inflammatory signaling. Whether that be astrocyte-astrocyte, astrocyte-neuron, or astrocyte-microglia has yet to be determined.

Microglial inflammatory signals, including production and release of complement C1q A-chain (C1qA), interleukin 1 α (IL-1α), and TNF, have been shown to activate astrocytes and induce A1 phenotypic conversion, also implicating this cell as a potential driver of neuroinflammation (Liddelow et al., 2017). The association of microglia and PD is long-standing and began in 1988 with the report of increased human leukocyte antigen-DR isotype positive ($HLA\text{-}DR^{+}$) microglia in the SN of PD patients (McGeer et al., 1988). Microglial mediated neurotoxicity in PD tends to be progressive, which could explain the pathological process that spans multiple decades (Block et al., 2007). Microglial cells are capable of mounting neuroinflammatory responses based on positive stimulation of TLRs, scavenger receptors, and macrophage antigen 1 (MAC-1) receptors. Microglia remain a unique glial sub-type in that there is evidence that these cells have the capacity to be 'trained' or retain a pseudo-adaptive immunological role. In fact, multi-exposure environmental models utilizing pesticides, heavy

metals, bacterial toxins, and diesel exhaust particles can directly affect neuronal survival but also tangentially determine neuronal fate through microglial immunological priming (Perry and Holmes, 2014). The exacerbated inflammatory effect that follows glial priming could very-well be the chronic stimuli that perpetuates this disease. Factors that are known to be produced by activated microglia in PD are TNF-α, Il-6, NOS2, cyclooxygenase 2 (COX2), and ROS which are all known products of the transcriptional regulator, NF-κB (Pizzi and Spano, 2006; Marogianni et al., 2020).

1.6 NF-κB

NF-κB is a ubiquitous pleotropic transcriptional regulator that targets genes responsible for physiological function as well as pathological processes associate with neurodegeneration (Crampton and O'Keeffe, 2013; Lanzillotta et al., 2015). NF-κB is a member in a family of transcriptional regulators that is controlled by inhibitory κB's (IκB). IκBs are bound to NF-κB complexes in the cytosol, ultimately inhibiting translocation to the nucleus and gene transcription. Upon cellular stimulation from receptor binding and recognition, IκB subunits are phosphorylated by IKK complexes which target them for polyubiquitination and recognition by the 26s proteosome. The degradation of IκBs liberate the active NF-κB complex and allows for translocation to the nucleus. Importantly, the IKK complex consists of two catalytic subunits, IKKα/IKK1 and IKKβ/IKK2, and a third subunit termed IKKγ. IKKα/IKK1 is involved in what is known as the alternative/non-canonical NF-κB activation, whereas IKKβ/IKK2 is responsible for NF-κB activation in the classical/canonical pathways. The canonical pathway involves the activation of the dimers p50 and p65/RelA which function in the process of immunoregulation, exerting transcripts that determine the appropriate innate immune response needed to address the

stimulus that was initially received. Immunohistochemical analysis of *postmortem* brain tissue from PD patients has revealed 70-fold increases in the proportions of DAn in the SN exhibiting nuclear p65 (Hunot et al., 1997). Due to the apparent immune regulation that this transcriptional factor has demonstrated, along with the increased prevalence within PD patient samples, it has become an attractive target for therapeutic intervention. However, the functional roll of the canonical NF-κB pathway in association with glial cell subpopulations, innate immunity, learned/primed immunity, protein aggregation, and neurodegeneration has yet to be fully elucidated.

1.7 Summary

Advancements in the last decade have underscored the importance of glial cells in the progressive pathology of multiple neurodegenerative diseases, specifically PD. The unknown etiology, accounting for ~90% of diagnosed cases only enhances the idea that environmental exposures to heavy metals, pesticides, and pathogens may be responsible for priming, inducing, modulating, and exacerbating the neuroinflammatory responses that are thought to lead to neurodegeneration. Microglia, the primary immune cell type of the brain, have gained considerable attention for their capability to recognize danger signals released by astrocytes and neurons, in addition to producing equal, if not greater, inflammatory signals. Accumulating evidence supports that activation of microglial innate immunity, driven by the canonical NF-κB pathway, is highly associated with PD severity and neurodegeneration. Aside from the immense complexity of the overarching pathophysiology of idiopathic PD, complexity at the individual cellular level has been elucidated, more specifically, by the ability of microglia to 'learn' by prior stimuli. These stimuli that are encountered throughout an individual's lifetime can lead to epigenetic alterations that are

heritably acquired in the distinct population of myeloid derived cells in the brain. These genetic alterations subsequently act as targeting messages for transcriptional regulators, like NF-κB, producing more rapid and toxic results. Yet, a precise understanding of disease chronology resulting from environmental exposures, microglial innate immunity during single exposures and microglial trained or adaptive immunity following multiple exposures remains largely unknown. Given this, we postulated that inhibition of microglial NF-κB would ultimately reduce glial mediated inflammation, α-syn protein misfolding and aggregation, and dopaminergic neurodegeneration in both single-exposure and multi-exposure models of PD, denoting microglial NF-κB as a potential therapeutic target in the progression of the disease.

To investigate the pathological progression of rotenone-induced neurodegeneration in a mouse model of PD, we conducted a time course study to examine various neuropathological parameters at multiple timepoints beginning at the conclusion of rotenone treatment, followed by further assessment at one week and two weeks post-rotenone administration. Quantification of microglial reactivity and recruitment, astrocyte activation, loss of DAn, and aggregation of α-synuclein protein allowed for modeling changes in these parameters by time, cell type and brain region in response to neurotoxin exposure. Developing such a comprehensive model of temporal and spatial changes in cellular phenotype revealed the complex interplay of each of these factors in the overall progression of rotenone-induced neuropathology (Chapter 2). To better understand the inflammatory contribution that microglial cells have in PD progression, we generated microglial specific IKK2/NF-κB KO animals. These animals were administered rotenone as described in Chapter 2. Quantification of pathological changes was determined through the extent of microglial recruitment and morphological changes in individual microglial cells, astrocytic activation, neurodegeneration, protein aggregation and transcriptional regulation of inflammatory

genes within the SN. These analyses were conducted separately in males and females to identify sex-specific changes within each of the individual cellular parameters under investigation (Chapter 3). Finally, to determine how the inflammatory activation of microglial cells contributed to multiple exposure scenarios, we investigated the possible 'priming' of microglia by administering Mn to animals during the juvenile stages, followed by rotenone exposure as adults. Microglial-specific IKK2 KO male animals were utilized in this study, where all parameters previously described in Chapter 3 were applied (Chapter 4).

The results presented herein represent the first description of progressive neuropathological changes in a mouse model of rotenone-induced parkinsonism using the 14-day systemic exposure paradigm first developed in rat. This approach permitted us to successfully model the neuroinflammatory and neurodegenerative features of chronic low level rotenone exposure, in addition to the complex cellular interactions that mediate the process of neurodegeneration. As detailed in the following chapters, microglial cells play essential roles in the induction of innate immune inflammation driven by NF-κB, where complex autophagy machinery, specific to microglia, that is driven by NF-κB is responsible for the degradation of misfolded α-synuclein. However, potential epigenetic alterations that take place during microglial 'priming' may activate other transcriptional regulation pathways that are independent of canonical NF-κB, and are still capable of inducing inflammatory products that leads to neurodegeneration of DAn in the SNpc. These data highlight the dynamic ability of brain regions, cells, and sub cellular components in the process of disease and further underscore the dramatic differences between male and female animals in the response to environmental toxin exposures.

CHAPTER 2

ROTENONE INDUCES REGIONALLY DISTINCT α-SYNUCLEIN PROTEIN AGGREGATION AND ACTIVATION OF GLIA PRIOR TO LOSS OF DOPAMINERGIC NEURONS IN C57BL/6 MICE[1]

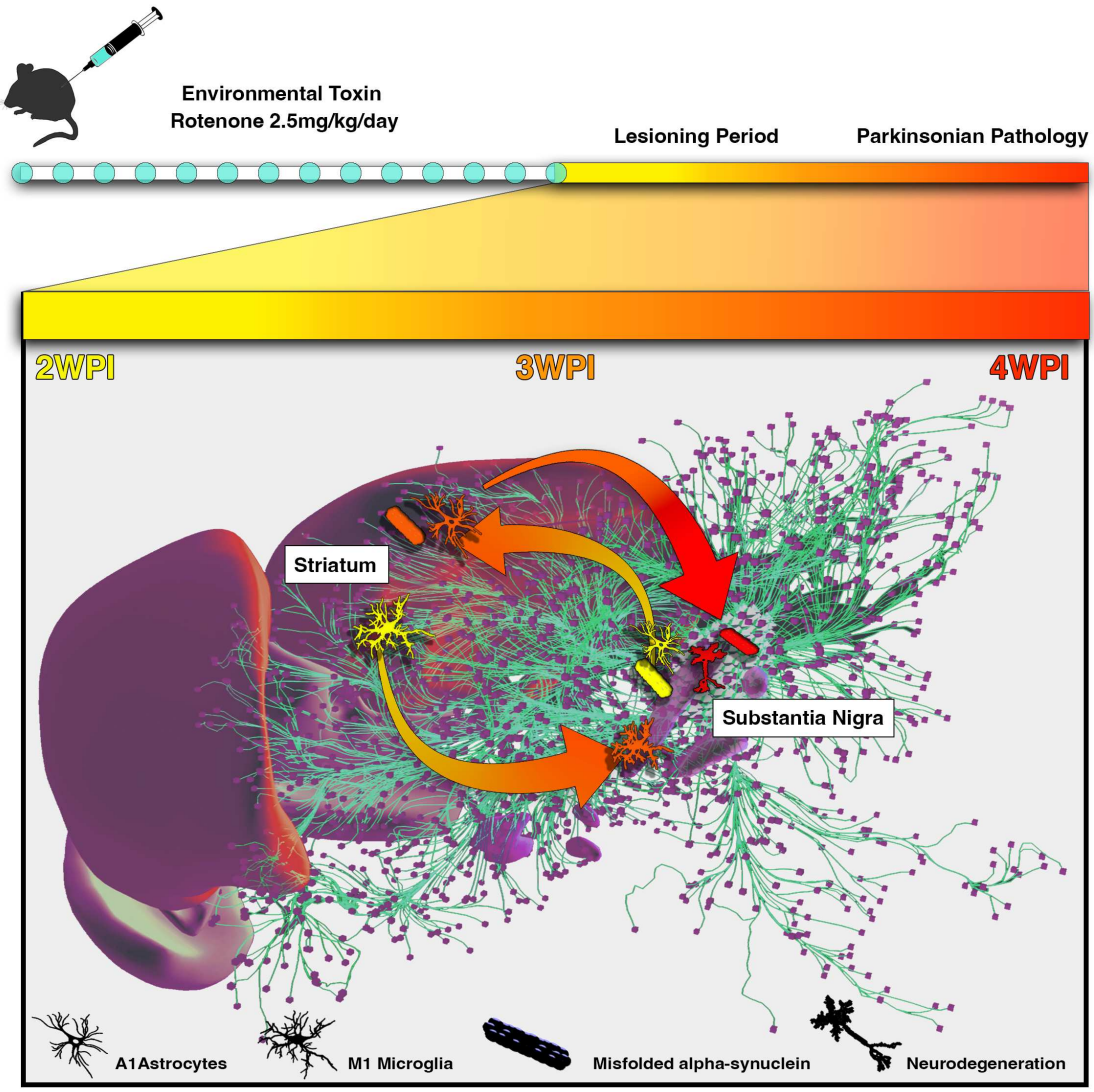

Figure 1. Graphical abstract of time dependent pathological progression of PD in rotenone exposure. Three-dimensional spatial progression of astrocyte activation, microglial recruitment, α-synuclein misfolding and neurodegeneration of dopaminergic neurons in the novel rotenone induced Parkinson's Disease model in C57Bl/6 mice.

[1] Copyright a 2022 by Neurobiology of Disease

2.1 Introduction

PD is a debilitating movement disorder affecting the CNS and the second most common neurodegenerative disease worldwide (Halliday et al., 2011; Pringsheim et al., 2014). PD is characterized by loss of DAn in the SNpc, loss of striatal DA, neuroinflammatory activation of glial cells and aggregation of the phosphorylated form of α-syn (phospho-serine 129/p129) (Samii et al., 2004; Grayson, 2016; Rocha et al., 2018; Domingues et al., 2020). There are no disease modifying therapies for PD in part because of limitations in many of the standard animal models used to study PD including a lack of critical features relevant to the idiopathic disease (Schober, 2004; Radhakrishnan and Goyal, 2018). Two widely used models that induce loss of DAn involve administration of the neurotoxins MPTP and 6-OHDA. However, there are aspects of these models that differ significantly from idiopathic PD, including the absence of p129-α-syn aggregates. The progressive development and spread of p129-α-syn aggregates leading to Lewy body formation in the SNpc is the central neuropathological feature of PD but is notoriously difficult to recapitulate in mice. Because the etiology and progression of PD is complex, involving genetic, environmental, and biological factors, as well as early and progressive neuroinflammatory changes in glial cells, additional models that more closely recapitulate the neurological and pathological deficits observed in PD are necessary to study disease mechanisms.

It has been shown that systemic administration of pesticides which inhibit mitochondrial complex I, such as paraquat, maneb and rotenone, can cause selective loss of DAn in the SNpc and might better recapitulate certain clinical and pathological features of PD than other neurotoxin-based models (Giasson and Lee, 2000; Kamel et al., 2007; Tanner et al., 2011; Johnson and Bobrovskaya, 2015). Rotenone, in particular, is a potent systemic inhibitor of mitochondrial complex I that results in high levels of ROS and peroxynitrate, as well as neuroinflammation and

progressive accumulation of p129-α-syn aggregates within neuronal dendrites and soma (Betarbet et al., 2000; Cannon et al., 2009). Rotenone is distributed and used worldwide as a pesticide and piscicide to reduce crop destruction and invasive fish species (Radad et al., 2019). Despite evidence that rotenone is associated with increased risk for PD, it is still used within the USA, Canada and 30 other countries worldwide (Betarbet et al., 2000; EPA., 2007; Guenther, 2011). Amongst pesticides that inhibit mitochondrial complex I, rotenone closely models pathological features of PD in both mammalian and non-mammalian species. Non-mammalian models of rotenone-induced dopaminergic neurotoxicity utilizing *Caenorhabditis elegans*, drosophila, zebrafish and *Lymnaea stagnalis* have been successful in achieving DAn cell loss and motor deficits following exposure (Vehovszky et al., 2007; Harrington et al., 2010; Hirth, 2010; Fontana et al., 2018). These models allow for rapid, high-throughput screening methodologies to investigate potential therapeutics and environmental exposures but are limited with respect to the array of motor and non-motor neurological symptoms that can be modeled, as well as the spread of p129 α-syn aggregates across teleologically relevant brain regions (Lim, 2010; Dung and Thao, 2018). In contrast, systemic rotenone exposure in Lewis rats induces behavioral deficits, loss of DAn and formation of Lewy bodies, closely mirroring the pathological changes seen in PD (Heikkila et al., 1985; Betarbet et al., 2000; Cannon et al., 2009). However, it has proven challenging to adapt this model to mice due to variations in lesion profiles and high mortality rates (Johnson and Bobrovskaya, 2015). This precludes the advantages offered by a greater array of transgenic mouse lines to study signaling pathways and molecular mechanisms. Attempts to orally deliver rotenone in mice take at least two months (Inden et al., 2011; Liu et al., 2017b), thus decreasing throughput for analyzing the therapeutic efficacy of pharmacologic and genetic interventions in the disease process.

We set out to characterize the efficacy of a 14 day systemic rotenone model used in Lewis rats by Greenamyre and colleagues (Betarbet et al., 2000; Sherer et al., 2003; Cannon et al., 2009) in eliciting PD-like neuropathological changes in mice, with particular emphasis on the capacity of this route of administration to promote progressive neuroinflammation and the formation of p129 aggregates. The key neuropathological features examined within lesioned brain regions included vacuolation of nerve cells, neuronal loss within the basal midbrain spatially progressing in a latero-temporal manor, glial cell activation and the accumulation of p129 aggregates within neurons. These changes were examined weekly across entire serial brain sections using scanning microscopy starting at the conclusion of the rotenone dosing period at 2 weeks through the end of the study at 4 weeks. This approach permitted the quantification of both regional and temporal patterns of gliosis, neuronal loss and p129 across multiple brain regions throughout the entire dosing and lesioning period. The results of this analysis revealed distinct patterns of neuropathology with maximal loss of DAn occurring nearly two weeks after the end of rotenone administration (4 WPI), after the peak of glial activation and coinciding with p129 aggregation. These data suggest that induction of p129 is a stress response to rotenone-induced mitochondrial dysfunction and that glial inflammatory responses are a key potentiator of both p129 aggregation and neuronal injury in this rotenone model of PD in mice.

2.2 Materials and Methods

3.3.10 Animals and In vivo Imaging

All animal protocols were approved by the Institutional Animal Care and Use Committee at Colorado State University (IACUC), mice were handled in compliance with the PHS Policy and Guide for the Care and Use of Laboratory Animals and procedures were performed in accordance with National Institutes of Health (NIH) guidelines. Mice were housed in microisolator cages (3-4 animals per cage), kept on a 12-h light/dark cycle and had access to both food and water *ad libitum*. Male and female C57Bl/6 background mice were used in studies at 2 months of age (*n*=12/control, *n*=21/rotenone). Male and female homozygous Tg(HIV-EGFP,luc)8Tsb/J mice were obtained from The Jackson Laboratory (Stock No. 027529, Bar Harbor ME) and bred to homozygosity onto a C57Bl/6 background for use in this study (*n*=8/control, *n*=9/rotenone). For imaging luciferase reporter activity *in situ*, Tg(HIV-EGFP,luc)8Tsb/J mice (2 WPI: *n*=8 control, *n*=9 rotenone; 3 WPI: *n*=7 control, *n*=7 rotenone; 4 WPI: *n*=6 control, *n*=5 rotenone) were anesthetized at weekly timepoints following exposure with rotenone (2 WPI) and then given a subcutaneous dose of luciferin substrate (150mg/kg) to the dorsal cervical spine 17 minutes prior to imaging. Exposure time was kept consistent for all animals. Living Image Software was used to obtain and analyze images on the IVIS Spectrum *in vivo* imaging system utilizing epi-illumination three-dimensional (3D) diffuse fluorescence tomography.

2.2.2 Rotenone Preparation and Dosing

Rotenone was first prepared in a 50X stock solution that was diluted in 100% dimethyl sulfoxide (DMSO). The rotenone solution was then diluted in medium-chain triglyceride, Miglyol 812 (Cannon et al., 2009) to obtain final working concentrations of 2.5mg/kg at a dosage of

2µL/gram body weight in 98% miglyol and 2% DMSO. The rotenone was prepared fresh every other day. Rotenone powder was pipetted until thoroughly dissolved into DMSO. The stock solution was aliquoted into amber septa vials within a -20 °C freezer to avoid contact with light. The head space of the vial was purged with nitrogen to prevent oxidation of the compound. The optimal concentration of rotenone was determined from a dosing regimen consisting of intraperitoneal dosing daily for 14 days. Male and female C57Bl/6 mice (*n*=4/control group/time-point, *n*=7/rotenone group/time-point) were injected daily for 14 days with a dose of 2µL/g weight. Mice were weighed daily before injection to determine the appropriate dosing amount. The rotenone/miglyol was carefully measured using a 50µL Hamilton syringe and then transferred to an insulin syringe with permanently attached needle which was used to administer the volume of solution. Control animals received injections of miglyol only. Hamilton syringes were cleaned every-day after use to prevent precipitation buildup within the needle. The syringe and plunger were submersed in ten percent bleach for a duration of 10 minutes, then 70% ethanol (EtOH) was aspirated into the syringe followed by sterile water. The plunger was removed from the syringe and the instrument was allowed to air dry for 24 hours.

To identify the optimal dose of rotenone to induce loss of DAn, pilot studies were conducted in which mice were administered several concentrations of rotenone at different dosing schedules. Rotenone was dissolved in 100% Miglyol 812 as described above. The final dosage used in subsequent studies was determined by quantitative analysis of DAn numbers within the SNpc using design-based stereology and scanning fluorescence microscopy. Regions of interest (ROI) were mapped for the striatum (ST) and the SNpc. Male and female C57Bl/6 mice (*n*=4/group) were injected intraperitoneally with 2.0 mg/kg/day, 2.5 mg/Kg/day, 3.0 mg/kg/day and 1.4mg/kg twice daily. Twice daily dosing at 1.4 mg/Kg was highly toxic and omitted from

further evaluation. Mice were terminated 14 days after the initial rotenone dose and neurodegeneration was assessed. Based upon initial results and minimal mortalities, a dose of 2.5 mg/Kg/day was selected for use in the 4-week study (*n*=4 animals/control groups, *n*=7 animals/rotenone groups).

2.2.3 Open Field Behavioral Analysis

Open field activity was assessed using the Versamax behavioral system with an infrared beam grid detection array (Accuscan Instruments, Inc., Columbus, OH). Mice were monitored for 5 minutes under low ambient light in the presence of white noise. Animals were pre-conditioned to the chambers the day before exposure started. The animals were recorded 1 hour prior to initial injection (0 DPI) to establish a baseline. Several behavioral assessments were performed at weekly timepoints (1 WPI, 2 WPI, 3 WPI and 4 WPI). Multiple behavioral parameters were obtained and analyzed using Versadat Software (Accuscan Instruments, Inc.) including rearing number, center time, margin time and rest time. We previously reported that these locomotor and behavioral parameters are accurate determinants of basal ganglia function associated with loss of ST DA (Liu et al., 2006; Moreno et al., 2009b). Data is reported as change from baseline (0 DPI) behavioral assessment. (*n*=10/control, *n*=14/rotenone).

2.2.4 Tissue Extraction and Fixation

Based upon initial pilot studies of rotenone-induced neurodegeneration in the SNpc, it was determined that a timepoint of 14 days or 2 WPI directly following the conclusion of the rotenone exposure would represent the first time-point for neuropathological analysis. Groups of mice were also evaluated each week for an additional two weeks (3 and 4 WPI, respectively) to identify

neuropathological changes associated with progressive neuroinflammation following rotenone exposure. Mice (*n*=4/control group, *n*=7/rotenone group) were euthanized by isoflurane anesthesia followed by cardiac puncture. Perfusion-fixation was immediately performed using 20 mL of 0.1M phosphate buffered-saline (PBS) sodium cacodylate buffer supplemented with heparin followed by 20 mL of 4% paraformaldehyde. Brain tissue was carefully removed once fully perfused and post-fixed in 10% neutral buffered formalin (NBF) for two weeks at room temperature. The tissue was then dissected for cassette preparation, paraffin embedding, sectioning and histological examination.

2.2.5 Tissue Preparation and Automated High-throughput Immunofluorescent Staining

Paraffin embedded brain tissue was sectioned at 6µm thickness and mounted onto poly-ionic slides (Histotox Labs, Boulder, CO). Slides were deparaffinized and immunofluorescently labeled using a Leica Bond RX_m automated robotic staining system. Antigen retrieval was performed by using Bond Epitope Retrieval Solution 1 and 2 for 20 minutes in conjunction with heat application. Sections were then incubated with primary antibodies diluted in 0.1% triton-X containing PBS (TBS): rabbit tyrosine hydroxylase (TH; Millipore; 1:500), mouse anti-neuronal nuclei (NeuN; Millipore, 1:100), mouse anti-GFAP (Cell Signaling, 1:100), rabbit anti-S100 calcium binding protein β (S100β, Abcam; 1:750), rat anti-complement component 3 (C3, Abcam; 1:250), goat anti-ionized calcium binding adaptor molecule 1 (IBA1; Abcam; 1:50), and mouse anti-α-syn phosphorylation at serine position 129 (p129; Wako; 1:100). Sections were stained for 4', 6-diamidino-2-phenylindole (DAPI, Sigma) and mounted on glass coverslips in ProLong Gold Antifade hard set mounting medium and stored at 4°C until time of imaging.

2.2.6 Histological Staining and Examination

Paraffin embedded brain tissue was sectioned at 6µm thickness and mounted to poly-ionic slides (Histotox Labs, Boulder, CO). Sections were deparaffinized and stained with hematoxylin and eosin. Each section was analyzed at a 10x and 40x magnification using an Olympus IX71 microscope (Center Valley, PA) with Retiga 2000R (Qimaging, Surrey, BC, Canada) and Qcolor3 (Olympus) camera and Slidebook software (v6.0, Intelligent Imaging Innovations, Inc., Denver, CO) for image acquisition and analysis. Stained SN and ST sections were investigated and read by a board-certified veterinary pathologist who was blinded to all groupings.

2.2.7 Unbiased Stereological Neuronal Counting and Striatal Terminal Analysis

Quantification of neurons was adapted from those previously reported (Tapias and Greenamyre, 2014; Sadasivan et al., 2015; Bantle et al., 2019). In brief, every 20th tissue section was selected for staining and counted, resulting in six sections per animal being counted. The studies described here were conducted blindly by a single investigator. Images were captured using an automated Olympus BX63 fluorescence microscope equipped with a Hamamatsu ORCA-flash 4.0 LT CCD camera and collected using Olympus CellSens software (v1.15). Quantitative analysis was performed on dually labeled fluorescent images generated by montage imaging of the entire coronal brain section by compiling single 100X magnification images acquired by using an Olympus X-Apochromat 10X air objective (0.40 N.A.). One hemisphere of the section was quantified by creating anatomically specific ROIs based on TH immunolabeling and reference to a coronal atlas of the mouse brain (Allen Brain Atlas). All images were obtained and analyzed under the same conditions for magnification, exposure time, LED intensity, camera gain and filter settings.

For quantitative assessment, TH^+ and $NeuN^+$ soma from the selected areas determined by the ROI parameters were semi-automatically counted by adaptive thresholding in the Count and Measure feature on the Olympus CellSens platform. Object filters for cellular perimeter size, minimum and maximum area, and shape factor thresholding were applied. Quantitative stereology analysis using the motorized stage method was performed as descried (Tapias and Greenamyre, 2014).

Caudal ST sections containing the caudate and the globus pallidus (GP) were stained dually or triply including TH as the main marker of interest. All slides were stained and imaged simultaneously to reduce variability in intensity measurements. Whole brain montaging was performed using a 10X Olympus X-Apochromat air objective (0.04 N.A.). ROIs specific to the individualized striatal anatomical brain region were applied and total average fluorescence intensity was determined by manual threshold masking within the CellSens platform. Representative whole brain montage images were generated using the 10X air objective and high magnification inserts were acquired using the Olympus X-Apochromat 100X oil objective (1.4 N.A.).

2.2.8 Skeletonization and Determination of Microglial Cell Phenotype

Skeletonization analysis was performed as previously described (Morrison et al., 2017). In brief, five randomized 400X images spanning the entirety of the substantia nigra pars reticulata (SNpr) were taken using a Olympus X-Apochromat 40X air objective (0.95 N.A). Image software (National Institutes of Health, Version 1.5a) and appropriate plug-ins (FFT bandpass filter, unsharp mask, and close) were downloaded and applied to each of the images prior to converting to binary and skeletonized images. Cell soma quantification was obtained by counting DAPI positive nuclei

that co-localized with IBA1 cytoplasmic staining. The Analyze Skeleton Plugin (developed and maintained by http://imagej.net/AnalyzeSkeleton3) was applied to all the skeletonized images. DAPI-positive nuclei were measured using the straight-line tool in order to determine a minimum positive threshold length that a respective generated data point had to meet to be considered in the data set allowing only for the counting of cells within the representative Z-plane counting frame. Data was then compiled and filtered further by endpoint number and threshold sizing. Microglia soma counts were then used to determine microglial branches/cell, branch length/cell and microglial junctions/cell.

2.2.9 Semi-Automated Glial Counting and Intensity Measurements within the Substantia Nigra and Striatum

Methods used to quantify values of glial cells throughout brain regions were performed as previously described (Bantle et al., 2019). Two total sections per animal were selected for glial counts based on anatomical region and proximity to slides that were used to quantify DAn values. The studies described herein were performed blinded by a single investigator. Images utilized for quantification were captured using an automated BX63 fluorescence microscope equipped with a Hamamatsu ORCA-flash 4.0 LT CCD camera and collected using Olympus CellSens software. Quantitative analysis was performed on dual or triple-labeled fluorescent images through full brain montage assessment. Each montage consisted of compiled individual 100X images taken using an Olympus X-Apochromat 10X air objective (0.4 N.A.). Dual hemispherical analysis was performed on active ROIs determined by anatomical structures identified by immunofluorescent labeling and referenced to the coronal mouse brain atlas (Allen Brain Atlas). All slides were imaged and

scanned using the same conditions of exposure time, binning time, magnification, lamp intensity and camera gain.

For identification of $GFAP^+$ and $IBA1^+$ cells, soma from the ROI labeled areas were detected using semi-automated cell counting software on the CellSens platform. Total area of soma, fluorescent intensity, mean grey intensity and cell shape object filters were used to determine positive cells by manual adjustment to identify thresholding parameters for accurate quantification of glial cells. Colocalization of S100β and C3 was determined by using the co-localization function on the CellSens platform, channel minimum and maximum were manually determined to ensure accuracy of dual label identification. Pearson correlation coefficients were determined and the colocalization algorithm was not accepted if the R value was below 0.85. Two sections per animal were used to identify glial specific markers within manually created ROIs, the total number of cells were then divided by the overall area (mm^2) of the ROI to allow for normalization across dosing groups.

S100β and C3 colocalization was quantified by utilizing the co-localization feature within the Count and Measure module of CellSens. Minimum and maximum intensity thresholds were manually determined for each staining channel per individual section to account for intensity variability between sections. Area of soma exclusion criterion was applied following completion of the algorithm further selecting for co-localized, dual-labeled cells. The number of infiltrating monocytes were quantified based upon immunohistochemical staining and morphological criteria as reported previously (Bantle et al., 2021b).

2.2.10 Artificial Intelligence-Based Identification of S100β$^+$ Astrocytes in Whole Brain Montage Images

Whole brain montage images acquired at 10X magnification using the same imaging parameters per section were utilized for quantification of S100β$^+$ cellular populations. Anatomical ROIs were hand drawn for each section to encompass the SNpc and SNpr, per standard anatomical landmarks (Allen Brain Atlas). Olympus CellSens software was used for analysis and identification of cells using the Deep Learning module. Training labels were created on a total of 8 sections across 4 control animals to train the artificial intelligence (AI) algorithm what a 'positive event' is (e.g., a cell), based on area, diameter, circumference, fluorescence intensity, multiple channel intensity ratios and cellular elongation factor. After 250 training labels were created spanning all animals and ROIs, neural networking generation was performed on standard basis with a total of 25,000 – 50,000 iterations including cellular identification based on fluorescence intensity of S100β$^+$ cells and DAPI intensity, with exclusion of background tissue architecture and intensity. Therefore, identification of astrocytic cells was made only possible if all criteria were met. The network was deemed adequate at the iteration where the similarity score was ≥0.80. Total objects within each ROI were detected and counted using the Count and Measure feature of Olympus CellSens where manual thresholding was applied to accurately detect the AI identified S100β$^+$ cells. Total cell counts were then normalized to the total area of the ROI.

2.2.11 Immunohistochemical Staining and Quantification of Protein Aggregates

Sections were processed for histology and immunohistochemistry using a Leica Bond-III RX_m automated staining system according to the manufacturer's protocols. Antigen retrieval was performed in Bond Epitope Retrieval Solution 1 and 2 for 20 minutes at 37 ℃. Reactive p129 cell/cell aggregates were stained using mouse monoclonal anti-phospho Ser129 (P129) antibody (1:100, clone pSYN#64, WAKO) (Jang et al., 2009a). Immunoreactions and neuropathological

scoring of $P129^+$ protein aggregates were conducted in the midbrain and ST on exposed and unexposed brain sections by a veterinary pathologist blinded to the exposure groups using scoring methodology that was adapted from previous reports (Rey et al., 2016; Rey et al., 2018). We assessed the presence of $P129^+$ inclusions on two coronal sections per animal that were 6µm in thickness with an *n*=4 control group/timepoint, *n*=7 rotenone group/timepoint for each exposure group. Each section was analyzed at a 10x and 40x magnification using an Olympus IX71 microscope (Center Valley, PA) with Retiga 2000R (Qimaging, Surrey, BC, Canada) and Qcolor3 (Olympus) camera and slidebook software (v6.0, Intelligent Imaging Innovations, Inc., Denver, CO) for image acquisition and analysis. A score of 0 to 5 was assigned to each brain region from a single coronal brain section and scored as follows: 0=no aggregation, 1= very sparse/few (1-2) $p129^+$ intra-cellular aggregates per cell per high magnification field, 2=mild (<10) $p129^+$ intra-cellular aggregates per cell per high magnification field, 3= moderate (<15) $p129^+$ intra-cellular aggregates per cell per high magnification field, 4=marked (<20) $p129^+$ intra-cellular aggregates per cell per high magnification field, 5= severe (>20) $p129^+$ intra and extra cellular aggregates per cell/surrounding cellular space per high magnification field.

2.2.12 Proteinase K Digestion of Paraffin Embedded Tissue Sections

Paraffin embedded tissue sections (6um) were run on a Leica Bond RX_m automated robotic staining system. Sections were dewaxed and epitopes were exposed using Leica Bond Epitope retrieval buffer 1. Sections were then permeabilized and treated with 100ug/mL proteinase K (pK, Roche) at 37 °C for 30 minutes. This was followed by serum blocking and primary antibody application. Sections that did not receive pK received 1X TBS incubations at 37 °C for 30 minutes. Appropriate secondary antibodies were applied to the sections and all images were obtained on an

automated BX63 fluorescence microscope equipped with a Hamamatsu ORCA-flash 4.0 LT CCD camera and collected using Olympus CellSens software. Sections that were previously quantified for being high p129 aggregate yield through IF and IHC pathological scoring were used as pK controls, to determine pK effectivity, along with absence of IBA1 and TH staining positivity.

2.2.13 Generation of Representative Normalized Pathological Overlays

To generate the representative overlays at each time point, the total number of DAn, microglia, macrophages, astrocytes cellular counts and P129 pathological scores from infected mice were normalized to controls according to the following equation: ((x-y)/(y-z))*100=normalized percentage value (Gopal Krishna Patro and Kumar Sahu, 2015). The control values obtained for each pathological parameter were averaged and then subtracted from the individual experimentally infected animal values yielding a pathological representative of activation (x). The minimum (y) and maximum (z) values were determined for each activation parameter dataset. Normalization was then performed by determining the difference between the control subtracted experimental infected values and the minimum overall value. The total obtained from this calculation serves as the numerator. The range of the data set was then determined by obtaining the difference from the minimum (y) and maximum (z) values, this would serve as the denominator. The value obtained from this overall calculation was then multiplied by 100 to represent total percentage activation of each parameter. The respective percentages at each time point (2, 3 and 4 WPI) were averaged and plotted using spline curve fitting within GraphPad software (version 9.1.0; Graph Pad Software, San Diego, CA).

2.2.14 Nigrostriatal Tract Mapping

Online access of Allen Brain Atlas mouse brain connectivity atlas (https://connectivity.brain-map.org/) was utilized to identify source search of substantia nigra (SNpc, SNpr) and target source of ST within C57BL/6J mice. Beta 3D browser-based atlas was then used to visualize mouse anatomy and axial projection from database AAV injection experiment number 100141993. Structural mapping was added with visualization tools and view planes of the tract were downloaded.

2.2.15 Statistical Analysis

All data was presented as mean +/- SEM, unless otherwise noted. Experimental values from each mean were analyzed with a ROUT (α=0.05) test to identify significant outliers and validate exclusions. Differences between time-exposure group was identified using a two-way ANOVA, where individual timepoint comparisons between exposure groupings were carried out using Sidak's *post hoc* multiple comparison test. Significance was identified as $*p<0.05$, $**p<0.01$, $***p<0.001$, $****p<0.0001$. All statistical analysis was performed using Prism (version 9.1.0; Graph Pad Software; San Diego, CA).

2.3 Results

3.3.10 Behavioral and locomotor deficits resulting from chronic rotenone exposure in mice.

Following optimization of rotenone dosing based on survival curve analysis (**Fig. 2A**), the effects of subacute systemic rotenone exposure on neurobehavioral function in C57Bl/6 mice were determined by open-field activity analysis. Heat maps (**Fig. 2B, C**) and linear pattern tracking graphs (**Fig. 2D, E**) of behavioral function revealed anxiety-like and depressive behavior and an overall reduction in exploratory movement, with increased time spent towards the margins of the chamber. Relative to individual baseline measurements, there were increases in rest time in mice exposed to rotenone compared to miglyol-exposed control animals (**Fig. 2F**). There were also trends of decreased rearing events from the rotenone animals at all timepoints, where the parameter of time accounted for the most variance. There were also decreases observed with the amount of time spent in the center of the chamber at 1 WPI in the rotenone-exposed group (**Fig. 2G, I**), with a corresponding increase in margin time **(Fig. 2H)** where the combination thereof rotenone exposure and time accounted for significant variance within regards to center time.

To determine the extent of neuroinflammation associated with rotenone exposure, transgenic NF-κB-GFP-luciferase dual reporter mice were administered rotenone for 14 days followed by two weeks of recovery during which the bioluminescence signal of the NF-κB-luciferase reporter was measured weekly. Following systemic administration of rotenone, expression of the NF-κB reporter as determined by whole-body bioluminescence imaging revealed increases in reporter signal from 3 – 4 WPI (**Fig. 2J-M**). Total flux of photons per second was determined for an equivalent region of interest (ROI) for each timepoint (**Fig. 2N**), indicating an increasing linear trend in the rotenone exposed group (Two-way ANOVA, $p<0.06$, $F(1,27)=3.624$) from 2 WPI to 4 WPI.

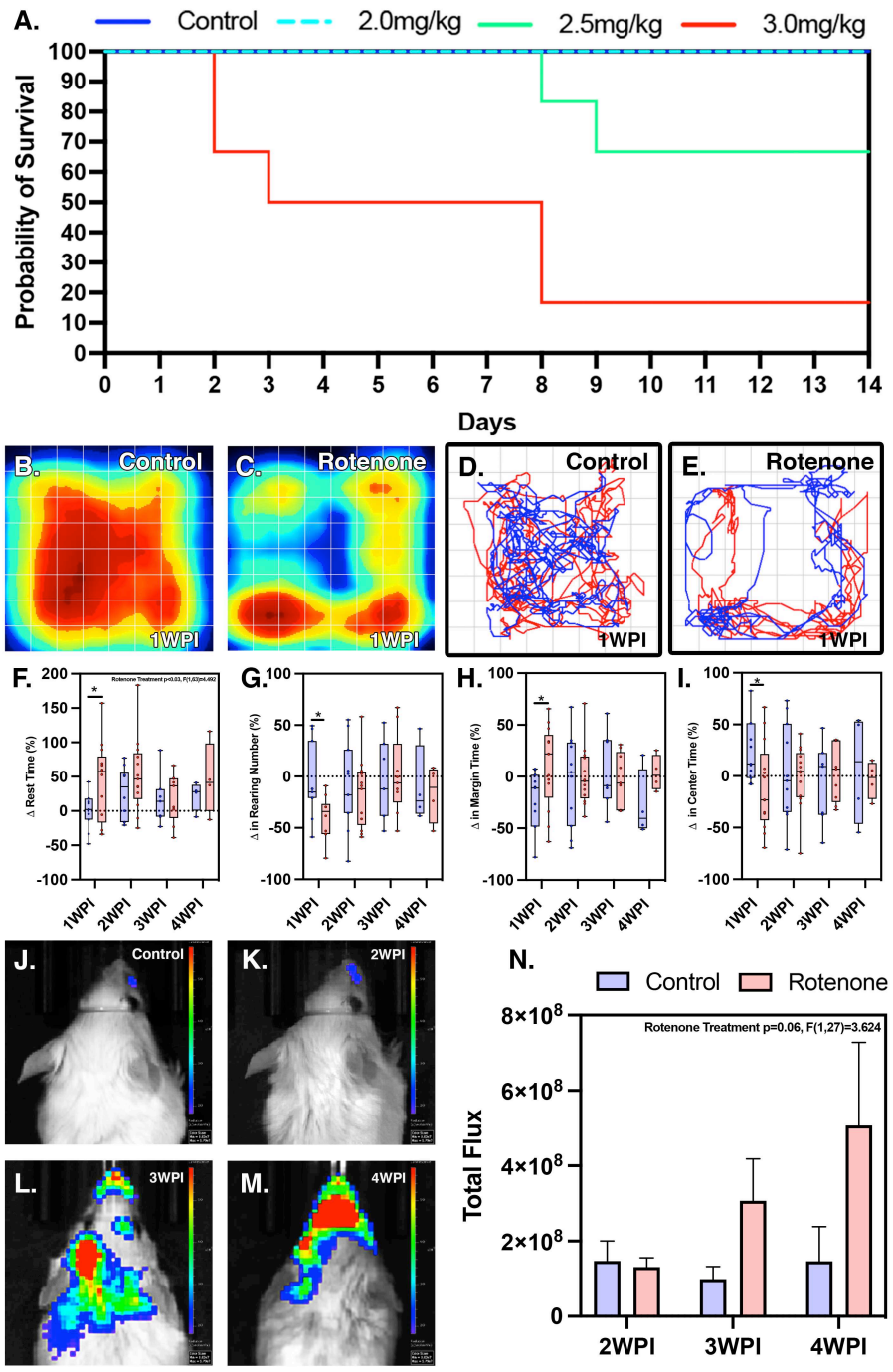

Figure 2. Behavioral and locomotor changes within rotenone treated animals occur prior to NF-κB activation. Open field tracking of C57/Bl6 behavioral patterns through heat mapping and linear movement recognition, respectively, in control **(A, B)** and rotenone treated animals **(C, D)** show behavioral differences. Quantitative analysis of changes in rest time **(E)**, rearing number **(F)**, margin time **(G)**, and center time **(H)** are shown. (*n*=4 control mice/group, *n*=7 rotenone mice/group) NF-κB-GFP-Luc dual reporter animals show increased levels of NF-κB luciferase photon flux beginning at 3 WPI **(K)** and increasing at 4 WPI **(L)**. Whereas 2 WPI **(J)** reflects that of control **(I)** levels. Rotenone exposure within these animals is sufficient enough to induce inflammatory activation and successive progression to the 4 WPI time-point **(M)**. (2 WPI: *n*=8 control, *n*=9 rotenone; 3 WPI: *n*=7 control, *n*=7 rotenone; 4 WPI: *n*=6 control, *n*=5 rotenone).

These findings were consistent with histopathological examination of nigro-striatal nuclei performed by a veterinary pathologist at 2, 3 and 4 WPI with rotenone (**Supplemental Fig. 1**). This analysis revealed focal neuronal apoptosis in the substantia nigra (SN) and caudate-putamen in rotenone-treated animals compared to the control group, where affected neurons appeared more angular and contained hyper-eosinophilic cytoplasm. Pyknotic and karyolitic nuclei were present with focal gliosis manifesting in occasional satellitosis and scattered Alzheimer Type II astrocytosis. This was accompanied by multifocal gliosis within the ST, especially within the striosomes, which exhibited axonal profile interruptions. By 4 WPI, the SN showed an overall decrease in neuronal density that was more pronounced in the left hemisphere. Apoptotic neurons were pyknotic and angular with decreased overall size, as well as separated from the neuropil, leaving prominent pericellular clear spaces.

2.3.2 Microglial activation and phenotypic profiling reveal dynamic M2-M1 conversion in response to rotenone.

Phenotypic conversion and pathological activation of microglia was assessed by quantification of $IBA1^+$ cell number and morphology within the SNpc, SNpr, ST and GP (**Fig. 3**). Dual immunolabeling with IBA1 and TH was used to identify microglial cell populations within DA brain regions. Montage images of entire coronal brain sections were scanned using a 10X objective and high-resolution images were acquired using a 100X objective. Representative baseline levels of microglia were present in the SN, ST and GP of control animals (**Fig. 3A, B**). Exposure to rotenone resulted in increased microglial cell populations in the SNpc and SNpr by 2 WPI (**Fig. 3C**), whereas the ST had minimal levels of microglial hypercellularity at this timepoint (**Fig. 3D**). Microglial phenotyping conducted at 2 WPI by skeletonization and filament tracing

analysis revealed conversion of resting/ramified microglia (M2) within the SN to activated ameboid microglia (M1), characterized by reduction in branch length, number of branches per cell and the total number of junctions per cell (**Fig. 3J, Q-S**). At 3 WPI there was reduced activation and recruitment of microglia in all brain regions examined, except for the SNpr where increases in microglial cell population and activation states were still present (**Fig. 3E, F**). Individual microglial cells within the SN were seen retaining a M1 phenotypic state (**Fig. 3K, Q-S**), similar to the activated amoeboid state observed at 2 WPI. By 4 WPI microglia showed decreased activation and proliferation within the SNpc, SNpr, ST, and GP (**Fig. 3G, H**), with a phenotypic return to a more ramified state characterized by increased branch length, number of branches and number of junctions per cell (**Fig. 3L, Q-S**). Quantification of the number of microglia within each region over time was calculated by semi-automated analysis of cells in designated ROIs encompassing anatomically consistent sections within the SNpc **(Fig. 3M)**, SNpr **(Fig. 3N)**, ST **(Fig. 3O)** and GP **(Fig. 3P)**. Microglia were discriminated from infiltrating peripheral macrophages by a previously established protocol that differentiates based on size and morphological differences and slides were read blinded by a pathologist (Smeyne et al., 2016). The number of infiltrating macrophages was determined within the entire SN and showed an increasing trend starting at 2 WPI and peaking at 4 WPI **(Fig. 3T)**. Inter-regional normalization of IBA1 positive cells was performed in each brain region relative to the start of rotenone exposure to model the temporal changes in cellular number over time with respect to the progression of rotenone-induced pathological changes. Regions are denoted as follows (**Fig. 3U**): SNpc (pink), SNpr (cyan), ST (red), SN – infiltrating macrophages (dashed green). Normalization of cellular responses indicated that microglial reactivity peaked first in the ST at 2 WPI followed by the SNpr at 3 WPI, with a secondary increase in microglia in the ST at 4 WPI. In contrast, the number of

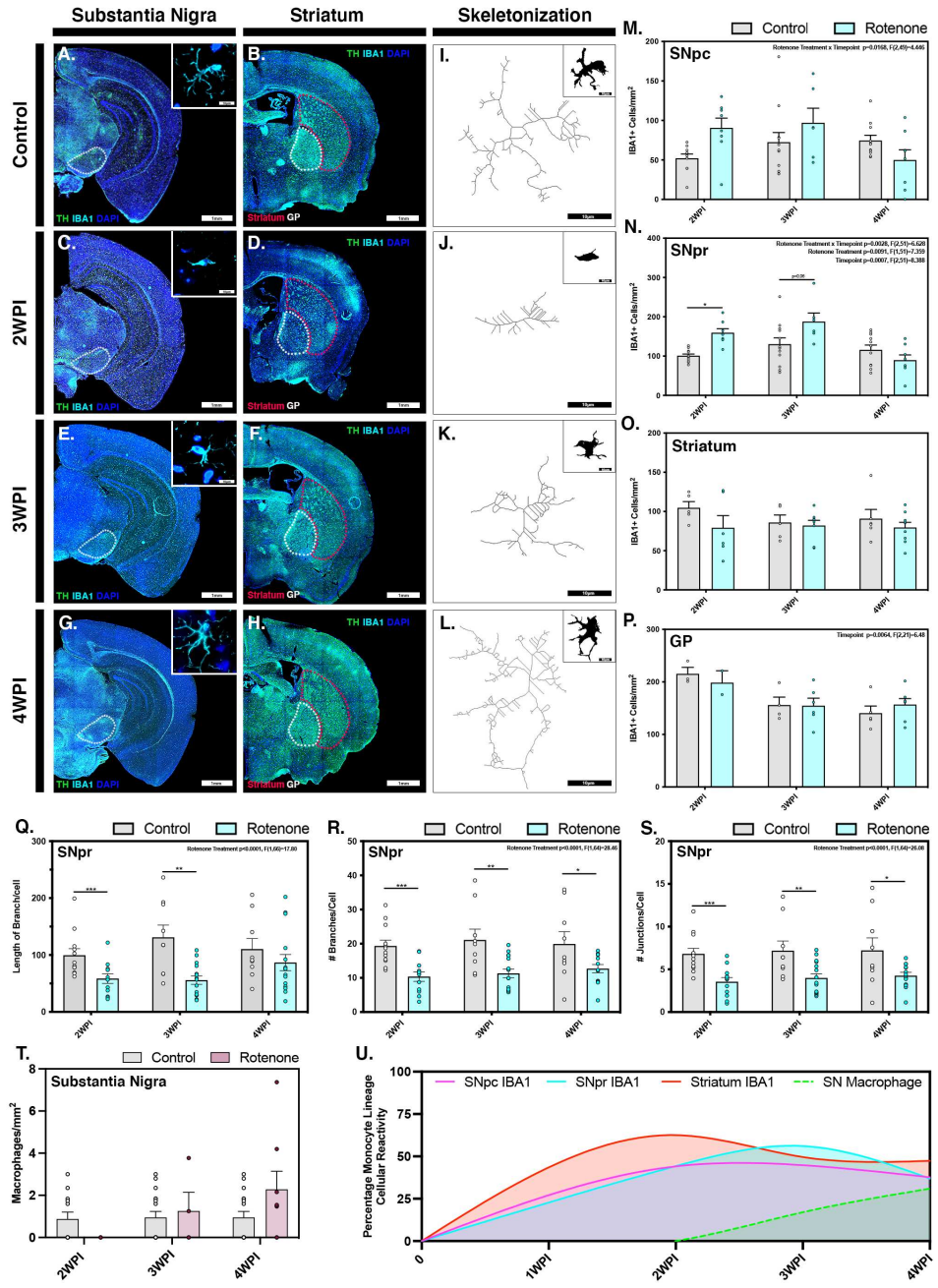

Figure 3. Systemic administration of rotenone causes temporally and regionally distinct patterns of microglia activation. Microglial activation from an M2 phenotypic state to an active ameboid M1 phenotype was investigated in control (**A, B**) and rotenone-treated animals at 2 WPI (**C, D**), 3 WPI (**E, F**) and 4 WPI (**G, H**) within the substantia nigra and the ST, respectively (TH, green). Analysis of microglia phenotype by skeletonization and filament tracing was conducted in the SNpr in control (**I**), 2 WPI (**J**), 3 WPI (**K**) and 4 WPI (**L**) animals. Quantification of IBA1$^+$ cells (cyan) associated with microgliosis/microcytosis was performed within the SNpc (**M**), SNpr (N**),** ST (**O**) and GP (**P**) at all timepoints. (**Q-S**) Changes in length of branches per cell (**Q**), number of branches per cell (**R**) and number of junctions per cell (**S**) was also quantified at each timepoint. (**T**) The number of invading monocytes was quantified in the substantia nigra. (**U**) Normalized counts of IBA1$^+$ cells in the SNpc (pink), SNpr (cyan), ST (red) and invading macrophages within the SNpc (green dashed line) were modeled over the 4-week time course of the study. (n=4 mice/control group, n=7 mice/rotenone group) *p<0.05, **p<0.01, ***p<0.001

microglia in the SNpc peaked between 2 and 3 WPI. Infiltrating macrophage numbers within the SN increased steadily from 2 WPI to 4 WPI, coinciding with the decrease of IBA1$^+$ microglia within the SNpc and SNpr.

2.3.3 Rotenone toxicity induces a reactive A1 phenotype in astrocytes in multiple brain regions

The changes in the inflammatory phenotype of astrocytes in response to rotenone exposure was determined by quantifying the number of S100β$^+$ (**Supplemental Fig. 2**) and GFAP$^+$ cells in concert with overall fluorescence intensity of GFAP, as well as the number of cells co-expressing S100β and C3, a marker for A1 reactive astrocytes (**Fig. 4**). In control animals, astrocytes displayed a resting stellate morphology in all brain regions examined, without evidence of hypertrophy or other features of inflammatory reactivity (**Fig. 4A, B**). By 2 WPI there were increased numbers of hypertrophic GFAP$^+$ cells in rotenone-treated animals, primarily in the SNpc, with no increase detected in the SNpr, ST or GP (**Fig. 4C, D**). This hypertrophy in GFAP$^+$ cells was less evident by 3 WPI in the SNpc and decreased further by 4 WPI (**Fig. 4E, F and G, H**). Quantification of the number of GFAP$^+$ cells and GFAP fluorescence intensity in each brain region supported these observations (**Fig. 4I, J**); two-way ANOVA analysis indicated a significant change in the number of GFAP$^+$ cells where rotenone exposure and time were parameters investigated within the SNpc (p=0.026, F(2,51)=3.923) and GFAP$^+$ intensity in the SNpr (p=0.038, F(2,43)=4.583). Expression of GFAP in the SNpr increased from 3 WPI to 4 WPI, later than that in the SNpc. The ST, interestingly, showed decreases in the number of reactive GFAP$^+$ astrocytes at 2 WPI **(Fig. 4D),** followed by levels similar to control at 3 WPI and 4 WPI **(Fig. 4F, H, K)**. In rotenone-exposed mice, the GP did not show any differences from that of control animals at any timepoint investigated **(Fig. 4L)**. The number of A1 astrocytes was determined in each region by

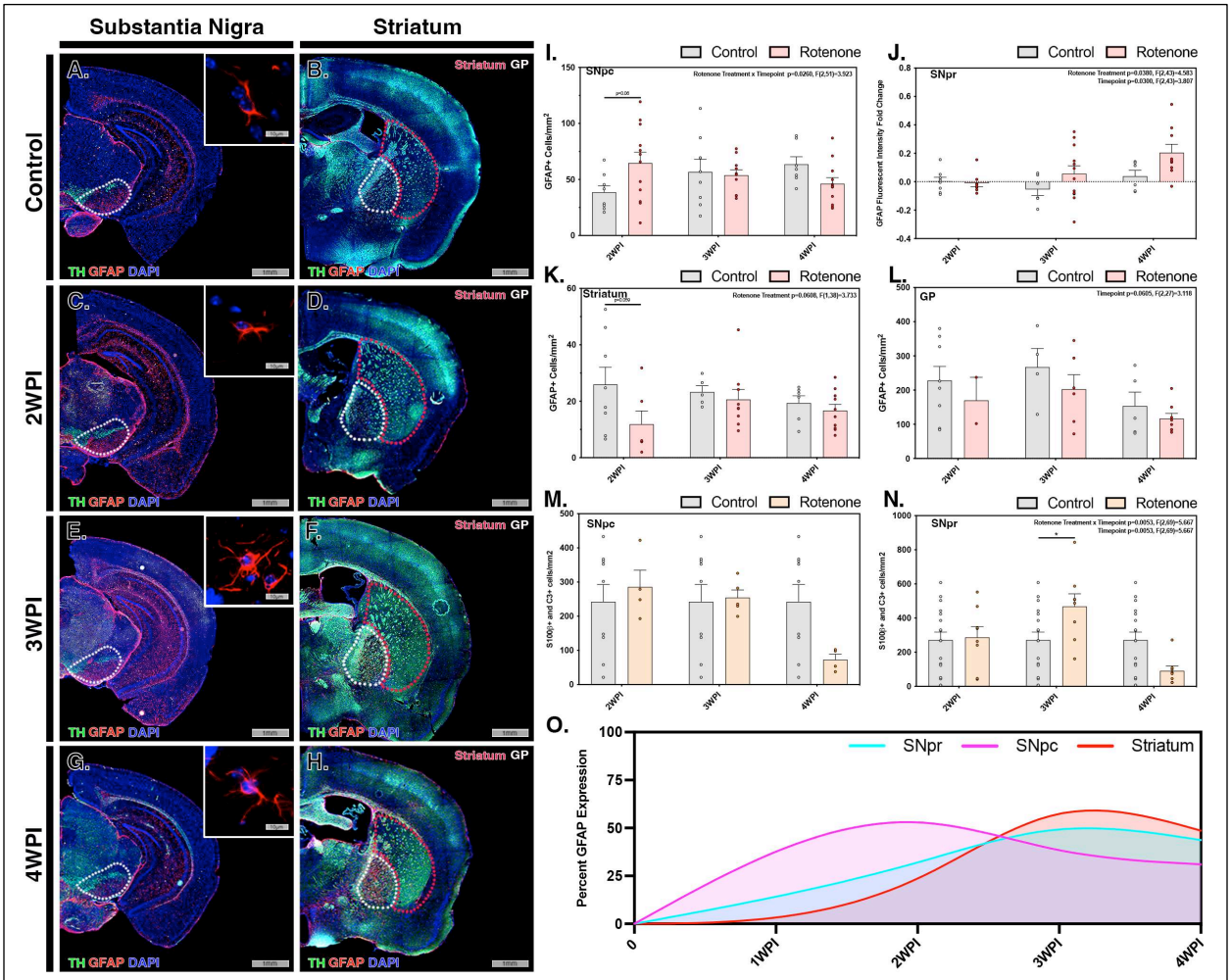

Figure 4. Rotenone exposure induces activation of astrocytes in the substantia nigra prior to the appearance of reactive A1 astrocytes in the striatum. Activation of astrocytes (GFAP, red) within the SN (TH, green) and ST were investigated in control (**A, B**) and rotenone-treated mice at 2 WPI (**C, D**), 3 WPI (**E, F**) and 4 WPI (**G, H**). Astrocytosis/astrogliosis was quantified in the SNpc (**I**), SNpr (**J**), ST (**K**) and GP (**L**) at 2 WPI, 3 WPI, and 4 WPI. Cell number and intensity was normalized to the respective control for each region to determine overall activation patterns throughout multiple brain regions at each timepoint. The number of A1 reactive astrocytes was determined by immunolabeling and co-localization of S100β^{+} C3 in the SNpc (**M**) and SNpr (**N**) for all timepoints. (**O**) Normalized GFAP intensity for the SNpr (cyan), SNpc (pink) and ST (red) was modeling for all regions at each timepoint. (n=4 mice/control group, n=7 mice/rotenone group) *p<0.05.

co-immunolabeling to identify cells positive for expression of S100β and C3. The number of $S100\beta^+$ cells co-expressing C3 did not change in the SNpc at any timepoint (**Fig. 4M**) but increased in the SNpr at 3 WPI (**Fig. 4N**). Modeling normalized changes in GFAP-expressing cells over time in the SN and ST indicated peaks in A1 astrocytes in the SNpc occurring early at 2 WPI, followed by the SNpr and ST at 3 WPI (**Fig. 4O**).

2.3.4 Rotenone exposure causes progressive loss of dopaminergic neurons and projecting striatal fibers

To determine the extent of neuronal loss in response to systemic administration of rotenone in C57Bl/6 mice, the number of neurons in multiple brain regions were assessed by quantitative stereology using scanning fluorescence microscopy of whole-brain sections coupled to semi-automated image analysis as described previously (Tapias et al., 2013) (**Fig. 5**). Imaging of DAn within the SNpc of control animals showed healthy neuronal cells forming a densely populated layer projecting to an intact neuropil, as well as intact DA terminals in the ST (**Fig. 5A, B**). By the end of rotenone exposure (2 WPI), there were evident deprecations in neuronal integrity and prevalence in the SNpc, without clear changes in TH staining in the ST (**Fig. 5C, D**). At 3 WPI, neurons began to decrease in radial size and lose morphological integrity, including loss of dendritic branching, decreased axon size and the appearance of cells with pyknotic nuclei. (**Fig. 5E**). Increases in the intensity of TH^+ DA terminals in the ST also became evident by 3 WPI (**Fig. 5F**). By the second week following the end of rotenone exposure (4 WPI), there was clear loss of DAn within the SNpc with progressive neurodegeneration characterized by decreases in the diameter of neuronal soma, loss of morphological integrity and an increase in the number of remaining cells that had pyknotic and fragmented nuclei (**Fig. 5G**). Striatal terminal integrity

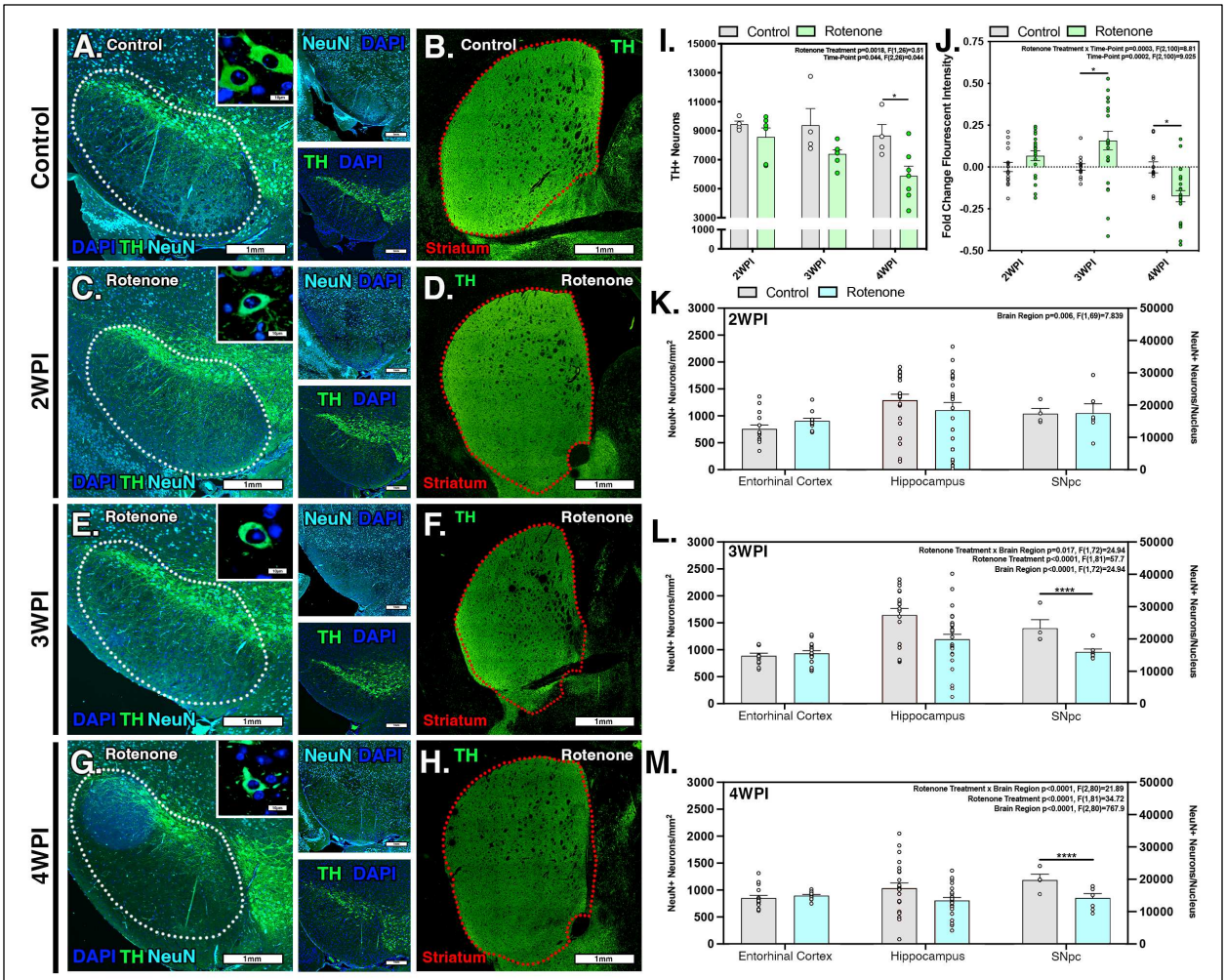

Figure 5. Rotenone induces selective loss of dopaminergic neurons in the substantia nigra pars compacta occurs that follows maximal inflammatory activation of glial cells. The number of DAn (TH, green) and total neurons (NeuN, cyan) in the SN was examined by quantitative stereology in control (**A**) and rotenone-treated mice at 2 WPI (**C**), 3 WPI (**E**), and 4 WPI (**G**). The intensity of TH^+ DAn terminals within the ST was also determined at each timepoint (**B, D, F, H**). (**I**) Quantification of the number of DAn and (**J**) dopaminergic terminals in the ST. The number of $NeuN^+$ neurons was quantified in the hippocampus, entorhinal cortex and SNpc at 2 WPI (**K**), 3 WPI (**L**), and 4 WPI (**M**). (*n*=4 mice/control group, *n*=7 mice/rotenone group) **p*<0.05, *****p*<0.0001

largely decreased at 4 WPI, with progressive loss of terminal intensity compared to the end of rotenone exposure at 2 WPI (**Fig. 5H**). Quantification of the number of TH^+ neurons in the SNpc and the intensity of TH staining in the ST confirmed these observations (**Fig. 5I, J**), indicating an approximate 35% loss in DA neurons, most of which occurred in the two-week lesioning period following the end of rotenone administration. To determine if neurodegeneration was specific to TH^+ neurons in the SNpc or generalized throughout the brain, NeuN staining was used to examine

the total number of neurons in multiple brain regions. Total neuronal counts within the SNpc were unchanged at 2 WPI, indicating that no neurodegeneration had yet occurred after two weeks of rotenone exposure (**Fig. 5K**). Likewise, no loss of $NeuN^+$ cells was detected in either the hippocampus or entorhinal cortex at this timepoint. However, during the lesioning period from 3 to 4 WPI with rotenone, there was a significant and progressive decrease in the total number of $NeuN^+$ cells within the nucleus of the SNpc ($p<0.001$ for rotenone exposure, $F(1,81)=34.72$). No change in the number of $NeuN^+$ cells was detected in the hippocampus or entorhinal cortex during the same period (**Fig. 5L, M**).

2.3.5 Rotenone exposure induces the formation of proteinase K-resistant α-synuclein aggregates

α-Syn aggregation and vacuolization is a hallmark of PD and is an important determinant of disease progression (Mehra et al., 2019). To characterize the formation and spread of p129 aggregates in response to rotenone exposure, immunohistochemical staining and pathological scoring of p129 was conducted in the SNpc and ST. Pathological scoring of the extent of aggregate formation was conducted by a veterinary pathologist using a ranking scale ranging from 0-5 according to the following metrics: 0=no aggregation, 1= very sparse/few (1-2) $p129^+$ intracellular aggregates per cell per high magnification field, 2=mild (<10) $p129^+$ intracellular aggregates per cell per high magnification field, 3= moderate (<15) $p129^+$ intracellular aggregates per cell per high magnification field, 4=marked (<20) $p129^+$ intracellular aggregates per cell per high magnification field, 5= severe (>20) $p129^+$ intra and extra cellular aggregates per cell/surrounding cellular space per high magnification field. Three dimensional maps of the nigro-striatal tract showing neuronal connectivity (highlighted in white) were generated using the pathway mapping feature of the Allan Brain Atlas (**Fig. 6A, B**). Region-specific analysis did not show significant

increases in p129 accumulation at the 2 WPI timepoint within the SN **(Fig. 6E, K)** but did show increases in the p129 staining within the ST, as noted by change in pathological score **(Fig. 6F, L)** compared to control animals **(Fig. 6C, D)**. Interestingly, at 3 WPI there was increased p129 aggregation in the SN **(Fig. 6G, K)** and a corresponding decrease within the ST **(Fig. 6H, L).** By the 4 WPI timepoint there was further accumulation of p129 aggregates in the SN and elevation in the pathological score within the ST above that of controls (**Fig. 6I-L**). The most prominent difference in misfolded protein occurred two weeks after the end of rotenone exposure (4 WPI), with the appearance of intensely staining intracellular aggregates of $p129^+$ α-syn in neuronal perikariya, with additional staining evident in glial cells surrounding $p129^+$ neurons.

To further investigate cellular responses to accumulation of p129 aggregates within individual brain regions, we used immunofluorescence imaging to detect the presence of p129 aggregates within both DAn and microglia in the SN and ST (**Fig. 7**). Overall accumulation of p129 was measured within the SNpc, SNpr and ST at each timepoint **(Fig. 7A-H)**. In control animals, little to no staining for p129 was detected in neuronal soma or in surrounding microglia, which were few in number and displayed a reticulated resting phenotype (**Fig. 7A, E**). From 2 WPI at the conclusion of rotenone exposure to 4 WPI, progressive increases in intracellular p129 were evident as intracellular puncta within both TH^+ neurons and microglia in the SN (**Fig. 7B-D**), as well as in TH^+ fibers and microglia in the ST (**Fig. 7F-H**). Quantification of total p129 fluorescence intensity by brain region indicated that $p129^+$ aggregates increased in the ST by 3 WPI, before the increase observed in the SN at 4 WPI (**Fig. 7I-K**). Levels of p129 in microglia increased at 4 WPI in the SN but were unchanged in the ST at the timepoints evaluated (**Fig. 7L-N**). In TH^+ neurons, p129 aggregates detected as fluorescence puncta in peri-nuclear regions were elevated over control at all timepoints (**Fig. 6O**). Normalized expression of overall p129

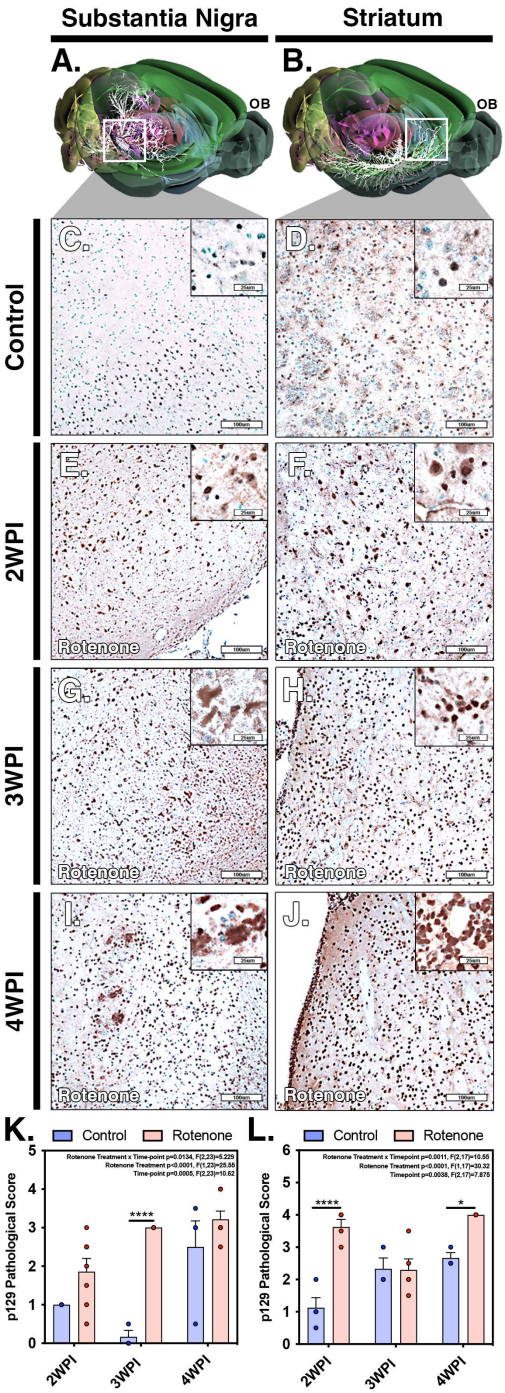

Figure 6. Pathological scoring of α-synuclein aggregates in the substantia nigra and striatum following systemic administration of rotenone. (**A, B**) Three dimensional models of neuronal connectivity (white) in the nigro-striatal pathway with spatial orientation to the olfactory bulb (OB) were generated from the Allan Brain Atlas. Paraffin-embedded sections were immunolabeled for phospho-(Ser129)-α-syn (p129) evaluated by blinded pathological scoring for the severity of aggregate formation in the SN and ST in control (**C, D**) and rotenone-treated animals at 2 WPI (**E, F**), 3 WPI (**G, H**) and 4 WPI (**I, J**). Quantitative comparison of pathological scores for the SN (**K**) and ST (**L**) for control and rotenone-treated animals was performed at each timepoint. (n=4 mice/control group, n=7 mice/rotenone group) *p<0.05, ****p<0.0001

expression was modeled within the brain regions, indicating peak accumulation within the SNpr at 2 WPI followed by the ST at 3 WPI and a bimodal increase within the SNpc at 2 and 4 WPI **(Fig. 7P)**.

Proteinase K (pK) digestion studies were performed to determine the stability of protein aggregates detected in the SN in rotenone-exposed animals to proteolytic degradation (**Fig. 8**). In brain sections from control animals very little aggregated p129 was detected in the SN by 4 WPI, seen as a lack of staining intensity following digestion with pK, which fully degraded the intact TH epitope (**Fig. 8A**). In brain sections from rotenone-exposed animals subjected to pK digestion, intense staining for p129 was still evident (**Fig. 8B**) that co-localized with TH^+ DAn, as seen in companion sections not incubated with pK (**Fig. 8C**). High resolution microscopic analysis revealed the presence of largely intracellular puncta within DAn in the SNpc that gradually accumulated from 2 – 4 WPI, with the highest levels occurring at latest timepoint evaluated. At this timepoint, $p129^+$ puncta were present throughout the neuronal perikaryon as well as in neighboring microglia (**Fig. 8D-H**). A similar pattern of accumulation was detected in TH^+ fibers in the ST, which peaked at 3 WPI and were similarly present within surrounding microglia (**Fig. 8I-M**). Microglial trafficking and dissemination of $p129^+$ aggregates were also investigated, revealing $IBA1^+$ cells located within the corpus callosum **(Fig. 8S)**, peri-vascular areas **(Fig. 8T)**, choroid plexus **(Fig. 8U)**, third ventricle **(Fig. 8U)** and migrating along TH^+ projecting neuronal fibers within the nigro-striatal pathway **(Fig. 8V),** as well as localized to peri-nuclear regions of the cell. There was a relative paucity of microglia in control animals in these brain regions and none that contained $P129^+$ aggregates **(Fig. 8N-R)**.

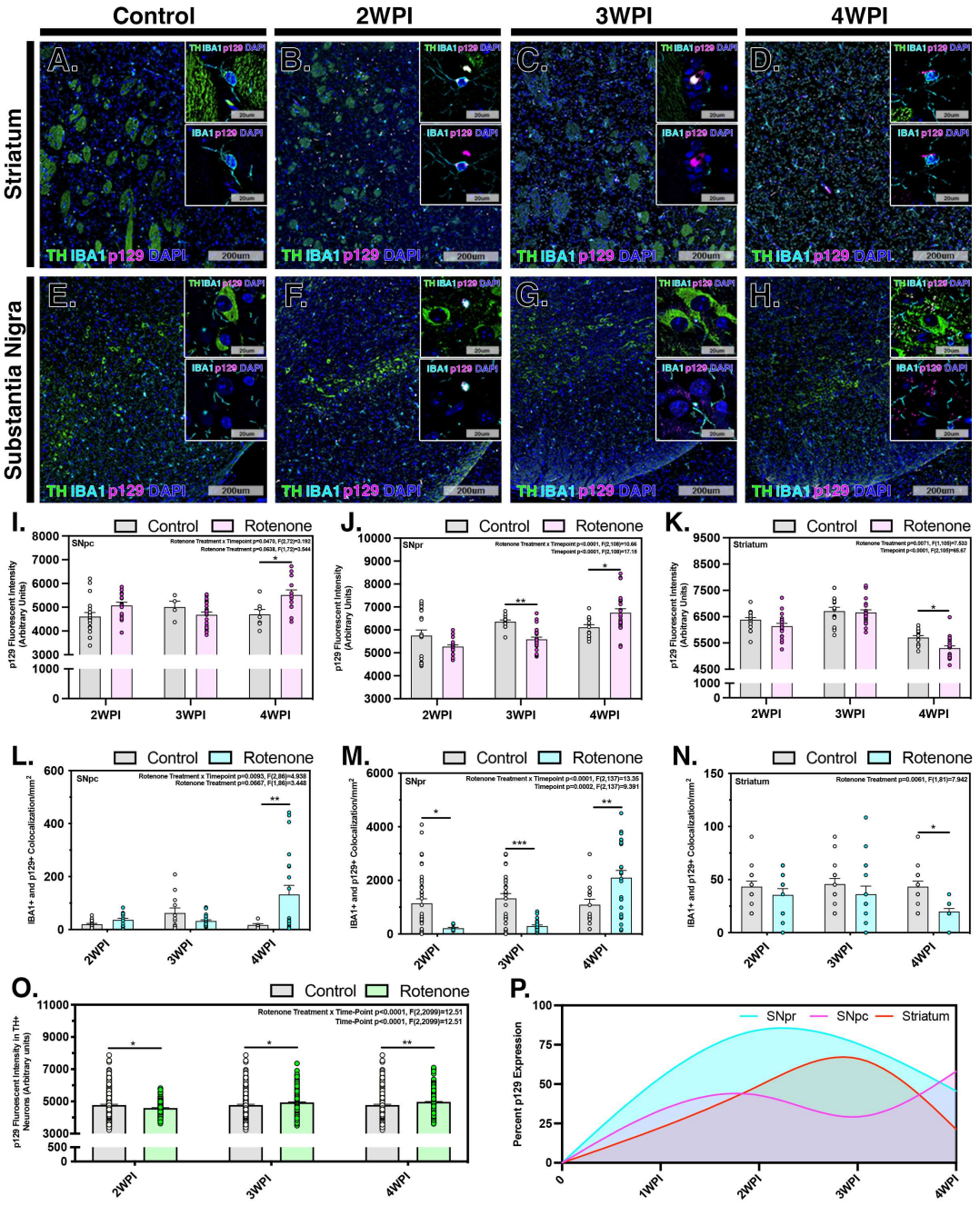

Figure 7. Formation and trafficking of α-synuclein protein aggregates in neurons and microglia following rotenone exposure. Accumulation of p129 was determined in the ST and SNpc in control (**A, E**) and rotenone-treated animals at 2 WPI (**B, F**), 3 WPI (**C, G**) and 4 WPI (**D, H**). Representative images of brain sections immunolabeled for p129 aggregates (p129, pink), microglia (IBA1, cyan) and DAn and terminals (TH, green) are depicted for respective brain regions at each timepoint. Overall intensity measurements of p129 accumulation were determined within the SNpc, SNpr and ST at 2 WPI, 3 WPI and 4 WPI in the SNpc (**I**), SNpr (**J**) and ST (**K**). Co-localization of p129 aggregates in microglia was determined at each timepoint in the SNpc (**L**), SNpr (**M**) and ST (**N**). The intensity of p129 aggregates in DAn was also determined at each timepoint (**O**). (**P**) The overall fluorescence intensity of p129 was plotted for each brain region over time to establish a normalized pathological model of disease progression. (n=4 mice/control group, n=7 mice/rotenone group) *p<0.05, **p<0.01, ***p<0.001

2.3.6 Glial-glial and glial-neuronal interactions mediate the progression of protein misfolding and neuronal injury following exposure to rotenone

The overall progression of pathological changes in the nigro-striatal pathway following systemic administration of rotenone for two weeks was modeled in **Figure 9**. Three dimensional pathways were overlayed with region-specific changes in microglial activation, p129 accumulation, astrocyte activation and loss of DA neurons, presented as a longitudinal model to depict connectivity of these pathological alterations between brain regions (**Fig. 9A**). This mapping approach indicates temporal, regional and cellular specificity with respect to the pathology induced by systemic exposure to rotenone. Within the SNpc, GFAP expression and initial accumulation of $p129^{+}$ aggregates were seen by the end of rotenone exposure at 2 WPI. This was followed by a peak of microglial cell increase at 3 WPI that coincided with a decrease in $p129^{+}$ aggregates and loss of DAn in this brain region (**Fig. 9B**). In the SNpr there was a similar early increase in p129 by 2 WPI, followed by the peak of microglia activation and A1 astrocyte reactivity at 3 WPI (**Fig. 9C**). The ST displayed an initial peak of microglia activation at 2 WPI followed by p129 aggregation at 3 WPI and then A1 astrocyte activation and degradation of DA terminals at 4 WPI (**Fig. 9D**). Schematic representation of all brain regions spanning the post-rotenone lesioning periods reveals specific cellular responses and activation in association with movement and accumulation of p129 leading to neurodegeneration **(Fig. 9E)**.

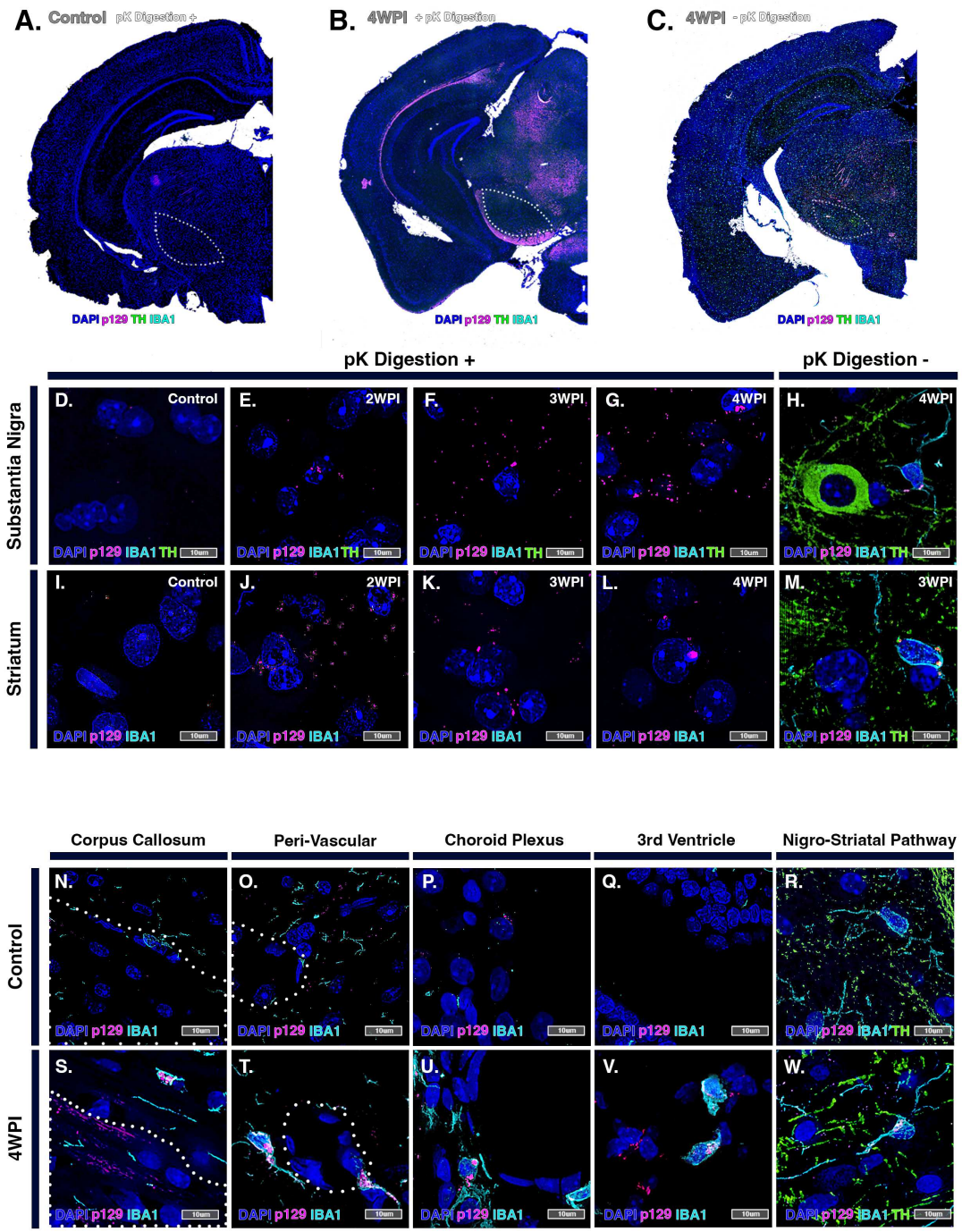

Figure 8. Microglia clear proteinase K-resistant α-synuclein aggregates in the brains of rotenone-treated mice. (**A-C**) High resolution hemispheric montage images of pK-digested brain sections from control (**A**) and rotenone-treated (**B**) animals, as well as a representative section from a rotenone-treated animal (-)pK digestion at 4 WPI (**C**). TH (green), p129 (pink) and IBA1 (cyan). High magnification images of pK-digested brain sections from control (**D, I**) and rotenone-treated groups at 2 WPI (**E, J**), 3 WPI (**F, K**) and 4 WPI (**G, L**). (**H, M**) 4 WPI rotenone-treated tissue without pK digestion. By comparing control (**N-R**) and rotenone-treated (**S-W**) brain tissue immunolabeled for IBA1, p129 and TH, $IBA1^{+}$ cells were identified trafficking intracellular $p129^{+}$ aggregates in rotenone-treated brains within the corpus callosum (**S**), peri-vascular areas (**T**), choroid plexus (**U**), third ventricle (**V**) and nigro-striatal pathway (**W**).

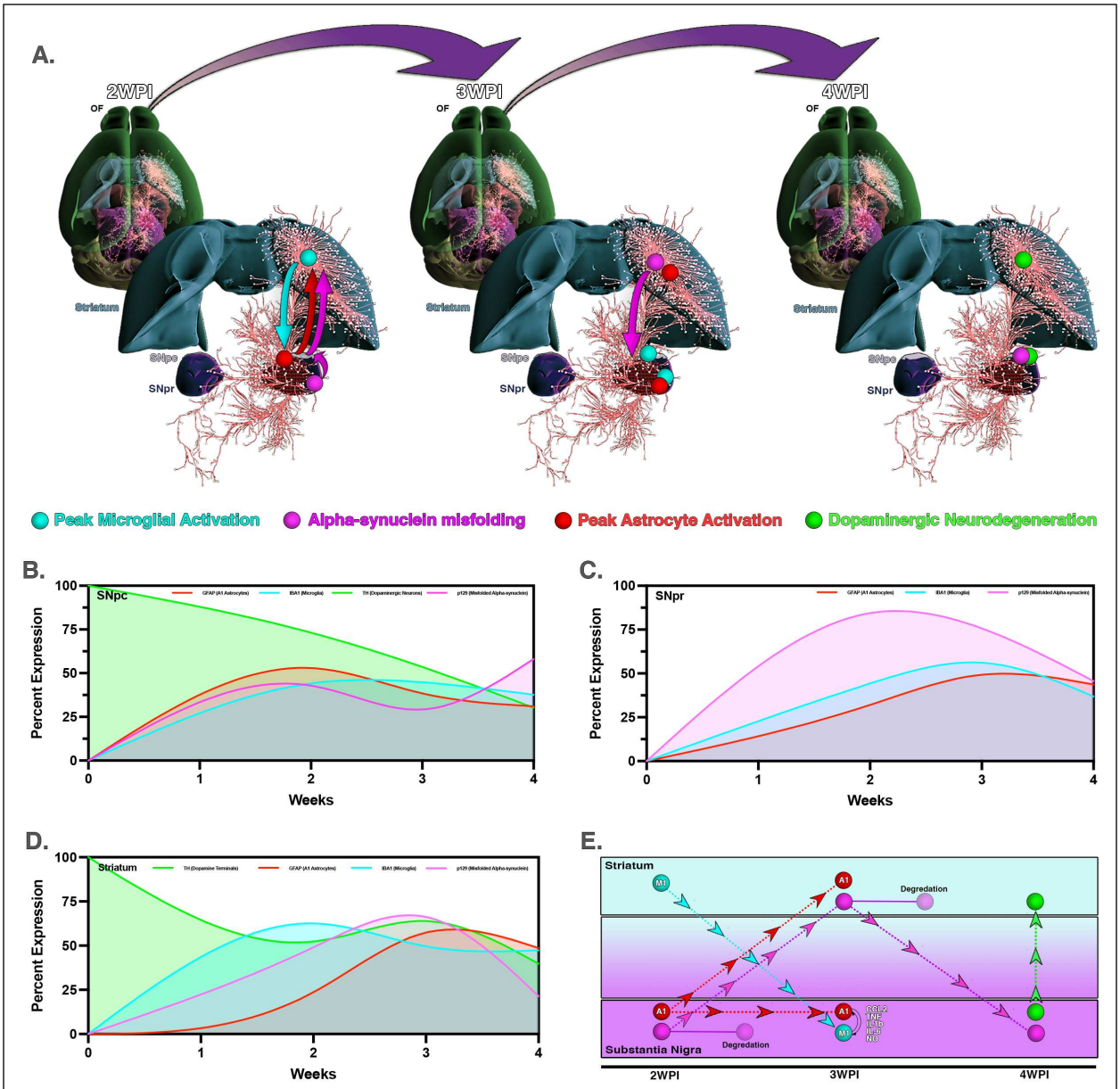

Figure 9. Modeling the progression of cytopathological changes in the nigro-striatal pathway following systemic exposure to rotenone. (A) Three dimensional pathways depicting neuronal connectivity were overlayed with region-specific changes at each timepoint for microglial activation, p129 accumulation, astrocyte activation and loss of DA neurons. Following two weeks of rotenone exposure, microglia activate initially in the ST, whereas activation of astrocytes and formation of p129 aggregates occurs first in in the SN, spreading thereafter to the ST. By 4 WPI these changes in glial phenotype and protein aggregation lead to loss of DAn in the SNpc. Changes in individual parameters were modeled to accurately depict normalized temporal changes in pathological features for the SNpc (**B**), SNpr (**C**) and ST (**D**). (**E**) Summary schematic representing cell-cell interactions, aggregation and trafficking of p129 and neurodegeneration for all brain regions over time.

2.4 Discussion

Rotenone has been used successfully to model multiple pathological features of PD, most notably in Lewis rats, where intraperitoneal administration induces behavioral deficits, loss of DA neurons, degeneration of striatal terminals and p129 aggregation (Betarbet et al., 2000; Cannon et al., 2009; Zeng et al., 2018). Studies attempting to adapt this model to mice have suffered from a number of limitations, including high mortality rates and a necessity for increased sample size due to systemic toxicity (Duty and Jenner, 2011). Additionally, translating doses of rotenone from rats to mice has proven challenging due to the two- to three-fold higher metabolic expenditure on a per gram basis in mice compared to rats (Radermacher and Haouzi, 2013). In mammals, the parent molecule, 2R, 6aS, 12aS)-1,2,6,61,12,12 a-hexahydro-2-isopropenyl-8,9-dimethoxychromeno [3,4-b] furo (2,3-h) chromen-6-one, is a potent mitochondrial complex I inhibitor, whereas the rotenone metabolites are 4-fold less toxic, underscoring the importance of species differences in expression of drug metabolizing enzymes that influence dosing with rotenone (Fukami et al., 1969). In addition, typical routes of administration such as oral gavage, inhalation, environmental-contact, and unilateral stereotactic injection are laborious and prone to variation in dosage between individual subjects (Inden et al., 2007; Rojo et al., 2007; Pan-Montojo et al., 2010; Inden et al., 2011; Liu et al., 2015; Wang et al., 2020a). In the present study, we show that daily administration of rotenone to mice by intraperitoneal injection for 14 days results in low mortality, marked activation of glial cells, formation of $p129^{+}$ aggregates and progressive neurodegeneration, all of which reaches a maximum during the two-week period following rotenone exposure. The progression of neuropathology during this post-rotenone lesioning period was characterized by behavioral changes, DAn loss, increased glial cell activation, recruitment of peripheral monocytes and the appearance of p129 inclusions similar to that seen in idiopathic PD (Cheng et al., 2010).

Behavioral changes such as depression and anxiety are common non-motor symptoms of PD and precede the onset of motor symptoms. These early neuropsychiatric changes can manifest from alterations in dopaminergic, serotonergic, cholinergic and adrenergic neurotransmission (Shiba et al., 2000; Gallagher and Schrag, 2012; Belovicova et al., 2017). Interestingly, mice that were exposed to rotenone presented with anxiety and depressive-like behaviors in open field assays at 1 WPI, evidenced by an increase in margin time and rest time and decreased in center time and rearing number (**Fig. 2**). Following this timepoint, the increase in luciferase signal in NF-κB-GFP-luciferase reporter mice indicated an overall progressive increase in neuroinflammation, similar to the spread of dystrophic, inflammatory microglia observed in idiopathic PD (Braak et al., 2007; Yao et al., 2021) and in rat models of rotenone-induced PD (Betarbet et al., 2000; Cannon et al., 2009).

Key cytopathological features of PD, such as mitochondrial dysfunction, p129 α-syn accumulation, neuroinflammation and oxidative stress (Schapira and Jenner, 2011), are not all reproduced in many mouse models of the disease. Mitochondrial dysfunction and aggregation of p129 are thought to drive activation of glia and progressive neurodegeneration, but many toxin-based and genetic models lack both of these important phenotypic features of PD in the SN (Lucking and Brice, 2000; Robinson, 2008; Xie et al., 2010). In this murine model of rotenone-induced PD, histopathological examination of treated mice revealed progressive glial cell activation within the nigro-striatal system. This activation was associated with neuronal resection from the neuropil, overall cellular loss, gliosis, ventricular edema and multifocal myelinic edema advancing from 3 – 4 WPI (**Supplemental Fig. 1**). Importantly, changes in astrocyte reactivity and phenotype in response to systemic exposure with rotenone occurred prior to neuronal loss in

the brain regions evaluated, consistent with the appearance of reactive, $p129^{+}$ astrocytes in idiopathic PD (Braak et al., 2007).

Reactive, dystrophic microglia appear prior to the majority of neurodegeneration in both PD and Lewy Body disease (Doorn et al., 2014). Microglial cells act as resident innate immune cells in the CNS, whereupon encountering pathogens or toxins, they quickly convert from a resting M2 state to a pro-inflammatory M1 state. M1 microglia are characterized by production of ROS and inflammatory cytokines such as TNF-α, IL-6, interleukin 12 (IL-12), IL-1β and CCL2 (Subramaniam and Federoff, 2017). These early innate inflammatory immune responses have been detected in PD patients as increased cerebrospinal fluid levels of IL-1β, IL-6 and human leukocyte antigen-DR isotype reactive microglia (McGeer et al., 1988; Blum-Degen et al., 1995). Notably, a study employing chronic exposure of C547Bl/6 mice to low levels of rotenone in diet reported increases in the astrocyte-derived cytokine, chemokine ligand 1 (CXCL1), as well as IL-1β, that were diminished in mice deficient in NLR Family Pyrin Domain Containing 3 (NLRP3), a key mediator of innate immunity in microglia (Martinez et al., 2017). In the present study, increases in both the number of microglia and the fraction of microglia displaying an M1 phenotype was seen within the SNpr and SNpc at 2 WPI in response to rotenone exposure (**Fig. 3**). Microglia remained activated at the 3 WPI timepoint, with a gradual return to a more resting, M2-like phenotype by 4 WPI (**Fig. 3**). Following rotenone exposure, there was an apparent increase in peripheral macrophages in the SN that peaked at 4 WPI, although this trend will require a greater number of animals to validate appropriately. This has also been reported in *postmortem* PD tissue (Fuzzati-Armentero et al., 2019). Infiltration of peripheral monocytes is likely mediated by disruption of blood-brain-barrier (BBB) integrity due to cytokines and chemokines released from M1 microglia

(Salvi et al., 2017). This infiltration and recruitment of macrophages aids in the clearance of p129 aggregates but also increases inflammatory activity and worsens the overall disease state.

Similar to the phenotypic responses observed in microglia, there was an increase in the number and reactivity of astrocytes in the nigro-striatal system that followed the peak of microglia activation in each brain region and coincided closely with the maximum extent of p129 aggregate formation. We observed an initial peak in hypertrophic, $GFAP^+$ cells expressing C3 at 2 WPI in the SNpc and overall regional decreases in total $S100\beta^+$ cell populations in the SNpc and SNpr, followed by an increase in $C3^+$ astrocytes within the striatum and increased populational distribution of astrocytes within the SNpr at 3 WPI (**Fig. 4, Supplemental Fig. 2**). C3 is reported to be a marker for reactive, neurotoxic A1 astrocytes (Liddelow et al., 2017) that is induced in response to C1qA and IL-1α released by M1 microglia (Wei et al., 2021). Intra-astrocytic C3 processing to C3a is followed by extra-cellular release and recognition by C3aR on microglia, thus reinforcing glial-glial interactions that amplify neuronal injury (Wei et al., 2021). In PD, activated astrocytes are seen in the SN in areas of DA neuron loss (Middeldorp and Hol, 2011), as we also noted in rotenone-treated mice. The initial appearance of reactive astrocytes in the SN at 2 WPI coincided with the peak of p129 in the SNpc (**Fig. 5**) and was followed by the peak of C3-expressing astrocytes in the striatum at 3 WPI. This suggests that rotenone-induced mitochondrial dysfunction occurs initially in the SN and drives innate immune activation of glial cells and protein aggregation in this brain region.

Stereological analysis revealed DAn loss within the SNpc and striatal terminal loss by 4 WPI (**Fig. 5**), similar to the pattern of DAn loss seen in idiopathic PD (Michel et al., 2016). Notably, loss of DAn was not observed following rotenone exposure at 2 WPI but occurred two weeks later (4 WPI), after the appearance of reactive microglia and astrocytes in the SNpc. This

strongly supports the assertion that innate immune activation of glia is an important mediator of neuronal injury during exposure to rotenone. Loss of TH^+ terminal density in the striatum also occurred at 4 WPI but, interestingly, was preceded by an increase in TH intensity within the striatum at 3 WPI (**Fig. 5**). Tyrosine-hydroxylase is the rate limiting enzyme of catecholamine biosynthesis and its expression is modulated by the redox-sensitive proteins, PARK7, which is up-regulated by oxidative stress, such as that caused by inhibition of complex I by rotenone (Zhong et al., 2006; Ariga et al., 2013). This may at least partly explain the apparent transient increase in TH intensity in the striatum observed at 3 WPI in rotenone-treated mice. The regional selectivity of rotenone-induced neuronal loss within the basal ganglia was assessed by determining the number of $NeuN^+$ neurons in the hippocampus and entorhinal cortex, which did not show loss of neurons compared to the SNpc (**Fig. 5**). Because rotenone is a systemic complex I inhibitor, these data indicate that DAn within the SNpc are selectively vulnerable to complex I inhibition in C57Bl/6 mice.

Formation of Lewy bodies in DA neurons in the SNpc are one of the central pathological features of PD but is difficult to replicate in most murine models of the disease. Because previous studies using intraperitoneal administration of rotenone in male Lewis rats reported accumulation of p129 in DAn in the SNpc (Sherer et al., 2003), we examined the formation of α-syn aggregates using immunostaining for the phosphorylated form of the protein (phosphorylation-Serine129-α-syn) in rotenone-treated mice (**Fig. 4 and 5**). There was increased formation of $p129^+$ puncta within TH neurons beginning at 3 WPI and progressing to 4 WPI. The size and intensity of these aggregates within microglia varied amongst brain region and timepoint (**Fig. 7**), suggesting that microglial clearance via the autophagy pathway is an important modulator of the neuronal burden of p129. Interestingly, rotenone reduces autophagy of p129 aggregates in DAn that is rescued by

overexpression of PARK7 (De Miranda et al., 2018), highlighting the importance of microglial clearance of p129^{+} aggregates in limiting neuronal injury. The kinetics of p129^{+} aggregate formation in response to rotenone suggests that this mouse model is relevant to understanding mechanisms underlying the alterations in autophagy and protein processing associated with the progression of PD (Pan et al., 2008; Lynch-Day et al., 2012).

α-Syn has been investigated as a potential biomarker for PD due to its presence in the blood and CSF of PD patients (El-Agnaf et al., 2003; Gao et al., 2015; Chang et al., 2019). However, the mechanism of clearance from the CNS by glial cells is not fully understood (Choi et al., 2020). Because microglial cells are long-lived and perform critical phagocytic functions in the CNS (Hefendehl et al., 2014), they are likely important modulators of p129 clearance. Data from rotenone-treated mice in these studies supports this mechanism, where IBA1^{+} cells containing p129^{+} aggregates were identified in perivascular regions and along projecting fibers of the nigro-striatal pathway, as well as within the corpus callosum at 4 WPI (**Fig. 8**). Migration of p129^{+} microglia along these routes in rotenone-treated mice is consistent with glial-lymphatic clearance of p129 and elevated circulating levels of p129 seen in PD patients. Moreover, the resistance of p129^{+} aggregates to digestion by pK (**Fig. 8**) echoes the results of p129 self-seeding studies reporting that recombinant fibrillar p129 aggregates were resistant to pK digestion (Kushnirov et al., 2020). The presence of highly stable, pK-resistant p129^{+} aggregates in rotenone-exposed mice is an important pathological feature of this model that reproduces aspects of protein misfolding observed in idiopathic PD (Kordower et al., 2008; Li et al., 2008; Lee et al., 2010; Angot et al., 2012). Notably, the presence of pK-resistant p129^{+} aggregates resemble the pattern of p129 aggregation we recently reported in virally induced parkinsonism in mice (Bantle et al., 2019;

Bantle et al., 2021b). Additional studies will be required to determine more precisely the role of microglia autophagy pathways in modulating levels of $p129^+$ aggregates in rotenone-treated mice.

These findings reveal a complex temporo-spatial progression of neuropathology in rotenone-induced parkinsonism involving numerous cell types, cell-to-cell signaling mechanisms and differential susceptibility amongst nigro-striatal brain regions. In addition, distinct patterns of α-syn p129 aggregation, movement of these aggregates along interconnected neural tracts and glial clearance all appear to influence the progression of pathology. The summary model of rotenone-induced neuropathology presented here **(Fig. 9)** highlights the relationship between both temporal and spatial patterns of glial activation and p129 aggregation that led to the loss of DAn within the SN. Early peaks of glial activation seen in the ST and SN after 2 WPI with rotenone resulted in rapid accumulation of pK-resistant $p129^+$ aggregates in these brain regions, which were followed by progressive loss of DAn in the SNpc (**Fig. 9**). Interestingly, $p129^+$ aggregates were seen within projecting TH^+ fibers of the nigro-striatal tract and in M1 phagocytic microglia surrounding DAn in the SNpc, suggesting that distribution of p129 in rotenone-treated mice is heavily influenced both by inter-neuronal spread and by glial clearance. The early appearance of reactive, dystrophic glial cells and deposition of $p129^+$ aggregates prior to the majority of neuronal loss are features of this murine model of rotenone-induced parkinsonism that compare favorably to the progression of neuropathology in idiopathic PD (Braak et al., 2007). Moreover, the rapid appearance of $p129^+$ aggregates within weeks of systemic rotenone exposure increases the utility of this model for basic as well as translational research. It will be important in future studies to determine more precisely the role of glial activation in the modulation, formation, and distribution of p129 following rotenone exposure. Studies will also need to delineate cell-specific changes in gene expression that

regulate phenotypic switching of glia to a reactive, neurotoxic state that negatively impacts neuronal survival in the basal midbrain.

CHAPTER 3

MICROGLIA-SPECIFIC NF-κB/IKK2 KNOCKOUT INCREASES ACCUMULATION OF MISFOLDED α-SYNUCLEIN THROUGH INHIBITION OF P62/SQSTM-1 DEPENDENT AUTOPHAGY IN THE ROTENONE MODEL OF PARKINSON'S DISEASE

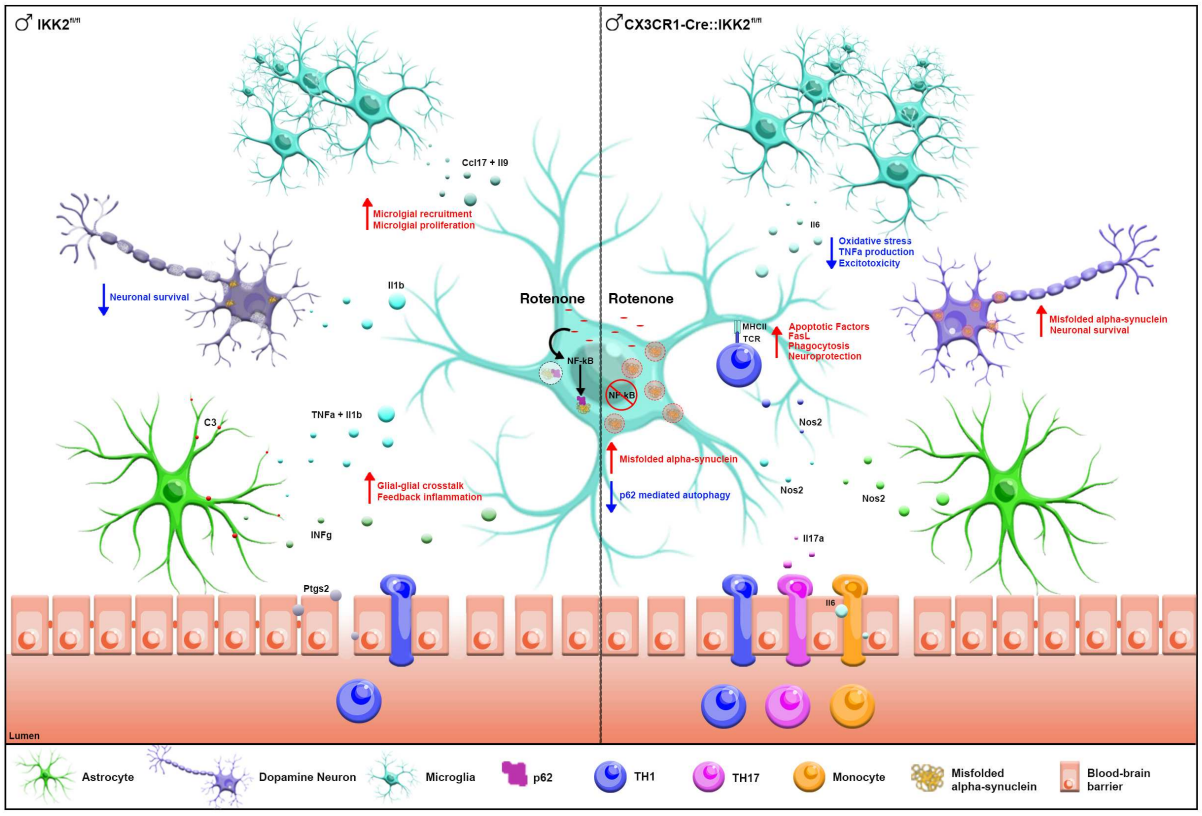

Figure 10. Graphical abstract of microglial mediated NF-κB inflammation in response to the environmental toxin, rotenone. Representation of intra- and inter-cellular responses initiated by rotenone exposure in wildtype (left panel) and microglial-specific NF-κB knockout of NF-κB (right panel).

3.1 Introduction

PD is the leading motor disorder and second most prevalent neurodegenerative disease in aging populations (Tysnes and Storstein, 2017; Marras et al., 2018). PD is characterized by progressive stages, which are clinically manifested by both non-motor and motor symptoms. In the prodromal stage of the disease, non-motor symptoms can occur decades prior to the appearance

of motor symptoms and include anxiety, depression, gastrointestinal dysfunction, and anosmia (Fasano et al., 2015; Schrag and Taddei, 2017; Tarakad and Jankovic, 2017). Subsequent motor manifestations are characterized by tremor, rigidity, postural instability, masked facies and general bradykinesia (Sveinbjornsdottir, 2016; Opara et al., 2017). Pathologically, PD is associated with a decrease in DAn in the SNpc, activation of glial cells and accumulation of misfolded α-syn protein aggregates, known as Lewy bodies, within surviving DAn soma.

α-Syn constitutes one percent of total cytosolic protein in the brain and is primarily expressed in the synaptic terminals of neurons. The physiologic function of α-syn remains largely unknown, but the regional expression of this protein increases in the diseased state and is a major component of Lewy bodies (Spillantini et al., 1997; Wakabayashi et al., 2007; Wakabayashi et al., 2013). During neuronal stress or injury, α-syn is thought to act in a prion-like manner, whereby misfolded forms of the native protein can 'seed' the formation of additional aggregates in neighboring cells (Nonaka et al., 2010; Lashuel et al., 2013). Clearance of protein aggregates by astrocytes and microglia is important to limiting the interneuronal spread of misfolded α-syn and therefore serves as a critical modulator of the progression of PD (Scheiblich et al., 2021). Recent studies demonstrated that selective autophagy of α-syn aggregates in microglia requires interactions between sequestosome 1 (SQSTM1/p62) interactions and ubiquinated α-syn (Choi et al., 2020). Expression of p62 is regulated by NF-κB and is therefore linked to activation of innate immune signaling pathways in microglia that respond to unfolded protein stress, such as damage associated recognition receptors (DAMPs) and PAMPs, including the TLRs and Nod-like receptors (Fiebich et al., 2018; Wang et al., 2020b). This suggests that NF-κB may have a dual function in microglia, whereby initial activation of innate immune signaling pathways promotes clearance of α-syn protein aggregates, but chronic unfolded protein stress might trigger a reactive

M1 state and the overproduction of neurotoxic inflammatory factors that further promote neuronal injury (Fernandez et al., 2021).

Microglia are specialized, myeloid-derived glial cells that function as the primary innate immune cell of the CNS. These cells respond to changes in the microenvironment of the CNS as they identify and mitigate foreign insults (Kraft et al., 2009; Kirkley et al., 2017). Upon activation, these cells undergo morphological changes from M2-ramified resting microglia to M1-ameboid microglia, apparent through reductions in branch length, branch number, and junction number. The existence of exclusive M1 and M2 populations is highly debated, and it is now thought that there is a spectrum in which these cells dynamically adapt morphometrically in response to surrounding environmental signals (Ransohoff, 2016). Nonetheless, activated microglia are associated with prototypic inflammatory responses resulting in increased release of inflammatory cytokines and oxidative/nitrative compounds with subsequent recruitment of resident and peripheral immune cells (Kirkley et al., 2017; Jurga et al., 2020).

Chronic activation of microglia is implicated as an important pathological determinant in many progressive neurodegenerative diseases including multiple sclerosis, stroke, AD, and PD (Gonzalez-Scarano and Baltuch, 1999; Block and Hong, 2005; Minghetti et al., 2005; Glass et al., 2010). These cells were first implicated in PD pathology in 1988, where enrichment of reactive microglia was observed in *postmortem* SN samples from PD patients (McGeer et al., 1988; Badanjak et al., 2021). NF-κB inflammatory signaling pathways in microglia have been recognized as potential drivers of the inflammatory cascade where pan-inhibition of NF-κB in brain reduces α-syn spread and neurodegeneration (Dutta et al., 2021). It remains unknown how cell-specific inhibition of NF-κB alters adjacent cellular population dynamics, peripheral cell infiltration and subsequent pathological outcome.

Here we demonstrate that microglia-specific knockout of NF-κB within rotenone-challenged mice is biologically sex-dependent and results in microcytosis and chemotaxis of resident and peripheral immune cells in male animals. Reduction in activated (A1) astrocytes was also apparent in the NF-κB devoid male animals. NF-κB deficient microglial cells harbored increases in lower-order $p129^{+}$ α-syn due to prevention of the p62-dependent autophagy pathway in male animals. Increases in $p129^{+}$ objects were also detected in DAn within the SNpc; however, despite excessive $p129^{+}$ α-syn accumulation in microglia and DAn, overall neurodegeneration was reduced in microglia-specific NF-κB knockout males compared to wildtype controls. These results suggest that accumulation of low order $p129^{+}$ α-syn, in and of itself, is non-toxic, rather the cellular response to the misfolded form of the protein is what drives neuroinflammation and results in pathology.

3.2 Materials and Methods

3.2.1 Generation of Microglia-Specific IKK2-NF-κB Knockout Mice.

All animal protocols were approved by IACUC at Colorado State University, mice were handled in compliance with PHS Policy and Guide for the Care and Use of Laboratory Animals and procedures were performed in accordance with NIH guidelines. Mice were housed in microisolator cages (3-4 animals per cage), kept on a 12-h light/dark cycle and had access to both food and water *ad libitum.* Male and female heterozygous B6J.BN6(Cg)-*Cx3r1*$^{tm1.1(cre)Jung}$ /J (CX3CR1-Cre) mice were obtained from the Jackson Laboratory (Stock No. 025524, Bar Harbor ME) and bred to homozygosity. These were then paired with homozygous IKK2$^{fl/fl}$ mice (Kirkley et al., 2019) and heterozygous CX3CR1-Cre$^{+/-}$::IKK2$^{fl/fl+/-}$ littermates were crossed to obtain homozygosity for both alleles resulting in CX3CR1-Cre$^{+/+}$::IKK2$^{fl/fl\ +/+}$ (KO). IKK2$^{fl/fl\ +/+}$ were utilized at wildtype (WT) animals throughout the studies.

3.2.2 Genotyping of Microglia-Specific NF-κB Knockout Mice.

Genomic DNA was extracted using Qiagen Dneasy Blood and Tissue Kits and was analyzed for concentration and purity using a Nanodrop spectrophotometer (Fisher Scientific). Primer sets spanning a single loxP site proximal to exon3 were ordered from Integrated DNA Technologies (IDT); Forward Primer 5'-AAGATGGGCAAACTGTGATGTG-3', Reverse Primer 5'-CATACAGGCATCCTGCAGAACA-3' and were ran in combination with iQ SYBR Green (Biorad), amplicons were then run on gel electrophoresis with ethidium bromide (EtBr) staining for visualization (**Supplemental Fig. 3**).

3.2.3 Rotenone Preparation and Dosing.

Rotenone was prepared as previously described (Rocha et al., 2022a), in brief, a 2.5mg/kg/day dosage of 2µL/gram body weight of rotenone was made where diluent compromised 98% medium chain-triglyceride, Miglyol 812 (Cannon et al., 2009), and DMSO 2%. Male and female mice (*n*=9/group) were injected daily for 14 days with a dose of 2µL/g weight. Mice were weighed daily prior to injection to determine the appropriate dose volume. The rotenone/miglyol solution was measured using a 50µL Hamilton syringe, which was then transferred to an insulin syringe with a fixed (29 gauge) needle and administered via intraperitoneal injection. Control animals received only miglyol injections. Hamilton syringes were cleaned every-day after use to prevent precipitation buildup within the needle. The barrel of the syringe and the plunger were submersed in 10% bleach for ten minutes, followed by aspiration of 70% EtOH then sterile water. The plunger was removed from the barrel and the syringe was allowed to air dry for 24 hours. The dosing period of 14 days was followed by a lesioning period of another 14 days. Animals were observed daily to determine morbidity or mortality.

3.2.4 Real-time Gait Analysis and Open Field Behavioral Assessment.

Locomotor function by analysis of gait was investigated by recording nonrestrictive movement patterns along a one-meter fixed trackway equipped with contrasting illumination pattern allowing for pawprint visualization and pressure sensing (Hammond et al., 2018; Damale et al., 2021). Mice were acclimated to the trackway 24 hours prior to experimentation. One hour before the first dose of rotenone/miglyol, baseline (0 DPI) measurements were collected for each animal. Parameters measured included run duration, diagonal stance support for each forelimb-hind limb combination, and four-point stance support. Data is reported as a change from 0 DPI measurement. Open field activity was measured using the Versamax behavioral system with an

infrared beam grid detection array (Accuscan Instruments, Inc. Columbus, OH). Mice were placed within individual chambers and were monitored for five minutes under low ambient light in the presence of white noise. Animals were pre-conditioned to the chambers the day before the experimentation started. The animals were recorded one hour prior to the first dose of rotenone (0 DPI) to obtain a baseline measurement of movement. Several behavioral parameters were obtained and analyzed using Versadat Software (Accuscan Instruments, Inc.) including change in total distance moved and the change in overall time spent moving. We have previously reported that these locomotor parameters are accurate determinants of basal ganglia function associated with decreased striatal DA and loss of dopaminergic innervation of the caudate/putamen (Kirkley et al., 2019; Hammond et al., 2020). Data are reported as change from 0 DPI behavioral assessment measurements.

3.2.5 Quantification of Catecholamines and Monoamines.

Determination of striatal catecholamine concentrations was assessed as previously described (Hammond et al., 2020). Briefly, brain tissue was rapidly removed after decapitation under isoflurane anesthesia. Gross dissection of the striatum was performed with the aid of a brain block and immediately flash frozen in liquid nitrogen, where the entire process from the time of anesthesia to flash freeze point lasted no longer than five minutes. Flash frozen striatal tissue samples were process using high-pressure liquid chromatography (HPLC) coupled with electrochemical detection to quantify the concentrations of DA, norepinephrine (NE), 3-methoxytyramine (3-MT), 3,4-dihydroxphenylacetic acid (DOPAC), homovanillic acid (HVA), serotonin (5-HT), and 5-Hydroxyindoleacetic acid (5-HIAA). Samples were analyzed using the Neurochemistry Core at Vanderbilt University's Center for Molecular Neuroscience Research

(Nashville, Tennessee), with randomized numerical labeling applied to all samples. All parameters obtained were normalized to overall protein concentration of each sample.

3.2.6 Tissue Sample Preparation.

Perfusion-fixation was performed under isoflurane anesthesia utilizing 20 mL of 0.1M PBS sodium cacodylate buffer supplemented with heparin followed by 20 mL of 4% paraformaldehyde. Brain tissue was then carefully removed and post-fixed in 10% NBF for two weeks at room temperature. Each tissue specimen was then trimmed according to consistent anatomical coordinates and placed in cassettes for histological processing.

3.2.7 Histological evaluation and pathological scoring of brain tissue.

Paraffin embedded brain tissue was sectioned at 4 and 6µm thickness and mounted to poly-ionic slides (Histotox Labs, Boulder, CO). Sections were deparaffinized and stained with hematoxylin and eosin on a fully automated Leica Bond RX staining robot. Each section was analyzed at 10X and 40X magnification using an Olympus IX71 microscope (Center Valley, PA) with Retiga 2000R (Qimaging, Surrey, BC, Canada) and Qcolor3 (Olympus) camera and Slidebook software (v6.0, Intelligent Imaging Innovations, Inc., Denver, CO) for image analysis. Full brain montage and high magnification images were acquired on an Olympus VS120 scanning microscope equipped with a Hamamatsu ORCA-R2 camera. Two sections per animal were analyzed by a single board certified veterinary pathologist and scored according to the following parameters: 0-unremarkable pathology; 1-more than 3-15 pyknotic neurons (up to 7 neurons) with perivascular clearing and prominent branched capillaries with mildly increased gliosis; 2-Relatively prominent gliosis on lower power magnification with multifocal clustering of apoptotic

neurons and prominent vascular branching; 3-Laminar apoptosis where the affected area is greater than one 40x high power field and marked gliosis; 4-Marked neuronal apoptosis and resection from the neuropil accounting for ≥60% of the total SN with marked gliosis; 5-Marked neuronal apoptosis and resection from the neuropil accounting for ≥80% of the total SN with marked gliosis.

3.2.8 Automated High-throughput Immunofluorescence Staining of Tissue Sections.

Paraffin embedded brain tissue was sectioned at 4 and 6µm thickness and mounted to poly-ionic slides (Histotox Labs, Boulder, CO). Sections were deparaffinized and stained with hematoxylin and eosin on a fully automated Leica Bond RX staining robot. Each section was analyzed at 10X and 40X magnification using an Olympus IX71 microscope (Center Valley, PA) with Retiga 2000R (Qimaging, Surrey, BC, Canada) and Qcolor3 (Olympus) camera and Slidebook software (v6.0, Intelligent Imaging Innovations, Inc., Denver, CO) for image analysis. Full brain montage and high magnification images were acquired on an Olympus VS120 scanning microscope equipped with a Hamamatsu ORCA-R2 camera. Two sections per animal were analyzed by a single board certified veterinary pathologist and scored according to the following parameters: 0-unremarkable pathology; 1-more than 3-15 pyknotic neurons (up to 7 neurons) with perivascular clearing and prominent branched capillaries with mildly increased gliosis; 2-Relatively prominent gliosis on lower power magnification with multifocal clustering of apoptotic neurons and prominent vascular branching; 3-Laminar apoptosis where the affected area is greater than one 40x high power field and marked gliosis; 4-Marked neuronal apoptosis and resection from the neuropil accounting for ≥60% of the total SN with marked gliosis; 5-Marked neuronal

apoptosis and resection from the neuropil accounting for ≥80% of the total SN with marked gliosis.

3.2.9 Unbiased Stereological Analysis of Neurons.

Paraffin embedded brain tissue was sectioned at either 4µm or 6µm thickness and mounted onto poly-ionic slides (Histotox Labs, Boulder, CO). Tissue sections were deparaffinized and immunofluorescently labeled using a Leica Bond RX_m automated robotic staining system. Antigen retrieval was performed by using Bond Epitope Retrieval Solution 1 for 20 minutes in conjunction with heat application. Sections were then incubated with primary antibodies diluted in 0.1% TBS: rabbit anti-TH (Millipore; 1:500), chicken anti-TH (Abcam; 1:200), mouse anti-NeuN (Abcam, 1:200), mouse anti-GFAP (Abcam, 1:1000), rabbit anti-S100β (Abcam; 1:750), rat anti- C3 (Abcam; 1:250), goat anti-IBA1 (Abcam; 1:50), mouse anti-p129 (Wako, 1:100), and guinea pig anti-p62 (Progen, 1:500). Sections were stained for DAPI (Sigma) and mounted on glass coverslips in ProLong Gold Antifade hard set mounting medium and stored at 4°C until time of imaging.

3.2.10 Morphological and Phenotypic Evaluation of Microglia.

Morphometric analysis was performed using Imaris for neuroscientists image analysis software (v9.8.2). Three to five randomized 400X images spanning the entirety of the SNpr and SNpc were taken using a Olympus X-Apochromat 40X air objective (0.95 N.A). Filament tracing modules were used to identify $IBA1^+$ microglial processes. Somal modeling and background reduction thresholding was applied to trace and map processes associated with individual microglial cells. Total sum of processes per cell (filament length (sum)), branch number per cell (filament number of dendrite terminal points), and overall volume of processes per cell (filament

volume (sum)), were utilized to determine morphometric changes present within each animal. Individual cell validation was conducted by DAPI positive nuclei co-localization with IBA1 cytoplasmic staining

Three-dimensional renderings of glial cells were performed by using Imaris software (v9.8.2) utilizing 100X high magnification deconvolved and mean-z projection images from 4-6 μm thickness tissue sections. Filament tracing was used to identify projection start and end points unique to individual cells based on maximal $IBA1^{+}$ staining intensity. Nuclei were added to renderings by spot detection determined by maximal DAPI staining intensity.

3.2.11 Identification and Quantification of Invading Monocyte Populations in the Basal Midbrain.

Tissue sections were processed for immunohistochemical analysis on a fully automated Leica Bond-III RX_m. Epitope retrieval was performed by addition of Leica Bond Epitope Retrieval Solutions 1 and 2 for a duration of 30 minutes at 37 °C. Cellular identification of monocyte lineage cell types was achieved by staining with rabbit anti-IBA1 (Abcam, 1:500) followed by 3,3'-Diaminobenzadine (DAB) chromogen. Nissel counterstain was applied for identification of cellular nuclei. Microglia were discriminated from infiltrating peripheral macrophages by a previously established protocol that differentiates based on size and morphological differences (Smeyne et al., 2016; Bantle et al., 2021b; Rocha et al., 2022a) . In brief, IBA1 staining outlining morphometric characteristics of each cell were scrutinized where small nuclei in combination with long thin processes denoted resting microglia, enlarged nuclei paired with shorter/thickened processes denoted activated microglia, and spherical atentril cells were peripherally invading macrophages. All quantification was performed blinded by a single investigator.

3.2.12 Deep Learning and Artificial Intelligence-based Quantification of Glia within the Substantia Nigra and Striatum.

Two total sections per animal were selected for glial counts based on anatomical region and proximity to slides that were used to quantify DAn values. The studies described herein were performed blinded by a single investigator. Images utilized for quantification were captured using an automated BX63 fluorescence microscope equipped with a Hamamatsu ORCA-flash 4.0 LT CCD camera and collected using Olympus CellSens software (v3.1). Quantitative analysis was performed on dual or triple-labeled fluorescent images through acquisition of full brain montage scans. Each montage consisted of compiled individual 100X images taken using an Olympus X-Apochromat 10X air objective (0.4 N.A.). Dual hemispherical analysis was performed on active ROIs determined by anatomical structures identified by immunofluorescent labeling using the coronal mouse brain atlas for anatomical reference (Allen Brain Atlas). All slides were imaged and scanned using the same conditions of exposure time, binning, magnification, lamp intensity and camera gain.

For identification of $GFAP^+$ cells, positive staining soma and projections within the manually drawn ROIs were detected using semi-automated cell counting software on the CellSens platform. Total area of GFAP reactivity compared to the total area sampled per animal was used to accurately quantify the amount of $GFAP^+$ astrocytes. $IBA1^+$ cell populations were identified by using deep learning artificial analysis software on the Olympus Deep Learning Platform. Optimization of neural networks was based on similarity scores ≥ 0.8. Manual thresholding was then applied on the probability segmentation layer to obtain total $IBA1^+$ cell counts for each specified ROI analyzed using optimized neural networks.

Fully automated deep learning neural networks were also constructed to identify S100β$^+$ cells. This was then applied to all images across all animals within the study using batch macro-analysis to sequentially analyze up to 150 images per AI run. S100β events were then converted to ROIs and the intensity of C3 positivity was interrogated on a cell-by-cell basis for the most accurate representation of A1 reactivity within the SNpc, SNpr and striatum. Manual thresholding within the Count and Measure module of CellSens was applied to batch analysis macros for mean intensity measurements of C3.

3.2.13 Immunohistochemical Staining and Quantification of Protein Aggregates.

Sections were processed for histology and immunohistochemistry using a Leica Bond-III RX_m automated staining system as described above. Reactive α-syn cell/cell aggregates were stained using mouse monoclonal anti-phosphorylated Ser129 (p129) antibody (1:100, clone pSYN#64, WAKO) (Jang et al., 2009a). Full-brain montage images were captured by using brightfield imaging on an Olympus VS120 equipped with a Hamamatsu OrcaR2 camera. Quantification of p129$^+$ staining was performed by using manual HSV thresholding within the Count and Measure features of CellSens, specifically adapted for RGB files. Thresholds were kept consistent throughout all images and object filters that spanned size and signal intensity were applied. Total positive staining area and object count were plotted against overall brain region specific ROI area sampled from individual sections to obtain animal-to-animal comparisons.

3.2.14 Quantification of p129 Protein Aggregates and Autophagy Markers.

Multi-factorial analysis was performed to determine p129 presence within two sections per animal. Overall regional intensities were measured from 10X full brain montages with the count

and measure module of CellSens (v3.1), where manual thresholding in the channel of interest was applied to obtain mean fluorescence intensity. Five total images per section, up to 10 total per animal depending on anatomical variation, were obtained using an Olympus X-Apochromat 40X (N.A. 0.16) magnification. Cell specific gaiting parameters were applied on microglia (IBA1) and DAn (TH) where average intensity of p129 was measured per cell within each section using manual and adaptive thresholding strategies within the count and measure module of CellSens (v3.1). Overall intensity of p62 within $IBA1^+$ staining was performed with manual thresholding to obtain average fluorescent intensity per $IBA1^+$ staining event.

3.2.15 Detection of Misfolded α-synuclein in Serum via Enzyme Linked Immunosorbent Assay (ELISA).

Terminal blood samples were collected by cardiac puncture of the right atrium under deep isoflurane anesthesia. Blood was centrifuged for 10 minutes and sera was then collected from the upper phase of the samples and frozen at -80 °C until quantification. Serum samples were removed from the freezer and diluted 1:100 in 1X PBS. Protein concentration was then determined by using the Pierce BCA Protein Assay Kit (ThermoFisher). A final volume of 50 µL of 0.01µg/µL serum, diluted in carbonate-bicarbonate buffer, was added to each well of the ELISA plate (NUNC, 96 well plate). Adhesion of the target proteins to the well surface was allowed for 1 hour at 37 °C. Blocking was then performed with superblock (ThermoFisher) for 1 hour at 37 °C. Primary p129 (clone pSyn#64, WAKO) was directly conjugated to horse-radish peroxidase (HRP; Lightning-Link, Abcam) and was diluted at a 1:2,000 in 1X PBS. 100µL of this was placed in each well and allowed to incubate at 37 °C for 1 hour. Three wash steps with 0.05% PBS containing Tween 20 were performed between each antibody incubation. One-Step Ultra 3,3',5,5'-

Tetramethylbenzidine ELISA Substrate Solution (ThermoFisher) was used to develop ELISA plates for five minutes at ambient temperature. Reactions were quenched using 0.5M sulfuric acid. Absorbance was measured at 450 nm on a BMG LabTech POLARstar Omega microplate reader to obtain total absorbance values.

3.2.16 qRT-PCR Array Analysis.

Tissue from the basal midbrain consisting primarily of SN was homogenized using a BeadBug 3 Position Head Homogenizer using 2.8 mm stainless steel beads submersed in RLT buffer from the Qiagen Rneasy Mini Kit. This buffer was supplemented with β-mercaptoethanol at a 1:100 dilution per sample. RNA extraction was then carried out following the Qiagen kit instructions and resulting RNA was analyzed on a Nanodrop for concentration and purity. A total of 1000 ng of RNA was used to make cDNA with iScript RT Supermix (Biorad). iQ SYBR Green (Biorad) and 50ng of cDNA was subsequently loaded into each well of the QuantiNova LNA PCR Focus Panel specific for mouse inflammatory response and autoimmune gene expression profiles (Qiagen). Relative expression ($2^{-\Delta CT}$) and fold change ($2^{-\Delta\Delta CT}$) methodology was used to determine expression changes compared to the reference genes of β-actin and β-2-microglobulin.

One step in-house arrays were also used to identify specific genes of interest associated with diseased state. RNA was isolated as previously described and was used as template in a one-step Taqman probe reaction with 1X reverse-transcriptase containing master mix and 20X Rtase (Tonbo), 400 nM primers directed at the genes of interest, 200 nM of each probe, and 200 nM primers corresponding to the reference gene (β-*actin*). Sequences (**Supplemental Table 1**) were validated individually and together within the same well prior to usage based on 90-110% efficiency and $R^2 \geq 0.99$. Primer and probe sequences were ordered from IDT where the probe

sequences synthesized were Prime Time Probes featuring individual reporter dyes with one or two quencher molecules to achieve higher signal-to-noise ratio. Delta cq and delta delta cq fold change methodology was applied to the resulting data to determine transcriptional regulation.

3.2.17 Gene Expression Profiling and Analysis.

Relative expression ($2^{-\Delta CT}$) and fold change ($2^{-\Delta\Delta CT}$) values were analyzed for outliers using ROUT testing, and full dataset analysis was performed on outlier excluded values using ClustVis (Metsalu and Vilo, 2015). Clade clustering was determined by cluster similarity in a correlation analysis method followed by Ward linkage. Unit variance scaling was applied and SVD with imputation settings were utilized for the generation of principal component analysis (PCA) plotting. Collapse of individual subjects into overall groups was applied for heat mapping with row centering. Fold regulation values greater than 2 (up-regulation) and less than -2 (down-regulation) were then analyzed by the programming software STRING (v.11.5; (Szklarczyk et al., 2021)) where full STRING networks were generated based on confidence with high interaction determination (0.700). Confidence was determined through textmining, experiments, databases, co-expression, neighborhood, gene fusion and co-occurrence parameters and was ultimately visualized though line thickness. Cluster differentiation within all significantly up or down-regulated genes was calculated from k-means resulting in six possible clusters, of which were then analyzed through STRING to determine appropriate GO Term associations. Radar graph generation was performed on Python (v3.9.7) software with JupyterLab computational platform where fold change values were input as data points.

3.2.18 Statistical Analysis.

All data was presented as mean +/- SEM, unless otherwise noted. Experimental values from each group were analyzed with a ROUT (α=0.05) test to identify significant outliers and validate exclusions. Differences between three-parameter variables were determined by three-way ANOVA with subsequent Tukey *post hoc* multiple comparisons testing. Variance differences between two-parameter variables were identified using a two-way ANOVA followed by a Sidak *post hoc* multiple comparisons test. All individual variables within the same timepoint or biological sex were analyzed for variance differences using an unpaired one-way ANOVA. Significance was identified as $*p<0.05$, $**p<0.01$, $***p<0.001$, $****p<0.0001$. All statistical analysis was performed using Prism (version 9.1.0; Graph Pad Software; San Diego, CA).

3.3 Results

3.3.1 Behavioral and locomotor changes are exposure, genotype, and sex dependent.

To identify locomotor deficits caused by exposure to rotenone, mice were evaluated by real time gait-analysis and open field behavioral monitoring. Real-time gait analysis of cadence and locomotor patterns through paw-print mapping (**Fig. 11A**) revealed genotype, biological-sex, and rotenone exposure differences regarding diagonal support (**Fig. 11B, F**). Biological sex and rotenone exposure difference were observed with four-point support (**Fig. 11C, G**) and run duration (**Fig. 11E, I**) where male WT rotenone exposed animals had a wider base of support (**Fig. 11D**) resulting in longer run durations to cover the same distance when compared to male animals within other genotypes and toxin exposures and female animals. Behavioral analysis using open-field chamber exploration was utilized to determine depressive and anxiety like behavior in male animals, similar to that seen in idiopathic-PD. Heat map and x,y,z plane coordinate line tracking was used to represent the overall movement by the animals over the 5 minute time-span in the chambers (**Fig. 11J-M**). Weekly time-point sampling throughout the rotenone dosing and progressive lesioning phase resulted in significant alterations in the total distance traveled by individual animals with respect to the genotype, biological-sex, and rotenone exposure and a combination thereof dependent on the timepoint of the recordings (**Fig. 11N-Q**). Total movement time was timepoint and genotype dependent, respectively. Male microglial-specific IKK2 knockout animals showed decreased movement time at 2 WPI (**Fig. 11O**) where females showed no significant changes between genotype or rotenone exposure groupings within each timepoint (**Fig. 11R**). Rearing number decreased within WT male rotenone exposed animals at 1 WPI, being timepoint dependent, where females, again, were unremarkable between groups at each timepoint.

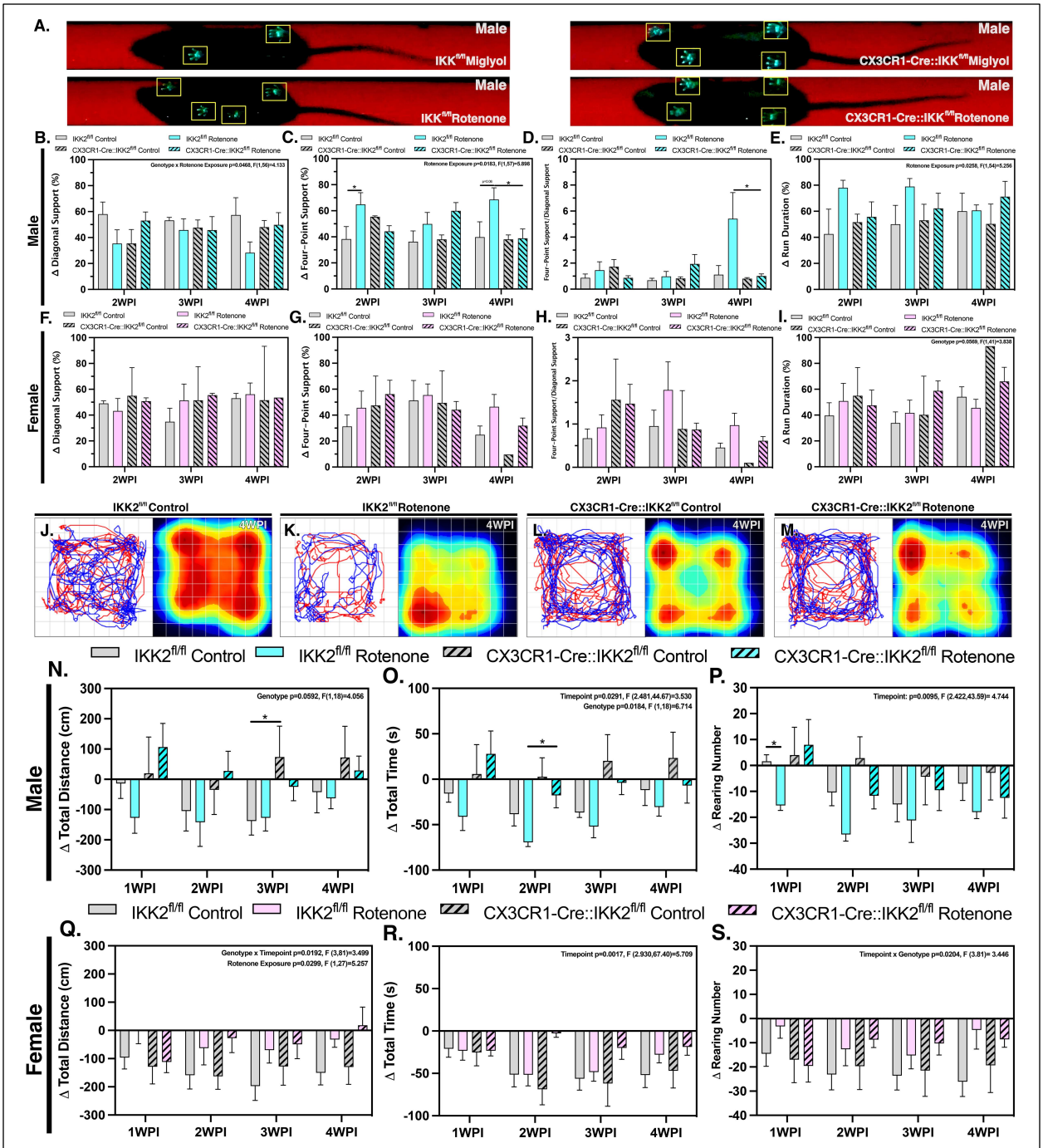

Figure 11. Real-time trackway gait analysis and open field behavioral testing reveal biological-sex, rotenone exposure, and genotypic differences resembling idiopathic PD. Footpad identification on real-time trackway analysis to identify gait specific parameters of diseased-state (**A**). Male and female, respectively, change in diagonal support (**B, F**), four-point support (**C, G**), balance determination ratio (**D, H**) and run duration (**E, I**) along the trackway. Linear and heatmap representation of male WT control (**J**), WT rotenone exposed (**K**), KO control (**I**), and KO rotenone exposed (**M**) animals during open-field analysis testing. Male and female, respectively, change in total distance moved (**N, Q**), total time spent moving (**O, R**) and rearing number (**P, S**) recorded during the 5-minute analysis window. Trackway analysis: *n*=9 per group. Open field analysis *n*=6 per group. *$p < 0.05$.

3.3.2 Neurochemical alterations similar to Parkinson's Disease are present within rotenone treated animals.

Neurochemical changes within the striatum were assessed to determine relative increases or reduction in neurotransmitters in the serotonin and DA metabolic pathways. Catecholamine quantification within striatal tissue revealed no significant changes with the levels of DA or 3-MT between genotype, exposure group, and biological sex (**Fig. 12A, C**). DOPAC was decreased within the male WT rotenone exposed animals when compared to male KO miglyol exposed animals, where overall biological sex, genotype, and rotenone exposure significance was observed (**Fig. 12B**). Terminal pathway metabolite, HVA showed significant decreased between KO rotenone exposed groups in male animals (**Fig. 12D**). DOPAC/DA metabolite to parent molecule ratio revealed rotenone exposure as a potentially biologically relevant determinate for behavioral changes previously observed (**Fig. 12E**), where total metabolite over parent molecule, DA, showed no significance between any grouping (**Fig. 12F**). 5-HT levels were decreased in the rotenone exposed male WT animals when compared to their WT control counterparts (**Fig. 12G**). NE was significantly decreased in male WT rotenone exposed animals when compared to male WT controls and KO rotenone exposed groupings. There were significant alterations in NE with the combinations of biological sex:genotype:rotenone exposure and biological sex:rotenone exposure (**Fig. 12H**). Metabolite analysis of serotonin (5-HIAA) revealed significant decreases in the male WT rotenone exposed animals in comparison to the WT controls and KO rotenone exposed males (**Fig. 12I**).

3.3.3 Microglial specific-IKK2 knockout results in increased microglial populations in male animals.

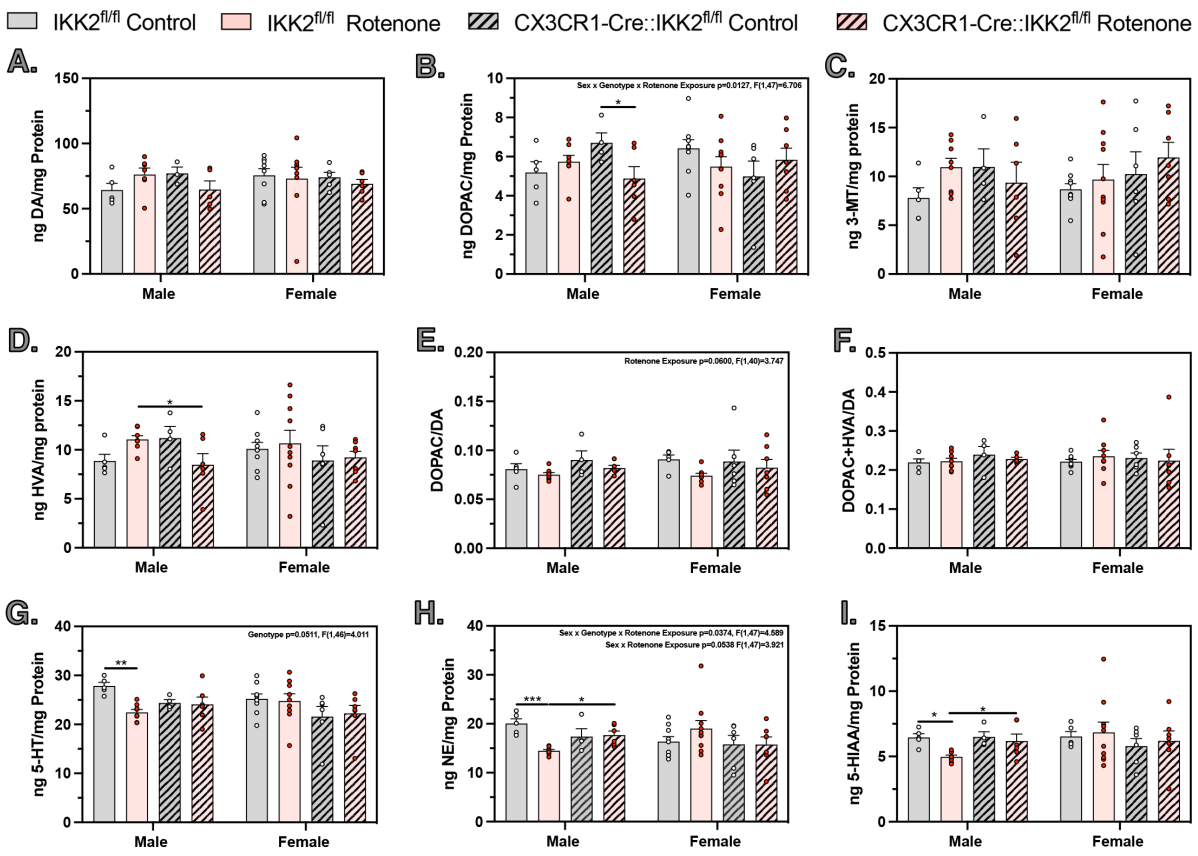

Figure 12. Neurochemical alterations in male animals indicate metabolic pathway specific inhibition of catecholamines resulting in behavioral changes that is rescued with microglial-specific IKK2 knockout. Catecholamine analysis between male and female animals within WT and KO control and rotenone exposed groups for dopamine (DA, **A**), 3-4-dihydroxyphenylacetic acid (DOPAC, **B**), 3-methoxytyramine (3-MT, **C**), homovanillic acid (HVA, **D**), DOPAC to DA ratio (**E**), metabolite to parent molecule ratio (**F**), 5-hyroxytryptamine (5-HT, **G**), norepenipherine (NE, **H**) and 5-hyrdoxyindoleacetic acid (5-HIAA, **I**). *n*=9 per group. **p*< 0.05, ***p*< 0.01, ****p*< 0.001.

Microglial cell involvement in the pathological progression of PD was determined by identification of the total number of microglia in the SN and ST in control and rotenone-exposed mice by immunofluorescence microscopy and whole-brain montage imaging for $IBA1^{+}$ microglia in relation to DAn of the SNpc. Representative montage imaging of male WT control and rotenone exposed, and KO control and rotenone exposed, respectively, in the SN (**Fig. 13A-D**) and ST (**Fig. 13E-H**). Morphological differences were determined through branch length per cell, number of branches per cell and the number of junctions per cell. High magnification insets of microglia

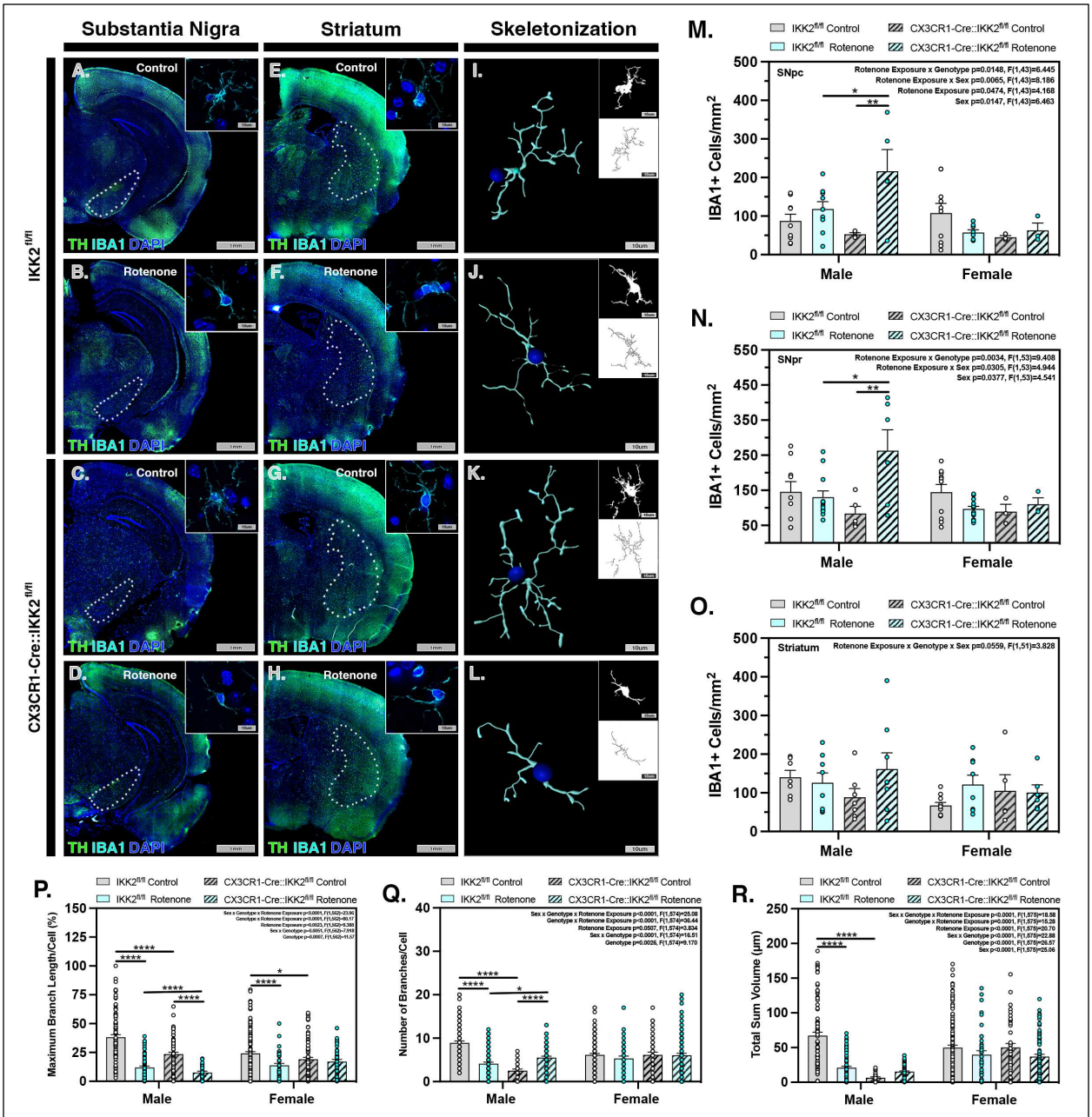

Figure 13. IKK2 knockout in male animals exposed to rotenone results in increased microglial recruitment, regional density and morphometric activation. Full brain 10X montage representative images of male hemispheres within the basal midbrain (**A-D**) and striatum (**E-H**) with microglia (IBA1, cyan) and DAn (TH, green). Single cell high magnification insets from the SN sections in 3-dimensional renderings along with binary and skeletonization representations (**I-L**). Regional identification of IBA1^{+} cells per area within the SNpc (**M**), SNpr (**N**), and striatum (**O**). Phenotypic and morphometric discrimination of microglia through maximal branch length (**P**), branch number per cell (**Q**), and branch volume per cell (**R**). n=9 per group. *p< 0.05, **p< 0.01, ****p<0.0001

within the SN were converted to binary form and skeletonized, alongside 3D rendering (**Fig. 13I-L**). Microcytois was observed within the SNpc and SNpr in male KO rotenone exposed animals in comparison to male WT rotenone exposed animals, and male KO control animals. These regions showed rotenone exposure:genotype, rotenone exposure:sex, and sex as determinants for statistical variance (**Fig. 13M, N**). The SNpc also showed rotenone exposure alone as a factor leading to increases in cellular populations (**Fig. 13M**). Striatal region analysis revealed rotenone exposure:genotype:sex differences that were trending (**Fig. 13O**). Morphometric changes in maximum branch length per cell were observed in males with decreases in WT rotenone exposed animals and KO rotenone exposed animals, whereas females only showed rotenone exposure differences in WT animals. Reduction in branch length was also observed in male and female KO control animals when compared to WT control animals (**Fig. 13P**). Total branches per microglial cell revealed male only changes with reduction on rotenone exposed animals and KO control animals. There were increases in total branches in the rotenone exposure groups when comparing genotypes (**Fig. 13Q**). Total sum volume of individual microglial cells was reduced in male animals in WT rotenone exposure and KO control when compared to WT control (**Fig. 13R**).

3.3.4 Differential astrocytic phenotyping and populational quantification show decreases in astrocytic activation and proliferation post-rotenone exposure in microglial IKK2 knockout animals.

Astrocytic involvement in progressive neurodegeneration was analyzed through cellular phenotyping and regional populational dynamic shifts in the SN and ST through 10X whole brain montage imaging for A1 astrocytes and overall astrocyte population numbers in concert with C3, a second A1 marker. Representative montage imaging of male WT control and rotenone exposed,

and KO control and rotenone exposed, respectively, in the SN (**Fig. 14A-D**) and ST (**Fig. 14E-H**). High magnification insets and 3D rendering from the SN depict GFAP abundance and C3 reactive protein within S100β^{+} soma and GFAP^{+} processes (**Fig. 14A-D**). Region specific analysis of the SNpc revealed significant increases in GFAP abundance in male WT rotenone exposed animals and KO control animals when compared to WT control animals. Interestingly, there were decreases in the abundance of GFAP in male KO rotenone exposed animals compared to the KO controls. There was no significant observation made within the female group alone. Group comparisons revealed sex:genotype:rotenone exposure, genotype:rotenone exposure, and genotype as determinants of variance difference (**Fig. 14I**). Within the SNpr, there were no statistically significant observations made with regards to GFAP expression (**Fig. 14J**). Striatal analysis of GFAP showed increases in male KO control animals when compared to WT control in addition to KO rotenone exposure to WT rotenone exposure. Decreases of GFAP were observed when comparing KO control to KO rotenone exposed groupings within the male population. There were no statistically significant observations made within the female populations. Overall, sex:rotenone exposure, sex:genotype, and genotype alone contributed to variance differences observed (**Fig. 14K**).

The reactive astrocyte process marker, GFAP, was used in conjunction with complement C3 staining to identify distal cellular C3 prevalence. Within the SNpc, there were statistical differences between genotypes in respective exposure groupings (**Fig. 14L, M**). Female astrocytes in the SNpc showed increases in A1 reactivity in WT rotenone exposed animals compared to WT controls, whereas this increase in C3 presence in GFAP^{+} processes with rotenone exposure was diminished in KO animals (**Fig. 14M**). SNpr analysis revealed variance between genotypes when comparing control and rotenone exposed animals in males and females (**Fig. 14N, O**). Male WT

and KO animals exposed to rotenone had increases in C3 protein within GFAP$^+$ processes. Interestingly, female WT rotenone exposed animals had decreases in C3 protein within GFAP$^+$ processes, and female KO rotenone exposed animals showed no statistical difference from the KO controls (**Fig. 14O**). Striatal analysis showed similar results to SNpc and SNpr where control and rotenone exposed KO animals had less C3 in GFAP$^+$ processes (**Fig. 14P, Q**). Male KO rotenone exposed animals had decreases in reactivity (**Fig. 14P**), in contrast to females where KO rotenone exposed animals had increases in reactive astrocytic processes and the WT rotenone exposed animals had decreases in C3 protein in GFAP$^+$ processes when compared to WT control (**Fig. 14Q**).

The pan-astrocytic somal marker, S100β, was used in conjunction with C3 to further determine reactive astrocytic phenotypes within the SNpc, SNpr, and ST. Somal C3 in the SNpc was increased in male control and rotenone exposed KO animals when compared to WT counterparts. Decreases in somal C3 were observed in rotenone exposed KO animals when evaluated against KO controls (**Fig. 14R**). Female SNpc analysis revealed decrease in reactive soma in rotenone exposed WT animals compared to WT controls (**Fig. 14S**). Somal reactivity in the SNpr of male animals was opposite of that in the SNpc, where decreases in WT rotenone exposed animals were present when compared to WT control, along with decreases in KO control animals compared to WT control animals (**Fig. 14T**). Female SNpr showed more somal reactivity than the female SNpc. Decreases between WT treatment groups were similar to that seen in the SNpc, however, large decreases were present in the SNpr between KO rotenone exposed and KO control animals. There were also increases in somal C3 between WT control and KO control, and decreases between WT control and WT rotenone exposed. Striatal somal C3 was decreased in male and female KO control and KO rotenone exposed animals, where decreases were present between

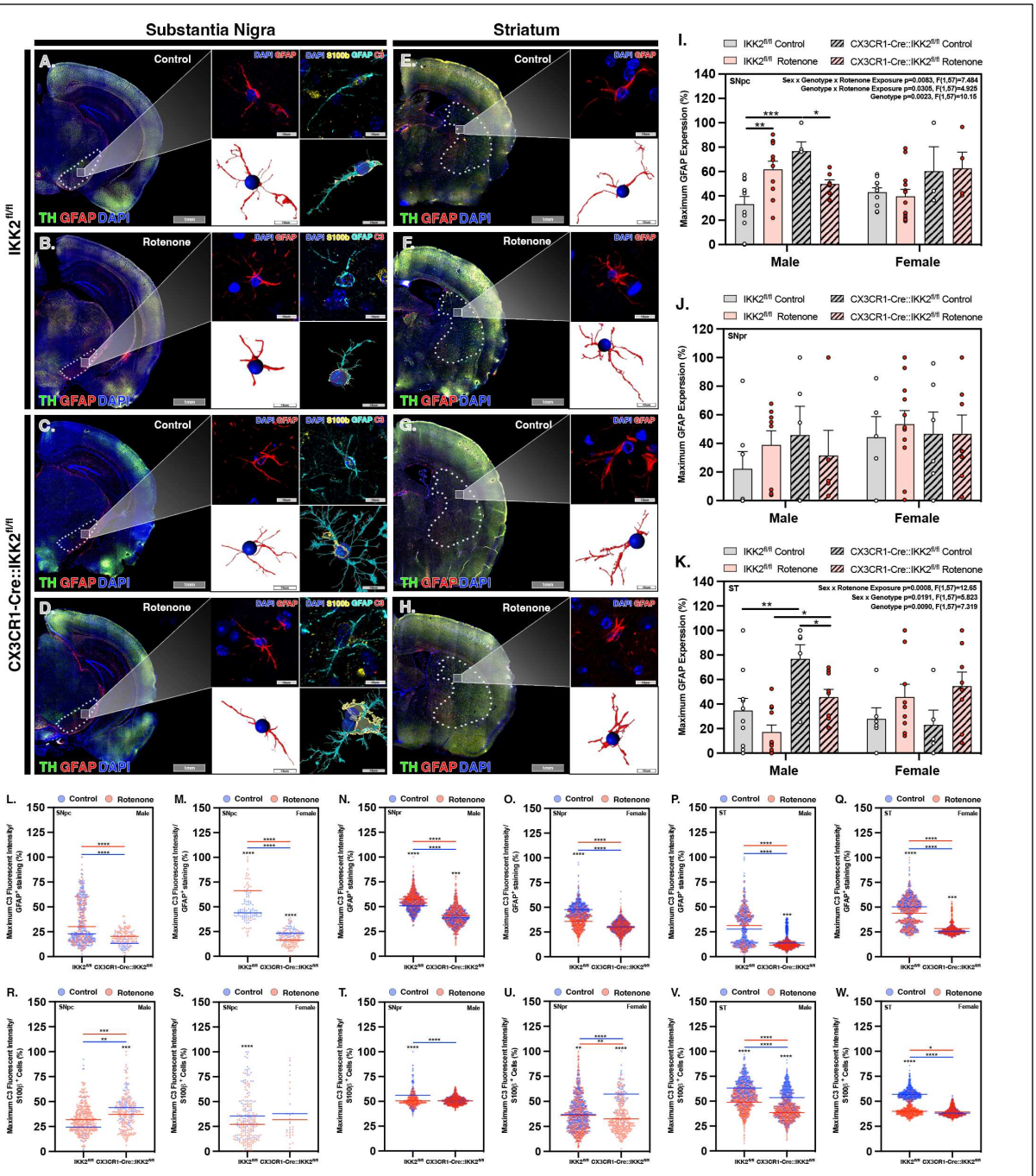

Figure 14. NF-κB inhibition in male microglia reduce reactive astrocyte populations and C3 in astrocytic processes. Full brain 10X montage representative images of male hemispheres within the basal midbrain (**A-D**) and striatum (**E-H**) with reactive astrocyte staining (GFAP, red) and DAn staining (TH, green) with 100X high magnification images and accompanying 3-dimensional renderings of reactive astrocytes (GFAP, red, cyan; S100β, yellow and C3, red). Maximum GFAP expression (%) per regional area within the SNpc (**I**), SNpr (**j**), and ST (**K**). Maximal C3 expression in GFAP$^+$ processes in male and female SNpc (**L, M**), SNpr (**N, O**), and ST (**P, Q**), respectively. Maximal C3 expression in S100β$^+$ soma in male and female SNpc (**R, S**), SNpr (**T, U**), and ST (**V, W**), respectively. *n*=9 per group. **p*< 0.05, ***p*< 0.01, ****p*< 0.001, *****p* <0.0001.

WT control and WT rotenone exposed (**Fig. 14V, W**). There were also somal C3 decreases in male KO rotenone exposed animals compared to male KO controls (**Fig. 14V**).

3.3.5 Inhibition of microglial NF-κB activation results in reduced dopaminergic neurotoxicity within the SNpc.

Neurodegeneration of DAn within the SNpc and projecting fibers to the striatum were determined through 10X full brain montage imaging throughout all groupings. Representative montage imaging and high magnification inset of male WT control and rotenone exposed, and KO control and rotenone exposed, respectively, in the SN (**Fig. 15A-D**) and striatum (**Fig. 15E-H**) show decreased TH^+ neuronal soma within male WT rotenone exposed animals when compared to WT controls. There were decreases in male neuronal soma in the KO rotenone exposed animals, however, these were not significant against the KO controls. There were no statistical differences of note within the female animals. Statistical variance within this analysis was due to rotenone exposure alone and biological sex alone (**Fig. 15I**). Pan-neuronal staining showed similar significance within males where WT rotenone exposed animals had decreased amounts of neurons when compared to WT control, and no significance seen between the KO groups. Likewise, the statistical variance was attributed to the same factors as previously observed for TH^+ soma (**Fig. 15J**). Striatal terminal endpoint analysis of TH^+ fibers showed significant decreases in male and female KO control animals when compared to WT control. Male KO rotenone exposed animals had less TH intensity when compared to WT rotenone exposed animals, but significantly more than that of male KO control animals. The overall variance within the striatum was attributed to genotype:rotenone exposure, genotype:sex, and genotype alone (**Fig. 15K**).

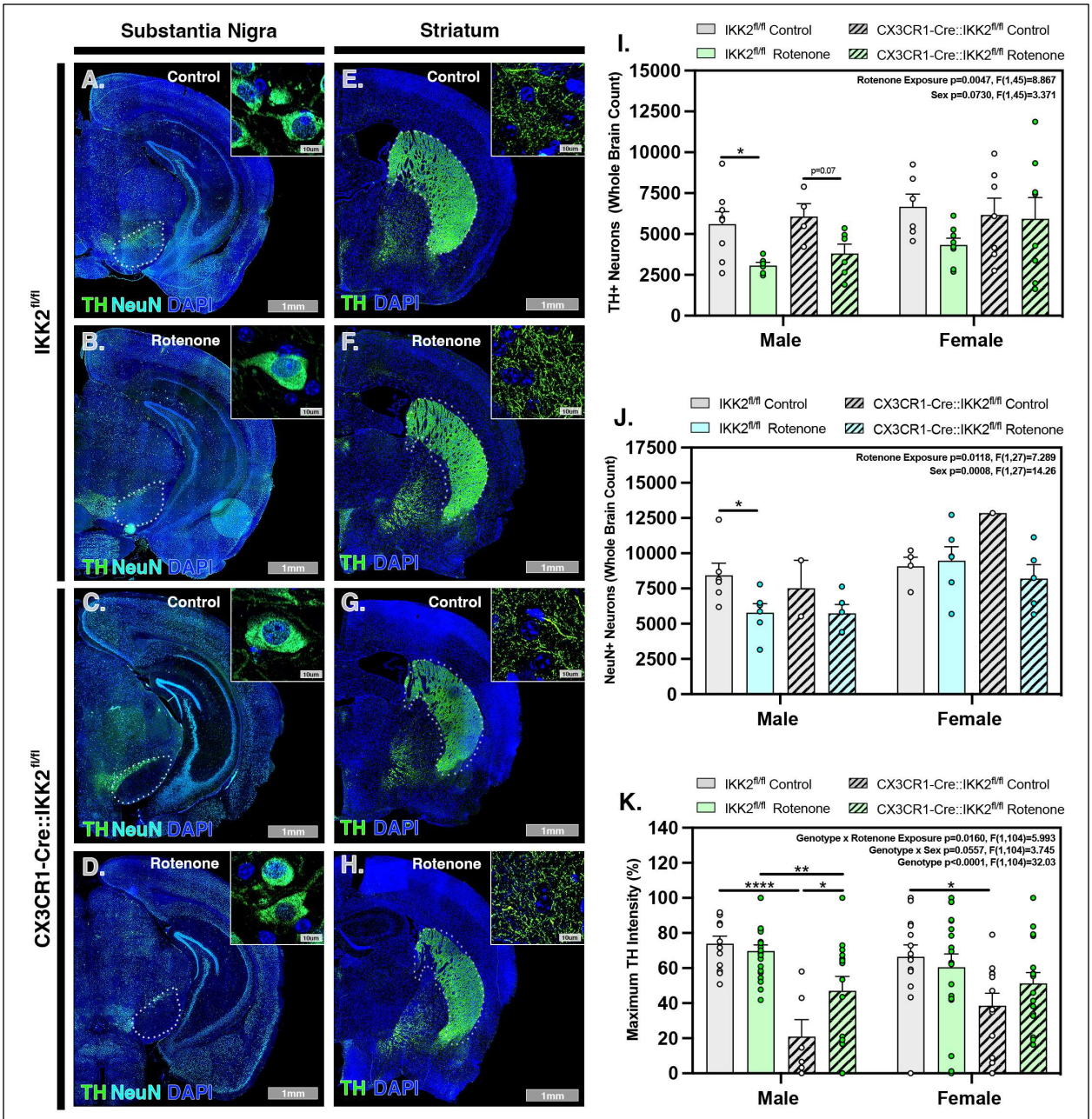

Figure 15. Microglial cell-specific IKK2 knockout reduces dopaminergic neuron degeneration in male animals. Full brain 10X montage representative images of male hemispheres within the basal midbrain (**A-D**) and striatum (**E-H**) with DAn (TH, green) and pan-neuronal staining (NeuN, cyan) with 100X high magnification insets. DAn soma were decreased in male WT rotenone exposed animals, which is recovered in the KO male rotenone exposed animals (**I**). Pan-neuronal staining shows decreases in overall neuronal soma within the SNpc in male WT rotenone exposed animals, which is also recovered in KO rotenone exposed animals (**J**). Striatal TH intensity measurements show decreases in TH intensity in female and male animals. There are also decreased in TH intensity within male KO rotenone exposed animals when compared to WT rotenone exposed animals (**K**). n=9 per group. *p< 0.05, **p< 0.01, ****p <0.0001.

3.3.6 Regional analysis indicate that microglial cells function to clear misfolded α-synuclein aggregates.

Immunohistochemical staining of the basal midbrain (**Fig. 16A-D**) and striatum (**Fig. 16E-H**) show sex and genotypic dependent variance with the total number of p129 positive staining events. Male KO rotenone exposed animals show more $p129^{+}$ objects within the SNpc, when compared to male WT rotenone exposed animals. Inversely, female WT rotenone exposed animals had more p129 positive objects detected than the KO rotenone exposed females within the SNpc (**Fig. 16I**). The total area of p129 positivity within the SNpc was greater in male KO rotenone exposed animals than was seen in WT rotenone exposed animals (**Fig. 16J**). Ratio analysis for aggregate determination based on area and object count, show that rotenone exposure and biological sex are variables in the aggregation of p129 in the SNpc (**Fig. 16K**).

Investigation of $p129^{+}$ events within the SNpr showed reduction in male WT rotenone exposed animals when compared to WT controls. Female WT rotenone exposed animals also had higher p129 object counts when compared to female KO rotenone exposed animals (**Fig. 16L**), where genotype was a statistical driver of variance between groups. The total area of p129 objects within the SNpr revealed increases in female WT rotenone exposed tissue when compared with female KO rotenone exposed tissue. Genotype was also the driver for statistical variance in total area within the SNpr (**Fig. 16M**). Ratio determination within the SNpr showed increases in overall value within male WT rotenone exposed animals when compared to control counterparts, indicating larger aggregates within this region. The same observation was present for female KO rotenone exposed animals in comparison to female KO control animals (**Fig. 16N**).

$p129^{+}$ analysis in the ST revealed increases in magnitude of object counts in male WT rotenone compared to WT control males. WT rotenone exposed females had decreased amounts

of overall p129^{+} objects when compared to WT control and KO rotenone exposed females (**Fig. 16O**). The total p129^{+} area occupied within the ST was increased in WT rotenone exposed and KO control male animals, where WT rotenone p129^{+} area decreased in females when compared to same sex WT control. The decreases observed in the WT rotenone exposed females were significant when compared to the increases observed in the KO rotenone females (**Fig. 16P**). Ratio analysis of p129^{+} area to object count of p129^{+} foci, showed no significant deviations in variance for females, however, there were significant increases in ratio values in KO control male animals when compared to WT control and KO rotenone of the same sex (**Fig. 16Q**). This indicated larger aggregate accumulation within KO control animals and smaller order accumulation of p129 in KO rotenone exposure in the striatum. The combination of sex:genotype:rotenone exposure, genotype alone and sex alone were contributing factors towards the variance observed within object counts and total p129^{+} area. These factors in addition to rotenone exposure alone accounted for the variance observed in the ratio analysis of p129 positivity in the ST.

3.3.7 Inhibition of NF-κB in microglia leads to increased misfolded α-syn accumulation within dopaminergic neurons of the substantia nigra.

Prevalence of misfolded α-syn was determined by regional and individual cellular staining intensity in the SNpc and SNpr. High magnification identification of p129 in DAn and IBA1^{+} cells in male WT control (**Fig. 17A**), WT rotenone exposed (**Fig. 17B**), KO control (**Fig. 17C**), and KO rotenone exposed (**Fig. 17D**). Maximal regional staining intensity analysis in the SNpc showed no significant changes in males, where there was significance between KO control and KO rotenone exposed females. Rotenone exposure:genotype:sex, rotenone exposure;sex, and rotenone exposure were driving factors of statistical variance (**Fig. 17E**). SNpr analysis was similar in such that there

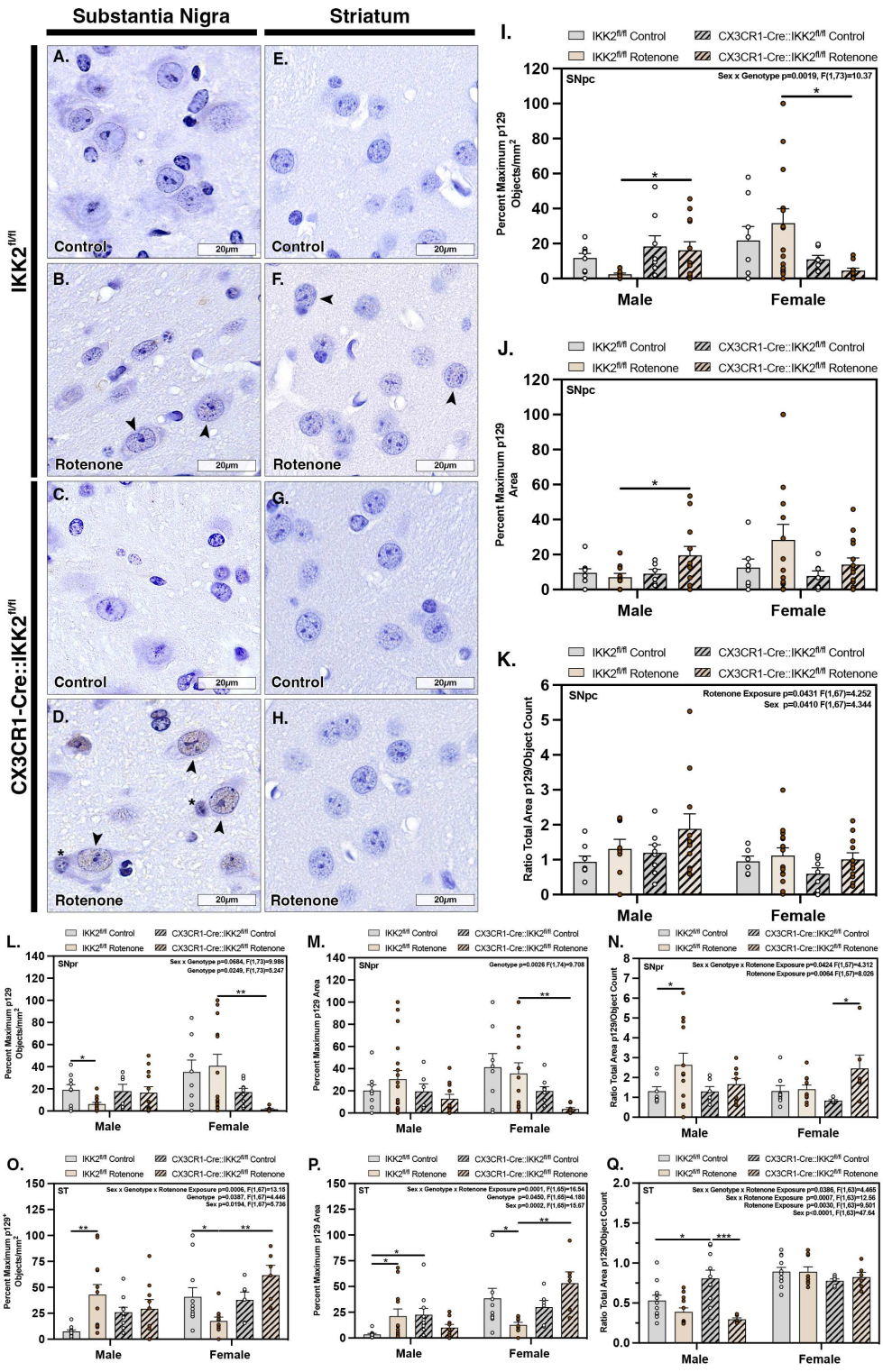

Figure 16. Microglial NF-κB inhibition results in accumulation of lower order misfolded α-synuclein that is regionally and sex dependent. Full brain 10X montages of male hemispheres in the basal midbrain (**A-D**) and striatum (**E-H**) with 100X high magnification insets of immunohistochemically stained tissue for p129. Regional determination of the amount of p129 events per area, maximal p129 occupied area, and ratio of occupied area to objects of p129 within the SNpc (**I-K**), SNpr (**L-N**), and ST (**O-Q**). *n*=9 per group. *$p< 0.05$, **$p< 0.01$.

were minimal changes in males, and differences between female KO control and KO rotenone exposure were present. Rotenone exposure:genotype:sex, rotenone exposure;sex, rotenone exposure, and sex were driving factors of statistical variance (**Fig. 17F**). When investigating maximal p129 intensity in TH soma, however, there were statistical changes observed in male animals. There were decreases between WT control and WT rotenone exposed and increases between WT and KO rotenone exposed. Female rotenone exposed animals, both WT and KO, had increased levels of p129 in TH^+ soma, when compared to genotype controls. KO rotenone exposed animals had increased levels of p129 in contrast to WT rotenone exposure. Rotenone exposure:genotype:sex, rotenone exposure;sex, rotenone exposure, and sex were driving factors of statistical variance (**Fig. 17G**).

Peripheral dissemination of p129 through serum ELISA showed decreases in overall absorbance between male WT control:WT rotenone exposure and WT control:KO control. There were increases in male serum p129 in KO rotenone exposed animals compared to KO control animals. Female animals only showed statistical decreases in serum p129 when KO control was compared to KO rotenone exposure. Sex:genotype:rotenone exposure, sex:genotype, and genotype were all drivers of statistical variance within p129 peripheral dissemination (**Fig. 17H**).

3.3.8 p62 mediated autophagy in microglia is reduced with NF-κB knockout and leads to subsequent reduction in peripheral dissemination of p129 in males.

Three-dimensional rendering of microglia within the SN shows differential amounts of p62 and p129 in male microglia (**Fig. 18A-D**). Genotype comparisons within males exposed to control or rotenone reveal that in WT animals p62 intensity within $IBA1^+$ cells increase significantly, of which is sequestered within KO animals (**Fig. 18E**). Similar biological modulation of p62 is

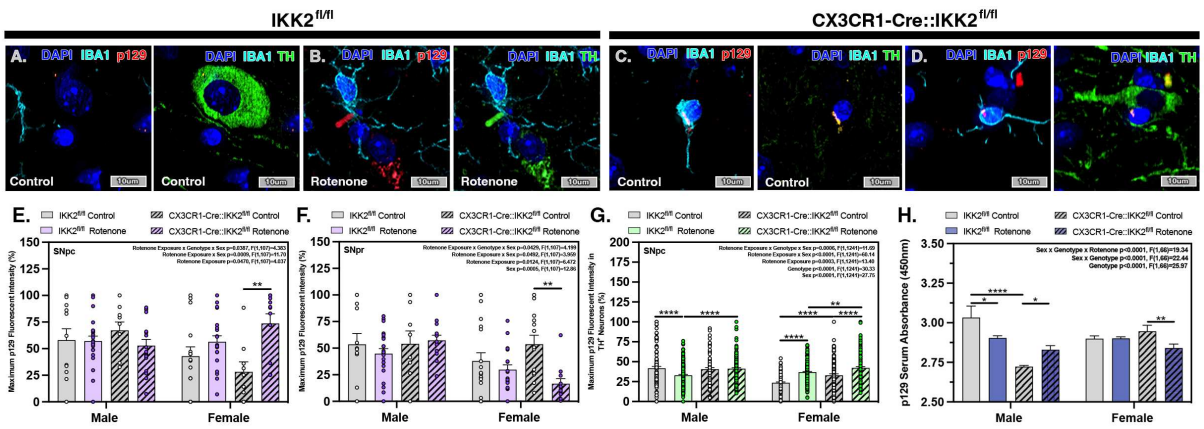

Figure 17. Inhibition of microglial NF-κB increases misfolded α-synuclein accumulation in dopaminergic neurons. High magnification 100X images of misfolded α-syn (p129, red), DAn (TH, green), and microglia (IBA1, cyan) in the SN of male WT control (**A**), rotenone exposed (**B**) and KO control (**C**) and rotenone exposed (**D**) animals. Regional maximal p129 intensity in the SNpc (**E**) and SNpr (**F**) of male and female animals. Total p129 maximal intensity in TH^+ DAn soma in male and female animals (**G**). ELISA absorbance units (A.U.) of p129 in serum samples from male and female animals (**H**). n=9 per group. *$p<$ 0.05, **$p<$ 0.01, ****$p<$0.0001.

observed within female animals (**Fig. 18F**). p129 intensity within WT males exposed to rotenone is significantly greater than the male WT control counter parts, which increases within the KO animals exposed to rotenone, showing an inverse relationship with the amount of p62 present within microglial cells (**Fig. 18G**). WT females also have increased amounts of p129 within microglia when exposed to rotenone. However, KO animals show decreased amounts of p129 in microglial cells, significantly less than in WT females exposed to rotenone (**Fig. 18H**). Principal component analysis of p62 (**Fig. 18I**) and p129 (**Fig. 18J**) show distinct clade patterns dependent upon biological sex, rotenone exposure and genotype

3.3.9 Transcriptional analysis of NF-κB mediated inflammatory genes reveal biological-sex dependent mechanisms of cellular function and recruitment.

Heat map comparison of gene transcription indicate biological sex differences in addition to microglial inflammatory pathways as drivers for pathological response (**Fig. 19A**). Radar plot

comparison of male and female fold change gene expression in WT rotenone exposed (**Fig. 19B**), KO control (**Fig. 19C**), and KO rotenone exposed animals (**Fig. 19D**) where cluster differentiation is as follows: Cluster 1- Regulation of TLRs by endogenous ligand; Cluster 2- Neutrophil and monocyte chemotaxis; Cluster 3-TNFR2 non-canonical Nf-κB pathway; Cluster 4- Astrocyte, monocyte and T-cell chemotaxis; Cluster 5-Jak-stat signaling; Cluster 6- Complement and coagulation cascades. Male WT animals exposed to rotenone show increases in gene regulation involving the Jak-stat pathways, and TNFR2 non-canonical NF-κB signaling (**Fig. 19B**). Male control KO animals show upregulation in genes responsible for regulation of TLRs and TNFR2 non-canonical NF-κB signaling pathways, whereas females show upregulation of neutrophil and monocyte chemotaxis transcription (**Fig. 19C**). Male KO rotenone exposed animals show the greatest variance in gene expression with increases in regulation of TLRs, neutrophil and monocyte chemotaxis, TNFR2 non-canonical NF-κB pathways, astrocyte, monocyte, and T-cell chemotaxis, and jak-stat signaling, where females interestingly show upregulation of complement and coagulation pathways (**Fig. 19D**).

Venn-diagram mapping of unique and shared upregulated genes in rotenone treated animals identify 9 inflammatory genes that are unique to male WT and male KO animals (**Fig. 19E**). Male rotenone exposed animals share 20 genes that are upregulated during the pathological exposure to rotenone, STRING mapping of these and corresponding GO-terms identify increases in chemotaxis, inflammatory cascades, microglial activation, and neutrophil recruitment as potential drivers of pathology (**Fig. 19F**).

3.3.10 Differential gene expression indicates male microglia as key potentiators of peripheral cell recruitment and exacerbated inflammatory stimuli.

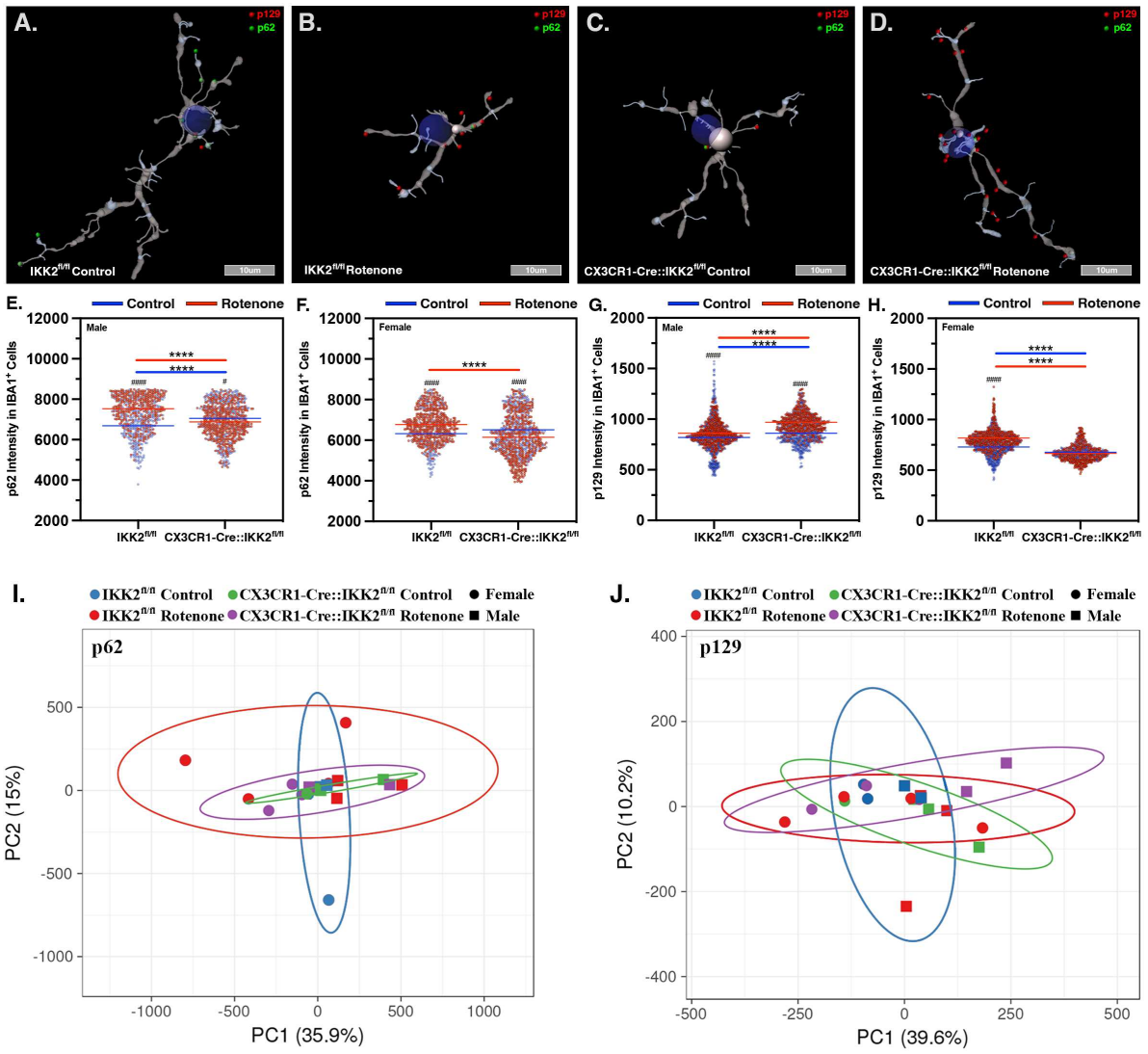

Figure 18. Sequestosome 1 mediated autophagy of p129 is inhibited in IKK2 knockout animals. High magnification 3-dimensional renderings from tri-stained fluorescent sections of individual microglial cells within the SN with areas of p62 positivity (green) and p129 positivity (red) in WT control (**A**), WT rotenone exposed (**B**), KO control (**C**) and KO rotenone exposed (**D**). Individual IBA1^{+} microglial cell analysis of overall p62 intensity in male (**E**) and female (**F**) animals in control (blue) and rotenone exposure (red). Overall fluorescent intensity of p129 in individual IBA1^{+} cells in male (**G**) and female (**H**) animals in control (blue) and rotenone exposure (red). Principal component analysis of individual exposure groups, genotype, and biological sex for p62 (**I**) and p129 (**J**). n=9 per group. #p<0.01 intra-genotype comparison, ####p<0.0001 intra-genotype comparison, ****p <0.0001.

Heat map comparison of male (**Fig. 20A**) and female (**Fig. 20D**) show distinct transcriptional regulation of inflammatory response patterns that are sex, genotype and exposure dependent. STRING association mapping of male and female up- and down-regulated genes in WT (**Fig. 20B, E**) and KO (**Fig. 20C, F**) rotenone exposed animals, respectively. Differential fold change expression of individual inflammatory genes shows increases in *Il1β* (**Fig. 20G**) and *Infγ* (**Fig. 20H**) in male WT rotenone exposed animals, significant when compared to WT control and KO rotenone exposed. In contrast, females showed reduction in these two genes with rotenone exposure and genotype. Increases in immune cellular recruitment transcription was observed in male KO rotenone exposed animals. There were no significant changes observed in these genes in female animals (**Fig. 20I-K**). The complement deposition protein, C4b, was increased in male KO controls, and no changes in females were observed (**Fig. 20L**).

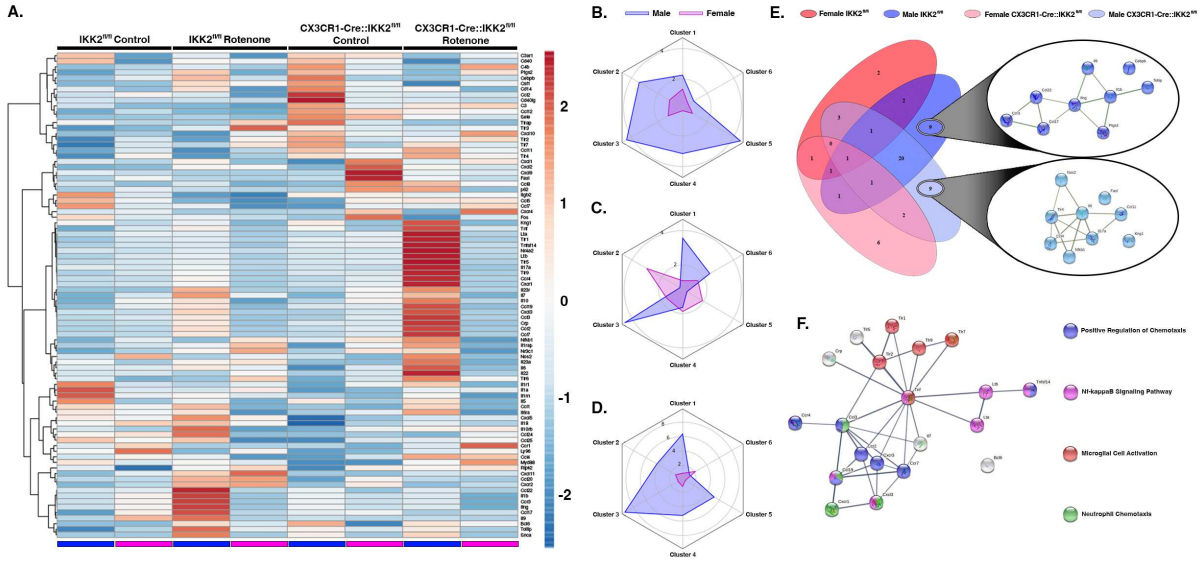

Figure 19. Genotype, biological sex, and rotenone exposure dependent gene transcription increases the amount of invading peripheral immune cells and resulting inflammation in the substantia nigra. Heat map analysis of the fold expression of genes regulated in the inflammatory process of rotenone induced neurodegeneration in WT and KO male (blue sub-indication) and female (pink sub-indication) animals (**A**). Radar graph mapping of cluster specific gene regulation in male (blue) and female (pink) animals in WT rotenone exposure (**B**), KO control (**C**) and KO rotenone exposure (**D**) where the clusters are as follows: 1) Regulation of TLRs by endogenous ligands, 2) neutrophil and monocyte chemotaxis, 3) TNFR2 non-canonical NF-κB pathway activation, 4) astrocyte, monocyte and T-cell chemotaxis, 5) Jak-stat signaling, and 6) complement and coagulation cascades. Venn diagram analysis of all significantly up-regulated genes in rotenone exposed animals (**E**) highlighting 9 genes that are discreetly upregulated in male WT rotenone exposed animals and male KO rotenone exposed animals. STRING mapping of the 20 shared genes upregulated in male rotenone exposed animals (**F**) highlighting genes responsible for positive regulation of chemotaxis (blue), NF-κB signaling pathway (pink), microglial cell activation (red), and neutrophil chemotaxis (green). *n*=3 per group.

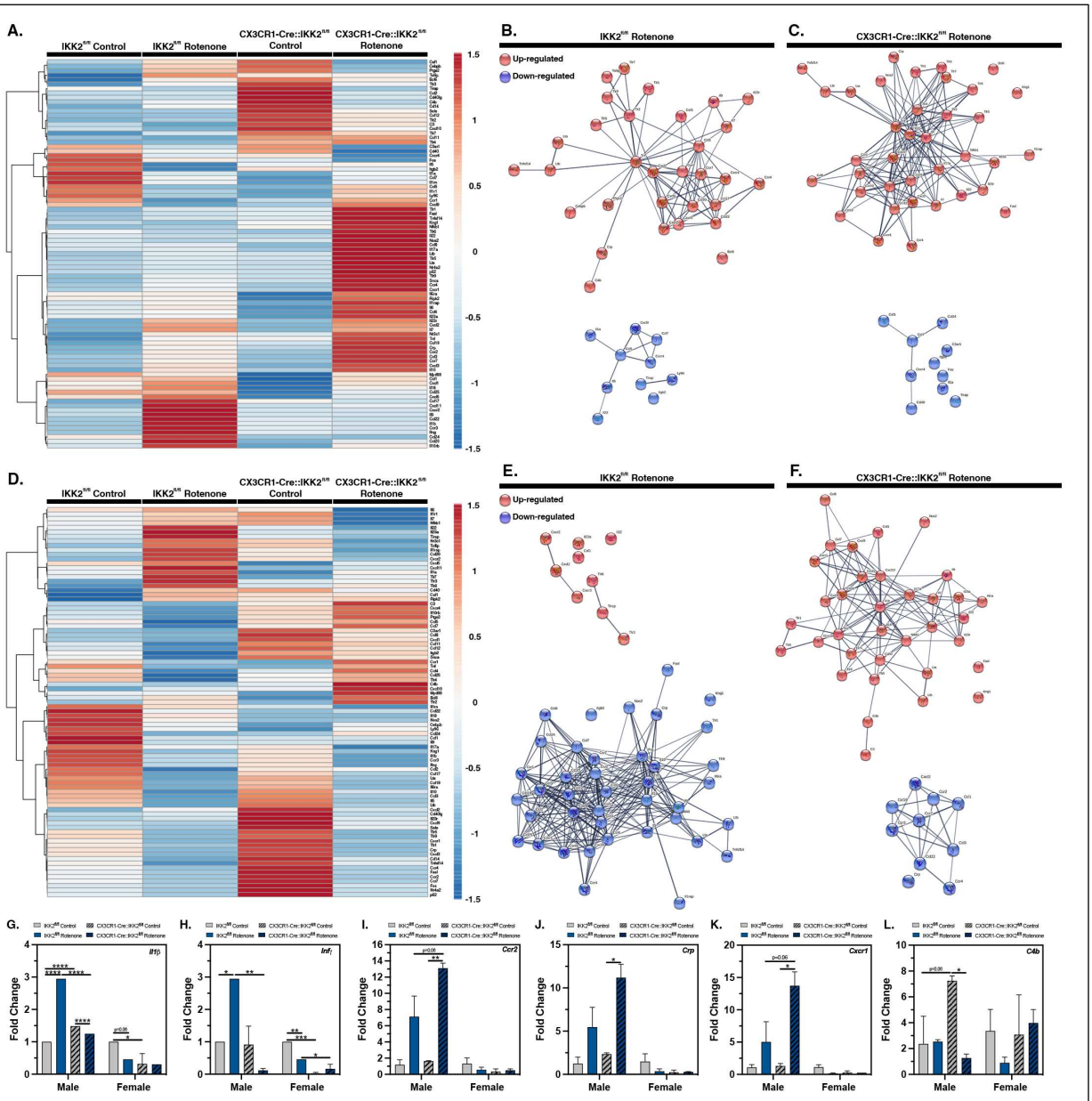

Figure 20. Biological sex dependent regulation of inflammatory transcriptional factors show male microglial involvement mediates cellular recruitment and T-cell interaction pathways. Heat map analysis of gene expression in male and female animals (**A-D**). STRING mapping of genes that are up-regulated and down-regulated in male WT animals (**B**) and KO animals (**C**), respectively. STRING mapping of genes that are up-regulated and down-regulated in female WT animals (**E**) and KO animals (**F**), respectively. Differential expression of *Il1β* (**G**), *Infγ* (**H**), *Ccr2* (**I**), *Crp* (**J**), and *C4b* (**K**) in male and female animals of all genotypic and exposure groupings. n=3 per group. *$p<0.05$, **$p<0.01$, ***$p<0.001$, ****$p<0.0001$.

3.4 Discussion

The importance of microglia-mediated inflammatory processes in the progressive pathology of neurodegenerative diseases has been increasingly demonstrated (Hickman et al., 2018). Activation of these cells from the resting/ramified state to the amoeboid/activated state results in activation of NF-κB-mediated inflammatory signaling cascades, which produce cytokines and chemokines that lead to enhanced resident and peripheral immune cell responses. Studies of whole-brain inhibition of NF-κB demonstrated a reduction in α-syn accumulation and spread, decreased neurodegeneration and reduction in resident glial cell activation (Bellucci et al., 2020), highlighting the importance of this pathway as a potential therapeutic target. Despite this, it is unclear how NF-κB activation in individual glial cell subtypes contributes to the overall disease state. Here, we demonstrate for the first time, that male microglia-specific knockout of NF-κB increases accumulation of low-order p129 in DAn and microglial cells with subsequent reduction in microglial trafficking and dissemination of p129 into the periphery. However, even with increased levels of p129, there was not an increase in neurodegeneration in the SNpc, supporting that microglial responses to physiologic and microenvironment changes are a main driver in eliciting pathological outcomes relevant to PD.

Prodromal stages of PD include behavioral and cognitive deficits that are in-part due to alterations in neurotransmitter levels that associated with neuropsychiatric symptoms that are often not associated with a diagnosis of PD until decades later. Behavioral patterns and coordinated motor-movement analysis revealed biological-sex dependent reduction in imbalance, ability to initiate movement, anxiety and depression in male KO animals exposed to the known environmental toxicant rotenone when compared to WT counterparts (**Fig. 1**). Initial impairments observed in rotenone-exposed WT male mice were not observed in females, and KO of NF-κB in

females resulted in only slight neurochemical changes from those observed in WT females (**Fig. 11**). Neurochemical alterations in male animals included changes in NE and HVA along with altered serotonin metabolism (5-HT, 5-HIAA; **Fig. 12**). Despite the focus on loss of DA in PD, there is growing support that DA may not be the first, nor the major neurotransmitter casualty in the neurodegenerative sequence of PD (Espay et al., 2014). It is recognized that NE alterations arising from noradrenergic pathway fluctuations in the locus coeruleus influence early stage alterations in projecting DAn of the striatum (Paredes-Rodriguez et al., 2020). Of importance, NE may act as a protector to DAn and resulting changes may condition DAn for pathological progression (Paredes-Rodriguez et al., 2020). Clinical and animal studies also provide strong evidence supporting involvement of serotonergic pathways in the motor and non-motor manifestations of PD that are independent of decreases in DA (Politis and Niccolini, 2015). These findings highlight the importance of microglial NF-κB signaling in the biochemical and cellular changes associated with altered neurotransmitter levels during the early phase of PD-like changes in rotenone-treated male mice.

Microglia function as the primary innate and adaptive immune cell of the brain, providing surveillance and continual sampling of the microenvironment (Lehnardt, 2010; Lenz and Nelson, 2018; Zengeler and Lukens, 2021). In the last decade, it has become apparent that microglial inflammatory activation and signaling parallel α-syn aggregation and neurodegeneration (Ferreira and Romero-Ramos, 2018). *Postmortem* analysis has consistently revealed microgliosis and microcytosis in areas of α-syn accumulation and surrounding the SNpc irrespective of the presence or absence of cell death (Hunot et al., 1996; Knott et al., 2000; Imamura et al., 2003; Doorn et al., 2014; Ferreira and Romero-Ramos, 2018). Increases in microglia within the SNpc, SNpr, and ST were dependent upon rotenone exposure, genotype and sex where male KO rotenone exposed

animals displayed the highest levels of microglia. Morphometric characterization of microglia has been adopted as a reliable parameter for identification of reactive, intermediate, and quiescent states (Fernandez-Arjona et al., 2019). Numerous cellular parameters have been investigated in relation to activation and disease state including cellular area, branch complexity, sphericity, number of branches per cell, branch length, and volume (Heindl et al., 2018; Fernandez-Arjona et al., 2019). Rotenone exposure in male animals resulted in reduction of branch length per cell, reduction in number of branches per cell, and the total sum volume of the branches. Inhibition of NF-κB in females showed reduction in branch length in control animals, of which was not observed with rotenone exposure. In comparison, inhibition of NF-κB in male animals resulted in a more reactive morphometry of microglia at a basal level, but upon rotenone exposure in the KO animals, microglia retained more branches per cell, yet these were small projections consistent with filopodia or lamellipodia (Franco-Bocanegra et al., 2019) (**Fig. 13**). Comprehensively, these data support microglial structural remodeling aiding in motility and recruitment towards chemoattractant signals originating from injured regions of the brain, resulting in microgliosis and microcytosis, and increased pathological scoring (**Supplemental Fig. 4**). In concert, these data show that inhibition of NF-κB does not obstruct microglial morphometric remodeling, rather the remodeling, migration, and inflammatory activation of microglial cells is a response to the crosstalk between neurons-microglia and astrocytes-microglia (Baxter et al., 2021).

Glial-glial crosstalk is a known modulator of neuroinflammation in neurodegenerative diseases. Activated microglia are able to secrete pro-inflammatory cytokines such as IL-1α, TNF and C1qA which together are sufficient in inducing reactive phenotypic switching of astrocytes (Liddelow et al., 2017). Knockout of NF-κB mediated cytokine signaling in microglia cells resulted in overall increases in regional GFAP reactivity in male animals (**Fig. 14**). The density of

GFAP$^+$ cells within the mesencephalon has been shown to increase with severity of DAn loss (Damier et al., 1993; Middeldorp and Hol, 2011). Further classification of astrocytes based on C3 expression in soma (S100β$^+$) indicated that astrocytes within male SNpc were induced when exposed to rotenone. However, male astrocytes contained more C3$^+$ soma basally when devoid of NF-κB signaling from microglia, which was diminished when exposed to rotenone. Interestingly, female astrocytes contained less somal C3 in the SNpc, SNpr, and ST when exposed to rotenone. Inhibition of microglial NF-κB in females resulted in reduction of somal C3 in the ST and in the SNpr when challenged with rotenone. C3 identification in GFAP$^+$ astrocytic processes were increased in male SNpr with rotenone exposure and when glial-glial inflammatory crosstalk was inhibited, reduction in C3 prevalence in processes was identified in the SNpc, SNpr, and ST of male animals independent of rotenone exposure. Female astrocytic processes contained increased levels of C3 in the SNpc with rotenone exposure, and in contrast to males, had less reactive astrocytic processes in the SNpr and ST. Nonetheless, reduction in C3 astrocytic process was also present in females that were devoid of microglial NF-κB signaling (**Fig. 14**). Together, these findings highlight the complexity of intracellular C3 accumulation, production, and subsequent release in association with disease state. Ultimately, inhibition of NF-κB signaling by microglia reduced the prevalence of C3 protein in astrocytic processes (GFAP$^+$) and increased C3 in astroglia soma (S100β$^+$) surrounding DAn. The exact function of astrocytic C3 (intracellular or secreted) are not equivocal, are context-dependent, and may have pro-inflammatory or neuroprotective effects (Pekna and Pekny, 2021), drawing attention to the importance of C3 cellular positioning, accumulation, and subsequent release and recognition.

Neurodegeneration of the DAn within the SNpc is a pathological hallmark of PD (Antony et al., 2013; Raza et al., 2019). Male animals exposed to rotenone experienced a significant loss of

DAn within the SNpc along with reduction of TH intensity within the ST. KO male animals exposed to rotenone presented with less severe neuronal loss within the SNpc and comparable ST TH intensity loss. It is known that neurodegeneration can be mediated by pathways associated with dysregulation of microglial housekeeping genes include *Trem2*, *Cxcr1* and progranulin, which act as immune checkpoints to keep microglial inflammatory responses under control and promote clearance of injurious stimuli (Hickman et al., 2018). Peripheral infiltration of immune cells along with systemic inflammation from the gut-microbiome can also alter progressive pathology, supporting that NF-κB inhibition in microglia reduce not only local inflammation that may lead to compromised BBB integrity and selective degeneration of DAn, but also reduces invading monocyte populations through tight-junction retention and reduction of astrocyte activation (**Fig. 14, Fig. 19, Supplemental Fig. 5**).

Another well accepted pathological hallmark of PD is the accumulation of misfolded α-syn in surviving DAn in the SNpc (Antony et al., 2013; Dickson, 2018). It has remained unclear if the accumulation of this protein is a driver of pathology or if it is a result of progressive neurodegeneration; however, a well-recognized principle of synucleiopathies is the existence of multiple conformational strains and the ability of each to 'seed' and self-propagate (Mecucci et al., 1982). Misfolded α-syn can exist in numerous conformational isoforms and varies in seeding capacity based on structural integrity, size, and ability to form fibrils. Misfolded conformations that are unable to form fibrils are not capable of inducing neurodegeneration within DAn of the SNpc (Winner et al., 2011). Immunohistochemical analysis investigating individual object size and total area occupied indicated WT rotenone exposed males had larger p129 aggregate formations compared to those in the KO rotenone exposed males (**Fig. 16**). Inhibition of NF-κB in microglia in male animals resulted in decreased regional immunofluorescent signal intensity of

p129 in SN, but increased intensity within individual DAn (**Fig. 17**). Taken together, this data show that rotenone exposure induces α-syn misfolding, potentially through specific stabilization of the amyloidogenic partially folded conformation of the protein (Breydo et al., 2012), but final conformational determination may rely on the compounding oxidative microenvironment set forth by inflammatory mediators produced by microglial cells (Lashuel et al., 2013).

Impairment of the lysosomal pathway has been observed in familial and sporadic PD, enhancing the importance of the functional ability to degrade and clear misfolded proteins (Zheng and Zhang, 2021). Investigation of microglial mediated uptake, degradation, and clearance of misfolded α-syn within the last decade has resulted in momentous findings linking p62 mediated protein autophagy to the successful clearance of p129 (Choi et al., 2020). P62 is known to recognize and interact with ubiquitinated cargo to initiate selective autophagy (Lamark et al., 2009; Choi et al., 2020). TLR ligand binding and recognition is known to induce MyD88-IRAK complex activation and cascade leading to phosphorylation of IκBα resulting liberation and translocation of active NF-κB to the nucleus where it serves as a transcriptional regulator for p62 (Liu et al., 2017c). WT rotenone exposed animals had high levels of p62 within microglial cells and inversely low levels of p129. However, KO male animals had significant decreases in p62 intensity within individual microglial cells and high accumulation of p129 fluorescent intensity (**Fig. 18**), supporting the role of p62 mediated autophagy in the degradation and clearance of p129 in microglia cells during PD pathogenesis.

Increased research efforts geared toward biomarker identification in PD have yielded detection of α-syn in CSF and serum of PD patients (Gao et al., 2015; Chang et al., 2019). Serum analysis of WT and KO rotenone exposed males showed decreased levels of p129 in serum from WT control animals, however, when compared to KO control, KO rotenone exposed animals had

significantly more p129. Females had less p129 in KO rotenone exposure when compared to same genotype controls, however, these were not significant from WT control or rotenone exposed animals (**Fig. 8**). It is possible that the decreased levels of p129 in serum observed in rotenone exposed animals is in part due to the specific conformational identification based on the detection method, in this case phosphorylation of serine 129. Strong evidence suggests the existence of various oligomeric α-syn species *in vivo* and numerous aggregate pattern formations *in vitro* (Lashuel et al., 2013). The extent of context-dependent conformational changes in the tertiary structure of α-syn leading to oligomer formation is largely unknown. However, studies have shown that 3 mutations in *SNCA* (A30P, E46K, and A53T) linked to PD accelerate α-syn oligomerization, but only two of those (E46K and A53T) induce the ability of the protein to form fibrils (Conway et al., 1998; El-Agnaf et al., 1998; Lashuel et al., 2013). It is known that there are increases in total α-syn prevalence in serum in association with PD, however, absolute concentrations of each misfolded α-syn strain type in serum fractions are yet to be determined (Chang et al., 2019). It is important to recognize the conformational limitations that may be present with the misfolding of proteins, subsequently restricting reporter molecule binding. The data herein provides compelling evidence to suggest that the phosphorylation event at serine 129 on α-syn is not the predominant misfolded form present in serum fractions of terminal blood. Other markers capable of identifying different conformational sites and post-translational modifications may be of better usage in the determination of circulating misfolded α-syn.

Advancements in single-cell transcriptomic and proteomic analysis in neurodegenerative disease states has revealed key genes regulating the pathological progression in PD, including *Il6*, *Il1β*, *Tnfα*, *Nr4a2* (*Nurr1*), *Tlr2*, *Tlr6*, *Tlr4*, *Infγ*, *Snca*, *Mapk*, *p62*, *Nlrp3*, and *Cxcr2* (Glass et al., 2010; Jiang et al., 2019; Giovannoni and Quintana, 2020; Pajares et al., 2020; Serdar et al., 2020;

Tan et al., 2020; Li et al., 2021). Profiling inflammatory gene expression using multiplex arrays revealed increases in genes responsible for neutrophil and monocyte chemotaxis, non-canonical NF-κB signaling, astrocyte and T-cell chemotaxis and Jak-stat signaling in male WT and KO animals exposed to rotenone. In contrast, KO females had increases in complement and coagulation cascade transcription when exposed to rotenone. Importantly, pathology induced by rotenone upregulated 9 distinct genes in WT, 9 distinct genes in KO, and 20 shared genes in male animals. The shared upregulated genes involved positive regulation of generalized chemotaxis, NF-κB signaling pathways, microglial cell activation, and neutrophil chemotaxis. Distinct differences in the 9 unique upregulated male genes in WT males exposed to rotenone harbored genes such as *Ccl17*, *Ccl22*, *Ccr3*, and *Ptgs2* (**Fig. 19**). *Ccl17* and *Ccl22* have been recently implicated as potent microglial cell activators capable of inducing ameboid morphology where knockout of *Ccl17* results in the reduction of microglial density (Fulle et al., 2018). CCR3 is found on astrocytes and when activated by CCL2626, has been shown to induce pro-inflammatory events that resulting in tissue damage and BBB impairment (Shou et al., 2019). Increases in *Ptgs2*/*Cox2* expression in the brain have been shown in both clinical PD cases along with MPTP mouse models. These finding provide evidence that increases in COX-2 contribute to the formation of the oxidant species DA-quinone, which has been implicated in idiopathic PD (Teismann et al., 2003; Minghetti, 2004). In contrast, inhibition of microglial NF-κB in males resulted in upregulation of *Nos2*, *Fasl*, *Ccl11*, *Il6*, *Tlr4*, *Ccl4*, *Nfkb1*, *Il17a*, and *Kng1*, which are genes associated with TLR signaling and non-canonical NF-κB signaling (**Fig. 19**). In line with other reports, decreased TNF-α levels in the brain confers neuroprotection, importantly, through interactions of microglia and $CD4^+$ T-cells. These interactions have been shown to promote microglial phagocytosis and

promote T-cell apoptosis through FasL signaling, ultimately inhibiting production of proinflammatory TH1 cytokines (Platten et al., 2005; Ottum et al., 2015).

Sex differences in the brain are results of both short-term and long-term epigenetic affects induced by gonadal hormones (Stephen et al., 2019; Caceres et al., 2020; Davis et al., 2020). Additionally, glial cell expression of hormone receptors fluctuates with age, sex, and under pathological conditions (Liu et al., 2007; Astiz et al., 2014; Chowen and Garcia-Segura, 2021). Models of traumatic brain injury have shown that selective G protein-coupled estrogen receptor 1 (GPER1) agonists exert anti-inflammatory effects and reduce microglial reactivity in males and ovariectomized females, but not in females with intact ovaries (Pan et al., 2020). Male microglia are inherently more mobile than female microglia and present with more reactiveness in physiological conditions, where female microglia express more phagocytic cups and higher levels of cellular repair and inflammatory control genes. These biological sex-differences in microglial cells are likely due to hormone stimulation in pre- and post-neonatal developmental stages that permanently alter microglial transcriptional differentiation throughout adulthood (Yanguas-Casas, 2020). In support of this, sex dependent classification of transcript levels revealed rotenone induced increases in chemokine driven recruitment (*Cxcr1*, *Cxcr3*, *Cxcr2*, *Cxcl3*, *Cxcl2*, *Ccr4*, *Ccl3*) and microglial proliferation (*Csf1* and *Il7*; **Fig. 20)**. In contrast, transcripts isolated from female rotenone exposed animals were tightly regulated regarding inflammation (**Fig. 20**).

Collectively, these results highlight the complexity and importance of sex differences in cellular reactivity that underly the pathophysiology of neurodegeneration in response to rotenone. Microglial knockout of canonical NF-κB in male animals exposed to rotenone resulted in increased microgliosis and accumulation of $p129^{+}$ α-syn in microglia and DAn of the SNpc. Despite this, there were reduced levels of C3 in astrocytes and an overall reduction in neurodegeneration,

consistent with other recently published findings on microglial IKK2 impairment and resulting neurodegeneration (Wang et al., 2022). These compounding findings effectively distinguish male microglial cells as key determinants in overt disease outcomes through primary activation of canonical NF-κB inflammatory signaling.

CHAPTER 4

INHIBITION OF CANONICAL IKK2/NF-κB SIGNALING IN MICROGLIA DOES NOT PROTECT AGAINST NEURODEGENERATION IN A DUAL-HIT ENVIRONMENTAL EXPOSURE MODEL OF PARKINSON'S DISEASE

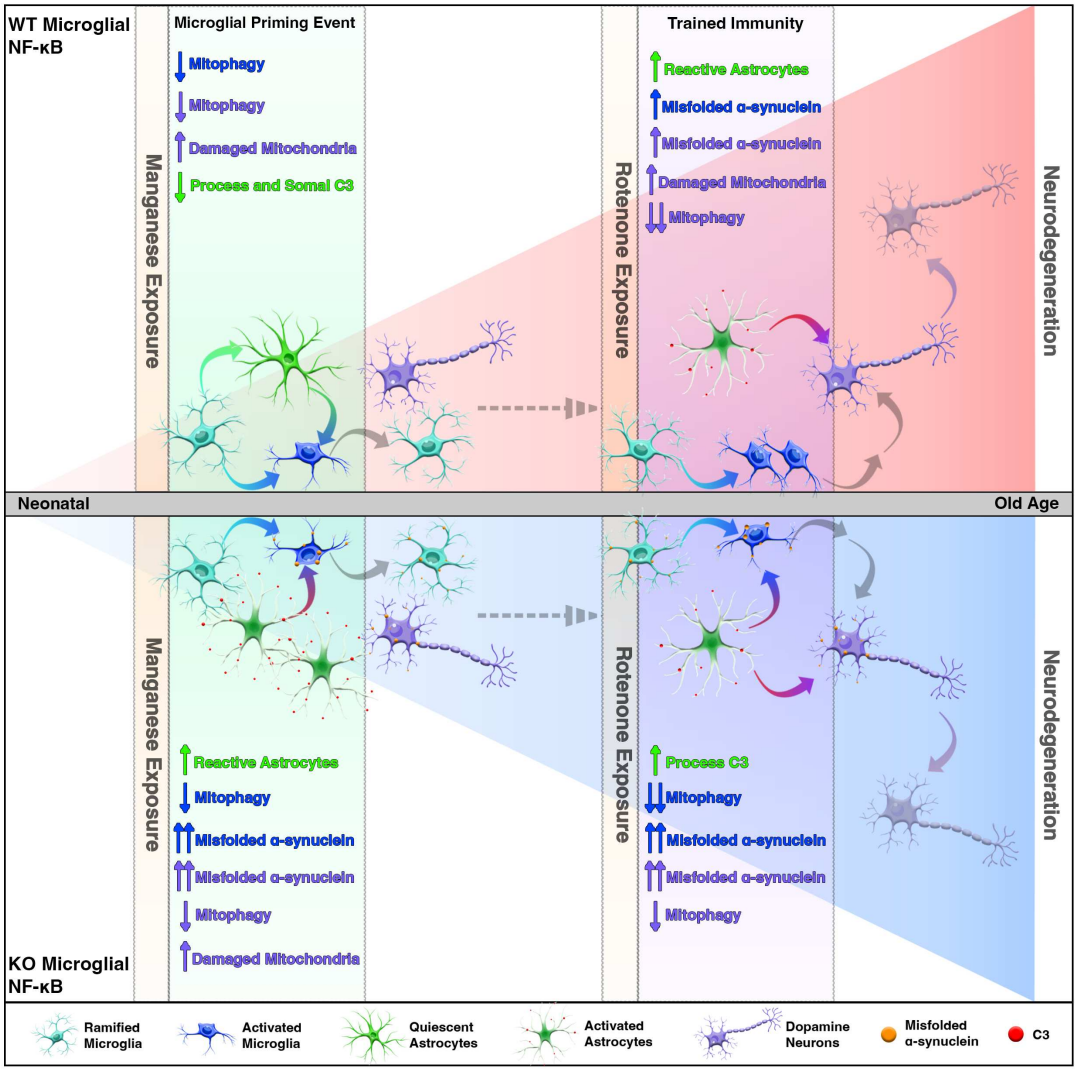

Figure 21. Graphical abstract of microglial NF-κB involvement in the process of immune priming in the dual hit model of PD. Representation of intra- and inter-cellular responses initiated by microglial immune priming by Mn exposure followed by the exacerbated microglial trained immune response initiated upon secondary rotenone insult.

4.1. Introduction

PD is the most common neurodegenerative movement disorder worldwide and is the fastest growing in prevalence, disability and deaths, independent of the size of the aging population (Collaborators, 2019). Despite rigorous scientific efforts, there are no disease-modifying therapies for PD and currently available treatment modalities address only symptomatic aspects of the disease. The cause of PD has been linked to genetic factors, age and exposure to environmental neurotoxins (Campdelacreu, 2014). Thus, a complex interplay of lifetime exposures with age and genetics is likely to influence disease etiology and progression. Prodromal features of PD, preceding overt motor deficits, include cognitive and behavioral changes, as well as gastrointestinal dysfunction. Late-stage clinical manifestations of PD include bradykinesia, postural instability, short-shuffling gait, difficulty initiating movement, 'pill-rolling' tremor, masked facies, anosmia, and rigidity (Jankovic, 2008; Hayes, 2019). Pathologically, selective degeneration of DAn within the SNpc occurs in conjunction with neuroinflammation of microglia and astrocytes, which surround misfolded α-syn protein aggregates, known as Lewy bodies, in surviving DAn (Braak et al., 2007).

Heavy metals and pesticides have both been implicated as environmental risk factors for PD. Mn is an essential micronutrient that is required for normal nerve and brain development and cognitive functioning (Takeda, 2003; Erikson et al., 2005; Kwakye et al., 2015; Balachandran et al., 2020). However, excessive, or prolonged exposure to Mn in occupations such as welding, mining, and refining results in accumulation of Mn in the brain that can cause a neurodegenerative extrapyramidal motor disorder, referred to as Manganism (Keen et al., 2000; Dobson et al., 2004; Aschner et al., 2005; Zoni et al., 2007; Kwakye et al., 2015; Racette et al., 2017). Mn is also a putative risk factor for developing PD (Gorell et al., 1999). Aside from occupational exposures,

excessive dietary consumption of Mn through food or drinking water can also lead to overexposure and subsequent accumulation in the brain. High Mn exposure in the early stages of life is associated with poor cognitive performance in children (Menezes-Filho et al., 2011), potentially due to excitotoxicity from the dysregulation of the glutamate-glutamine cycle in astrocytes surrounding synaptic terminals (Ke et al., 2019). Both neurons and astrocytes express transporters for Mn, including DMT-1, zinc transporter 8 ZIP8 (ZIP8) and the transferrin receptor (Aschner et al., 2009). These are balanced by efflux pumps such as SLC30A10, which protects against neurotoxicity and the development of PD (Taylor et al., 2019), with astrocytes serving as the major homeostatic regulator and storage site for Mn in the brain (Aschner and Aschner, 1991; Araque et al., 2001). Microglia are also capable of transporting Mn from the surrounding interstitium, which induces production of inflammatory cytokines and chemokines that can amplify inflammatory activation of astrocytes (Kirkley et al., 2017). In the cell, Mn accumulates in the mitochondria via the Ca^{2+} uniporter, resulting in inhibition of Na^{+}-dependent Ca^{2+} efflux and increases in matrix Ca^{2+} (Gavin et al., 1990), leading to production of ROS (Tjalkens et al., 2006). This also inhibits production of ATP and the activity of MAO-B, which impacts synaptic function (Zhang et al., 2003). Mn also activates the NLRP3 inflammasome pathway in microglia (Sarkar et al., 2019), increasing expression of inflammatory cytokines and chemokines (Kirkley et al., 2017). Neuronal cells lines exposed to Mn had dependent epigenetic alterations through histone modifications (Guo et al., 2018). Therefore, excess accumulation of this metal in the juvenile stages of life may confer mitochondria dysfunction, inflammasome activation, and epigenetic alterations which may play a key role in microglial priming. Our laboratory has previously shown that juvenile exposure to Mn potentiates reactive state glial phenotypes, which are further enhanced by adulthood exposure to viral and chemical toxin challenge (Moreno et al., 2009a; Hammond et al., 2020; Bantle et al.,

2021a). Mn, therefore, has the potential to interact with other environmental neurotoxins to promote more severe activation of innate immune responses in glial cells.

Numerous chronic environmental exposures have been linked to PD-like pathological outcomes, one of which is the widely used pesticide, rotenone (Lawana, 2020). Rotenone is a potent mitochondrial complex I inhibitor that leads to increased matrix Ca^{2+} and production of ROS (ref) and results in recapitulation of neuropathological features observed in PD such as neuroinflammation, aggregation of α-syn and loss of DAn in the SNpc (Cannon et al., 2009; Tanner et al., 2011; Rocha et al., 2022a). Our laboratory has previously demonstrated that rotenone exposure, alone, is capable of inducing astrogliosis and astrocytosis, activation of inflammatory microglial phenotypes that produce microenvironments conducive to α-syn protein misfolding, and ultimately eliciting neurodegeneration of DAn in the SNpc (Rocha et al., 2022a). Of importance, mitochondrial impairment in glial cells is associated with the activation of DAMPS, like NLRP3 and stinulator of interferon genes (STING), which have the potential to induce IKK2 driven canonical NF-κB pathways in response to ROS and mitochondrial DNA (mtDNA) release. In spite of detailed pathological outcomes resulting from solely rotenone exposure, it remains unknown how multi-stage exposure modalities involving rotenone contributes to disease pathology.

Microglial cells have had a long-standing implication in PD due to the increase in population prevalence in clinical *postmortem* tissue and morphologically activated phenotypes (Hartmann, 2004). These cells function as primary respondents to microenvironment changes within the brain, gaining attention for innate immune capabilities. It is important to recognize that recent findings have highlighted that innate immune cells are capable of remembering a first encounter with a perceived pathogen, and innate immune memory is mediated by epigenetic

processes and regulation of transcription factors (Netea et al., 2016; Haley et al., 2019). Unlike peripheral innate immune cells, microglial cells are longer-lived, proliferating at a rate 20-fold slower than tissue resident macrophages (Lawson et al., 1992), with a median life-span of 15 months in mice and up to 20 years in humans (Fuger et al., 2017; Reu et al., 2017). The prolonged lifespan and reported genomic modifications in microglia would support hyper-inflammatory activation due to pre-existing genetic modifications, facilitating memory (Haley et al., 2019) across dual or multi-toxicant/pathogen exposures over a microglial lifespan.

Chronic activation of microglial cells is implicated as an important pathological determinant in many progressive neurodegenerative diseases including multiple sclerosis, stroke, AD, and PD (Gonzalez-Scarano and Baltuch, 1999; Block and Hong, 2005; Minghetti et al., 2005; Glass et al., 2010). NF-κB inflammatory signaling pathways in microglia have been recognized as potential drivers of the inflammatory cascade in PD and are known drivers of misfolded protein accumulation, spreading and toxicity in AD and PD (Rocha et al., 2022c; Wang et al., 2022). It remains unknown how microglial cell-specific inhibition of in NF-κB alter adjacent cellular responses, protein misfolding, neurodegeneration and progressive pathology in multi-exposure models of PD.

Here we demonstrate that microglia-specific KO of canonical NF-κB activation in mice exposed to Mn followed by rotenone does not protect against degeneration of DAn, unlike KO animals exposed only to rotenone. NF-κB-deficient microglial cells did not exhibit inhibition of morphological remodeling and harbored increases in p129 due to impairments in the autophagy pathway (Rocha et al., 2022c). Increases in $p129^{+}$ objects were also detected in DAn within the SNpc. These results suggest that inhibition of NF-κB signaling in microglia at the stage of primary toxic stimuli prevents neurodegeneration; however, upon secondary toxin exposure, canonical NF-

κB impairment fails to protect overall DAn loss along with protein misfolding and accumulation. Multi-exposure modeling is a critical next step that needs to be implemented in PD research being that it more closely models numerous insults that a patient would likely encounter. Taken together, inflammatory responses mounted by microglia in multi-exposures that lead to PD-like pathological outcomes are independent of canonical NF-κB signaling, impressing the importance of microglial priming and trained immunity in the complex interactions of glial and neuronal cells in progressive PD.

4.2. Materials and Methods

4.2.1 Generation of Microglial-Specific IKK2/NF-κB Knockout Mice.

All animal protocols were approved by IACUC at Colorado State University, mice were handled in compliance with PHS Policy and Guide for the Care and Use of Laboratory Animals and procedures were performed in accordance with NIH guidelines. Mice were housed in microisolator cages (3-4 animals per cage), kept on a 12-h light/dark cycle and had access to both food and water *ad libitum.* Homozygous CX3CR1-Cre$^{+/+}$::IKK2$^{fl/fl}$ animals were generated as previously described (Rocha et al., 2022c). Briefly, male and female heterozygous B6J.BN6(Cg)-*Cx3r1$^{tm1.1(cre)Jung}$* /J (CX3CR1-Cre) mice were obtained from the Jackson Laboratory (Stock No. 025524, Bar Harbor ME) and bred to homozygosity. These were then paired with homozygous IKK2$^{fl/fl}$ mice (Kirkley et al., 2019) and resulting heterozygous genotype for both alleles were bred to homozygosity (CX3CR1-Cre$^{+/+}$::IKK2$^{fl/fl\ +/+}$;KO). IKK2$^{fl/fl\ +/+}$ were utilized as WT animals throughout the studies. Male WT and KO animals were utilized in the dosing and analysis of the study.

4.2.2 Manganese Preparation and Dosing.

At day PN21, male WT and KO animals were exposed to Mn through ingestion of drinking water. $MnCl_2$ (50mg/kg/day) was administered for the duration of 30 days (PN51), as previously described (Hammond et al., 2020). In short, $MnCl_2$ was diluted in drinking water where total water intake/cage/day and weight gain/mouse/day were used as parameters to identify total Mn consumption for individual animals (**Supplemental Fig. 6**). Control animals received standard facility drinking water. Following the 30-day exposure period, all animals were placed on normal drinking water for a period of 2 months. This dose of Mn recapitulates known chronic level

exposures that induce behavioral and neurochemical alterations in male animals during the postnatal period from contaminated drinking water and soy-based formulas (Moreno et al., 2009b; Hammond et al., 2020).

4.2.3 Rotenone Preparation and Dosing.

Rotenone was prepared as previously described (Rocha et al., 2022a), in brief, a 2.5mg/kg/day dosage of 2µL/gram body weight of rotenone was made where diluent compromised 98% medium chain-triglyceride, miglyol 812 (Cannon et al., 2009), and 2% DMSO. Male mice (*n*=9/group) were injected daily for 14 days with a dose of 2µL/g weight. Mice were weighed daily prior to injection to determine the appropriate dose volume. The rotenone/miglyol solution was measured using a 50µL Hamilton syringe, which was then transferred to an insulin syringe with a fixed (29 gauge) needle and administered via intraperitoneal injection. Control animals received miglyol only injections. The dosing period of 14 days was followed by a progressive posy-lesioning period consisting of another 14 days.

4.2.4 Real-time Gait and Locomotor Analysis.

Locomotor function by analysis of gait was investigated by recording nonrestrictive movement patterns along a 1-meter fixed trackway equipped with contrasting illumination pattern allowing for pawprint visualization and pressure sensing (Hammond et al., 2018; Damale et al., 2021; Rocha et al., 2022c). Mice were acclimated to the trackway 24 hours prior to experimentation. One hour before the first dose of rotenone/miglyol, baseline (0 DPI) measurements were collected for each animal. Parameters measured included, diagonal stance

support for each forelimb-hind limb combination, four-point stance support, run duration and average steps per second (cadence). Data is reported as a change from 0 DPI measurements.

4.2.5 Analytical Determination of Catecholamines and Monoamines.

Determination of striatal catecholamine concentrations was assessed as previously described (Hammond et al., 2020; Rocha et al., 2022c). Briefly, brain tissue was rapidly removed after decapitation under isoflurane anesthesia. Gross dissection of the striatum was performed with the aid of a brain block and immediately flash frozen in liquid nitrogen, where the entire process from the time of anesthesia to flash freeze point lasted no longer than 5 minutes. Flash frozen striatal tissue samples were process using HPLC coupled with electrochemical detection to quantify the concentrations of DA, DOPAC, 3-MT, HVA, NE, epinephrine I, 5-HT, and 5-HIAA. Samples were analyzed using the Neurochemistry Core at Vanderbilt University's Center for Molecular Neuroscience Research (Nashville, Tennessee). All parameters obtained were normalized to overall protein concentration of each sample. Randomized numerical labeling was applied to all samples for unbiased analysis.

4.2.6 Tissue Sample Preparation.

Brain tissue was carefully removed from the cranial vault and hemispheres were split down midline with the aid of a brain block. One hemisphere was then post-fixed in 10% NBF for two weeks at room temperature. Each tissue specimen was then trimmed according to consistent anatomical coordinates and placed in cassettes for histological processing.

4.2.7 Automated High-throughput Immunofluorescence Staining of Tissue Sections.

Paraffin embedded brain tissue was sectioned at 6µm thickness and mounted onto poly-ionic slides (Histotox Labs, Boulder, CO). Tissue sections were deparaffinized and immunofluorescently labeled using a Leica Bond RX_m automated robotic staining system. Antigen retrieval was performed by using Bond Epitope Retrieval Solution 1 for 20 minutes in conjunction with heat application. Sections were then incubated with primary antibodies diluted in 0.1% TBS: rabbit anti-TH (Millipore; 1:500), chicken anti-TH (Abcam; 1:200), mouse anti-NeuN (Abcam, 1:200), mouse anti-GFAP (Abcam, 1:1000), rabbit anti-S100β (Abcam; 1:750), rat anti-C3 (Abcam; 1:250), goat anti-IBA1 (Abcam; 1:50), mouse anti-p129 (Wako, 1:100), rabbit anti-phosphorylation at serine 65 on PARK2 (pS65; ThermoFisher; 1:100), and mouse anti-heat shock protein 60 (HSP60; Abcam; 1:500). Appropriate species-specific secondary antibodies conjugated to FITC, AlexaFluor488, TRITC, AlexaFluor555, or AlexaFluor647 were applied for fluorescent detection. Sections were stained with DAPI (Sigma, 1:5000) and mounted on glass coverslips in ProLong Gold Antifade hard set mounting medium and stored at 4 °C until time of imaging.

4.2.8 Unbiased Stereological Analysis of Neurons.

Quantification of neurons was adapted from previously reported methods (Tapias and Greenamyre, 2014; Sadasivan et al., 2015; Bantle et al., 2019; Rocha et al., 2022a; Rocha et al., 2022c). In brief, a 1:29 sampling fraction was used, resulting in six sections per animal being counted spanning the entire SN. Neuronal counts were conducted blindly by a single investigator. Images were captured using an automated Olympus BX63 fluorescence microscope equipped with a Hamamatsu ORCA-flash 4.0 LT CCD camera and collected using Olympus CellSens software (v3.1). Quantitative analysis was performed on triple labeled fluorescent images generated by montage imaging of the entire coronal hemisphere by compiling single 100X magnification images

acquired by using an Olympus X-Apochromat 10X air objective (0.40 N.A.). One hemisphere of the section was quantified by creating anatomically specific regions of interest (ROIs) based on TH immunolabeling and reference to a coronal atlas of the adult mouse brain (Allen Brain Atlas). All images were obtained and analyzed under the same conditions for magnification, exposure time, LED intensity, camera gain and filter settings. For quantitative assessment, TH^+ and $NeuN^+$ soma from the selected areas determined by the ROI parameters were semi-automatically counted by adaptive thresholding on staining intensity in the Count and Measure feature on the Olympus CellSens platform. Object filters for cellular perimeter size, minimum and maximum area, shape factor, and sphericity thresholding were applied. Quantitative stereology analysis using the motorized stage method was performed as descried (Tapias and Greenamyre, 2014).

Caudal ST sections containing caudate, and GP were dually stained where TH was the main marker of interest. All slides were stained and imaged simultaneously using consistent exposure times and CCD gain and binning parameters to reduce degradation variability in intensity measurements. Whole brain montaging was performed using a 10X Olympus X-Apochromat air objective (0.04 N.A.). ROIs specific to the individualized striatal brain regions were applied and total average fluorescence intensity was determined by manual threshold masking within the CellSens platform. Representative whole brain montage images were generated using the 20X air objective (N.A. 0.80) and high magnification inserts were acquired using the Olympus Plan Fluorite 100X oil objective (1.30 N.A.).

4.2.9 Morphological and Phenotypic Evaluation of Microglia.

Morphometric analysis was performed using Imaris for neuroscientists image analysis software (v9.8.2). Three to five randomized 400X images spanning the entirety of the SNpr and

SNpc were taken using a Olympus X-Apochromat 40X air objective (0.95 N.A). Filament tracing modules were used to identify $IBA1^+$ microglial processes. Somal modeling and background reduction thresholding was applied to trace and map processes associated with individual microglial cells. Total sum of processes per cell (filament length (sum)), branch number per cell (filament number of dendrite terminal points), Scholl intersections, and overall area of soma were utilized to determine morphometric changes present within each animal. Individual cell validation was conducted by DAPI positive nuclei co-localization with $IBA1^+$ cytoplasmic staining. Radar graph generation was performed on Python (v3.9.7) software with JupyterLab computational platform where fold normalized morphological parameters were input as data points.

Three-dimensional renderings of glial cells were performed by using Imaris software (v9.8.2) utilizing 100X high magnification Z-stack images from 6 μm thickness tissue sections. Filament tracing was used to identify projection start and end points unique to individual cells based on maximal $IBA1^+$ staining intensity. Nuclei were identified using the somal modeling parameters within the filament tracing module of Imaris.

4.2.10 Deep Learning and Artificial Intelligence-based Quantification of Glia within the Substantia Nigra and Striatum.

Two total sections per animal were selected for glial counts based on anatomical region and proximity to slides that were used to quantify DAn values. The studies described herein were performed blinded by a single investigator. Images utilized for quantification were captured using an automated BX63 fluorescence microscope equipped with a Hamamatsu ORCA-flash 4.0 LT CCD camera and collected using Olympus CellSens software (v3.1). Quantitative analysis was performed on di-, tri- or quad-labeled fluorescent images through acquisition of entire hemisphere

montage scans. Each montage consisted of compiled individual 100X images taken using an Olympus X-Apochromat 10X air objective (0.4 N.A.). Hemispherical analysis was performed on active ROIs determined by anatomical structures identified by immunofluorescent labeling using the coronal adult mouse brain atlas for anatomical reference (Allen Brain Atlas). All slides were imaged and scanned using the same conditions of exposure time, binning, magnification, lamp intensity and camera gain and binning.

For identification of $GFAP^+$ cells, positive staining soma and projections within the manually drawn ROIs were detected using semi-automated cell counting software on the CellSens platform. Total area of $GFAP^+$ reactivity compared to the total area sampled per animal was used to accurately quantify the percentage of $GFAP^+$ astrocytes. $GFAP^+$ processes and soma were then converted to ROIs and manual thresholding was applied to each ROI to determine average C3 intensity. $IBA1^+$ cell populations were identified by using deep learning AI analysis software on the Olympus Deep Learning Platform. Optimization of neural networks was based on similarity scores ≥ 0.8. Manual thresholding was then applied on the probability segmentation layer to obtain total $IBA1^+$ cell counts for each specified ROI analyzed using optimized neural networks.

Fully automated deep learning neural networks were also constructed to identify $S100\beta^+$ cells. This was then applied to all images across all animals within the study using batch macro-analysis to sequentially analyze up to 150 images per AI run. S100β events were then converted to ROIs and the intensity of C3 positivity was interrogated on a cell-by-cell basis for the most accurate representation of astrocytic reactivity within the SNpc, SNpr and ST. Manual thresholding within the Count and Measure module of CellSens was applied to batch analysis macros for mean intensity measurements of C3.

4.2.11 Immunohistochemical Staining and Quantification of Invading Peripheral Macrophages.

Tissue sections were processed for immunohistochemical analysis on a fully automated Leica Bond-III RX_m. Epitope retrieval was performed by addition of Leica Bond Epitope Retrieval Solutions 1 and 2 for a duration of 30 minutes at 37 °C. Cellular identification of monocyte lineage cell types was achieved by staining with rabbit anti-IBA1 (Abcam, 1:500) followed by DAB chromogen. Nissel counterstain was applied for identification of cellular nuclei. Selective identification of peripherally invading macrophages was determined as previously described (Bantle et al., 2021b; Rocha et al., 2022a). In brief, IBA1 staining outlining morphometric characteristics of each cell were scrutinized where small nuclei in combination with long thin processes denoted resting microglia, enlarged nuclei paired with shorter/thickened processes denoted activated microglia, and spherical atentril cells were peripherally invading macrophages. All quantification was performed blinded by a single investigator.

4.2.12 Immunohistochemical Staining and Quantification of Protein Aggregates.

Sections were processed for histology and immunohistochemistry using a Leica Bond-III RX_m automated staining system as described above. Reactive α-syn cell/cell aggregates were stained using mouse monoclonal anti-phosphorylated Ser129 (p129) antibody (1:100, clone pSYN#64, WAKO) (Jang et al., 2009a). Full-brain montage images were captured by using brightfield imaging on an Olympus VS120 equipped with a Hamamatsu OrcaR2 camera. Quantification of p129 positive staining was performed by using manual HSV thresholding within the Count and Measure features of CellSens, specifically adapted for RGB files. Thresholds were kept consistent throughout all images and object filters that spanned size and signal intensity were

applied. Total positive staining area and object count were plotted against overall brain region specific ROI area sampled from individual sections to obtain animal-to-animal comparisons.

4.2.13 Quantification of p129 Protein Aggregates.

Multi-factorial analysis was performed to determine p129 presence within two sections per animal. Overall regional intensities were measured from 10X full brain montages with the Count and Measure module of CellSens (v3.1), where manual thresholding in the channel of interest was applied to obtain mean fluorescence intensity. Five total images per section, up to 10 total per animal depending on anatomical variation, were obtained using an Olympus X-Apochromat 40X (N.A. 0.16) magnification. Cell specific gaiting parameters were applied on microglia (IBA1) and DAn (TH) where average intensity of p129 was measured per cell within each section using manual and adaptive thresholding strategies within the Count and Measure module of CellSens (v3.1).

4.2.14 Detection of Misfolded α-synuclein in Serum Enzyme Linked Immunosorbent Assay (ELISA).

Terminal blood samples were collected by cardiac puncture of the right atrium under deep isoflurane anesthesia. Blood was centrifuged for 10 minutes and sera was collected from the upper phase of the samples and frozen at -80 °C until quantification. Serum samples were removed from the freezer and diluted 1:100 in 1X PBS. Protein concentration was then determined by using the Pierce BCA Protein Assay Kit (ThermoFisher). A final volume of 50 µL of 0.01µg/µL serum, diluted in carbonate-bicarbonate buffer, was added to each well of the ELISA plate (NUNC, 96 well plate). Adhesion of the target proteins to the well surface was allowed for 1 hour at 37 °C.

Blocking was then performed with superblock (ThermoFisher) for 1 hour at 37 °C. Primary p129 (clone pSyn#64, WAKO) was directly conjugated to HRP (Lightning-Link, Abcam) and was diluted at a 1:2,000 in 1X PBS. 100µL of this was placed in each well and allowed to incubate at 37 °C for 1 hour. Three wash steps with PBS containing 0.05% Tween 20 were performed between each antibody incubation. One-Step Ultra 3,3',5,5'-Tetramethylbenzidine (TMB) ELISA Substrate Solution (ThermoFisher) was used to develop ELISA plates for 5 minutes at ambient temperature. Reactions were quenched using 0.5M sulfuric acid. Absorbance was measured at 450nm on a BMG LabTech POLARstar Omega microplate reader to obtain total absorbance values.

4.2.15 Identification and Quantification of Mitophagy in Dopaminergic Neurons and Microglia.

Quantification of mitophagy associated proteins was performed by 100X z-stack imaging through 6um sections with subsequential Weiner deconvolution with the deconvolution module of CellSens and maximal z-projection. Line profiles (2-5 per TH^+ cell) were drawn with the parameters that ≥2 $HSP60^+$ mitochondria were intersected. Intensity profiles along the line for respective fluorophores were analyzed and individual pixel pS65 PARK2 intensity co-localizing with $HSP60^+$ was reported. $IBA1^+$ staining was determined through adaptive thresholding in the Count and Measure module of CellSens where background and unspecific intensity from vasculature was excluded. $HSP60^+$ objects within each $IBA1^+$ object were also identified based on adaptive thresholding techniques. Mean fluorescent intensity of pS65 within each microglial associated $HSP60^+$ mitochondria was determined through manual fluorescence thresholding. Resulting datasets represent whole microglial cell prevalence of pS65 association with $HSP60^+$ mitochondria.

4.2.16 Focus Panel Multi-plex Array Detection and Quantification of Transcriptional Regulation.

One step focus panel multi-plex gene profiling arrays were used to identify specific genes of interest associated with diseased state. Tissue from the basal midbrain consisting primarily of SN was homogenized using a BeadBug 3 Position Head Homogenizer using 2.8mm stainless steel beads submersed in RLT buffer from the Qiagen Rneasy Mini Kit. This buffer was supplemented with β-mercaptoethanol at a 1:1000 dilution per sample. RNA extraction was then carried out following the Qiagen kit instructions and resulting RNA was analyzed on a Nanodrop for concentration and purity. Primer and probe combinations were custom designed for optimal function in an array platform (Geneious Prime v.2022.0.2). RNA was used as template in a one-step Taqman probe reaction with 1X reverse-transcriptase containing master mix and 20X Rtase (Tonbo), 400nM primers directed at the genes of interest, 200nM of each probe, and 200nM primers corresponding to the reference gene (β-*actin*). Sequences (**Supplemental Table 2**) were validated individually and together within the same well prior to usage based on 90-110% efficiency and $R^2 \geq 0.99$. Primer and probe sequences were ordered from IDT where the probe sequences synthesized were Prime Time Probes featuring individual reporter dyes with one or two quencher molecules to achieve higher signal-to-noise ratio. Delta delta cq fold change methodology was applied to the resulting data to determine transcriptional regulation.

4.2.17 Gene Expression Profiling and Analysis.

Fold change ($2^{-\Delta\Delta CT}$) values were analyzed for outliers using ROUT testing, and full dataset analysis was performed on outlier excluded values using ClustVis (Metsalu and Vilo, 2015). Unit variance scaling was applied and SVD with imputation settings were utilized within

rows of heat mapping to determine genotype and exposure differences. Dataset mean collapse of individual animals into overall groups was applied for heat mapping with row centering. All genes investigated were analyzed for functional connectivity by the programming software STRING (v.11.5; (Szklarczyk et al., 2021)) where full STRING networks were generated based on confidence with high interaction determination (0.700). Confidence was determined through textmining, experiments, databases, co-expression, neighborhood, gene fusion and co-occurrence parameters and was ultimately visualized though corresponding line thickness.

4.2.18 Statistical Analysis.

All data was presented as mean +/- SEM, unless otherwise noted. Experimental values from each group were analyzed with a ROUT (α=0.05) test to identify significant outliers and validate exclusions. Variance differences between three-parameter variables were determined by three-way ANOVA with subsequent Tukey *post hoc* multiple comparisons testing. Variance differences between two-parameter variables were identified using a two-way ANOVA followed by a Sidak *post hoc* multiple comparisons test. All individual variables within the same timepoint or genotype were analyzed for variance differences using an unpaired one-way ANOVA. Fold change gene expression through volcano plotting was determined as differential change from mean between genotype:exposure combinations in comparison to WT control. Multiple comparison for gene regulation was conducted through false-discovery rate (FDR) analysis with two-stage step-up method of Benjamini, Krieger and Yekutieli with an FDR of 0.05. Significance was identified as *$*p<0.05, **p<0.01, ***p<0.001, ****p<0.0001$*, or as otherwise noted in figure legends. All statistical analysis was performed using Prism (version 9.3.1; Graph Pad Software; San Diego, CA).

4.3. Results

4.3.1 Microglial innate immune signaling through NF-κB contributes to PD-like locomotor changes.

To determine microglial NF-κB inflammatory signaling contribution in alterations of gait and locomotor abnormalities associated with rotenone and Mn induced PD-like diseased states, gait and locomotion patterns were assessed post-initial rotenone exposure on a weekly basis (2 WPI, 3 WPI, 4 WPI) through real-time pawprint tracking along a 1-meter trackway (**Fig. 22A-F**). Postural stability and balance were assessed through diagonal dual support and four-point support. WT animals exposed to Mn followed by rotenone experienced alterations in balance and stability resulting in decreased diagonal dual support and increased 4-point support at 2 WPI (**Fig. 22G, J**) and 3 WPI (**Fig. 22H, K**). Rotenone exposure and Mn exposure independent of each other were significant factors that contributed to variation observed at 3 WPI (**Fig. 22K**). The 4 WPI timepoint revealed no significant changes in support and balance between groupings (**Fig. 22I, L**). Assessment of speed and motor initiation was interrogated by the total time (seconds) the animals utilized to move along the entirety of the trackway. Significant time differences were observed at 3 WPI where WT Mn exposed animals took longer to complete the length of the trackway in comparison to the WT rotenone exposed animals (**Fig. 22N**). Genotype:rotenone exposure, genotype:Mn exposure, and Mn exposure alone contributed to the speed at which these animals were able to complete ambulation across the trackway. The 2 WPI (**Fig. 22M**) and 4 WPI (**Fig. 22O**) timepoints showed no significant differences in the duration of time taken to ambulate the full length of the trackway. Further observation of ability to initiate movement and propagate continuous movement was identified through cadence (steps/s) quantification. Rotenone exposure at 2 WPI was seen to effect cadence patterns, where genotype contributed to the overall cadence

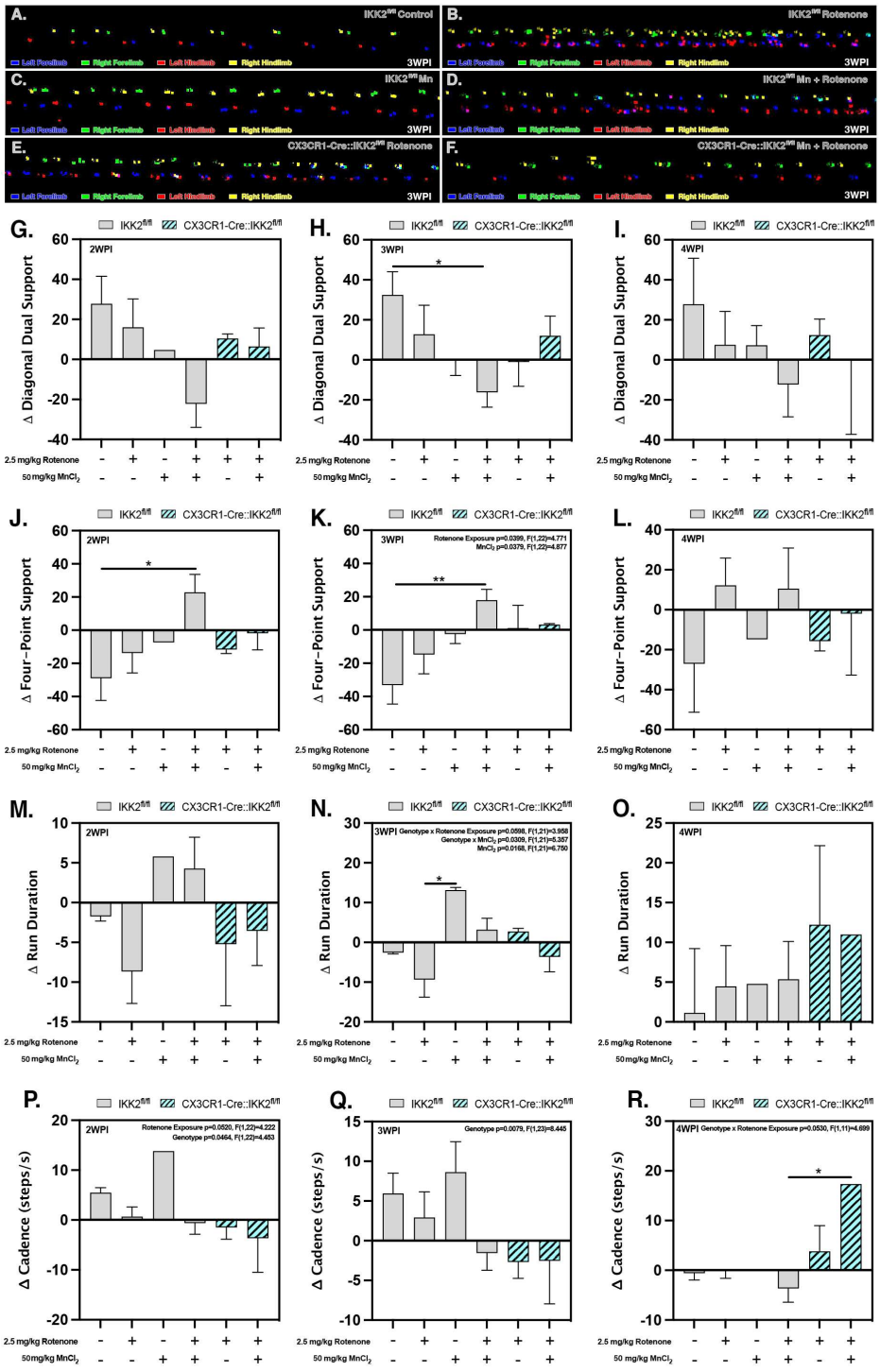

Figure 22. Microglial NF-κB knockout alleviates PD-like locomotor changes in a time and exposure-dependent manor. Individual pawprint tracking of locomotion across a 1-meter trackway showing left forelimb (blue), right forelimb (green), left hindlimb (red), and right hindlimb (yellow) in WT control (**A**), WT rotenone exposure (**B**), WT Mn exposure (**C**), WT dual exposure (**D**), KO rotenone exposure (**E**), and KO dual exposure (**F**). Change in diagonal dual stance support (**G-I**), four-point stance support (**J-L**), run duration (**M-O**), and cadence (steps/second, **P-R**) compared to individual animal baseline at 2 WPI, 3 WPI, and 4WPI rotenone exposure, respectively. *n*=9 per group per timepoint. *$p<0.05$, **$p<0.001$.

measured at 2 WPI (**Fig. 22P**) and 3 WPI (**Fig. 22Q**). The combination of genotype and rotenone exposure at 4 WPI trended toward significance, with variance differences detected between WT dual exposed and KO dual exposed animals (**Fig. 22R**).

4.3.2 Neurochemical alterations in dopamine and serotonin metabolic pathways intimately connect to innate microglial NF-κB activation and subsequent immune training.

HPLC quantification of striatal tissue was performed to determine the levels of DA (**Fig. 23A**), DOPAC (**Fig. 23B**), 3-MT (**Fig. 23C**), HVA (**Fig. 23D**), metabolite to parent molecule ratios (**Fig. 23E, F**), NE (**Fig. 2G**), epinephrine (E; **Fig. 23H**), 5-HT (**Fig. 23I**), and 5-HIAA (**Fig. 23J**). There were no significant groupwise comparisons observed in DA, DOPAC, 3-MT, HVA or DOPAC/DA ratios (**Fig. 23A-E**). However, when metabolite to parent molecule ratio included HVA, there was a significant increase observed in WT rotenone exposed animals had trending increases in WT Mn exposed animals when compared to WT control (**Fig. 23F**). Decreases from WT control levels of NE were observed in WT rotenone exposed animals, and trending decreases occurred in KO dual exposure. These decreases reverted to basal levels in dually exposed WT animals (**Fig. 23G**). Mn exposure in WT animals increased the levels of E when compared to WT rotenone exposure, WT dual exposure, KO rotenone exposure, and KO dual exposure groupings (**Fig. 23H**). A significant decrease in the levels of serotonin receptor (5-HT) were observed in WT rotenone animals in comparison to WT controls (**Fig. 23I**), with no significant changes occurring in levels of 5-HIAA (**Fig. 23J**). The combination of Mn exposure, rotenone exposure and genotype contributed to variance observed in HVA (**Fig. 23D**), DOPAC+HVA/DA (**Fig. 23F**), NE (**Fig. 23G**), and 5-HT (**Fig. 23I**). Rotenone exposure in combination with genotypic changes in microglia contributed to variance observed in DA (**Fig. 23A**) and DOPAC (**Fig. 23B**). Mn

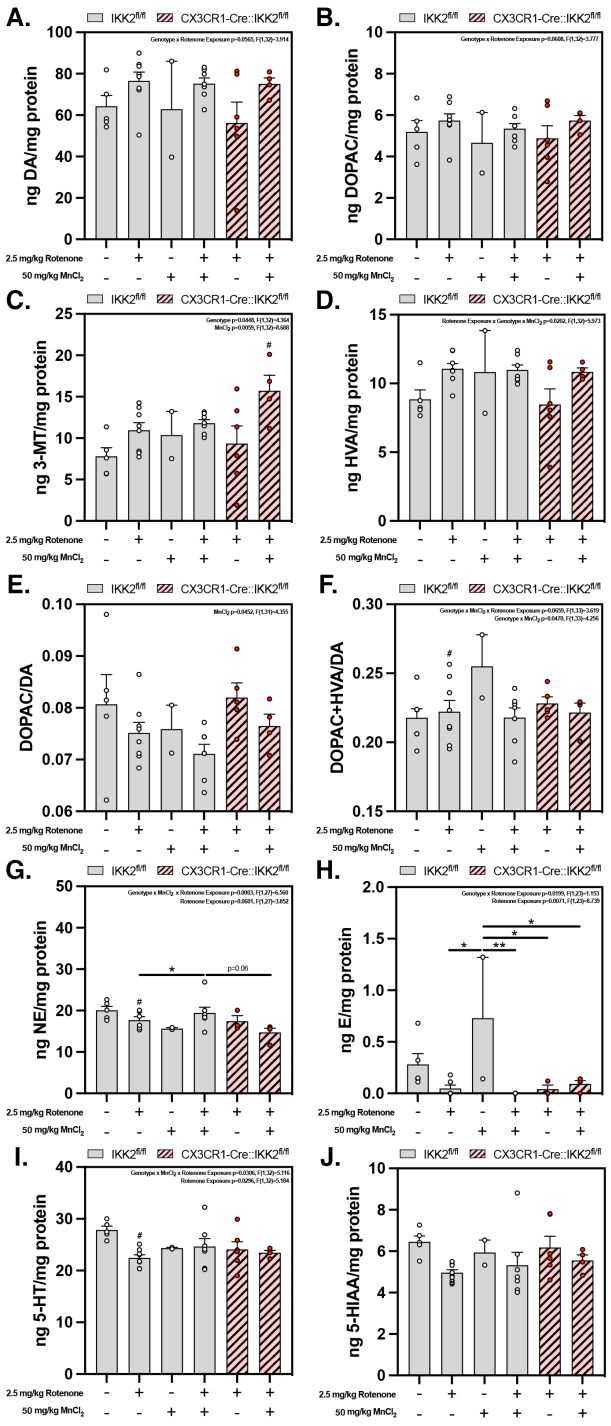

Figure 23. Inhibition of microglial NF-κB protects early-stage catecholamine and monoamine fluctuations in PD Striatal quantification of dopamine (DA; **A**), 3,4-dihydroxphenylacetic acid (DOPAC; **B**), 3-methoxytyramine (3-MT; **C**), homovanillic acid (HVA; **D**), DOPAC/DA ratio (**E**), and DOPAC+HVA/DA ratio (**F**) show genotype and exposure dependent fluctuations in the dopamine metabolism pathways. Quantification of norepinephrine (NE; **G**), epinephrine (E; **H**), serotonin (5-HT; **I**), and 5-hydroxyindoleacetic acid (5-HIAA; **J**) also show genotype and exposure dependent alterations. *n*=9 per group. #*p*<0.05 compared to WT control animals. **p*<0.05, ***p*<0.01.

exposure and genotypic alterations accounted for variance in DOPAC+HVA/DA (**Fig. 23F**), and Mn exposure alone contributed to alterations in 3-MT (**Fig. 23C**) and DOPAC/DA (**Fig. 23E**). Rotenone exposure alone affected levels of NE (**Fig. 23G**), E (**Fig. 23H**), and 5-HT (**Fig. 23I**) involved in serotonin uptake and metabolic processes.

4.3.3 Pathological response of secondary primed immunological memory in microglia is independent of the canonical NF-κB signaling pathway.

Examination of microglial involvement in the pathological progression of PD and PD-like diseases induced by rotenone and Mn exposure was performed through whole hemisphere montaging of the basal midbrain containing SN and the corresponding signaling region of the striatum (**Fig. 24A-F**). Individual microglial morphometric characteristics were determined through binary, skeletonization and 3-D cellular reconstruction allowing for overall branch length and branch magnitude to be investigated (**Fig. 24G-L**). Total branch length per cell (**Fig. 24M**), branch terminals per cell (**Fig. 24N**), and Sholl intersections per cell (**Fig. 24O**) for 1) WT control, 2) WT rotenone, 3) WT Mn Rotenone, 4) WT Mn, 5) KO Mn Rotenone, and 6) KO rotenone were plotted in conjunction with the somal area of each individual microglia. This illustrated somal enlargement corresponded with retraction and reduction of branches. This morphological change was primarily observed in KO rotenone exposed, KO dually exposed, and WT rotenone exposed animals. Sholl intersections provide a basis of measurement that encompass both the length of the microglial branches and the overall magnitude of branches at each length, ultimately resulting in a multi-dimensional measurement of cellular complexity. Intersection numbering begins at the nucleus of the cell and moves in stepwise spherical increments outward. Terminal branch points are identified and the intersection number where the terminal branch points are located is the

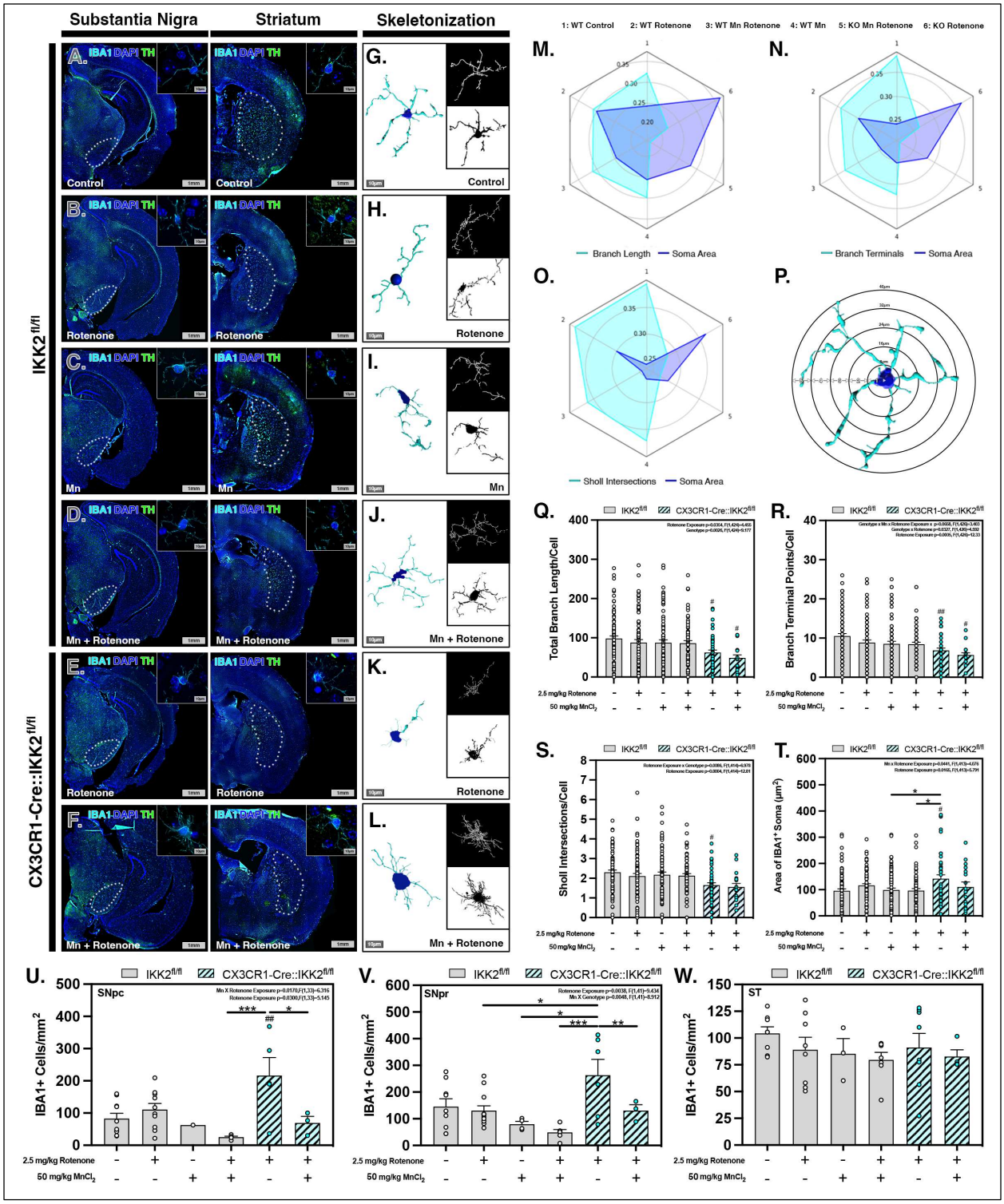
Substantia Nigra
Striatum
Skeletonization
IKK2fl/fl
CX3CR1-Cre::IKK2fl/fl
A. IBA1 DAPI TH
Control
B. IBA1 DAPI TH
Rotenone
C. IBA1 DAPI TH
Mn
D. IBA1 DAPI TH
Mn + Rotenone
E. IBA1 DAPI TH
Rotenone
F. IBA1 DAPI TH
Mn + Rotenone
G.
Control
H.
Rotenone
I.
Mn
J.
Mn + Rotenone
K.
Rotenone
L.
Mn + Rotenone
1: WT Control
2: WT Rotenone
3: WT Mn Rotenone
4: WT Mn
5: KO Mn Rotenone
6: KO Rotenone
M.
Branch Length
Soma Area
N.
Branch Terminals
Soma Area
O.
Sholl Intersections
Soma Area
P.
Q.
Total Branch Length/Cell
R.
Branch Terminal Points/Cell
S.
Sholl Intersections/Cell
T.
Area of IBA1+ Soma (μm2)
IKK2fl/fl
CX3CR1-Cre::IKK2fl/fl
2.5 mg/kg Rotenone
50 mg/kg MnCl2
U.
SNpc
IBA1+ Cells/mm2
V.
SNpr
IBA1+ Cells/mm2
W.
ST
IBA1+ Cells/mm2

Figure 24. Microglia deficient in canonical NF-κB pathway activation retain activated morphological phenotypes and genotype-independent priming results in reduction of microcytosis. Whole hemisphere montage imaging of WT control, WT rotenone exposure, WT Mn, WT dual exposure, KO rotenone exposure, and KO dual exposure in the SN and ST of microglia (IBA1, cyan), DAn and projecting fibers (TH, green) and cellular neuclei (DAPI, blue), with high magnification insets of individual microglial cells (**A-F**). Three-dimensional renderings of microglial insets from the SN with binary and skeletonized illustration for WT control (**G**), WT rotenone exposure (**H**), WT Mn (**I**), WT dual exposure (**J**), KO rotenone exposure (**K**), and KO dual exposure (**L**). Radar plots comparing process parameters to somal dilation or constriction in 1) WT control, 2) WT rotenone exposure, 3) WT dual exposure, 4) WT Mn, 5) KO dual exposure, and 6) KO rotenone exposure through branch length:somal area (**M**), branch terminals:somal area (**N**), and Sholl intersections:somal area (**O**). Sholl intersection rendering showing how each Sholl intersection is determined based on increasing spherical distance from nuclei, allowing for the complexity and branch number of the microglial cell to be interpreted as a single integer (**P**). Quantitative measurement comparing exposure groups and genotype in total branch length/cell (**Q**), branch terminal points/cell (**R**), Sholl intersections/cell (**S**) and area of soma/cell (**T**). Identification of regional microcytosis in the SNpc (**U**), SNpr (**V**), and ST (**W**). n=9 per group. #p<0.05, ##p<0.01 in comparison to WT control. *p<0.05, **p<0.01, ***p<0.001.

numerical value obtained for the cell. For example, there would be a Sholl intersection of the following for the cell depicted in **Figure 24P**: 1, 2, 4, 4, 5, 5. Specific size and volume parameters are implemented to exclude 'branch extensions' that may represent more than main branch characteristics, and further complicate analysis.

Individual morphometric parameter quantification of total branch length per cell, number of branch terminal points per cell, and Sholl intersections per cell all showed decreases in KO rotenone exposed animals compared to WT controls (**Fig. 24Q-S**). Reduction in total branch length per cell and branch terminal points per cell was also observed in KO dually exposed animals when compared to WT controls (**Fig. 24Q, R**). Likewise inverse increases in somal area were observed in KO rotenone exposed animals in comparison to WT control, WT Mn, and WT dually exposed animals (**Fig. 24T**). Rotenone exposure was a consistent contributor to branch and somal morphological remodeling of microglia (**Fig. 24Q-T**), whereas genotype:rotenone exposure (**Fig. 24R, S**) contributed to a reduction in branch magnitude and overall complexity. Genotype alone was observed to contribute to branch length (**Fig. 24Q**), dual exposure resulted in somal enlargement (**Fig. 24T**) and the combination of genotype and dual exposure trended towards significance in magnitude of branches per cell.

Regional increases in microglial population prevalence, microcytosis, were identified through quantification of $IBA1^+$ cells per area in the SNpc (**Fig. 24U**), SNpr (**Fig. 24V**), and ST (**Fig. 24W**). Rotenone exposure alone, and the combination of Mn and rotenone exposure led to increases in microglial cells in the SNpc (**Fig. 24U**), where rotenone alone and genotype:Mn led to increases in the SNpr (**Fig. 3V**). Interestingly, KO rotenone exposed animals presented with significant increases in microglia within the SNpc and SNpr when compared to WT dual exposed and KO dual exposed (**Fig. 24U, V**). SNpc microglial increased in the rotenone exposed KO animals were also significant from WT controls (**Fig. 24U**). SNpr microglial increases in the rotenone exposed KO animals were also significantly larger than those in WT Mn and WT rotenone exposure (**Fig. 24V**). Rostral microglial analysis in the striatum revealed no populational differences (**Fig. 24W**).

4.3.4 Astrocytic activation is highly dependent on exposure and microglial NF-κB signaling in primary and secondary immune challenges.

Astrocytic reactivity mediated by exposure and glial-glial crosstalk through microglial canonical NF-κB inflammatory signaling pathways were identified through whole hemisphere montaging in the SN. High magnification insets acquired within the SN show astrocytic expression of GFAP (red) and DAPI (blue). Adjacent high magnification panels show S100β (yellow), C3 (red) and GFAP (cyan) staining with companion 3-D renderings of individual cell staining expression and positional localization of C3 (**Fig. 25A-F**). Astrocytic reactivity was also quantified in the ST using whole hemisphere montages, where high magnification insets depict astroglial expression of GFAP (**Fig. 25G-L**). Regional quantification of $S100\beta^+$ cells per area was performed in the SNpc (Fig. 4M), SNpr (**Fig. 25N**), and ST (**Fig. 25O**). There were no changes observed

within the SNpc, but Mn in combination with rotenone exposure drove increases in S100β$^+$ cell prevalence in the SNpr. There were increasing cellular trends observed in both WT rotenone exposed and KO rotenone exposed animals when compared to WT control (**Fig. 25N**). There were also increases observed within the ST with genotype in combination with dual exposure driving these dynamics (**Fig. 25O**). Regional GFAP expression was also investigated, which revealed increases in the SNpc of WT rotenone exposure and WT dual exposure in comparison to WT controls. Genotype in part with rotenone exposure significantly impacted the variance observed (**Fig. 25P**). Mn exposure alone contributed to the variation differences observed within the SNpr of animals (**Fig. 25Q**), and Mn:rotenone exposure and genotype alone were driving factors in GFAP variation within the ST. Increases in GFAP$^+$ expression within the ST were evident between KO dual exposure and WT rotenone exposure (**Fig. 25R**).

Further characterization of activated state astrocytes was identified by C3 expression in the soma (S100β$^+$) or processes (GFAP$^+$) of astrocytes. Fluorescent intensity of C3 within individual S100β$^+$ areas of somal staining in the SNpc showed gneotype:rotenone exposure, genotype:Mn exposure, and Mn exposure dependence and trending dependence upon genotype. Rotenone exposure in WT animals resulted in increased C3 when compared to all other WT exposure groupings. Dual exposed WT animals had increases in somal C3 when compared to Mn alone exposure. Mn exposure in any capacity decreased C3 expression in astrocyte soma significantly when compared to WT control. Inhibition of microglial NF-κB reduced somal C3 in rotenone exposed animals but increased it in Mn only exposed animals (**Fig. 25S**). Somal C3 in the SNpr showed similar trends to that seen in the SNpc with increases in WT rotenone exposure, decreases in Mn exposure (alone or in combination with rotenone), increases in Mn + rotenone::Mn alone comparisons, and overall decreases in somal C3 expression in WT Mn exposed animals. KO

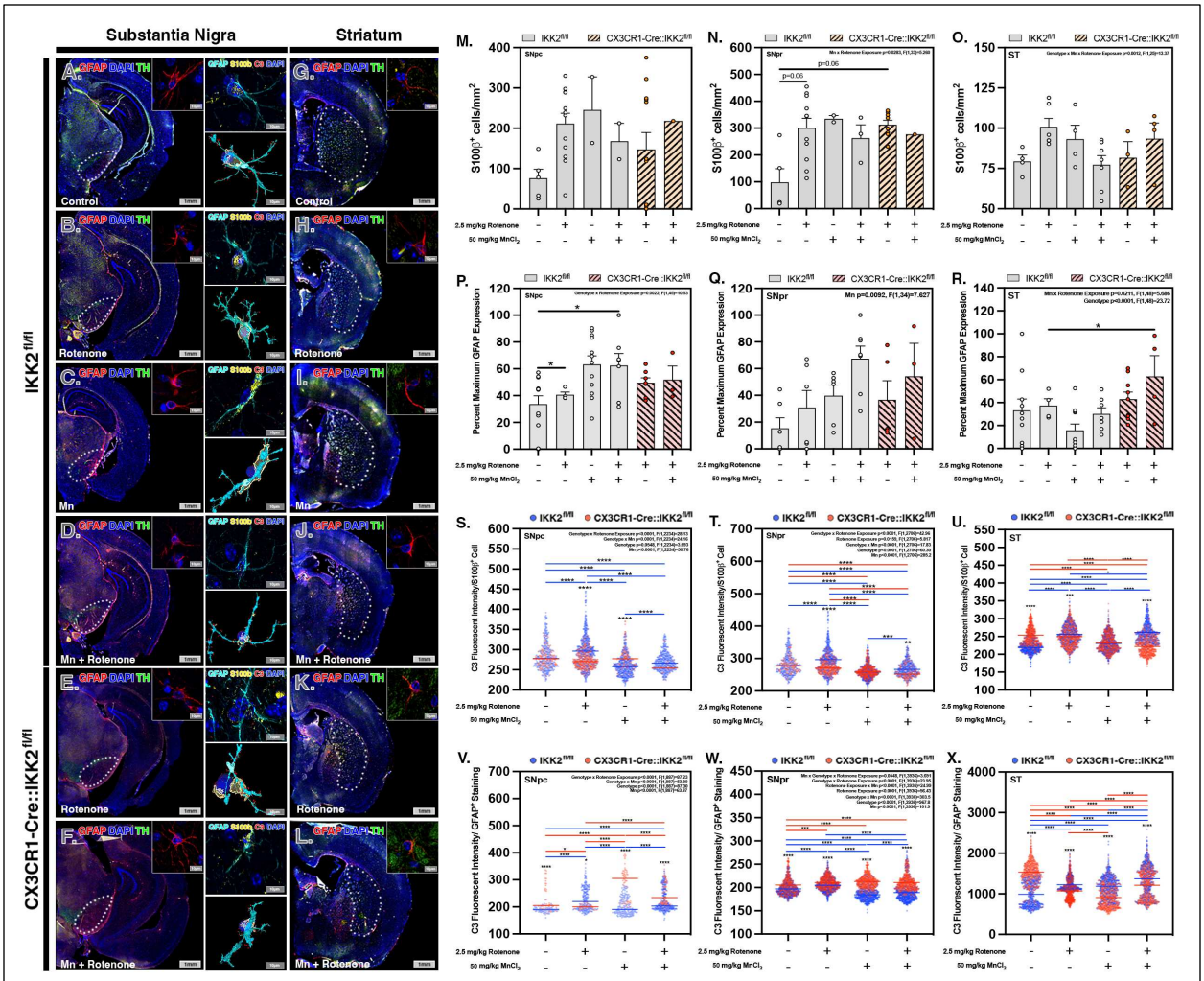

Figure 25. Inflammatory phenotypic activation of astrocytes is highly dependent upon microglial canonical NF-κB signaling and juvenile Mn exposure surrounding the nigrostriatal pathway. Whole hemisphere montage imaging and high magnification insets of astrocytes (GFAP, red), DAn and projecting fibers (TH, green) and cellular nuclei (DAPI, blue) in WT control, WT rotenone exposure, WT Mn, WT dual exposure, KO rotenone exposure, and KO dual exposure in the SN (**A-F**). High magnification insets of astrocytes in the SN with GFAP (cyan), S100β (yellow), C3 (red), and cellular nuclei (DAPI, blue) along with identical cell three-dimensional rendering showing C3 somal (S100β) or process (GFAP) localization. Whole hemisphere montage imaging and high magnification insets of astrocytes (GFAP, red), DAn and projecting fibers (TH, green) and cellular nuclei (DAPI, blue) in WT control, WT rotenone exposure, WT Mn, WT dual exposure, KO rotenone exposure, and KO dual exposure in the ST (**G-L**). Regional quantification of S100β$^+$ astrocytosis in the SNpc (**M**), SNpr (**N**), and ST (**O**) along with percent increases in GFAP$^+$ astrocytic hypertrophy in the SNpc (**P**), SNpr (**Q**), and ST (**R**). Quantification of cellular C3 location based on intensity measurements in the soma (S100β$^+$) and processes (GFAP$^+$) of astrocytes in the SNpc (**S, V**), SNpr (**T, W**), and ST (**U, X**), respectively. *n*=9 per group. **p*<0.05, ***p*<0.01, ****p*<0.001, *****p*<0.0001.

rotenone exposed animals and dual exposed animals also showed somal decreases in C3 when compared to WT counterparts. Striatal somal C3 intensity, again, increased with rotenone exposure, but was most predominant in WT dual exposure animals. Canonical NF-κB inhibition in microglia resulted in basal level increases in somal C3, which decreased with the exposure of Mn (**Fig. 25U**). C3 localizing in astrocytic processes was increased from basal WT control levels in WT rotenone exposure and WT dual exposure. KO control animals expressed C3 in processes more so than WT control and was seen to be significantly increased in KO Mn and KO dual exposure within the SNpc (**Fig. 25V**). SNpr analysis of C3 expression in the processes of WT animals showed similar patterns to WT somal C3 with rotenone exposure inducing C3 expression, and Mn (single or dual) decreasing expression. However, astrocytes in KO animals had significantly more C3 in processes at basal levels, of which further increased with rotenone, Mn, and dual exposures (**Fig. 25W**). C3 prevalence in processes of astrocytes in the ST was, in fact, similar to somal C3, apart from Mn exposure in KO animals which resulted in significant decreases of expression (**Fig. 25X**).

4.3.5 Dopaminergic neurodegeneration is modulated by microglial canonical NF-κB in primary but not secondary exposures.

Degeneration of DAn within the SNpc was determined through stereological analysis of regional montage imaging of the SN (**Fig. 26A-F**). Projecting dopaminergic terminal density was determined through TH^+ fiber intensity within whole hemisphere montages of the ST (**Fig. 26G-L**). Quantification of overall TH^+ soma within the SNpc elucidated dual, rotenone, and Mn exposure as drivers resulting in neurodegeneration. Neurodegeneration was significant in WT rotenone, WT dual, and KO dual exposure (**Fig. 26M**). ST TH intensity was observed to increase

in WT dual and KO dual when compared to WT Mn exposed animals. WT dual exposure intensity was also increased compared to KO rotenone exposure and there was a trend of increase between KO dual exposure and KO rotenone exposure. Dual exposure, rotenone exposure, genotype and Mn exposure and genotype were all contributing factors in the TH intensity changes observed within the ST (**Fig. 26N**). Overall reduction in neurons staining positive for the pan-neuronal stain NeuN, was evident in the SNpc where dual, rotenone and Mn exposure contributed to the variance observed (**Fig. 26O**).

4.3.6 Microglial innate immunity functions as primary respondent to misfolded α-synuclein protein aggregation.

Determination of misfolded α-syn protein was identified by multi-factorial analysis and ratio metric quantification based on individual regions. Whole hemisphere montage images of the SNpc, SNpr, and ST were obtained along with high magnification insets, allowing for accurate determination of regional p129 characteristics in WT control (**Fig. 27A, G**), WT rotenone (**Fig. 27B, H**), WT Mn (**Fig. 27C, I**), WT dual exposure (**Fig. 27D, J**), KO rotenone (**Fig. 27E, K**), and KO dual exposure (**Fig. 27F, L**), respectfully. Maximum area occupied by p129 in the SNpc was significantly increased in KO dual exposure animals (**Fig. 27M**), where the same held true for the number of $p129^+$ objects (**Fig. 27N**). Ratio analysis of $p129^+$ area to $p129^+$ object count, however, indicated KO rotenone exposure trended toward having larger area occupying aggregates (**Fig. 27O**). Statistically, the same observations were observed in the SNpr that were observed in the SNpc (**Fig. 27P-R**). Genotype:Mn:rotenone exposure, Mn:rotenone exposure, and genotype contributed to statistical variance observed in $p129^+$ area (**Fig. 27S**) and $p129^+$ object count (**Fig. 27T**) within the ST, where Mn also contributed to the variance of maximal $p129^+$ area (**Fig. 27S**).

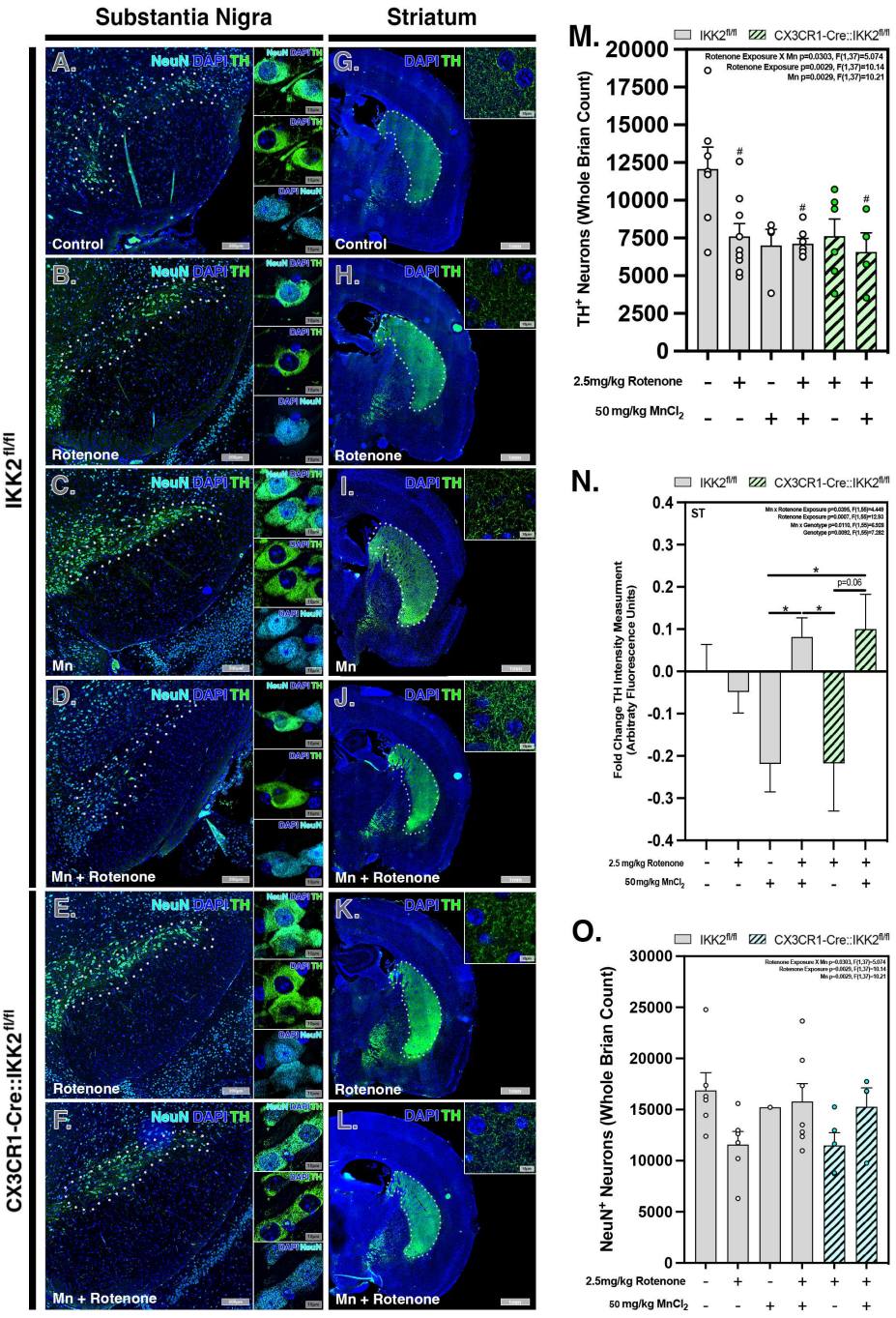

Figure 26. Microglial priming through juvenile Mn and adult rotenone exposure results in neurodegeneration of dopaminergic neurons independent of the canonical NF-κB signaling pathway. Whole hemisphere montage imaging and high magnification insets of DAn (TH, green), total neurons (NeuN, cyan) and cellular nuclei (DAPI, blue) in WT control, WT rotenone exposure, WT Mn, WT dual exposure, KO rotenone exposure, and KO dual exposure in the SN (**A-F**). Whole hemisphere montage imaging and high magnification insets of dopaminergic projecting fibers (TH, green) and cellular nuclei (DAPI, blue) in WT control, WT rotenone exposure, WT Mn, WT dual exposure, KO rotenone exposure, and KO dual exposure in the ST (**G-L**). Whole nuclei quantification of DAn and total neurons in the SNpc (**M, O**), and average overall TH intensity in the projecting fibers of the caudate nucleus (**N**). n=9 per group. #p<0.05 in comparison to WT control animals. *p<0.05.

No statistical significance between groupings was observed within the ST, however there were trends indicating dual exposure in WT animals may result in larger order p129 aggregates in the ST (**Fig. 27U**).

4.3.7 Microglial priming and impairment of canonical NF-κB results in increased accumulation of misfolded α-synuclein and a reduction of peripheral protein deposition.

To determine how the involvement of microglial NF-κB through innate and learned immunity led to a reduction or induction of misfolding of α-syn, p129 staining at a regional level and cellular level was assessed. Representative images of p129 in microglia and TH^+ neurons of the SNpc show staining increases in microglia and DAn (**Fig. 28A-F**) where prevalence increases in WT dual exposure (**Fig. 28D**) and rotenone and dual exposure of the KO groupings (**Fig. 28E, F**). Representative imaging of the adjacent anatomical region of the SNpr show p129 sequestered within microglial cells (**Fig. 28G-L**). ST staining for p129 intensity in microglial and associated TH^+ fiber tracts (**Fig. 28M-R**). Upon quantifying p129 intensity within individual DAn of the SNpc there were increases observed in WT rotenone, WT Mn and WT dual exposure groupings when compared to genotype matched controls. KO rotenone and dual exposed animals had increased DAn p129 in comparison to WT rotenone exposed animals. The combined effects of genotype, rotenone exposure and Mn exposure led to statistically significant variance in addition to rotenone alone and Mn alone (**Fig. 28S**). Microglial p129 intensity increases, from basal WT control levels, were present within WT rotenone, WT dual, KO rotenone, and KO dual exposed animals. Mn alone did not increase p129 in microglia, but combined effects of Mn and rotenone increased p129 prevalence which was greater than WT rotenone and KO rotenone. KO dual exposure animals had the largest accumulation of misfolded α-syn harborization where the

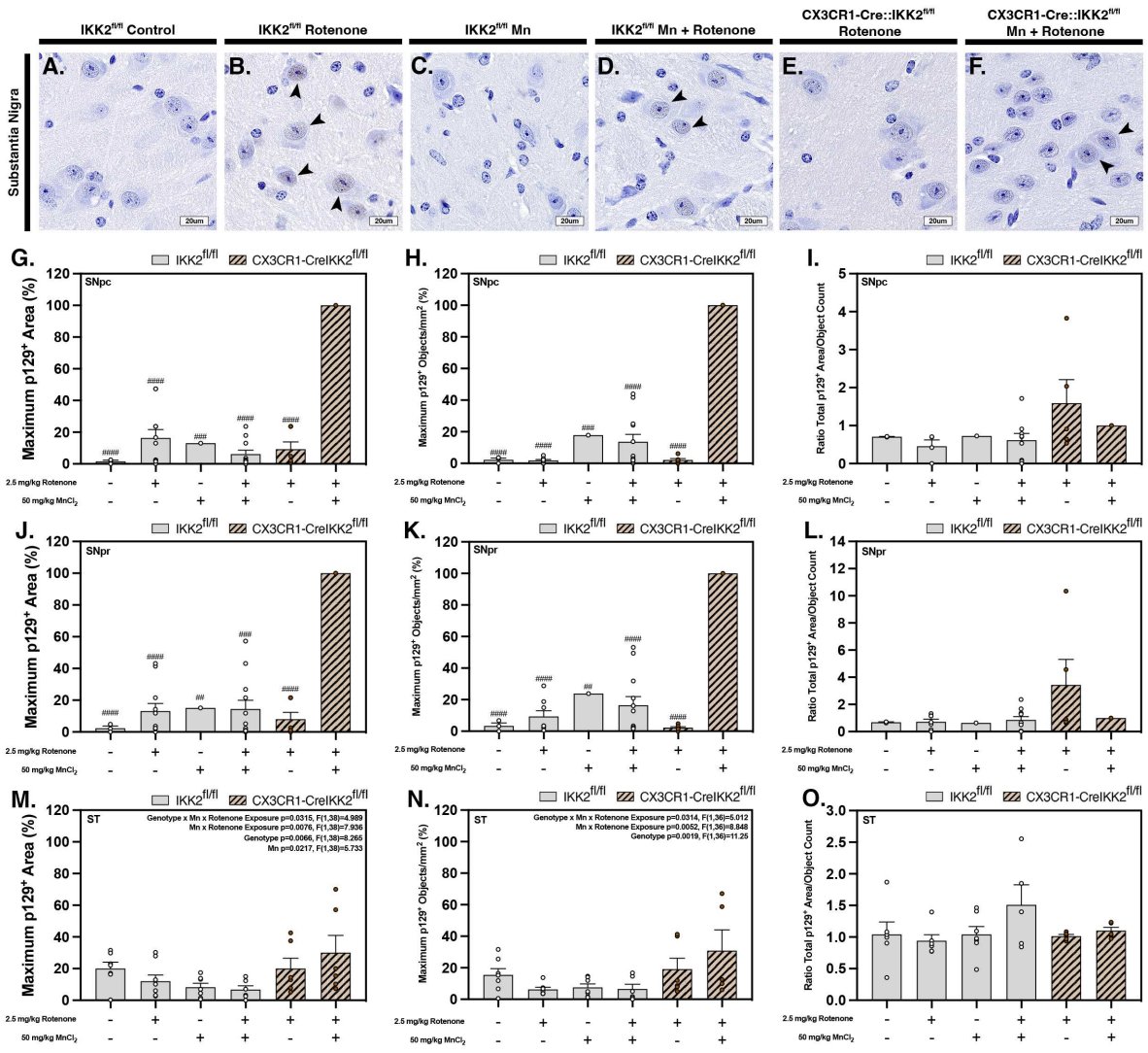

Figure 27. Microglial NF-κB modulates the regional clearance and degradation of misfolded p129^{+} α-syn that occurs from rotenone exposure. High magnification imaging of immunohistochemically stained SN for p129 α-syn shows marked peri-nuclear p129^{+} α-syn accumulation within neurons (black arrowheads) of WT rotenone (**B**), WT dual exposure (**D**), and KO dual exposure (**F**) when compared to WT control (**A**), WT Mn (**C**), and KO rotenone (**E**). Regional quantification of maximal p129^{+} area, maximal p129^{+} objects per area, and resulting ratio to identify larger-order aggregates in the SNpc (**G-I**), SNpr (**J-L**), and ST (**M-O**) show trending increases in larger-order aggregate occurrence in KO rotenone exposed animals within the SNpc (**I**) and SNpr (**L**). *n*=6 per group. ##*p*<0.01, ###*p*<0.001, ####*p*<0.0001 in comparison to KO dual exposure.

increase was significant against all genotype and exposure groupings (**Fig. 28T**). Striatal p129 intensity within microglia rendered WT dual exposure significant against KO dual exposure. Genotype in concert with rotenone and genotype alone were modulators that affected p129 accumulation within the ST (**Fig. 28U**). Peripheral dissemination of p129 in the serum fraction of blood revealed KO rotenone exposed animals had significantly less p129 than WT control, which was observed to return to basal levels in KO dual exposure animals. Genotype in conjunction with rotenone exposure and Mn, as well as solely was a source for statistical variance, in addition to Mn exposure (**Fig. 28V**). Regional intensity measurements of p129 revealed increases in KO dual exposure with Mn and Mn in combination with genotype driving variation in the SNpc (**Fig. 28W**). SNpr regional p129 intensity increased in WT dual exposure when compared to WT rotenone alone exposure, and there were trends of increase between KO rotenone exposure and WT rotenone exposure. The combination of genotype, Mn, and rotenone exposure as well as Mn exposure alone mediated total regional p129 intensity (**Fig. 28X**). Regional p129 intensity within the striatum showed marked differences where WT rotenone and KO dual exposure had a reduction in intensity compared to WT control (**Fig. 28Y**). Interestingly, KO dual exposure animals had the lowest p129 intensity within the striatum of all groupings, whereas the SNpc had an increase in intensity (**Fig. 28W, Y**).

4.3.8 Canonical NF-κB activation and inflammatory signaling of microglia result in impairment of mitophagy in dopaminergic neurons of the SNpc.

Cell-specific mitochondrial dysfunction in association with pathological progression of PD was assessed through immunofluorescent staining of HSP60 and pS65 with high magnification z-stack imaging of DAn (**Fig. 29A-F**) and microglia (**Fig. 29G-L**) within the SN. Cellular

localization of $HSP60^+$ mitochondria and recruited PARK2 in both TH^+ neurons and $IBA1^+$ microglia was observed through confocal microscopy of WT control and KO dual exposure animals, respectively (**Fig. 29M-P**). Quantification of $HSP60^+$ events and $pS65^+$ association with HSP60 mitochondria was determined by linear pixel tracing. TH^+ neuronal analysis revealed increases in $HSP60^+$ staining intensity in WT rotenone, WT Mn, and WT dual exposed, while there were significant decreases in $HSP60^+$ intensity within KO rotenone and KO dually exposed animals (**Fig. 29Q**). Intensity of pS65 association with $HSP60^+$ staining in TH^+ neurons was significantly decreased in all groups compared to control animals, where WT dual exposure and KO rotenone exposure showed the lowest levels of co-localization (**Fig. 29R**). Linear intensity mapping of PARK2 association with $HSP60^+$ mitochondria in TH^+ neurons show increased association in WT control animals and decreased association of mitophagy mediation in WT rotenone, WT Mn, WT dual exposure, KO rotenone, and KO dual exposure groupings (**Fig. 29S**).

Whole cell analysis of microglia elucidated pS65 intensity within $HSP60^+$ staining areas were decreased in WT rotenone, WT Mn, KO rotenone and KO dual exposure when compared to WT control. There were no significant changes in WT dual exposure microglial mitophagy in comparison to WT control (**Fig. 29T**). Quantification within microglial cell of total $HSP60^+$ objects per imaging frame revealed increased $HSP60^+$ mitochondria in WT rotenone exposed animals, with trending increases in KO rotenone and KO dual exposure (**Fig. 29U**). PCA of microglial PARK2 association with $HSP60^+$ mitochondria, magnitude of $HSP60^+$ mitochondria, and the ratio of the two variables show similar mitophagy associated responses between the following: WT rotenone:WT Mn:KO dual exposure; WT dual exposure:KO rotenone exposure. Where variation from basal level mitophagy was less prevalent in WT dual exposure and KO rotenone exposed animals (**Fig. 29V**). Correlational analysis of mitophagy responses in microglia

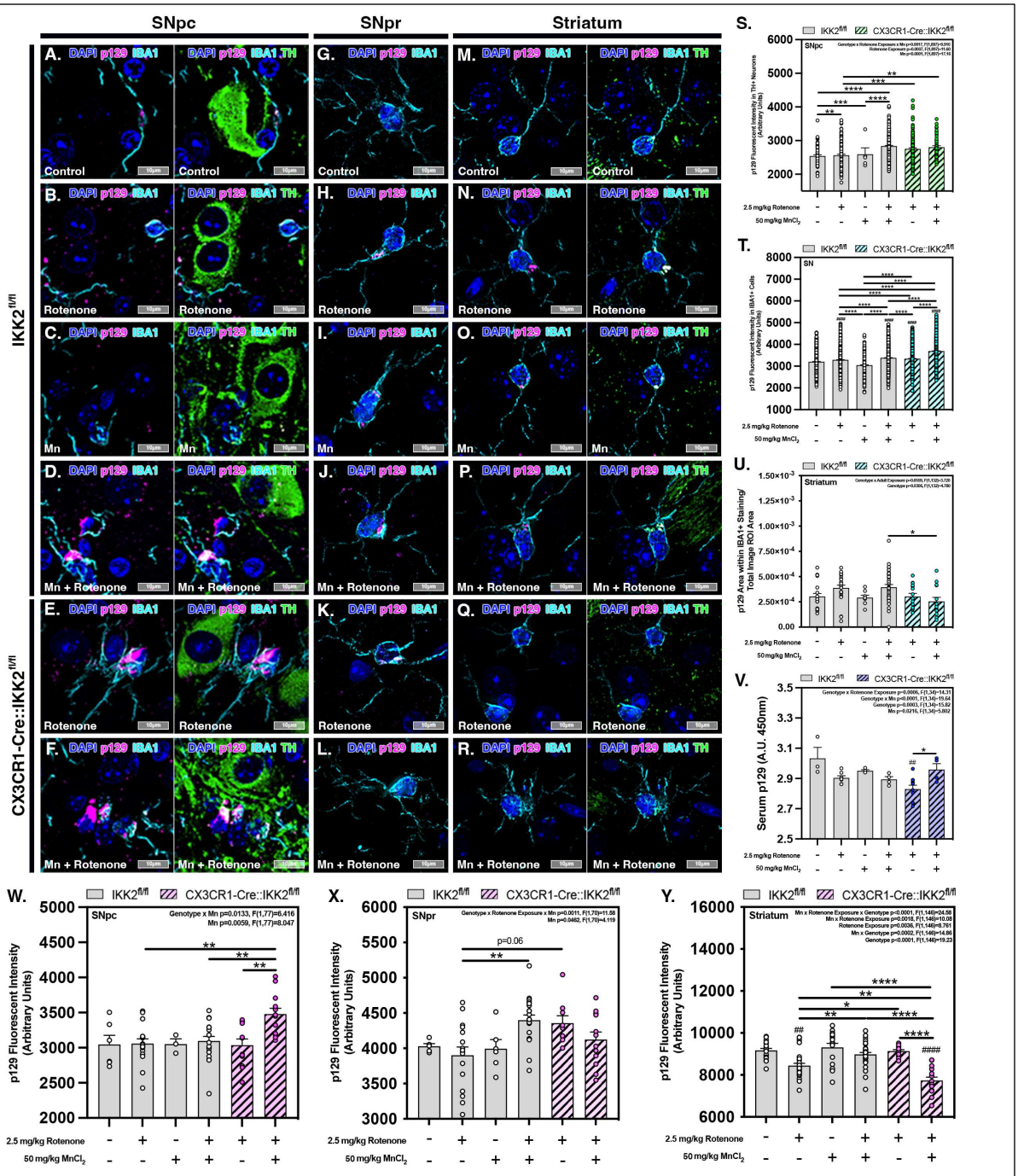

Figure 28. Accumulation of misfolded α-synuclein in dopaminergic neurons and microglia is α-synuclein upon microglial innate and exacerbated in Mn and rotenone induced adaptive immunity. High magnification images of microglia (IBA1, cyan), DAn (TH, green), misfolded α-syn (pink) and cellular nuclei (DAPI, blue) in WT control, WT rotenone exposed, WT Mn, WT dual exposure, KO rotenone exposure, and KO dual exposure in the SNpc (**A-F**), SNpr (**G-L**), and ST (**M-R**). Individual cell identification and quantification of misfolded α-syn prevalence by average p129 fluorescence intensity in TH^+ neuronal soma in the SNpc (**S**), and $IBA1^+$ microglial cells in the SN (**T**) and ST (**U**). ELISA quantification of peripheral dissemination of p129 in the serum phase of blood (**V**). Total overall regional intensity of p129 in the SNpc (**W**), SNpr (**X**), and ST (**Y**). *n*=9 per group. ##*p*<0.01, ###*p*<0.001, ####*p*<0.0001 in comparison to WT control animals. **p*<0.05, ***p*<0.01, ****p*<0.001, *****p*<0.0001.

were further quantified through Pearson Correlation Coefficients (**Fig. 29W**). Linear intensity mapping along single IBA1^{+} microglial cells revealed tandem intensity increases of HSP60 and PARK2 staining in WT control animals (**Fig. 29X**), whereas HSP60^{+} mitochondria in KO dual exposure animals had decreased intensity profiles of associated pS65 PARK2 (**Fig. 29Y**).

4.3.9 Gene transcription modulated by canonical microglial NF-κB in primary exposure drives disease-associated inflammatory cascade.

Modulation of intracellular signaling, inflammation, and cellular recruitment driven by canonical NF-κB in microglia of the SN was analyzed through fold change differences. Heat mapping of pro-inflammatory astrocytic genes (red), anti-inflammatory astrocytic genes (orange), pro-inflammatory microglial genes (green), anti-inflammatory microglial genes (teal), mitophagy (cyan), neuron associated (blue), pan-inflammatory (purple), glial-mediated inflammation (pink) revealed similar transcriptional profiles between WT control and KO rotenone exposed animals. WT rotenone, WT Mn and rotenone, WT Mn, and KO dual exposure grouped similarly in transcriptional expression (**Fig. 30A**). STRING association networks of all genes interrogated showed close claustral mapping and resulting association of each grouping of genes (**Fig. 30B**). Visual violin plot comparison of WT control (**Fig. 30C**), WT rotenone (**Fig. 30D**), WT Mn (**Fig. 30E**), WT dual exposure (**Fig. 30F**), KO rotenone (**Fig. 30G**), and KO dual exposure (**Fig. 30H**), gene expression indicate WT Mn exposure, WT dual exposure, KO rotenone exposure, and KO dual exposure provide large contributions regarding upregulation of gene fold change dynamics. Differential gene expression analysis showed significant increases in *Ccl2* (**Fig. 30I**), *Il1α* (**Fig. 30J**), *Il1β* (**Fig. 30K**), *Nos2* (**Fig. 30L**), *Nlrp3* (**Fig. 30M**), *Snca* (**Fig. 30N**), *Serping1* (**Fig. 30O**), and *Tlr4* (**Fig. 30P**) within KO rotenone exposed animals when compared to WT control and WT

rotenone exposure. Whereas WT dual exposure had increases in *Ccl5* compared to WT control and WT rotenone exposed animals (**Fig. 30Q**). Genotype and exposure group analysis against WT controls showed significant upregulation of *Ccl5*, *Il1α*, *Nos2*, *Tlr4*, *Il1β*, *Nr4a2*, *Gfap*, *p62*, *Tlr2*, *Tlr9*, *Myd88*, and *Park2* in KO rotenone exposed animals and *Ccl5* in WT dual exposure animals. WT rotenone exposure animals had a significant down regulation in *Stat1* and *C3* (**Fig. 30R**). PCA of mean fold change in pan-inflammatory genes show close association of WT rotenone, WT Mn, and WT dual exposure groupings, where KO rotenone and KO dual exposure were the least similar based on quadrant location (**Fig. 30S**). Pro-inflammatory microglia PCA analysis showed WT Rotenone, WT Mn, WT dual, and KO dual exposure clustering closely within the same quadrant, with WT control being the next closest association, followed by KO rotenone (**Fig. 30T**). Total gene PCA plotting once again revealed close association of transcriptional regulation between WT rotenone, WT Mn, WT dual, and KO dual exposure. In total, KO rotenone exposed animals had the least similar transcriptional patterns to WT rotenone, WT Mn, WT dual, and KO dual exposure animals (**Fig. 30U**).

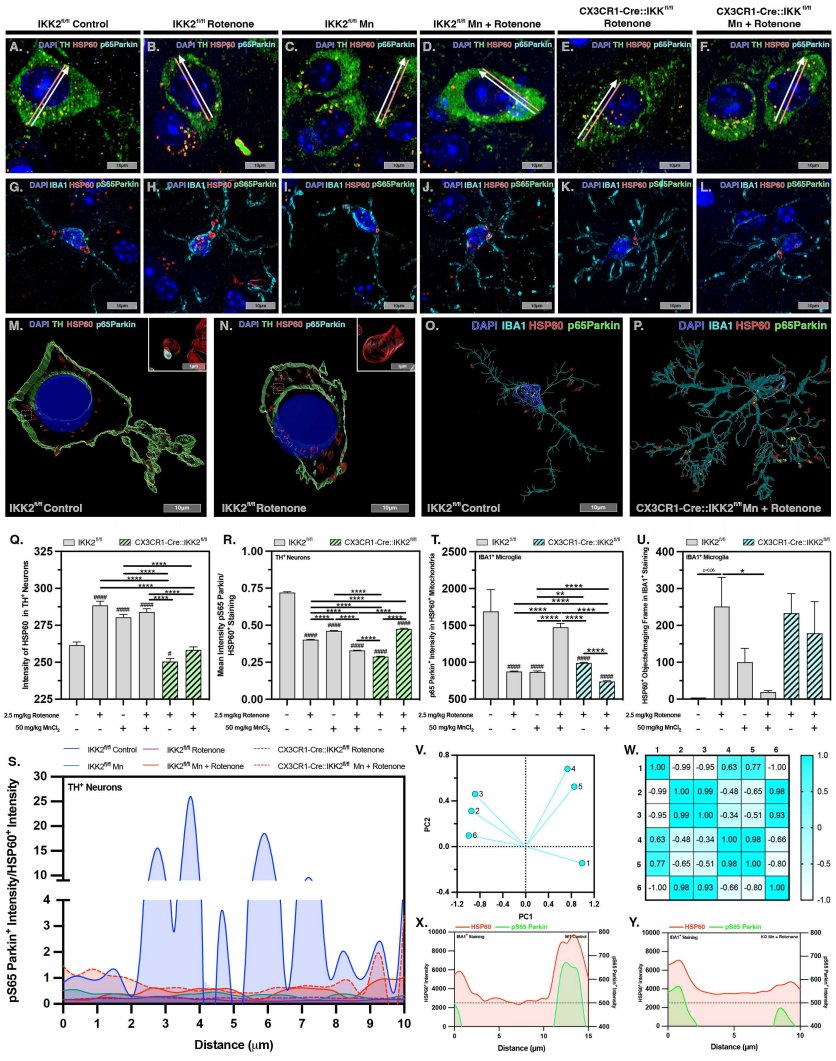

Figure 29. Microglial innate NF-κB response to initial insult is a driver of neuronal and microglial mitophagy impairment. High magnification analysis of TH$^+$ neurons (green) in the SNpc utilizing linear line profiling spanning complete cellular diameters in WT control (**A**), WT rotenone exposed (**B**), WT Mn exposed (**C**), WT dual exposure (**D**), KO rotenone exposure (**E**), and KO dual exposure (**F**) for HSP60$^+$ mitochondria (red) and phosphorylated serine 65 of PARK2 (cyan). Whole-cell IBA1$^+$ (pS65; cyan) microglial visualization of HSP60$^+$ mitochondria (red) and phosphorylation of serine 65 of PARK2 (cyan) using high magnification imaging across previously mentioned genotypes and exposures, respectively (**G-L**). Three-dimensional (3-D) renderings of TH$^+$ neurons (green) in WT control and WT rotenone exposure show HSP60$^+$ mitochondrial (red) increases with decreases in pS65 (cyan) (**M**, **N**). Similar observations were made in the 3-D renderings generated for IBA1$^+$ microglia (cyan) for HSP60$^+$ mitochondria (red) and pS65 (green) (**O, P**). Quantitative assessment of HSP60$^+$ mitochondria in TH$^+$ neurons show increases in exposure groupings of WT animals, with decreases in KO animals with same exposures (**Q**). There were decreases in the association of pS65 with HSP60$^+$ mitochondria in all exposure groupings in both WT and KO genotypes (**R**). Line intensity profiling shows individual micron intensities along the 1-pixel line drawn through TH$^+$ cells, where WT control animals had successful association of pS65 with HSP60$^+$ mitochondria (**S**). Whole cell microglial analysis shows similar results for pS65 HSP60 association but increases in HSP60$^+$ mitochondria in KO animals exposed to rotenone and dual exposure (**T, U**). Principal component analysis of HSP60 and pS65 association, HSP60$^+$ mitochondrial prevalence, and the ratio thereof yield Pearson correlation coefficients for each exposure and genotype (**V, W**). Individual line intensity profiling in WT control and KO Mn+ rotenone exposure animals for HSP60 (red) and pS65 (green; **X, Y**). n=9 per group. #p<0.05, ####p<0.0001 difference from WT control animals. *p<0.05, **p<0.01, ****p<0.0001.

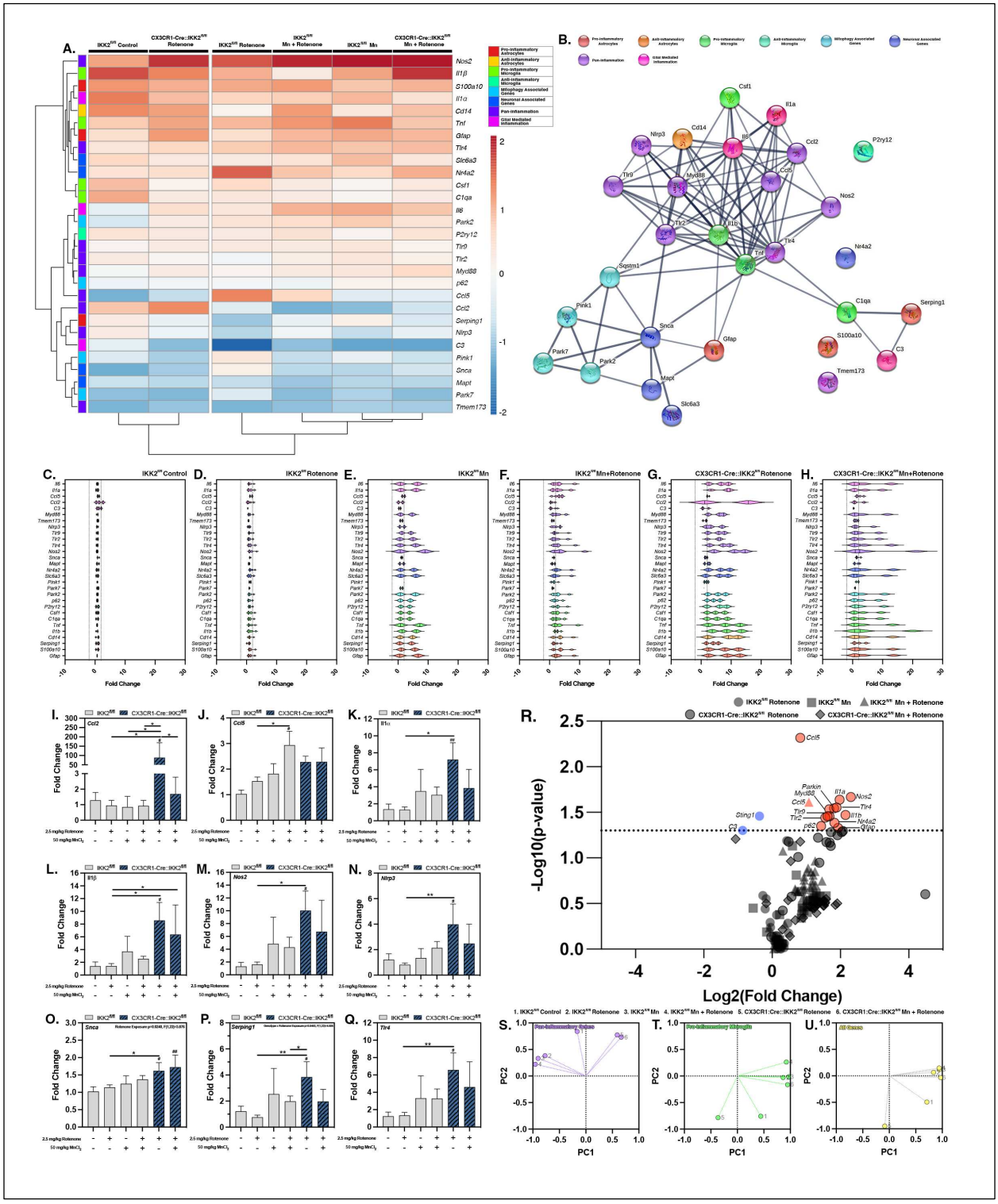
A.
IKK2fl/fl Control
CX3CR1-Cre::IKK2fl/fl Rotenone
IKK2fl/fl Rotenone
IKK2fl/fl Mn + Rotenone
IKK2fl/fl Mn
CX3CR1-Cre::IKK2fl/fl Mn + Rotenone
Nos2
Il1β
S100a10
Il1α
Cd14
Tnf
Gfap
Tlr4
Slc6a3
Nr4a2
Csf1
C1qa
Il6
Park2
P2ry12
Tlr9
Tlr2
Myd88
p62
Ccl5
Ccl2
Serping1
Nlrp3
C3
Pink1
Snca
Mapt
Park7
Tmem173
B.
Csf1
Il1a
Nlrp3
Cd14
Il6
Ccl2
P2ry12
Tlr9
Myd88
Ccl5
Nos2
Tlr2
Il1b
Tlr4
Nr4a2
Tnf
Sqstm1
C1qa
Serping1
Pink1
Snca
S100a10
Gfap
C3
Park7
Park2
Tmem173
Mapt
Slc6a3
C.
IKK2fl/fl Control
D.
IKK2fl/fl Rotenone
E.
IKK2fl/fl Mn
F.
IKK2fl/fl Mn+Rotenone
G.
CX3CR1-Cre::IKK2fl/fl Rotenone
H.
CX3CR1-Cre::IKK2fl/fl Mn+Rotenone
Fold Change
I.
Ccl2
J.
Ccl5
K.
Il1α
L.
Il1β
M.
Nos2
N.
Nlrp3
O.
Snca
P.
Serping1
Q.
Tlr4
2.5 mg/kg Rotenone
50 mg/kg MnCl2
R.
IKK2fl/fl Rotenone
IKK2fl/fl Mn
IKK2fl/fl Mn + Rotenone
CX3CR1-Cre::IKK2fl/fl Rotenone
CX3CR1-Cre::IKK2fl/fl Mn + Rotenone
-Log10(p-value)
Log2(Fold Change)
Ccl5
Parkin
Myd88
Ccl5
Tlr9
Tlr2
Sting1
C3
Il1a
Nos2
Tlr4
Il1b
Nr4a2
Gfap
p62
1. IKK2fl/fl Control
2. IKK2fl/fl Rotenone
3. IKK2fl/fl Mn
4. IKK2fl/fl Mn + Rotenone
5. CX3CR1-Cre::IKK2fl/fl Rotenone
6. CX3CR1-Cre::IKK2fl/fl Mn + Rotenone
S.
Pro-Inflammatory Tetrad
T.
Pro-Inflammatory Hexagon
U.
All Genes
PC1
PC2

Figure 30. Microglial NF-κB modulates transcriptional regulation of TIR domain activated inflammatory pathways in rotenone exposure but not in dual exposure induced disease. Fold change transcriptional up- (red) and down-regulation (blue) of pro-inflammatory astrocyte (red grouping), anti-inflammatory astrocyte (orange grouping), pro-inflammatory microglia (green grouping), anti-inflammatory microglia (teal grouping), mitophagy (cyan grouping), neuronal (blue grouping), pan-inflammatory (purple grouping), and glial mediated inflammatory (pink grouping) genes in the SN (**A**). STRING connectivity network mapping of all genes investigated with corresponding color denominations based on cellular and functional grouping (**B**). Violin plot comparison of gene regulation for WT control (**C**), WT rotenone (**D**), WT Mn (**E**), WT dual exposure (**F**), KO rotenone (**G**), and KO dual exposure (**H**) gene expression where color corresponds to the respective gene grouping. Differential gene expression of *Ccl2* (**I**), *Ccl5* (**J**), *Il1α* (**K**), *Il1β* (**L**), *Nos2* (**M**), *Nlrp3* (**N**), *Snca* (**O**), *Serping1* (**P**), and *Tlr4* (**Q**) genes. Significantly up- (red) and down-regulated (blue) genes for WT rotenone (open circle), WT Mn (open square), WT Mn + rotenone (open triangle), KO rotenone (closed circle) and KO Mn + rotenone (closed diamond) in the SN compared to WT control expression (**R**). PCA of pan-inflammatory (**S**), pro-inflammatory microglial associated (**T**), and all genes (**U**) within 1) WT control, 2) WT rotenone, 3) WT Mn, 4) WT Mn + rotenone, 5) KO rotenone, and 6) KO Mn + rotenone. n=6 per group. #p<0.05, ##p<0.01 in comparison to WT control animals. *p<0.05, **p<0.01

4.4. Discussion

Only about 10-15% of PD cases have a known heritable genetic cause, highlighting the importance of environmental exposures as potential complementary etiologic factors in disease onset and progression (Ball et al., 2019). Clinical, epidemiological and laboratory studies have linked environmental exposure to a number of agents to increased risk for PD, including heavy metals, pesticides, illicit drugs, organic solvents and infectious pathogens (Elbaz et al., 2009; Goldman et al., 2012; Pezzoli and Cereda, 2013; Castillo et al., 2017; Gunnarsson and Bodin, 2017; Macerollo et al., 2017; Huang et al., 2018; Bantle et al., 2019; Bantle et al., 2021a; Rocha et al., 2022a). Although these individual agents can induce certain pathological outcomes similar to those observed in idiopathic PD, little is known about the compounding effects of these exposures and how this may affect disease onset and progression (Chen and Ritz, 2018). All exposures encountered during and individuals' lifespan are formally known as the exposome, and can become increasingly complicated to interrogate and monitor from a public health prospective. However, a better understanding of individual cellular mechanisms underlying overt disease state can aid in narrowing the immense range of complexity. The idea of microglial priming/training was introduced twenty years ago but has gained significant traction in the scientific community in the last decade (Cunningham et al., 2005). This idea has challenged the thought that long-standing resident microglia are only capable of innate immune responses and signaling pathways. Here, we demonstrate that canonical NF-κB signaling pathways in microglia are not responsible for the neuroinflammation and degeneration that is initiated upon multi-exposure toxicity induced by Mn and rotenone. However, canonical NF-κB mediated epigenetic changes occurring during activation in the primary stimulation of microglial cells may very well lead to the adverse inflammatory response microglia demonstrate upon secondary exposure.

Early, or prodromal, stages of PD occur up to two decades prior to clinical diagnosis of disease and include gastrointestinal dysfunction, hyposmia/anosmia, resting eye movement sleep behavior disorder, anxiety, visuospatial dissociation, and depression (Murueta-Goyena et al., 2019; Bang et al., 2021). WT animals exposed to Mn and rotenone presented with decreased stability during locomotion and trending decreases in cadence, suggesting a deficit in motor initiation and visuospatial awareness (**Fig. 22**). KO animals that were exposed to both environmental toxins did not experience the same deficits but did have increased cadence levels (**Fig. 22**), which could be a predictor of PD-like motor changes induced by neurotransmitter fluctuations (Zanardi et al., 2021).

Lingering questions persist regarding neurotransmitter alterations that are responsible for cognitive, behavioral, and physiological changes observed in PD. Several studies have suggested the early involvement of the noradrenergic system which regulate levels of noradrenaline/norepinephrine (NA/NE). NA is capable of modulating innate microglial inflammatory responses, favoring neuroprotective environments. This delectate microenvironment was disturbed with rotenone exposure alone and the combination of dual exposure and microglial NF-κB (**Fig. 23**). Interestingly, trending increases of DA were observed in WT rotenone, WT dual-exposure, and KO dual exposure groupings. Traditional investigations into PD pathology would argue that disease results in DA decreases, however, several studies have shown that early increases in $p129^{+}$ α-syn accumulation increase DA uptake, independent of transporter expression (Hara et al., 2013). Strikingly, increases in $p129^{+}$ α-syn were observed in the group that had increased DA profiles, supporting previously reported experimentation (**Fig. 28**). Additionally, increased levels of the DA metabolite, 3-MT, were elevated in KO dually exposed animals which has previously been associated with disorganized abnormal movement presentation that included

tremor, head bobbing, grooming, and transient hyperactivity (Sotnikova et al., 2010). Together, the neurochemical profile and locomotor analysis indicate microglial NF-κB cascades may suppress roles of 3-MT as a neuromodulator of motor control (Sotnikova et al., 2010).

Microglia have long been known to function as specialized immune cells of the brain, providing constant surveillance and operating as primary respondents to external and internal pathological stimuli of the CNS. Uniquely, these cells can hyperpolarize their membranes through $Ca2^{+}$ flux and form pseudopodia allowing these cells to migrate to sites of injury (Laprell et al., 2021). Long-standing *postmortem* analysis and animal modeling of PD have consistently shown increased microglial population prevalence irrespective of neurodegeneration (Woulfe et al., 2000; Doorn et al., 2014). Increases in the volume of individual microglial cells were observed in the SNpc and SNpr of KO rotenone exposed animals, where all other genotype and exposure groupings remained consistent with basally expressed levels (**Fig. 24**). The combination of exposures along with rotenone exposure alone contributed to the increases observed, consistent with previous studies performed within our laboratory (Rocha et al., 2022b). Traditionally, microglia were thought to partake in primarily innate immune functions, however, they have recently been recognized for their ability to be primed/trained (Herrera et al., 2015). The milieu of microglial priming events remains complex and extensive, where initial priming may be temporally separated from secondary challenge (Knuesel et al., 2014). A functional consequence of microglial priming is an exaggerated inflammatory response to secondary, tertiary, or chronic stimuli that is referred to as the hyper-responsive state (Cunningham, 2013; Norden et al., 2015; Haley et al., 2019). Identification of hyper-responsive microglia, in part, is possible through IBA1 staining that reveals de-ramified cells with thick process and hypertrophic soma (Mouzon et al., 2014; Norden et al., 2015; Haley et al., 2019). Both morphometric alterations were abundant in

microglial NF-κB KO animals exposed to Mn followed by rotenone, exemplifying reduced complexity of cellular structure (**Fig. 24**). Importantly, these data show that microglial actin remodeling allowing for chemotaxis is not dependent upon canonical NF-κB, but rather is a physiological response to microenvironment shifts in Ca^{2+} induced by astrocytes and neurons (Baxter et al., 2021; Laprell et al., 2021).

Glial-glial crosstalk occurring between microglia and astrocytes has been implicated as a potential driver and potentiator of PD. Activated microglia are capable of secreting factors, such as C1q, TNFα, and Il-1α, which elicit activated pro-inflammatory astrocytes (Liddelow et al., 2017). Activation of astrocytes was observed in response to rotenone exposure in WT animals. Interestingly, the increase in astrocyte reactivity that was present with rotenone exposure alone was diminished with Mn and rotenone exposure in WT animals (**Fig. 25**). This observation indicates that the rapid 'trained' response mounted by microglial cells may reduce astroglia reactivity, and these cells may be working in a compensatory state in multi-exposure instances. Surprisingly, upon canonical NF-κB inhibition in microglia, C3 reactivity increased in $GFAP^{+}$ astrocytic processes within the SNpr upon rotenone exposure alone, Mn exposure alone, and the combination thereof. A large increase in reactivity was also observed with Mn exposure in the SNpc resident astrocytes (**Fig. 25**). These observations indicate that glial-glial crosstalk is not a clear-cut direct line of communication where inflammatory induction of one cell results in the activation of the other; rather, the signaling cascade may in part be a compensatory mechanism where inhibition of microglial NF-κB results in over-activated pro-inflammatory astrocytes.

Previous investigation into microglial specific signaling cascades involving canonical NF-κB conducted in our lab and others have recently demonstrated that inhibition of IKK2 in microglia results in protective microenvironments that foster the survival of neurons in AD and PD (Rocha

et al., 2022b; Wang et al., 2022). Importantly, these studies were conducted by implementing one driver of pathology, be that genetic or environmental. However, for the first time, we demonstrate here that the neurotoxic effects of compounded environmental exposures are independent of microglial canonical NF-κB. Consistent with previous results, rotenone exposure in WT animals resulted in neurodegeneration of DAn in the SNpc; dual exposure in WT animals resulted in comparable degeneration. Animals that had canonical NF-κB impairments in microglia, and were exposed to rotenone, experienced a reduction in DAn degeneration, where this protection was lost in dual-exposure (**Fig. 26**). Terminal TH intensity measurements have been consistently used in PD research to determine the extent of DA terminal loss. However, due to the enzymatic nature of TH, fluctuations in the expression are known to occur, notably so in PD. Compared to WT control, there were no statistically significant differences noted in overall TH intensity. However, it is important to remember that statistical significance does not always coincide with physiological functionality. The largest trending decreases in striatal TH intensity were observed in WT Mn exposure and KO rotenone exposure, where astrocytic uptake of Mn and astrocytic inflammatory compensation may be influential factors in the enzymatic activation of TH (**Fig. 26**). In addition, increases in $p129^{+}$ α-syn aggregates in TH^{+} neurons in KO DAn coincide with previously reported studies that have shown phosphorylation and activation of TH was altered by α-syn aggregation. Ultimately, increased levels of pK resistant α-syn resulted in low total-TH immunoreactivity, but high phosphoserine-TH reactivity (Alerte et al., 2008). Again, these results in concert with the data herein implicate intracellular reactions between aberrant forms of protein and functional enzymatic activation.

α-Syn misfolding and aggregation has been recognized as a hallmark of PD since the seminal characterization of Lewy bodies in 1912. Since, extensive research into the pathologic

function of this misfolded protein and its numerous possible strains have emerged. Immunohistochemical and immunofluorescence analysis of $p129^+$ α-syn revealed increased regional intensity within the SNpc of KO dual-exposure animals (**Fig. 6** and **Fig. 7**). Individual cellular analysis of TH^+ DAn and microglia showed increases in p129 accumulation in WT dual-exposure, KO rotenone exposure, and KO dual exposure (**Fig. 7**). These findings support other work conducted implicating that the misfolded protein autophagy pathway involving p62 is impaired in microglial NF-κB KO animals, which reduces these cell's capacity to degrade misfolded α-syn. It is important to identify that the excessive intracellular accumulation of misfolded α-syn observed herein depicts a single post-translational modification of the protein; nonetheless this modification is commonly reported in *postmortem* PD patient tissue samples (Paleologou et al., 2008). P129 post-translational modifications have been reported to induce toxicity *in vivo* and *in vitro* by inducing the formation of aggregates (Fujiwara et al., 2002; Chen et al., 2009). However, there have also been protective roles associated with this phosphorylation event (Smith et al., 2005; Gorbatyuk et al., 2008). Critically, the majority of characterization studies investigating phosphorylation of serine 129 in α-syn have been focused to neurons, excluding how this modification may influence glial cell inflammatory responses. To expand upon this, the extensive accumulation of $p129^+$ aggregation in KO rotenone exposed animals does not induce neurodegeneration of DAn, whereas comparable accumulation of $p129^+$ α-syn in WT rotenone exposure, WT dual exposure, and KO dual exposure were present with DAn degeneration (**Fig. 26, Fig. 28**). These differences highlight that underlying inflammatory responses that are initiated by glia are responsible for the neurodegeneration that occurs and the accumulation of $p129^+$ α-syn does not necessarily indicate overt disease state.

Emerging evidence gathered over the last 40 years has identified mitochondrial dysfunction as a contributor of PD progression. Processes that regulate the turnover of damaged mitochondria are highly selective and are a form of autophagy, formally termed mitophagy. Impairment of proteins that participate in the induction of mitophagy have been shown in aging and lifespan models. Dysfunction of two of these proteins, PINK1 and PARK2, have been extensively associated with selective loss of DAn in the SNpc (Ge et al., 2020). Identification of damaged mitochondria through HSP60 staining in DAn in the SNpc revealed elevated levels of damaged mitochondria in WT rotenone, WT Mn, and WT dual exposure. Investigation of mitophagy in DAn revealed decreases in PARK2 association with $HSP60^{+}$ mitochondria in all exposures, independent of genotype. Akin to p129 α-syn, PINK1 and PARK2 deficits are mainly described in the context of neurons, where a pronounced gap remains for glial cells. Individual analysis of microglia in the SN, astonishingly, only indicated rotenone exposure alone as a factor in induction of mitochondria damage (**Fig. 29**). Whereas microglial PARK2 $HSP60^{+}$ association was diminished in all exposure groupings except WT dual exposure. Ratio metric normalization of these parameters revealed that microglial mitophagy, and exposure associated dysfunction, were similar in quadrant location for WT rotenone, WT Mn and KO dual-exposure; while WT dual exposure and KO rotenone exposure shared proximity within a separate quadrant (**Fig. 29**).

Significant strides have been made in detailing transcriptional regulation of genes associated with activation states of glia (Das et al., 2020). These states are immensely complex where numerous dynamic intermediate phenotypes may lie between A1/A2 and M1/M2, which the full extent is currently unknown (Dubbelaar et al., 2018; Gil-Martinez et al., 2018; Batiuk et al., 2020). Considering the inherent complexity of transcriptional regulation, multi-dimensional PCA and correlational analysis was implemented to gain insight into how each of the

environmental exposures, singly or concurrently, influenced transcriptional profiles. Inhibition of canonical NF-κB in microglia in combination with exposure to rotenone showed same quadrant loadings with KO control animals in the groupings of pro-inflammatory microglia (*Csf1*, *Tnf*, *Il1β*, *C1qa*), mitophagy associated (*Pink1*, *Park2*, *Park7*, *Sqstm1*), neuronal associated (*Nr4a2*, *Snca*, *Mapt*, *Slc6a3*), and glial mediated inflammatory genes (*Il1α*, *Il6*, *C3*), indicating the involvement of these genes as potentially neuroprotective. Strikingly, the profile that did not respond similarly between WT dual and KO dual was that of the pro-inflammatory microglia, but arguably most importantly, lead to the same levels of neurodegeneration in the SNpc (**Fig. 26**, **Fig. 30**, **Supplemental Fig. 7-9**). Further investigation into the transcription profiles that were associated with disease revealed neurodegenerative outcome was associated with *Ccl5*, *Mapt*, *Snca*, *Tlr2*, and *Tlr4* expression. Fascinatingly, the transcriptional regulation of *Park7* was dependent on these genes in diseased state. *Snca*, *Mapt*, *Tlr2*, and *Tlr4* were inversely correlated in transcription with *Park7*, and *Ccl5* was positively correlated with *Park7* in groupings that were positive for neurodegeneration (WT rotenone, WT dual exposure, KO dual exposure; (**Fig. 26**, **Supplemental Fig. 10**). Pro-inflammatory astrocytic activation and upregulation of Tlr2 through CCR5/CCL5 induced NF-κB has previously been reported, where KO of CCR5 reduced Tlr2 transcription to basal levels (Kobayashi et al., 2019), supporting the observed increases in transcriptional correlation between *Ccl5* and *Tlr2* observed herein (**Supplemental Fig. 10**). *Postmortem* analysis of PD patient SN has also revealed increases in the amount of TLR2 and TLR4 expression, where TLR2 colocalizes with α-syn in Lewy bodies (Dzamko et al., 2017). Importantly, astrocytic TLR3 activation through molecular antagonism has been shown to induce *Tlr2* and *Tlr4* expression, along with inducing sustained inflammatory damage and increasing the vulnerability of DAn to oxidative stress (Jack et al., 2005; Kim et al., 2013). Furthermore, TLR3 is known to localize to

intra and extra-cellular membranes where is serves the function of recognizing dsRNA (viral) and initiating immunogenic responses. Recent research has shown upon mitochondrial distress, mt-RNAs can be exported through endosomal trafficking and successfully act as TLR3 ligands (Kim et al., 2020). These observations serve as critical links between the correlational regulation of pro-inflammatory astrocytes, TLRs, α-syn, mitochondrial dysfunction and oxidation, and the overall neurodegeneration observed with rotenone and dual hit environmental exposures.

Together, these results provide compelling evidence that microglial innate immunity modulated by the canonical NF-κB pathway is a key inducer in single environmental exposures that lead to PD pathology. However, these data also show remarkable shifts in gene transcription, gliosis, and neurodegeneration in multiple exposure instances that indicate astrocytic response as a driving factor in progressive disease. Previous results from our lab have shown that hGFAP-Cre::IKK2$^{fl/fl}$ mice challenged with highly neurotropic WEEV, known to induce PD-like pathology, were spared of extensive neuroinflammation and had reduction in the loss of DAn within the SNpc (Bantle et al., 2019; Bantle et al., 2021b). Although this model is considered a 'single hit' environmental exposure it does elicit more inflammation than chronic low-level exposures to chemicals; nonetheless, neuroprotection achieved through innate immune blockade in astrocytes demonstrates a future direction of investigation for dual hit environmental toxin models. It is also imperative to recognize the role that microglial 'priming' may contribute to overt disease in KO dual exposure animals. This could be possible through epigenetic modification from the initial exposure (Mn) which allow the microglial cells to respond more readily to astrocytic derived signaling factors or vis versa. Ultimately, the inherent complexity of PD pathology is highly dependent upon cellular responses driven by glial subtypes and the exposures encountered. These data provide novel findings that underscore the importance of identifying glial reactivity

between multiple chemical, biological, and toxin exposures allowing for better determination and targeted treatment modalities.

CHAPTER 5

CONCLUSIONS

PD remains the most prevalent movement disorder worldwide despite over 200 years of research examining the cause(s) and progression of the disease. The etiology of PD is largely unknown, but genetics, age, and environmental exposures may act individually or in concert to result in the complex pathological changes that underlie the complex neurological symptoms characterizing PD. To date, minimally invasive symptomatic treatment, which is only effective for short periods of time, does not address or curtail the pathological progression of PD. Difficulties in understanding underlying molecular causes of the pathology have occurred due to lack of a model that recapitulates neuroinflammation, α-syn misfolding and aggregation, and DAn neurodegeneration in the SNpc.

The data herein, demonstrates the successful optimization of a murine model of PD utilizing the environmental toxin, rotenone, that mirrors the gliosis, neuroinflammation, neurodegeneration and α-syn misfolding that is present in idiopathic PD. Chronological examination of disease progression revealed time, cell, and region dependent alterations. Pathological initiation was observed to begin with astrocytes and α-syn misfolding, which then activated the immune cell of the brain, the microglia. Cascades of glial-glial crosstalk and inflammatory mediators then led to a second activation stage of astrocytes and further α-syn misfolding. These events preceded neuronal loss of DAn, demonstrating glial cell activation and protein misfolding drive onset of reported symptomology.

Neuroinflammation and glial cell reactivity are consistently observed in PD patient brain tissue, along with increases in microglial cell populations. The co-occurrence of these underscore the importance that this cell type may have in the pathological progression of this disease. For the first time, we successfully adapted the rotenone environmental exposure model in a microglial cell-specific knockout of the innate immune signaling pathway and saw neuroprotection of DAn in the SNpc. These data provide evidence to suggest that chronic exposure to rotenone induces microglial NF-κB signaling, which functions as a main mediator in progressive PD pathology. Of long-standing debate in the field, α-syn misfolding and aggregation has been implicated as toxic, and once misfolded, converts native proteins of homologous sequence structure to adopt the misfolded state. Surprisingly, inhibition of innate immune signaling in microglia led to an over-accumulation of misfolded α-syn. Investigation into this over-accumulation revealed that NF-κB-mediated expression of p62 in microglial cells is critical for autophagy of misfolded α-syn and that loss of p62 expression in microglia-specific NF-κB KO mice significantly contributed to the reduction of autophagy and accumulation of misfolded protein in male animals. Controversially, the accumulation of misfolded α-syn did not lead to increased neurodegeneration. Examination of sex-based differences in autophagy responses revealed pathological characteristics that were unique to males and resulted in increased neurodegeneration and worse neurological outcomes, similar to those observed in idiopathic PD.

Another difficulty faced in PD research has been the ability to replicate multiple exposures that a patient may encounter over a lifetime. This becomes increasingly problematic when trying to incorporate the variables of age, lifestyle, accurate reporting of exposures, and the successive chronology of exposures. To begin to address this functional gap in knowledge, juvenile Mn exposure followed by exposure to rotenone in adulthood yielded reduction in the number of

microglial cells present within the SNpc, however the microglia that were present had a more reactive phenotype. Increased astrocytic reactivity was also observed in dual exposure animals conveying that glial-glial crosstalk does influence regional shifts in reactivity state. The experimentation performed with the dual hit exposure also showed that inhibition of microglial NF-κB was not neuroprotective, despite the protection that was observed with the single exposure of rotenone. This pivotal finding has not been demonstrated in *in vivo* environmental exposure models of PD prior to these studies and highlights the importance of exposure specific reactivity and the ability of microglial cells to adapt their immune responses over lifelong exposures. These studies have also shown that gene expression patterns related to astrocyte activation, α-syn, and oxidative stress contribute to the selective neurodegeneration of DAn in the SNpc.

The pathophysiology of neurodegenerative diseases is complex and the understanding, characterization, and integration of exposure type, age of individuals at the time of exposure, and multiple exposures in association with disease onset and progression has only just begun. The studies described herein provide substantial contributions to the field, detailing the regional, cellular, and sub-cellular components involved in response to the environmental toxicant rotenone. In addition, results gained from dual environmental exposure modeling utilizing Mn and rotenone revealed critical microglial and astrocytic mediated responses that are ultimately detrimental to DAn survival. Further efforts dedicated to understanding glial responses to environmental exposures, independently and in succession, will enhance the ability to produce target therapeutic strategies that ameliorate the pathological drivers behind disease progression and not merely address immediate symptomology.

REFERENCES

(1933). *Rotenone as an Insecticide.* Nature.

Alam, P., Bousset, L., Melki, R., and Otzen, D.E. (2019). alpha-synuclein oligomers and fibrils: a spectrum of species, a spectrum of toxicities. *J Neurochem* 150(5)**,** 522-534. doi: 10.1111/jnc.14808.

Alberts, B., Johnson, A., and Lewis, J. (2002). Molecular Biology of the Cell 4.

Alcalay, R.N., Mejia-Santana, H., Tang, M.X., Rakitin, B., Rosado, L., Ross, B., et al. (2010). Self-report of cognitive impairment and mini-mental state examination performance in PRKN, LRRK2, and GBA carriers with early onset Parkinson's disease. *J Clin Exp Neuropsychol* 32(7)**,** 775-779. doi: 10.1080/13803390903521018.

Alerte, T.N., Akinfolarin, A.A., Friedrich, E.E., Mader, S.A., Hong, C.S., and Perez, R.G. (2008). Alpha-synuclein aggregation alters tyrosine hydroxylase phosphorylation and immunoreactivity: lessons from viral transduction of knockout mice. *Neurosci Lett* 435(1)**,** 24-29. doi: 10.1016/j.neulet.2008.02.014.

Angot, E., Steiner, J.A., Lema Tome, C.M., Ekstrom, P., Mattsson, B., Bjorklund, A., et al. (2012). Alpha-synuclein cell-to-cell transfer and seeding in grafted dopaminergic neurons in vivo. *PLoS One* 7(6)**,** e39465. doi: 10.1371/journal.pone.0039465.

Antony, P.M., Diederich, N.J., Kruger, R., and Balling, R. (2013). The hallmarks of Parkinson's disease. *FEBS J* 280(23)**,** 5981-5993. doi: 10.1111/febs.12335.

Araque, A., Carmignoto, G., and Haydon, P.G. (2001). Dynamic signaling between astrocytes and neurons. *Annu Rev Physiol* 63**,** 795-813. doi: 10.1146/annurev.physiol.63.1.795.

Ariga, H., Takahashi-Niki, K., Kato, I., Maita, H., Niki, T., and Iguchi-Ariga, S.M. (2013). Neuroprotective function of DJ-1 in Parkinson's disease. *Oxid Med Cell Longev* 2013**,** 683920. doi: 10.1155/2013/683920.

Aschner, J.L., and Aschner, M. (2005). Nutritional aspects of manganese homeostasis. *Mol Aspects Med* 26(4-5)**,** 353-362. doi: 10.1016/j.mam.2005.07.003.

Aschner, M., and Aschner, J.L. (1991). Manganese neurotoxicity: cellular effects and blood-brain barrier transport. *Neurosci Biobehav Rev* 15(3)**,** 333-340. doi: 10.1016/s0149-7634(05)80026-0.

Aschner, M., Erikson, K.M., and Dorman, D.C. (2005). Manganese dosimetry: species differences and implications for neurotoxicity. *Crit Rev Toxicol* 35(1)**,** 1-32. doi: 10.1080/10408440590905920.

Aschner, M., Erikson, K.M., Herrero Hernandez, E., and Tjalkens, R. (2009). Manganese and its role in Parkinson's disease: from transport to neuropathology. *Neuromolecular Med* 11(4)**,** 252-266. doi: 10.1007/s12017-009-8083-0.

Aschner, M., Guilarte, T.R., Schneider, J.S., and Zheng, W. (2007). Manganese: recent advances in understanding its transport and neurotoxicity. *Toxicol Appl Pharmacol* 221(2)**,** 131-147. doi: 10.1016/j.taap.2007.03.001.

Askew, K., Li, K., Olmos-Alonso, A., Garcia-Moreno, F., Liang, Y., Richardson, P., et al. (2017). Coupled Proliferation and Apoptosis Maintain the Rapid Turnover of Microglia in the Adult Brain. *Cell Rep* 18(2)**,** 391-405. doi: 10.1016/j.celrep.2016.12.041.

Astiz, M., Acaz-Fonseca, E., and Garcia-Segura, L.M. (2014). Sex differences and effects of estrogenic compounds on the expression of inflammatory molecules by astrocytes exposed to the insecticide dimethoate. *Neurotox Res* 25(3)**,** 271-285. doi: 10.1007/s12640-013-9417-0.

Badanjak, K., Fixemer, S., Smajic, S., Skupin, A., and Grunewald, A. (2021). The Contribution of Microglia to Neuroinflammation in Parkinson's Disease. *Int J Mol Sci* 22(9). doi: 10.3390/ijms22094676.

Balachandran, R.C., Mukhopadhyay, S., McBride, D., Veevers, J., Harrison, F.E., Aschner, M., et al. (2020). Brain manganese and the balance between essential roles and neurotoxicity. *J Biol Chem* 295(19)**,** 6312-6329. doi: 10.1074/jbc.REV119.009453.

Ball, M.J. (2003). Unexplained sudden amnesia, postencephalitic Parkinson disease, subacute sclerosing panencephalitis, and Alzheimer disease: does viral synergy produce neurofibrillary tangles? *Arch Neurol* 60(4)**,** 641-642. doi: 10.1001/archneur.60.4.641.

Ball, N., Teo, W.P., Chandra, S., and Chapman, J. (2019). Parkinson's Disease and the Environment. *Front Neurol* 10**,** 218. doi: 10.3389/fneur.2019.00218.

Bang, Y., Lim, J., and Choi, H.J. (2021). Recent advances in the pathology of prodromal non-motor symptoms olfactory deficit and depression in Parkinson's disease: clues to early diagnosis and effective treatment. *Arch Pharm Res* 44(6)**,** 588-604. doi: 10.1007/s12272-021-01337-3.

Bantle, C.M., French, C.T., Cummings, J.E., Sadasivan, S., Tran, K., Slayden, R.A., et al. (2021a). Manganese exposure in juvenile C57BL/6 mice increases glial inflammatory

responses in the substantia nigra following infection with H1N1 influenza virus. *PLoS One* 16(1)**,** e0245171. doi: 10.1371/journal.pone.0245171.

Bantle, C.M., Phillips, A.T., Smeyne, R.J., Rocha, S.M., Olson, K.E., and Tjalkens, R.B. (2019). Infection with mosquito-borne alphavirus induces selective loss of dopaminergic neurons, neuroinflammation and widespread protein aggregation. *NPJ Parkinsons Dis* 5**,** 20. doi: 10.1038/s41531-019-0090-8.

Bantle, C.M., Rocha, S.M., French, C.T., Phillips, A.T., Tran, K., Olson, K.E., et al. (2021b). Astrocyte inflammatory signaling mediates alpha-synuclein aggregation and dopaminergic neuronal loss following viral encephalitis. *Exp Neurol* 346**,** 113845. doi: 10.1016/j.expneurol.2021.113845.

Barazzuol, L., Giamogante, F., Brini, M., and Cali, T. (2020). PINK1/Parkin Mediated Mitophagy, Ca(2+) Signalling, and ER-Mitochondria Contacts in Parkinson's Disease. *Int J Mol Sci* 21(5). doi: 10.3390/ijms21051772.

Batiuk, M.Y., Martirosyan, A., Wahis, J., de Vin, F., Marneffe, C., Kusserow, C., et al. (2020). Identification of region-specific astrocyte subtypes at single cell resolution. *Nat Commun* 11(1)**,** 1220. doi: 10.1038/s41467-019-14198-8.

Baxter, P.S., Dando, O., Emelianova, K., He, X., McKay, S., Hardingham, G.E., et al. (2021). Microglial identity and inflammatory responses are controlled by the combined effects of neurons and astrocytes. *Cell Rep* 34(12)**,** 108882. doi: 10.1016/j.celrep.2021.108882.

Bellucci, A., Bubacco, L., Longhena, F., Parrella, E., Faustini, G., Porrini, V., et al. (2020). Nuclear Factor-kappaB Dysregulation and alpha-Synuclein Pathology: Critical Interplay in the Pathogenesis of Parkinson's Disease. *Front Aging Neurosci* 12**,** 68. doi: 10.3389/fnagi.2020.00068.

Belovicova, K., Bogi, E., Csatlosova, K., and Dubovicky, M. (2017). Animal tests for anxiety-like and depression-like behavior in rats. *Interdiscip Toxicol* 10(1)**,** 40-43. doi: 10.1515/intox-2017-0006.

Bernal-Conde, L.D., Ramos-Acevedo, R., Reyes-Hernandez, M.A., Balbuena-Olvera, A.J., Morales-Moreno, I.D., Arguero-Sanchez, R., et al. (2019). Alpha-Synuclein Physiology and Pathology: A Perspective on Cellular Structures and Organelles. *Front Neurosci* 13**,** 1399. doi: 10.3389/fnins.2019.01399.

Betarbet, R., Sherer, T.B., MacKenzie, G., Garcia-Osuna, M., Panov, A.V., and Greenamyre, J.T. (2000). Chronic systemic pesticide exposure reproduces features of Parkinson's disease. *Nat Neurosci* 3(12)**,** 1301-1306. doi: 10.1038/81834.

Billingsley, K.J., Bandres-Ciga, S., Saez-Atienzar, S., and Singleton, A.B. (2018). Genetic risk factors in Parkinson's disease. *Cell Tissue Res* 373(1)**,** 9-20. doi: 10.1007/s00441-018-2817-y.

Blauwendraat, C., Nalls, M.A., and Singleton, A.B. (2020). The genetic architecture of Parkinson's disease. *Lancet Neurol* 19(2)**,** 170-178. doi: 10.1016/S1474-4422(19)30287-X.

Block, M.L., and Hong, J.S. (2005). Microglia and inflammation-mediated neurodegeneration: multiple triggers with a common mechanism. *Prog Neurobiol* 76(2)**,** 77-98. doi: 10.1016/j.pneurobio.2005.06.004.

Block, M.L., Zecca, L., and Hong, J.S. (2007). Microglia-mediated neurotoxicity: uncovering the molecular mechanisms. *Nat Rev Neurosci* 8(1)**,** 57-69. doi: 10.1038/nrn2038.

Blum-Degen, D., Muller, T., Kuhn, W., Gerlach, M., Przuntek, H., and Riederer, P. (1995). Interleukin-1 beta and interleukin-6 are elevated in the cerebrospinal fluid of Alzheimer's and de novo Parkinson's disease patients. *Neurosci Lett* 202(1-2)**,** 17-20. doi: 10.1016/0304-3940(95)12192-7.

Bousset, L., Pieri, L., Ruiz-Arlandis, G., Gath, J., Jensen, P.H., Habenstein, B., et al. (2013). Structural and functional characterization of two alpha-synuclein strains. *Nat Commun* 4**,** 2575. doi: 10.1038/ncomms3575.

Bowman, A.B., Kwakye, G.F., Herrero Hernandez, E., and Aschner, M. (2011). Role of manganese in neurodegenerative diseases. *J Trace Elem Med Biol* 25(4)**,** 191-203. doi: 10.1016/j.jtemb.2011.08.144.

Braak, H., Ghebremedhin, E., Rub, U., Bratzke, H., and Del Tredici, K. (2004). Stages in the development of Parkinson's disease-related pathology. *Cell Tissue Res* 318(1)**,** 121-134. doi: 10.1007/s00441-004-0956-9.

Braak, H., Sastre, M., and Del Tredici, K. (2007). Development of alpha-synuclein immunoreactive astrocytes in the forebrain parallels stages of intraneuronal pathology in sporadic Parkinson's disease. *Acta Neuropathol* 114(3)**,** 231-241. doi: 10.1007/s00401-007-0244-3.

Breydo, L., Wu, J.W., and Uversky, V.N. (2012). Alpha-synuclein misfolding and Parkinson's disease. *Biochim Biophys Acta* 1822(2)**,** 261-285. doi: 10.1016/j.bbadis.2011.10.002.

Brochard, V., Combadiere, B., Prigent, A., Laouar, Y., Perrin, A., Beray-Berthat, V., et al. (2009). Infiltration of CD4+ lymphocytes into the brain contributes to neurodegeneration in a mouse model of Parkinson disease. *J Clin Invest* 119(1)**,** 182-192. doi: 10.1172/JCI36470.

Brown, T.P., Rumsby, P.C., Capleton, A.C., Rushton, L., and Levy, L.S. (2006). Pesticides and Parkinson's disease--is there a link? *Environ Health Perspect* 114(2)**,** 156-164. doi: 10.1289/ehp.8095.

Burre, J., Sharma, M., and Sudhof, T.C. (2015). Definition of a molecular pathway mediating alpha-synuclein neurotoxicity. *J Neurosci* 35(13)**,** 5221-5232. doi: 10.1523/JNEUROSCI.4650-14.2015.

Burre, J., Sharma, M., and Sudhof, T.C. (2018). Cell Biology and Pathophysiology of alpha-Synuclein. *Cold Spring Harb Perspect Med* 8(3). doi: 10.1101/cshperspect.a024091.

Bushong, E.A., Martone, M.E., Jones, Y.Z., and Ellisman, M.H. (2002). Protoplasmic astrocytes in CA1 stratum radiatum occupy separate anatomical domains. *J Neurosci* 22(1)**,** 183-192.

Caceres, A., Jene, A., Esko, T., Perez-Jurado, L.A., and Gonzalez, J.R. (2020). Extreme downregulation of chromosome Y and Alzheimer's disease in men. *Neurobiol Aging* 90**,** 150 e151-150 e154. doi: 10.1016/j.neurobiolaging.2020.02.003.

Campdelacreu, J. (2014). Parkinson disease and Alzheimer disease: environmental risk factors. *Neurologia* 29(9)**,** 541-549. doi: 10.1016/j.nrl.2012.04.001.

Cannon, J.R., Tapias, V., Na, H.M., Honick, A.S., Drolet, R.E., and Greenamyre, J.T. (2009). A highly reproducible rotenone model of Parkinson's disease. *Neurobiol Dis* 34(2)**,** 279-290. doi: 10.1016/j.nbd.2009.01.016.

Castellani, R.J., and Perry, G. (2012). Pathogenesis and disease-modifying therapy in Alzheimer's disease: the flat line of progress. *Arch Med Res* 43(8)**,** 694-698. doi: 10.1016/j.arcmed.2012.09.009.

Castillo, S., Munoz, P., Behrens, M.I., Diaz-Grez, F., and Segura-Aguilar, J. (2017). On the Role of Mining Exposure in Epigenetic Effects in Parkinson's Disease. *Neurotox Res* 32(2)**,** 172-174. doi: 10.1007/s12640-017-9736-7.

Cerri, S., Mus, L., and Blandini, F. (2019). Parkinson's Disease in Women and Men: What's the Difference? *J Parkinsons Dis* 9(3)**,** 501-515. doi: 10.3233/JPD-191683.

Chai, H., Diaz-Castro, B., Shigetomi, E., Monte, E., Octeau, J.C., Yu, X., et al. (2017). Neural Circuit-Specialized Astrocytes: Transcriptomic, Proteomic, Morphological, and Functional Evidence. *Neuron* 95(3)**,** 531-549 e539. doi: 10.1016/j.neuron.2017.06.029.

Chang, C.W., Yang, S.Y., Yang, C.C., Chang, C.W., and Wu, Y.R. (2019). Plasma and Serum Alpha-Synuclein as a Biomarker of Diagnosis in Patients With Parkinson's Disease. *Front Neurol* 10**,** 1388. doi: 10.3389/fneur.2019.01388.

Chen, H., and Ritz, B. (2018). The Search for Environmental Causes of Parkinson's Disease: Moving Forward. *J Parkinsons Dis* 8(s1)**,** S9-S17. doi: 10.3233/JPD-181493.

Chen, L., Periquet, M., Wang, X., Negro, A., McLean, P.J., Hyman, B.T., et al. (2009). Tyrosine and serine phosphorylation of alpha-synuclein have opposing effects on neurotoxicity and soluble oligomer formation. *J Clin Invest* 119(11)**,** 3257-3265. doi: 10.1172/JCI39088.

Cheng, H.C., Ulane, C.M., and Burke, R.E. (2010). Clinical progression in Parkinson disease and the neurobiology of axons. *Ann Neurol* 67(6)**,** 715-725. doi: 10.1002/ana.21995.

Choi, I., Zhang, Y., Seegobin, S.P., Pruvost, M., Wang, Q., Purtell, K., et al. (2020). Microglia clear neuron-released alpha-synuclein via selective autophagy and prevent neurodegeneration. *Nat Commun* 11(1)**,** 1386. doi: 10.1038/s41467-020-15119-w.

Chowen, J.A., and Garcia-Segura, L.M. (2021). Role of glial cells in the generation of sex differences in neurodegenerative diseases and brain aging. *Mech Ageing Dev* 196**,** 111473. doi: 10.1016/j.mad.2021.111473.

Clinton, L.K., Blurton-Jones, M., Myczek, K., Trojanowski, J.Q., and LaFerla, F.M. (2010). Synergistic Interactions between Abeta, tau, and alpha-synuclein: acceleration of neuropathology and cognitive decline. *J Neurosci* 30(21)**,** 7281-7289. doi: 10.1523/JNEUROSCI.0490-10.2010.

Cohen, S.I., Vendruscolo, M., Dobson, C.M., and Knowles, T.P. (2012). From macroscopic measurements to microscopic mechanisms of protein aggregation. *J Mol Biol* 421(2-3)**,** 160-171. doi: 10.1016/j.jmb.2012.02.031.

Collaborators, G.B.D.N. (2019). Global, regional, and national burden of neurological disorders, 1990-2016: a systematic analysis for the Global Burden of Disease Study 2016. *Lancet Neurol* 18(5)**,** 459-480. doi: 10.1016/S1474-4422(18)30499-X.

Conway, K.A., Harper, J.D., and Lansbury, P.T. (1998). Accelerated in vitro fibril formation by a mutant alpha-synuclein linked to early-onset Parkinson disease. *Nat Med* 4(11)**,** 1318-1320. doi: 10.1038/3311.

Crampton, S.J., and O'Keeffe, G.W. (2013). NF-kappaB: emerging roles in hippocampal development and function. *Int J Biochem Cell Biol* 45(8)**,** 1821-1824. doi: 10.1016/j.biocel.2013.05.037.

Csordas, G., Weaver, D., and Hajnoczky, G. (2018). Endoplasmic Reticulum-Mitochondrial Contactology: Structure and Signaling Functions. *Trends Cell Biol* 28(7)**,** 523-540. doi: 10.1016/j.tcb.2018.02.009.

Cunha, B.A. (2004). Influenza: historical aspects of epidemics and pandemics. *Infect Dis Clin North Am* 18(1)**,** 141-155. doi: 10.1016/S0891-5520(03)00095-3.

Cunningham, C. (2013). Microglia and neurodegeneration: the role of systemic inflammation. *Glia* 61(1)**,** 71-90. doi: 10.1002/glia.22350.

Cunningham, C., Wilcockson, D.C., Campion, S., Lunnon, K., and Perry, V.H. (2005). Central and systemic endotoxin challenges exacerbate the local inflammatory response and increase neuronal death during chronic neurodegeneration. *J Neurosci* 25(40)**,** 9275-9284. doi: 10.1523/JNEUROSCI.2614-05.2005.

Damale, P.U., Chong, E.K.P., Hammond, S.L., and Tjalkens, R.B. (2021). A Low-Cost, Autonomous Gait Detection and Estimation System for Analyzing Gait Impairments in Mice. *J Healthc Eng* 2021**,** 9937904. doi: 10.1155/2021/9937904.

Damier, P., Hirsch, E.C., Zhang, P., Agid, Y., and Javoy-Agid, F. (1993). Glutathione peroxidase, glial cells and Parkinson's disease. *Neuroscience* 52(1)**,** 1-6. doi: 10.1016/0306-4522(93)90175-f.

Das, S., Li, Z., Noori, A., Hyman, B.T., and Serrano-Pozo, A. (2020). Meta-analysis of mouse transcriptomic studies supports a context-dependent astrocyte reaction in acute CNS injury versus neurodegeneration. *J Neuroinflammation* 17(1)**,** 227. doi: 10.1186/s12974-020-01898-y.

Davidsson, L., Cederblad, A., Lonnerdal, B., and Sandstrom, B. (1991). The effect of individual dietary components on manganese absorption in humans. *Am J Clin Nutr* 54(6)**,** 1065-1070. doi: 10.1093/ajcn/54.6.1065.

Davis, E.J., Broestl, L., Abdulai-Saiku, S., Worden, K., Bonham, L.W., Minones-Moyano, E., et al. (2020). A second X chromosome contributes to resilience in a mouse model of Alzheimer's disease. *Sci Transl Med* 12(558). doi: 10.1126/scitranslmed.aaz5677.

De Miranda, B.R., Rocha, E.M., Bai, Q., El Ayadi, A., Hinkle, D., Burton, E.A., et al. (2018). Astrocyte-specific DJ-1 overexpression protects against rotenone-induced neurotoxicity in a rat model of Parkinson's disease. *Neurobiol Dis* 115**,** 101-114. doi: 10.1016/j.nbd.2018.04.008.

Deng, H., Wang, P., and Jankovic, J. (2018). The genetics of Parkinson disease. *Ageing Res Rev* 42**,** 72-85. doi: 10.1016/j.arr.2017.12.007.

Dickson, D.W. (2018). Neuropathology of Parkinson disease. *Parkinsonism Relat Disord* 46 Suppl 1**,** S30-S33. doi: 10.1016/j.parkreldis.2017.07.033.

Dobson, A.W., Erikson, K.M., and Aschner, M. (2004). Manganese neurotoxicity. *Ann N Y Acad Sci* 1012**,** 115-128. doi: 10.1196/annals.1306.009.

Domingues, A.V., Pereira, I.M., Vilaca-Faria, H., Salgado, A.J., Rodrigues, A.J., and Teixeira, F.G. (2020). Glial cells in Parkinson s disease: protective or deleterious? *Cell Mol Life Sci* 77(24)**,** 5171-5188. doi: 10.1007/s00018-020-03584-x.

Doorn, K.J., Moors, T., Drukarch, B., van de Berg, W., Lucassen, P.J., and van Dam, A.M. (2014). Microglial phenotypes and toll-like receptor 2 in the substantia nigra and hippocampus of incidental Lewy body disease cases and Parkinson's disease patients. *Acta Neuropathol Commun* 2**,** 90. doi: 10.1186/s40478-014-0090-1.

Dubbelaar, M.L., Kracht, L., Eggen, B.J.L., and Boddeke, E. (2018). The Kaleidoscope of Microglial Phenotypes. *Front Immunol* 9**,** 1753. doi: 10.3389/fimmu.2018.01753.

Dung, V.M., and Thao, D.T.P. (2018). Parkinson's Disease Model. *Adv Exp Med Biol* 1076**,** 41-61. doi: 10.1007/978-981-13-0529-0_4.

Dutta, D., Jana, M., Majumder, M., Mondal, S., Roy, A., and Pahan, K. (2021). Selective targeting of the TLR2/MyD88/NF-kappaB pathway reduces alpha-synuclein spreading in vitro and in vivo. *Nat Commun* 12(1)**,** 5382. doi: 10.1038/s41467-021-25767-1.

Duty, S., and Jenner, P. (2011). Animal models of Parkinson's disease: a source of novel treatments and clues to the cause of the disease. *Br J Pharmacol* 164(4)**,** 1357-1391. doi: 10.1111/j.1476-5381.2011.01426.x.

Dzamko, N., Gysbers, A., Perera, G., Bahar, A., Shankar, A., Gao, J., et al. (2017). Toll-like receptor 2 is increased in neurons in Parkinson's disease brain and may contribute to alpha-synuclein pathology. *Acta Neuropathol* 133(2)**,** 303-319. doi: 10.1007/s00401-016-1648-8.

El-Agnaf, O.M., Jakes, R., Curran, M.D., and Wallace, A. (1998). Effects of the mutations Ala30 to Pro and Ala53 to Thr on the physical and morphological properties of alpha-synuclein protein implicated in Parkinson's disease. *FEBS Lett* 440(1-2)**,** 67-70. doi: 10.1016/s0014-5793(98)01419-7.

El-Agnaf, O.M., Salem, S.A., Paleologou, K.E., Cooper, L.J., Fullwood, N.J., Gibson, M.J., et al. (2003). Alpha-synuclein implicated in Parkinson's disease is present in extracellular biological fluids, including human plasma. *FASEB J* 17(13)**,** 1945-1947. doi: 10.1096/fj.03-0098fje.

Elbaz, A., Clavel, J., Rathouz, P.J., Moisan, F., Galanaud, J.P., Delemotte, B., et al. (2009). Professional exposure to pesticides and Parkinson disease. *Ann Neurol* 66(4)**,** 494-504. doi: 10.1002/ana.21717.

Eliezer, D., Kutluay, E., Bussell, R., Jr., and Browne, G. (2001). Conformational properties of alpha-synuclein in its free and lipid-associated states. *J Mol Biol* 307(4)**,** 1061-1073. doi: 10.1006/jmbi.2001.4538.

Eng, L.F., Ghirnikar, R.S., and Lee, Y.L. (2000). Glial fibrillary acidic protein: GFAP-thirty-one years (1969-2000). *Neurochem Res* 25(9-10)**,** 1439-1451. doi: 10.1023/a:1007677003387.

Eng, L.F., Vanderhaeghen, J.J., Bignami, A., and Gerstl, B. (1971). An acidic protein isolated from fibrous astrocytes. *Brain Res* 28(2)**,** 351-354. doi: 10.1016/0006-8993(71)90668-8.

EPA., U. (2007). Re-registration eligibility decision for rotenone. *US EPA Case #0255*.

Erikson, K.M., Syversen, T., Aschner, J.L., and Aschner, M. (2005). Interactions between excessive manganese exposures and dietary iron-deficiency in neurodegeneration. *Environ Toxicol Pharmacol* 19(3)**,** 415-421. doi: 10.1016/j.etap.2004.12.053.

Erikson, K.M., Thompson, K., Aschner, J., and Aschner, M. (2007). Manganese neurotoxicity: a focus on the neonate. *Pharmacol Ther* 113(2)**,** 369-377. doi: 10.1016/j.pharmthera.2006.09.002.

Escartin, C., Galea, E., Lakatos, A., O'Callaghan, J.P., Petzold, G.C., Serrano-Pozo, A., et al. (2021). Reactive astrocyte nomenclature, definitions, and future directions. *Nat Neurosci* 24(3)**,** 312-325. doi: 10.1038/s41593-020-00783-4.

Espay, A.J., LeWitt, P.A., and Kaufmann, H. (2014). Norepinephrine deficiency in Parkinson's disease: the case for noradrenergic enhancement. *Mov Disord* 29(14)**,** 1710-1719. doi: 10.1002/mds.26048.

Fagre, A., Lewis, J., Eckley, M., Zhan, S., Rocha, S.M., Sexton, N.R., et al. (2021). SARS-CoV-2 infection, neuropathogenesis and transmission among deer mice: Implications for spillback to New World rodents. *PLoS Pathog* 17(5)**,** e1009585. doi: 10.1371/journal.ppat.1009585.

Fan, Y.Y., and Huo, J. (2021). A1/A2 astrocytes in central nervous system injuries and diseases: Angels or devils? *Neurochem Int* 148**,** 105080. doi: 10.1016/j.neuint.2021.105080.

Fasano, A., Visanji, N.P., Liu, L.W., Lang, A.E., and Pfeiffer, R.F. (2015). Gastrointestinal dysfunction in Parkinson's disease. *Lancet Neurol* 14(6)**,** 625-639. doi: 10.1016/S1474-4422(15)00007-1.

Fernandez, D., Geisse, A., Bernales, J.I., Lira, A., and Osorio, F. (2021). The Unfolded Protein Response in Immune Cells as an Emerging Regulator of Neuroinflammation. *Front Aging Neurosci* 13**,** 682633. doi: 10.3389/fnagi.2021.682633.

Fernandez-Arjona, M.D.M., Grondona, J.M., Fernandez-Llebrez, P., and Lopez-Avalos, M.D. (2019). Microglial Morphometric Parameters Correlate With the Expression Level of IL-1beta, and Allow Identifying Different Activated Morphotypes. *Front Cell Neurosci* 13**,** 472. doi: 10.3389/fncel.2019.00472.

Ferreira, S.A., and Romero-Ramos, M. (2018). Microglia Response During Parkinson's Disease: Alpha-Synuclein Intervention. *Front Cell Neurosci* 12**,** 247. doi: 10.3389/fncel.2018.00247.

Fiebich, B.L., Batista, C.R.A., Saliba, S.W., Yousif, N.M., and de Oliveira, A.C.P. (2018). Role of Microglia TLRs in Neurodegeneration. *Front Cell Neurosci* 12**,** 329. doi: 10.3389/fncel.2018.00329.

Fontana, B.D., Mezzomo, N.J., Kalueff, A.V., and Rosemberg, D.B. (2018). The developing utility of zebrafish models of neurological and neuropsychiatric disorders: A critical review. *Exp Neurol* 299(Pt A)**,** 157-171. doi: 10.1016/j.expneurol.2017.10.004.

Franco-Bocanegra, D.K., McAuley, C., Nicoll, J.A.R., and Boche, D. (2019). Molecular Mechanisms of Microglial Motility: Changes in Ageing and Alzheimer's Disease. *Cells* 8(6). doi: 10.3390/cells8060639.

Frost, B., and Diamond, M.I. (2010). Prion-like mechanisms in neurodegenerative diseases. *Nat Rev Neurosci* 11(3)**,** 155-159. doi: 10.1038/nrn2786.

Fuger, P., Hefendehl, J.K., Veeraraghavalu, K., Wendeln, A.C., Schlosser, C., Obermuller, U., et al. (2017). Microglia turnover with aging and in an Alzheimer's model via long-term in vivo single-cell imaging. *Nat Neurosci* 20(10)**,** 1371-1376. doi: 10.1038/nn.4631.

Fujiwara, H., Hasegawa, M., Dohmae, N., Kawashima, A., Masliah, E., Goldberg, M.S., et al. (2002). alpha-Synuclein is phosphorylated in synucleinopathy lesions. *Nat Cell Biol* 4(2)**,** 160-164. doi: 10.1038/ncb748.

Fukami, J.I., Shishido, T., Fukunaga, K., and Casida, J.E. (1969). Oxidative Metabolism of Rotenone in Mammals, Fish, and Insects and Its Relation to Selective Toxicity.

Fulle, L., Offermann, N., Hansen, J.N., Breithausen, B., Erazo, A.B., Schanz, O., et al. (2018). CCL17 exerts a neuroimmune modulatory function and is expressed in hippocampal neurons. *Glia* 66(10)**,** 2246-2261. doi: 10.1002/glia.23507.

Fuzzati-Armentero, M.T., Cerri, S., and Blandini, F. (2019). Peripheral-Central Neuroimmune Crosstalk in Parkinson's Disease: What Do Patients and Animal Models Tell Us? *Front Neurol* 10**,** 232. doi: 10.3389/fneur.2019.00232.

Gallagher, D.A., and Schrag, A. (2012). Psychosis, apathy, depression and anxiety in Parkinson's disease. *Neurobiol Dis* 46(3)**,** 581-589. doi: 10.1016/j.nbd.2011.12.041.

Galvin, J.E., Lee, V.M., and Trojanowski, J.Q. (2001). Synucleinopathies: clinical and pathological implications. *Arch Neurol* 58(2)**,** 186-190. doi: 10.1001/archneur.58.2.186.

Gao, L., Tang, H., Nie, K., Wang, L., Zhao, J., Gan, R., et al. (2015). Cerebrospinal fluid alpha-synuclein as a biomarker for Parkinson's disease diagnosis: a systematic review and meta-analysis. *Int J Neurosci* 125(9)**,** 645-654. doi: 10.3109/00207454.2014.961454.

Garcia-Garcia, C.R., Parron, T., Requena, M., Alarcon, R., Tsatsakis, A.M., and Hernandez, A.F. (2016). Occupational pesticide exposure and adverse health effects at the clinical, hematological and biochemical level. *Life Sci* 145**,** 274-283. doi: 10.1016/j.lfs.2015.10.013.

Gavin, C.E., Gunter, K.K., and Gunter, T.E. (1990). Manganese and calcium efflux kinetics in brain mitochondria. Relevance to manganese toxicity. *Biochem J* 266(2)**,** 329-334. doi: 10.1042/bj2660329.

Gavin, C.E., Gunter, K.K., and Gunter, T.E. (1999). Manganese and calcium transport in mitochondria: implications for manganese toxicity. *Neurotoxicology* 20(2-3)**,** 445-453.

Ge, P., Dawson, V.L., and Dawson, T.M. (2020). PINK1 and Parkin mitochondrial quality control: a source of regional vulnerability in Parkinson's disease. *Mol Neurodegener* 15(1)**,** 20. doi: 10.1186/s13024-020-00367-7.

Giasson, B.I., and Lee, V.M. (2000). A new link between pesticides and Parkinson's disease. *Nat Neurosci* 3(12)**,** 1227-1228. doi: 10.1038/81737.

Gibb, W.R., and Lees, A.J. (1988). The relevance of the Lewy body to the pathogenesis of idiopathic Parkinson's disease. *J Neurol Neurosurg Psychiatry* 51(6)**,** 745-752. doi: 10.1136/jnnp.51.6.745.

Gil-Martinez, A.L., Cuenca, L., Sanchez, C., Estrada, C., Fernandez-Villalba, E., and Herrero, M.T. (2018). Effect of NAC treatment and physical activity on neuroinflammation in subchronic Parkinsonism; is physical activity essential? *J Neuroinflammation* 15(1)**,** 328. doi: 10.1186/s12974-018-1357-4.

Ginhoux, F., and Prinz, M. (2015). Origin of microglia: current concepts and past controversies. *Cold Spring Harb Perspect Biol* 7(8)**,** a020537. doi: 10.1101/cshperspect.a020537.

Giovannoni, F., and Quintana, F.J. (2020). The Role of Astrocytes in CNS Inflammation. *Trends Immunol* 41(9)**,** 805-819. doi: 10.1016/j.it.2020.07.007.

Glass, C.K., Saijo, K., Winner, B., Marchetto, M.C., and Gage, F.H. (2010). Mechanisms underlying inflammation in neurodegeneration. *Cell* 140(6)**,** 918-934. doi: 10.1016/j.cell.2010.02.016.

Goedert, M. (2001). Alpha-synuclein and neurodegenerative diseases. *Nat Rev Neurosci* 2(7)**,** 492-501. doi: 10.1038/35081564.

Goedert, M. (2015). NEURODEGENERATION. Alzheimer's and Parkinson's diseases: The prion concept in relation to assembled Abeta, tau, and alpha-synuclein. *Science* 349(6248)**,** 1255555. doi: 10.1126/science.1255555.

Goes, A.T.R., Jesse, C.R., Antunes, M.S., Lobo Ladd, F.V., Lobo Ladd, A.A.B., Luchese, C., et al. (2018). Protective role of chrysin on 6-hydroxydopamine-induced neurodegeneration a mouse model of Parkinson's disease: Involvement of neuroinflammation and neurotrophins. *Chem Biol Interact* 279**,** 111-120. doi: 10.1016/j.cbi.2017.10.019.

Goldman, S.M., Quinlan, P.J., Ross, G.W., Marras, C., Meng, C., Bhudhikanok, G.S., et al. (2012). Solvent exposures and Parkinson disease risk in twins. *Ann Neurol* 71(6)**,** 776-784. doi: 10.1002/ana.22629.

Gomez-Benito, M., Granado, N., Garcia-Sanz, P., Michel, A., Dumoulin, M., and Moratalla, R. (2020). Modeling Parkinson's Disease With the Alpha-Synuclein Protein. *Front Pharmacol* 11**,** 356. doi: 10.3389/fphar.2020.00356.

Gonzalez-Scarano, F., and Baltuch, G. (1999). Microglia as mediators of inflammatory and degenerative diseases. *Annu Rev Neurosci* 22**,** 219-240. doi: 10.1146/annurev.neuro.22.1.219.

Gopal Krishna Patro, S., and Kumar Sahu, K. (2015). Noramlization: A Preporcessing Stage

Gorbatyuk, O.S., Li, S., Sullivan, L.F., Chen, W., Kondrikova, G., Manfredsson, F.P., et al. (2008). The phosphorylation state of Ser-129 in human alpha-synuclein determines neurodegeneration in a rat model of Parkinson disease. *Proc Natl Acad Sci U S A* 105(2)**,** 763-768. doi: 10.1073/pnas.0711053105.

Gorell, J.M., Johnson, C.C., Rybicki, B.A., Peterson, E.L., Kortsha, G.X., Brown, G.G., et al. (1999). Occupational exposure to manganese, copper, lead, iron, mercury and zinc and the risk of Parkinson's disease. *Neurotoxicology* 20(2-3)**,** 239-247.

Gosavi, N., Lee, H.J., Lee, J.S., Patel, S., and Lee, S.J. (2002). Golgi fragmentation occurs in the cells with prefibrillar alpha-synuclein aggregates and precedes the formation of fibrillar inclusion. *J Biol Chem* 277(50)**,** 48984-48992. doi: 10.1074/jbc.M208194200.

Grayson, M. (2016). Parkinson's disease. *Nature* 538(7626)**,** S1. doi: 10.1038/538S1a.

Gu, X.L., Long, C.X., Sun, L., Xie, C., Lin, X., and Cai, H. (2010). Astrocytic expression of Parkinson's disease-related A53T alpha-synuclein causes neurodegeneration in mice. *Mol Brain* 3**,** 12. doi: 10.1186/1756-6606-3-12.

Guenther, H. (2011). "Rotenone review advisory committee final report and recommendations to the Arizona game and fish department ", (ed.) U.S.D.o. Agriculture.).

Gunnarsson, L.G., and Bodin, L. (2017). Parkinson's disease and occupational exposures: a systematic literature review and meta-analyses. *Scand J Work Environ Health* 43(3)**,** 197-209. doi: 10.5271/sjweh.3641.

Guo, J.L., Covell, D.J., Daniels, J.P., Iba, M., Stieber, A., Zhang, B., et al. (2013). Distinct alpha-synuclein strains differentially promote tau inclusions in neurons. *Cell* 154(1)**,** 103-117. doi: 10.1016/j.cell.2013.05.057.

Guo, Z., Zhang, Z., Wang, Q., Zhang, J., Wang, L., Zhang, Q., et al. (2018). Manganese chloride induces histone acetylation changes in neuronal cells: Its role in manganese-induced damage. *Neurotoxicology* 65**,** 255-263. doi: 10.1016/j.neuro.2017.11.003.

Gupta, R.C. (2012). *Veterinary Toxicology.* Elsevier

Guttenplan, K.A., Stafford, B.K., El-Danaf, R.N., Adler, D.I., Munch, A.E., Weigel, M.K., et al. (2020). Neurotoxic Reactive Astrocytes Drive Neuronal Death after Retinal Injury. *Cell Rep* 31(12)**,** 107776. doi: 10.1016/j.celrep.2020.107776.

Haley, M.J., Brough, D., Quintin, J., and Allan, S.M. (2019). Microglial Priming as Trained Immunity in the Brain. *Neuroscience* 405**,** 47-54. doi: 10.1016/j.neuroscience.2017.12.039.

Halliday, G., Lees, A., and Stern, M. (2011). Milestones in Parkinson's disease--clinical and pathologic features. *Mov Disord* 26(6)**,** 1015-1021. doi: 10.1002/mds.23669.

Hammond, S.L., Bantle, C.M., Popichak, K.A., Wright, K.A., Thompson, D., Forero, C., et al. (2020). NF-kappaB Signaling in Astrocytes Modulates Brain Inflammation and Neuronal Injury Following Sequential Exposure to Manganese and MPTP During Development and Aging. *Toxicol Sci* 177(2)**,** 506-520. doi: 10.1093/toxsci/kfaa115.

Hammond, S.L., Popichak, K.A., Li, X., Hunt, L.G., Richman, E.H., Damale, P.U., et al. (2018). The Nurr1 Ligand,1,1-bis(3'-Indolyl)-1-(p-Chlorophenyl)Methane, Modulates Glial Reactivity and Is Neuroprotective in MPTP-Induced Parkinsonism. *J Pharmacol Exp Ther* 365(3)**,** 636-651. doi: 10.1124/jpet.117.246389.

Hara, S., Arawaka, S., Sato, H., Machiya, Y., Cui, C., Sasaki, A., et al. (2013). Serine 129 phosphorylation of membrane-associated alpha-synuclein modulates dopamine transporter function in a G protein-coupled receptor kinase-dependent manner. *Mol Biol Cell* 24(11)**,** 1649-1660, S1641-1643. doi: 10.1091/mbc.E12-12-0903.

Hardenberg, M.C., Sinnige, T., Casford, S., Dada, S.T., Poudel, C., Robinson, E.A., et al. (2021). Observation of an alpha-synuclein liquid droplet state and its maturation into Lewy body-like assemblies. *J Mol Cell Biol* 13(4)**,** 282-294. doi: 10.1093/jmcb/mjaa075.

Harischandra, D.S., Ghaisas, S., Zenitsky, G., Jin, H., Kanthasamy, A., Anantharam, V., et al. (2019). Manganese-Induced Neurotoxicity: New Insights Into the Triad of Protein Misfolding, Mitochondrial Impairment, and Neuroinflammation. *Front Neurosci* 13**,** 654. doi: 10.3389/fnins.2019.00654.

Harms, A.S., Ferreira, S.A., and Romero-Ramos, M. (2021). Periphery and brain, innate and adaptive immunity in Parkinson's disease. *Acta Neuropathol* 141(4)**,** 527-545. doi: 10.1007/s00401-021-02268-5.

Harms, A.S., Thome, A.D., Yan, Z., Schonhoff, A.M., Williams, G.P., Li, X., et al. (2018). Peripheral monocyte entry is required for alpha-Synuclein induced inflammation and Neurodegeneration in a model of Parkinson disease. *Exp Neurol* 300**,** 179-187. doi: 10.1016/j.expneurol.2017.11.010.

Harrington, A.J., Hamamichi, S., Caldwell, G.A., and Caldwell, K.A. (2010). C. elegans as a model organism to investigate molecular pathways involved with Parkinson's disease. *Dev Dyn* 239(5)**,** 1282-1295. doi: 10.1002/dvdy.22231.

Hartmann, A. (2004). Postmortem studies in Parkinson's disease. *Dialogues Clin Neurosci* 6(3)**,** 281-293.

Hasegawa, S., Goto, S., Tsuji, H., Okuno, T., Asahara, T., Nomoto, K., et al. (2015). Intestinal Dysbiosis and Lowered Serum Lipopolysaccharide-Binding Protein in Parkinson's Disease. *PLoS One* 10(11)**,** e0142164. doi: 10.1371/journal.pone.0142164.

Hatcher, J.M., Pennell, K.D., and Miller, G.W. (2008). Parkinson's disease and pesticides: a toxicological perspective. *Trends Pharmacol Sci* 29(6)**,** 322-329. doi: 10.1016/j.tips.2008.03.007.

Hatcher, J.M., Richardson, J.R., Guillot, T.S., McCormack, A.L., Di Monte, D.A., Jones, D.P., et al. (2007). Dieldrin exposure induces oxidative damage in the mouse nigrostriatal dopamine system. *Exp Neurol* 204(2)**,** 619-630. doi: 10.1016/j.expneurol.2006.12.020.

Hayes, M.T. (2019). Parkinson's Disease and Parkinsonism. *Am J Med* 132(7)**,** 802-807. doi: 10.1016/j.amjmed.2019.03.001.

Healy, D.G., Falchi, M., O'Sullivan, S.S., Bonifati, V., Durr, A., Bressman, S., et al. (2008). Phenotype, genotype, and worldwide genetic penetrance of LRRK2-associated Parkinson's disease: a case-control study. *Lancet Neurol* 7(7)**,** 583-590. doi: 10.1016/S1474-4422(08)70117-0.

Hefendehl, J.K., Neher, J.J., Suhs, R.B., Kohsaka, S., Skodras, A., and Jucker, M. (2014). Homeostatic and injury-induced microglia behavior in the aging brain. *Aging Cell* 13(1)**,** 60-69. doi: 10.1111/acel.12149.

Heikkila, R.E., Nicklas, W.J., Vyas, I., and Duvoisin, R.C. (1985). Dopaminergic toxicity of rotenone and the 1-methyl-4-phenylpyridinium ion after their stereotaxic administration to rats: implication for the mechanism of 1-methyl-4-phenyl-1,2,3,6-tetrahydropyridine toxicity. *Neurosci Lett* 62(3)**,** 389-394. doi: 10.1016/0304-3940(85)90580-4.

Heindl, S., Gesierich, B., Benakis, C., Llovera, G., Duering, M., and Liesz, A. (2018). Automated Morphological Analysis of Microglia After Stroke. *Front Cell Neurosci* 12**,** 106. doi: 10.3389/fncel.2018.00106.

Hemling, N., Roytta, M., Rinne, J., Pollanen, P., Broberg, E., Tapio, V., et al. (2003). Herpesviruses in brains in Alzheimer's and Parkinson's diseases. *Ann Neurol* 54(2)**,** 267-271. doi: 10.1002/ana.10662.

Henchcliffe, C., and Beal, M.F. (2008). Mitochondrial biology and oxidative stress in Parkinson disease pathogenesis. *Nat Clin Pract Neurol* 4(11)**,** 600-609. doi: 10.1038/ncpneuro0924.

Henry, J., Smeyne, R.J., Jang, H., Miller, B., and Okun, M.S. (2010). Parkinsonism and neurological manifestations of influenza throughout the 20th and 21st centuries. *Parkinsonism Relat Disord* 16(9)**,** 566-571. doi: 10.1016/j.parkreldis.2010.06.012.

Herrera, A.J., Espinosa-Oliva, A.M., Carrillo-Jimenez, A., Oliva-Martin, M.J., Garcia-Revilla, J., Garcia-Quintanilla, A., et al. (2015). Relevance of chronic stress and the two faces of microglia in Parkinson's disease. *Front Cell Neurosci* 9**,** 312. doi: 10.3389/fncel.2015.00312.

Hickman, S., Izzy, S., Sen, P., Morsett, L., and El Khoury, J. (2018). Microglia in neurodegeneration. *Nat Neurosci* 21(10)**,** 1359-1369. doi: 10.1038/s41593-018-0242-x.

Hirth, F. (2010). Drosophila melanogaster in the study of human neurodegeneration. *CNS Neurol Disord Drug Targets* 9(4)**,** 504-523. doi: 10.2174/187152710791556104.

Hoozemans, J.J., van Haastert, E.S., Eikelenboom, P., de Vos, R.A., Rozemuller, J.M., and Scheper, W. (2007). Activation of the unfolded protein response in Parkinson's disease. *Biochem Biophys Res Commun* 354(3)**,** 707-711. doi: 10.1016/j.bbrc.2007.01.043.

Hsu, H.W., Bondy, S.C., and Kitazawa, M. (2018). Environmental and Dietary Exposure to Copper and Its Cellular Mechanisms Linking to Alzheimer's Disease. *Toxicol Sci* 163(2)**,** 338-345. doi: 10.1093/toxsci/kfy025.

Huang, H.K., Wang, J.H., Lei, W.Y., Chen, C.L., Chang, C.Y., and Liou, L.S. (2018). Helicobacter pylori infection is associated with an increased risk of Parkinson's disease: A population-based retrospective cohort study. *Parkinsonism Relat Disord* 47**,** 26-31. doi: 10.1016/j.parkreldis.2017.11.331.

Huang, M., Wang, B., Li, X., Fu, C., Wang, C., and Kang, X. (2019). alpha-Synuclein: A Multifunctional Player in Exocytosis, Endocytosis, and Vesicle Recycling. *Front Neurosci* 13**,** 28. doi: 10.3389/fnins.2019.00028.

Hunot, S., Boissiere, F., Faucheux, B., Brugg, B., Mouatt-Prigent, A., Agid, Y., et al. (1996). Nitric oxide synthase and neuronal vulnerability in Parkinson's disease. *Neuroscience* 72(2)**,** 355-363. doi: 10.1016/0306-4522(95)00578-1.

Hunot, S., Brugg, B., Ricard, D., Michel, P.P., Muriel, M.P., Ruberg, M., et al. (1997). Nuclear translocation of NF-kappaB is increased in dopaminergic neurons of patients with parkinson disease. *Proc Natl Acad Sci U S A* 94(14)**,** 7531-7536. doi: 10.1073/pnas.94.14.7531.

Imamura, K., Hishikawa, N., Sawada, M., Nagatsu, T., Yoshida, M., and Hashizume, Y. (2003). Distribution of major histocompatibility complex class II-positive microglia and cytokine profile of Parkinson's disease brains. *Acta Neuropathol* 106(6)**,** 518-526. doi: 10.1007/s00401-003-0766-2.

Inden, M., Kitamura, Y., Abe, M., Tamaki, A., Takata, K., and Taniguchi, T. (2011). Parkinsonian rotenone mouse model: reevaluation of long-term administration of rotenone in C57BL/6 mice. *Biol Pharm Bull* 34(1)**,** 92-96. doi: 10.1248/bpb.34.92.

Inden, M., Kitamura, Y., Takeuchi, H., Yanagida, T., Takata, K., Kobayashi, Y., et al. (2007). Neurodegeneration of mouse nigrostriatal dopaminergic system induced by repeated oral administration of rotenone is prevented by 4-phenylbutyrate, a chemical chaperone. *J Neurochem* 101(6)**,** 1491-1504. doi: 10.1111/j.1471-4159.2006.04440.x.

Jack, C.S., Arbour, N., Manusow, J., Montgrain, V., Blain, M., McCrea, E., et al. (2005). TLR signaling tailors innate immune responses in human microglia and astrocytes. *J Immunol* 175(7)**,** 4320-4330. doi: 10.4049/jimmunol.175.7.4320.

Jahn, T.R., and Radford, S.E. (2008). Folding versus aggregation: polypeptide conformations on competing pathways. *Arch Biochem Biophys* 469(1)**,** 100-117. doi: 10.1016/j.abb.2007.05.015.

Jang, H., Boltz, D., Sturm-Ramirez, K., Shepherd, K.R., Jiao, Y., Webster, R., et al. (2009a). Highly pathogenic H5N1 influenza virus can enter the central nervous system and induce neuroinflammation and neurodegeneration. *Proc Natl Acad Sci U S A* 106(33)**,** 14063-14068. doi: 10.1073/pnas.0900096106.

Jang, H., Boltz, D.A., Webster, R.G., and Smeyne, R.J. (2009b). Viral parkinsonism. *Biochim Biophys Acta* 1792(7)**,** 714-721. doi: 10.1016/j.bbadis.2008.08.001.

Jankovic, J. (2008). Parkinson's disease: clinical features and diagnosis. *J Neurol Neurosurg Psychiatry* 79(4)**,** 368-376. doi: 10.1136/jnnp.2007.131045.

Jarrett, J.T., and Lansbury, P.T., Jr. (1993). Seeding "one-dimensional crystallization" of amyloid: a pathogenic mechanism in Alzheimer's disease and scrapie? *Cell* 73(6)**,** 1055-1058. doi: 10.1016/0092-8674(93)90635-4.

Jiang, P., Scarpa, J.R., Gao, V.D., Vitaterna, M.H., Kasarskis, A., and Turek, F.W. (2019). Parkinson's Disease is Associated with Dysregulations of a Dopamine-Modulated Gene Network Relevant to Sleep and Affective Neurobehaviors in the Striatum. *Sci Rep* 9(1)**,** 4808. doi: 10.1038/s41598-019-41248-4.

Johnson, M.E., and Bobrovskaya, L. (2015). An update on the rotenone models of Parkinson's disease: their ability to reproduce the features of clinical disease and model gene-environment interactions. *Neurotoxicology* 46**,** 101-116. doi: 10.1016/j.neuro.2014.12.002.

Jurga, A.M., Paleczna, M., and Kuter, K.Z. (2020). Overview of General and Discriminating Markers of Differential Microglia Phenotypes. *Front Cell Neurosci* 14**,** 198. doi: 10.3389/fncel.2020.00198.

Kamel, F., Tanner, C., Umbach, D., Hoppin, J., Alavanja, M., Blair, A., et al. (2007). Pesticide exposure and self-reported Parkinson's disease in the agricultural health study. *Am J Epidemiol* 165(4)**,** 364-374. doi: 10.1093/aje/kwk024.

Kanthasamy, A.G., Kitazawa, M., Kanthasamy, A., and Anantharam, V. (2005). Dieldrin-induced neurotoxicity: relevance to Parkinson's disease pathogenesis. *Neurotoxicology* 26(4)**,** 701-719. doi: 10.1016/j.neuro.2004.07.010.

Kapila, C.C., Kaul, S., Kapur, S.C., Kalayanam, T.S., and Banerjee, D. (1958). Neurological and hepatic disorders associated with influenza. *Br Med J* 2(5108)**,** 1311-1314. doi: 10.1136/bmj.2.5108.1311.

Kaufman, S.K., Sanders, D.W., Thomas, T.L., Ruchinskas, A.J., Vaquer-Alicea, J., Sharma, A.M., et al. (2016). Tau Prion Strains Dictate Patterns of Cell Pathology, Progression Rate, and Regional Vulnerability In Vivo. *Neuron* 92(4)**,** 796-812. doi: 10.1016/j.neuron.2016.09.055.

Ke, T., Sidoryk-Wegrzynowicz, M., Pajarillo, E., Rizor, A., Soares, F.A.A., Lee, E., et al. (2019). Role of Astrocytes in Manganese Neurotoxicity Revisited. *Neurochem Res* 44(11)**,** 2449-2459. doi: 10.1007/s11064-019-02881-7.

Keen, C.L., Ensunsa, J.L., and Clegg, M.S. (2000). Manganese metabolism in animals and humans including the toxicity of manganese. *Met Ions Biol Syst* 37**,** 89-121.

Kelly, J.W. (1996). Alternative conformations of amyloidogenic proteins govern their behavior. *Curr Opin Struct Biol* 6(1)**,** 11-17. doi: 10.1016/s0959-440x(96)80089-3.

Kelly, J.W. (1998). The alternative conformations of amyloidogenic proteins and their multi-step assembly pathways. *Curr Opin Struct Biol* 8(1)**,** 101-106. doi: 10.1016/s0959-440x(98)80016-x.

Kim, C., Ho, D.H., Suk, J.E., You, S., Michael, S., Kang, J., et al. (2013). Neuron-released oligomeric alpha-synuclein is an endogenous agonist of TLR2 for paracrine activation of microglia. *Nat Commun* 4**,** 1562. doi: 10.1038/ncomms2534.

Kim, S., Kwon, S.H., Kam, T.I., Panicker, N., Karuppagounder, S.S., Lee, S., et al. (2019). Transneuronal Propagation of Pathologic alpha-Synuclein from the Gut to the Brain Models Parkinson's Disease. *Neuron* 103(4)**,** 627-641 e627. doi: 10.1016/j.neuron.2019.05.035.

Kim, S., Lee, K., Seok Choi, Y., Ku, J., Lee, Y., and Kim, Y. (2020). Mitochondrial dsRNAs activate PKR and TLR3 to promote chondrocyte degeneration in osteoarthritis. *BioRxiv*.

King, A., Szekely, B., Calapkulu, E., Ali, H., Rios, F., Jones, S., et al. (2020). The Increased Densities, But Different Distributions, of Both C3 and S100A10 Immunopositive Astrocyte-Like Cells in Alzheimer's Disease Brains Suggest Possible Roles for Both A1 and A2 Astrocytes in the Disease Pathogenesis. *Brain Sci* 10(8). doi: 10.3390/brainsci10080503.

Kirkley, K.S., Popichak, K.A., Afzali, M.F., Legare, M.E., and Tjalkens, R.B. (2017). Microglia amplify inflammatory activation of astrocytes in manganese neurotoxicity. *J Neuroinflammation* 14(1)**,** 99. doi: 10.1186/s12974-017-0871-0.

Kirkley, K.S., Popichak, K.A., Hammond, S.L., Davies, C., Hunt, L., and Tjalkens, R.B. (2019). Genetic suppression of IKK2/NF-kappaB in astrocytes inhibits neuroinflammation and reduces neuronal loss in the MPTP-Probenecid model of Parkinson's disease. *Neurobiol Dis* 127**,** 193-209. doi: 10.1016/j.nbd.2019.02.020.

Klopfleisch, R., Werner, O., Mundt, E., Harder, T., and Teifke, J.P. (2006). Neurotropism of highly pathogenic avian influenza virus A/chicken/Indonesia/2003 (H5N1) in experimentally infected pigeons (Columbia livia f. domestica). *Vet Pathol* 43(4)**,** 463-470. doi: 10.1354/vp.43-4-463.

Knott, C., Stern, G., and Wilkin, G.P. (2000). Inflammatory regulators in Parkinson's disease: iNOS, lipocortin-1, and cyclooxygenases-1 and -2. *Mol Cell Neurosci* 16(6)**,** 724-739. doi: 10.1006/mcne.2000.0914.

Knuesel, I., Chicha, L., Britschgi, M., Schobel, S.A., Bodmer, M., Hellings, J.A., et al. (2014). Maternal immune activation and abnormal brain development across CNS disorders. *Nat Rev Neurol* 10(11)**,** 643-660. doi: 10.1038/nrneurol.2014.187.

Kobayashi, K., Umeda, K., Ihara, F., Tanaka, S., Yamagishi, J., Suzuki, Y., et al. (2019). Transcriptome analysis of the effect of C-C chemokine receptor 5 deficiency on cell response to Toxoplasma gondii in brain cells. *BMC Genomics* 20(1)**,** 705. doi: 10.1186/s12864-019-6076-4.

Kordower, J.H., Chu, Y., Hauser, R.A., Freeman, T.B., and Olanow, C.W. (2008). Lewy body-like pathology in long-term embryonic nigral transplants in Parkinson's disease. *Nat Med* 14(5)**,** 504-506. doi: 10.1038/nm1747.

Kouli, A., Torsney, K.M., and Kuan, W.L. (2018). "Parkinson's Disease: Etiology, Neuropathology, and Pathogenesis," in *Parkinson's Disease: Pathogenesis and Clinical Aspects,* eds. T.B. Stoker & J.C. Greenland. (Brisbane (AU)).

Kraft, A.D., McPherson, C.A., and Harry, G.J. (2009). Heterogeneity of microglia and TNF signaling as determinants for neuronal death or survival. *Neurotoxicology* 30(5)**,** 785-793. doi: 10.1016/j.neuro.2009.07.001.

Kumar, V., Sami, N., Kashav, T., Islam, A., Ahmad, F., and Hassan, M.I. (2016). Protein aggregation and neurodegenerative diseases: From theory to therapy. *Eur J Med Chem* 124**,** 1105-1120. doi: 10.1016/j.ejmech.2016.07.054.

Kumari, P., Rothan, H.A., Natekar, J.P., Stone, S., Pathak, H., Strate, P.G., et al. (2021). Neuroinvasion and Encephalitis Following Intranasal Inoculation of SARS-CoV-2 in K18-hACE2 Mice. *Viruses* 13(1). doi: 10.3390/v13010132.

Kushnirov, V.V., Dergalev, A.A., and Alexandrov, A.I. (2020). Proteinase K resistant cores of prions and amyloids. *Prion* 14(1)**,** 11-19. doi: 10.1080/19336896.2019.1704612.

Kwakye, G.F., Paoliello, M.M., Mukhopadhyay, S., Bowman, A.B., and Aschner, M. (2015). Manganese-Induced Parkinsonism and Parkinson's Disease: Shared and Distinguishable Features. *Int J Environ Res Public Health* 12(7)**,** 7519-7540. doi: 10.3390/ijerph120707519.

Lamark, T., Kirkin, V., Dikic, I., and Johansen, T. (2009). NBR1 and p62 as cargo receptors for selective autophagy of ubiquitinated targets. *Cell Cycle* 8(13)**,** 1986-1990. doi: 10.4161/cc.8.13.8892.

Lanzillotta, A., Porrini, V., Bellucci, A., Benarese, M., Branca, C., Parrella, E., et al. (2015). NF-kappaB in Innate Neuroprotection and Age-Related Neurodegenerative Diseases. *Front Neurol* 6**,** 98. doi: 10.3389/fneur.2015.00098.

Laprell, L., Schulze, C., Brehme, M.L., and Oertner, T.G. (2021). The role of microglia membrane potential in chemotaxis. *J Neuroinflammation* 18(1)**,** 21. doi: 10.1186/s12974-020-02048-0.

Lashuel, H.A., Overk, C.R., Oueslati, A., and Masliah, E. (2013). The many faces of alpha-synuclein: from structure and toxicity to therapeutic target. *Nat Rev Neurosci* 14(1)**,** 38-48. doi: 10.1038/nrn3406.

Lashuel, H.A., Petre, B.M., Wall, J., Simon, M., Nowak, R.J., Walz, T., et al. (2002). Alpha-synuclein, especially the Parkinson's disease-associated mutants, forms pore-like annular and tubular protofibrils. *J Mol Biol* 322(5)**,** 1089-1102. doi: 10.1016/s0022-2836(02)00735-0.

Lawana, V., Cannon, J. (2020). "Rotenone neurotoxicity: Relevance to Parkinson's disease," in *Advances in Neurotoxicology*. Elsevier), 209-254.

Lawson, L.J., Perry, V.H., and Gordon, S. (1992). Turnover of resident microglia in the normal adult mouse brain. *Neuroscience* 48(2)**,** 405-415. doi: 10.1016/0306-4522(92)90500-2.

Lee, H.J., Khoshaghideh, F., Patel, S., and Lee, S.J. (2004). Clearance of alpha-synuclein oligomeric intermediates via the lysosomal degradation pathway. *J Neurosci* 24(8)**,** 1888-1896. doi: 10.1523/JNEUROSCI.3809-03.2004.

Lee, H.J., Suk, J.E., Patrick, C., Bae, E.J., Cho, J.H., Rho, S., et al. (2010). Direct transfer of alpha-synuclein from neuron to astroglia causes inflammatory responses in synucleinopathies. *J Biol Chem* 285(12)**,** 9262-9272. doi: 10.1074/jbc.M109.081125.

Lehnardt, S. (2010). Innate immunity and neuroinflammation in the CNS: the role of microglia in Toll-like receptor-mediated neuronal injury. *Glia* 58(3)**,** 253-263. doi: 10.1002/glia.20928.

Lenz, K.M., and Nelson, L.H. (2018). Microglia and Beyond: Innate Immune Cells As Regulators of Brain Development and Behavioral Function. *Front Immunol* 9**,** 698. doi: 10.3389/fimmu.2018.00698.

Lesne, S.E. (2014). Toxic oligomer species of amyloid-beta in Alzheimer's disease, a timing issue. *Swiss Med Wkly* 144**,** w14021. doi: 10.4414/smw.2014.14021.

Li, J.Y., Englund, E., Holton, J.L., Soulet, D., Hagell, P., Lees, A.J., et al. (2008). Lewy bodies in grafted neurons in subjects with Parkinson's disease suggest host-to-graft disease propagation. *Nat Med* 14(5)**,** 501-503. doi: 10.1038/nm1746.

Li, W.W., Yang, R., Guo, J.C., Ren, H.M., Zha, X.L., Cheng, J.S., et al. (2007). Localization of alpha-synuclein to mitochondria within midbrain of mice. *Neuroreport* 18(15)**,** 1543-1546. doi: 10.1097/WNR.0b013e3282f03db4.

Li, Y., Xia, Y., Yin, S., Wan, F., Hu, J., Kou, L., et al. (2021). Targeting Microglial alpha-Synuclein/TLRs/NF-kappaB/NLRP3 Inflammasome Axis in Parkinson's Disease. *Front Immunol* 12**,** 719807. doi: 10.3389/fimmu.2021.719807.

Liddelow, S.A., Guttenplan, K.A., Clarke, L.E., Bennett, F.C., Bohlen, C.J., Schirmer, L., et al. (2017). Neurotoxic reactive astrocytes are induced by activated microglia. *Nature* 541(7638)**,** 481-487. doi: 10.1038/nature21029.

Lim, K.L. (2010). Non-mammalian animal models of Parkinson's disease for drug discovery. *Expert Opin Drug Discov* 5(2)**,** 165-176. doi: 10.1517/17460440903527675.

Ling, N. (2003). "Rotenone- a review of its toxicity and use for fisheries management ", in: *3414.* (ed.) D.f. Conservation. (New Zealand Department for Conservation).

Liu, B., Fang, F., Pedersen, N.L., Tillander, A., Ludvigsson, J.F., Ekbom, A., et al. (2017a). Vagotomy and Parkinson disease: A Swedish register-based matched-cohort study. *Neurology* 88(21)**,** 1996-2002. doi: 10.1212/WNL.0000000000003961.

Liu, H.F., Ho, P.W., Leung, G.C., Lam, C.S., Pang, S.Y., Li, L., et al. (2017b). Combined LRRK2 mutation, aging and chronic low dose oral rotenone as a model of Parkinson's disease. *Sci Rep* 7**,** 40887. doi: 10.1038/srep40887.

Liu, M., Hurn, P.D., Roselli, C.E., and Alkayed, N.J. (2007). Role of P450 aromatase in sex-specific astrocytic cell death. *J Cereb Blood Flow Metab* 27(1)**,** 135-141. doi: 10.1038/sj.jcbfm.9600331.

Liu, T., Zhang, L., Joo, D., and Sun, S.C. (2017c). NF-kappaB signaling in inflammation. *Signal Transduct Target Ther* 2. doi: 10.1038/sigtrans.2017.23.

Liu, X., Sullivan, K.A., Madl, J.E., Legare, M., and Tjalkens, R.B. (2006). Manganese-induced neurotoxicity: the role of astroglial-derived nitric oxide in striatal interneuron degeneration. *Toxicol Sci* 91(2)**,** 521-531. doi: 10.1093/toxsci/kfj150.

Liu, Y., Sun, J.D., Song, L.K., Li, J., Chu, S.F., Yuan, Y.H., et al. (2015). Environment-contact administration of rotenone: A new rodent model of Parkinson's disease. *Behav Brain Res* 294**,** 149-161. doi: 10.1016/j.bbr.2015.07.058.

Ljung, K., and Vahter, M. (2007). Time to re-evaluate the guideline value for manganese in drinking water? *Environ Health Perspect* 115(11)**,** 1533-1538. doi: 10.1289/ehp.10316.

Lucking, C.B., and Brice, A. (2000). Alpha-synuclein and Parkinson's disease. *Cell Mol Life Sci* 57(13-14)**,** 1894-1908. doi: 10.1007/PL00000671.

Lynch-Day, M.A., Mao, K., Wang, K., Zhao, M., and Klionsky, D.J. (2012). The role of autophagy in Parkinson's disease. *Cold Spring Harb Perspect Med* 2(4)**,** a009357. doi: 10.1101/cshperspect.a009357.

Macerollo, A., Lu, M.K., Huang, H.C., Chen, H.J., Lin, C.C., Kao, C.H., et al. (2017). Colonic diverticular disease: A new risk factor for Parkinson's disease? *Parkinsonism Relat Disord* 42**,** 61-65. doi: 10.1016/j.parkreldis.2017.06.011.

Malatesta, P., Hack, M.A., Hartfuss, E., Kettenmann, H., Klinkert, W., Kirchhoff, F., et al. (2003). Neuronal or glial progeny: regional differences in radial glia fate. *Neuron* 37(5)**,** 751-764. doi: 10.1016/s0896-6273(03)00116-8.

Marogianni, C., Sokratous, M., Dardiotis, E., Hadjigeorgiou, G.M., Bogdanos, D., and Xiromerisiou, G. (2020). Neurodegeneration and Inflammation-An Interesting Interplay in Parkinson's Disease. *Int J Mol Sci* 21(22). doi: 10.3390/ijms21228421.

Maroteaux, L., Campanelli, J.T., and Scheller, R.H. (1988). Synuclein: a neuron-specific protein localized to the nucleus and presynaptic nerve terminal. *J Neurosci* 8(8)**,** 2804-2815.

Marras, C., Beck, J.C., Bower, J.H., Roberts, E., Ritz, B., Ross, G.W., et al. (2018). Prevalence of Parkinson's disease across North America. *NPJ Parkinsons Dis* 4**,** 21. doi: 10.1038/s41531-018-0058-0.

Martinez, E.M., Young, A.L., Patankar, Y.R., Berwin, B.L., Wang, L., von Herrmann, K.M., et al. (2017). Editor's Highlight: Nlrp3 Is Required for Inflammatory Changes and Nigral Cell Loss Resulting From Chronic Intragastric Rotenone Exposure in Mice. *Toxicol Sci* 159(1)**,** 64-75. doi: 10.1093/toxsci/kfx117.

Martinez-Finley, E.J., Gavin, C.E., Aschner, M., and Gunter, T.E. (2013). Manganese neurotoxicity and the role of reactive oxygen species. *Free Radic Biol Med* 62**,** 65-75. doi: 10.1016/j.freeradbiomed.2013.01.032.

Massey, A.R., and Beckham, J.D. (2016). Alpha-Synuclein, a Novel Viral Restriction Factor Hiding in Plain Sight. *DNA Cell Biol* 35(11)**,** 643-645. doi: 10.1089/dna.2016.3488.

Matias, I., Morgado, J., and Gomes, F.C.A. (2019). Astrocyte Heterogeneity: Impact to Brain Aging and Disease. *Front Aging Neurosci* 11**,** 59. doi: 10.3389/fnagi.2019.00059.

Matsuda, N., Sato, S., Shiba, K., Okatsu, K., Saisho, K., Gautier, C.A., et al. (2010). PINK1 stabilized by mitochondrial depolarization recruits Parkin to damaged mitochondria and activates latent Parkin for mitophagy. *J Cell Biol* 189(2)**,** 211-221. doi: 10.1083/jcb.200910140.

Maurizi, C.P. (2010). Influenza caused epidemic encephalitis (encephalitis lethargica): the circumstantial evidence and a challenge to the nonbelievers. *Med Hypotheses* 74(5)**,** 798-801. doi: 10.1016/j.mehy.2009.12.012.

Mazzoni, P., Shabbott, B., and Cortes, J.C. (2012). Motor control abnormalities in Parkinson's disease. *Cold Spring Harb Perspect Med* 2(6)**,** a009282. doi: 10.1101/cshperspect.a009282.

McClay, W. (2000). Rotenone Use in North America (1988-1997). *Fisheries* 15-21.

McGeer, P.L., Itagaki, S., Boyes, B.E., and McGeer, E.G. (1988). Reactive microglia are positive for HLA-DR in the substantia nigra of Parkinson's and Alzheimer's disease brains. *Neurology* 38(8)**,** 1285-1291. doi: 10.1212/wnl.38.8.1285.

McNaught, K.S., Belizaire, R., Isacson, O., Jenner, P., and Olanow, C.W. (2003). Altered proteasomal function in sporadic Parkinson's disease. *Exp Neurol* 179(1)**,** 38-46. doi: 10.1006/exnr.2002.8050.

Mecucci, C., Donti, E., Bocchini, V., Tabilio, A., and Martelli, M.F. (1982). 5q-Syndrome in a patient with chronic exposure to ionizing radiation. *Cancer Genet Cytogenet* 5(1)**,** 75-80. doi: 10.1016/0165-4608(82)90042-5.

Mehra, S., Sahay, S., and Maji, S.K. (2019). alpha-Synuclein misfolding and aggregation: Implications in Parkinson's disease pathogenesis. *Biochim Biophys Acta Proteins Proteom* 1867(10)**,** 890-908. doi: 10.1016/j.bbapap.2019.03.001.

Melki, R. (2015). Role of Different Alpha-Synuclein Strains in Synucleinopathies, Similarities with other Neurodegenerative Diseases. *J Parkinsons Dis* 5(2)**,** 217-227. doi: 10.3233/JPD-150543.

Menezes-Filho, J.A., Novaes Cde, O., Moreira, J.C., Sarcinelli, P.N., and Mergler, D. (2011). Elevated manganese and cognitive performance in school-aged children and their mothers. *Environ Res* 111(1)**,** 156-163. doi: 10.1016/j.envres.2010.09.006.

Metsalu, T., and Vilo, J. (2015). ClustVis: a web tool for visualizing clustering of multivariate data using Principal Component Analysis and heatmap. *Nucleic Acids Res* 43(W1)**,** W566-570. doi: 10.1093/nar/gkv468.

Mezzaroba, L., Alfieri, D.F., Colado Simao, A.N., and Vissoci Reiche, E.M. (2019). The role of zinc, copper, manganese and iron in neurodegenerative diseases. *Neurotoxicology* 74**,** 230-241. doi: 10.1016/j.neuro.2019.07.007.

Michel, P.P., Hirsch, E.C., and Hunot, S. (2016). Understanding Dopaminergic Cell Death Pathways in Parkinson Disease. *Neuron* 90(4)**,** 675-691. doi: 10.1016/j.neuron.2016.03.038.

Middeldorp, J., and Hol, E.M. (2011). GFAP in health and disease. *Prog Neurobiol* 93(3)**,** 421-443. doi: 10.1016/j.pneurobio.2011.01.005.

Minghetti, L. (2004). Cyclooxygenase-2 (COX-2) in inflammatory and degenerative brain diseases. *J Neuropathol Exp Neurol* 63(9)**,** 901-910. doi: 10.1093/jnen/63.9.901.

Minghetti, L., Ajmone-Cat, M.A., De Berardinis, M.A., and De Simone, R. (2005). Microglial activation in chronic neurodegenerative diseases: roles of apoptotic neurons and chronic stimulation. *Brain Res Brain Res Rev* 48(2)**,** 251-256. doi: 10.1016/j.brainresrev.2004.12.015.

Miraglia, F., Ricci, A., Rota, L., and Colla, E. (2018). Subcellular localization of alpha-synuclein aggregates and their interaction with membranes. *Neural Regen Res* 13(7)**,** 1136-1144. doi: 10.4103/1673-5374.235013.

Moreno, J.A., Streifel, K.M., Sullivan, K.A., Legare, M.E., and Tjalkens, R.B. (2009a). Developmental exposure to manganese increases adult susceptibility to inflammatory activation of glia and neuronal protein nitration. *Toxicol Sci* 112(2)**,** 405-415. doi: 10.1093/toxsci/kfp221.

Moreno, J.A., Yeomans, E.C., Streifel, K.M., Brattin, B.L., Taylor, R.J., and Tjalkens, R.B. (2009b). Age-dependent susceptibility to manganese-induced neurological dysfunction. *Toxicol Sci* 112(2)**,** 394-404. doi: 10.1093/toxsci/kfp220.

Moreno-Gonzalez, I., and Soto, C. (2011). Misfolded protein aggregates: mechanisms, structures and potential for disease transmission. *Semin Cell Dev Biol* 22(5)**,** 482-487. doi: 10.1016/j.semcdb.2011.04.002.

Mori, F., Inenaga, C., Yoshimoto, M., Umezu, H., Tanaka, R., Takahashi, H., et al. (2002). Alpha-synuclein immunoreactivity in normal and neoplastic Schwann cells. *Acta Neuropathol* 103(2)**,** 145-151. doi: 10.1007/s004010100443.

Morrison, H., Young, K., Qureshi, M., Rowe, R.K., and Lifshitz, J. (2017). Quantitative microglia analyses reveal diverse morphologic responses in the rat cortex after diffuse brain injury. *Sci Rep* 7(1)**,** 13211. doi: 10.1038/s41598-017-13581-z.

Moustafa, A.A., Chakravarthy, S., Phillips, J.R., Gupta, A., Keri, S., Polner, B., et al. (2016). Motor symptoms in Parkinson's disease: A unified framework. *Neurosci Biobehav Rev* 68**,** 727-740. doi: 10.1016/j.neubiorev.2016.07.010.

Mouzon, B.C., Bachmeier, C., Ferro, A., Ojo, J.O., Crynen, G., Acker, C.M., et al. (2014). Chronic neuropathological and neurobehavioral changes in a repetitive mild traumatic brain injury model. *Ann Neurol* 75(2)**,** 241-254. doi: 10.1002/ana.24064.

Murueta-Goyena, A., Andikoetxea, A., Gomez-Esteban, J.C., and Gabilondo, I. (2019). Contribution of the GABAergic System to Non-Motor Manifestations in Premotor and Early Stages of Parkinson's Disease. *Front Pharmacol* 10**,** 1294. doi: 10.3389/fphar.2019.01294.

Nandipati, S., and Litvan, I. (2016). Environmental Exposures and Parkinson's Disease. *Int J Environ Res Public Health* 13(9). doi: 10.3390/ijerph13090881.

Narasimhan, S., Guo, J.L., Changolkar, L., Stieber, A., McBride, J.D., Silva, L.V., et al. (2017). Pathological Tau Strains from Human Brains Recapitulate the Diversity of Tauopathies in Nontransgenic Mouse Brain. *J Neurosci* 37(47)**,** 11406-11423. doi: 10.1523/JNEUROSCI.1230-17.2017.

Nelson, L.H., and Lenz, K.M. (2017). The immune system as a novel regulator of sex differences in brain and behavioral development. *J Neurosci Res* 95(1-2)**,** 447-461. doi: 10.1002/jnr.23821.

Netea, M.G., Joosten, L.A., Latz, E., Mills, K.H., Natoli, G., Stunnenberg, H.G., et al. (2016). Trained immunity: A program of innate immune memory in health and disease. *Science* 352(6284)**,** aaf1098. doi: 10.1126/science.aaf1098.

Nixon, R.A., Wegiel, J., Kumar, A., Yu, W.H., Peterhoff, C., Cataldo, A., et al. (2005). Extensive involvement of autophagy in Alzheimer disease: an immuno-electron microscopy study. *J Neuropathol Exp Neurol* 64(2)**,** 113-122. doi: 10.1093/jnen/64.2.113.

Nolen, L.T., Mukerji, S.S., and Mejia, N.I. (2022). Post-acute neurological consequences of COVID-19: an unequal burden. *Nat Med* 28(1)**,** 20-23. doi: 10.1038/s41591-021-01647-5.

Nonaka, T., Watanabe, S.T., Iwatsubo, T., and Hasegawa, M. (2010). Seeded aggregation and toxicity of {alpha}-synuclein and tau: cellular models of neurodegenerative diseases. *J Biol Chem* 285(45)**,** 34885-34898. doi: 10.1074/jbc.M110.148460.

Norden, D.M., Muccigrosso, M.M., and Godbout, J.P. (2015). Microglial priming and enhanced reactivity to secondary insult in aging, and traumatic CNS injury, and neurodegenerative disease. *Neuropharmacology* 96(Pt A)**,** 29-41. doi: 10.1016/j.neuropharm.2014.10.028.

Ogata, K., and Kosaka, T. (2002). Structural and quantitative analysis of astrocytes in the mouse hippocampus. *Neuroscience* 113(1)**,** 221-233. doi: 10.1016/s0306-4522(02)00041-6.

Olson, J.K., and Miller, S.D. (2004). Microglia initiate central nervous system innate and adaptive immune responses through multiple TLRs. *J Immunol* 173(6)**,** 3916-3924. doi: 10.4049/jimmunol.173.6.3916.

Opara, J., Malecki, A., Malecka, E., and Socha, T. (2017). Motor assessment in Parkinson`s disease. *Ann Agric Environ Med* 24(3)**,** 411-415. doi: 10.5604/12321966.1232774.

Ottum, P.A., Arellano, G., Reyes, L.I., Iruretagoyena, M., and Naves, R. (2015). Opposing Roles of Interferon-Gamma on Cells of the Central Nervous System in Autoimmune Neuroinflammation. *Front Immunol* 6**,** 539. doi: 10.3389/fimmu.2015.00539.

Pajares, M., A, I.R., Manda, G., Bosca, L., and Cuadrado, A. (2020). Inflammation in Parkinson's Disease: Mechanisms and Therapeutic Implications. *Cells* 9(7). doi: 10.3390/cells9071687.

Paleologou, K.E., Schmid, A.W., Rospigliosi, C.C., Kim, H.Y., Lamberto, G.R., Fredenburg, R.A., et al. (2008). Phosphorylation at Ser-129 but not the phosphomimics S129E/D inhibits the fibrillation of alpha-synuclein. *J Biol Chem* 283(24)**,** 16895-16905. doi: 10.1074/jbc.M800747200.

Pan, M.X., Li, J., Ma, C., Fu, K., Li, Z.Q., and Wang, Z.F. (2020). Sex-dependent effects of GPER activation on neuroinflammation in a rat model of traumatic brain injury. *Brain Behav Immun* 88**,** 421-431. doi: 10.1016/j.bbi.2020.04.005.

Pan, T., Kondo, S., Le, W., and Jankovic, J. (2008). The role of autophagy-lysosome pathway in neurodegeneration associated with Parkinson's disease. *Brain* 131(Pt 8)**,** 1969-1978. doi: 10.1093/brain/awm318.

Pan-Montojo, F., Anichtchik, O., Dening, Y., Knels, L., Pursche, S., Jung, R., et al. (2010). Progression of Parkinson's disease pathology is reproduced by intragastric administration of rotenone in mice. *PLoS One* 5(1)**,** e8762. doi: 10.1371/journal.pone.0008762.

Pandey, H.S., Kapoor, R., Bindu, and Seth, P. (2022). Coronin 1A facilitates calcium mobilization and promotes astrocyte reactivity in HIV-1 neuropathogenesis. *FASEB Bioadv* 4(4)**,** 254-272. doi: 10.1096/fba.2021-00109.

Papageorgiou, I.E., Lewen, A., Galow, L.V., Cesetti, T., Scheffel, J., Regen, T., et al. (2016). TLR4-activated microglia require IFN-gamma to induce severe neuronal dysfunction and death in situ. *Proc Natl Acad Sci U S A* 113(1)**,** 212-217. doi: 10.1073/pnas.1513853113.

Paredes-Rodriguez, E., Vegas-Suarez, S., Morera-Herreras, T., De Deurwaerdere, P., and Miguelez, C. (2020). The Noradrenergic System in Parkinson's Disease. *Front Pharmacol* 11**,** 435. doi: 10.3389/fphar.2020.00435.

Peelaerts, W., Bousset, L., Van der Perren, A., Moskalyuk, A., Pulizzi, R., Giugliano, M., et al. (2015). alpha-Synuclein strains cause distinct synucleinopathies after local and systemic administration. *Nature* 522(7556)**,** 340-344. doi: 10.1038/nature14547.

Pekna, M., and Pekny, M. (2021). The Complement System: A Powerful Modulator and Effector of Astrocyte Function in the Healthy and Diseased Central Nervous System. *Cells* 10(7). doi: 10.3390/cells10071812.

Perry, V.H., and Holmes, C. (2014). Microglial priming in neurodegenerative disease. *Nat Rev Neurol* 10(4)**,** 217-224. doi: 10.1038/nrneurol.2014.38.

Pezzoli, G., and Cereda, E. (2013). Exposure to pesticides or solvents and risk of Parkinson disease. *Neurology* 80(22)**,** 2035-2041. doi: 10.1212/WNL.0b013e318294b3c8.

Pizzi, M., and Spano, P. (2006). Distinct roles of diverse nuclear factor-kappaB complexes in neuropathological mechanisms. *Eur J Pharmacol* 545(1)**,** 22-28. doi: 10.1016/j.ejphar.2006.06.027.

Platten, M., Ho, P.P., Youssef, S., Fontoura, P., Garren, H., Hur, E.M., et al. (2005). Treatment of autoimmune neuroinflammation with a synthetic tryptophan metabolite. *Science* 310(5749)**,** 850-855. doi: 10.1126/science.1117634.

Poirier, M.A., Li, H., Macosko, J., Cai, S., Amzel, M., and Ross, C.A. (2002). Huntingtin spheroids and protofibrils as precursors in polyglutamine fibrilization. *J Biol Chem* 277(43)**,** 41032-41037. doi: 10.1074/jbc.M205809200.

Politis, M., and Niccolini, F. (2015). Serotonin in Parkinson's disease. *Behav Brain Res* 277**,** 136-145. doi: 10.1016/j.bbr.2014.07.037.

Pringsheim, T., Jette, N., Frolkis, A., and Steeves, T.D. (2014). The prevalence of Parkinson's disease: a systematic review and meta-analysis. *Mov Disord* 29(13)**,** 1583-1590. doi: 10.1002/mds.25945.

Racette, B.A., Searles Nielsen, S., Criswell, S.R., Sheppard, L., Seixas, N., Warden, M.N., et al. (2017). Dose-dependent progression of parkinsonism in manganese-exposed welders. *Neurology* 88(4)**,** 344-351. doi: 10.1212/WNL.0000000000003533.

Radad, K., Al-Shraim, M., Al-Emam, A., Wang, F., Kranner, B., Rausch, W.D., et al. (2019). Rotenone: from modelling to implication in Parkinson's disease. *Folia Neuropathol* 57(4)**,** 317-326. doi: 10.5114/fn.2019.89857.

Radermacher, P., and Haouzi, P. (2013). A mouse is not a rat is not a man: species-specific metabolic responses to sepsis - a nail in the coffin of murine models for critical care research? *Intensive Care Med Exp* 1(1)**,** 26. doi: 10.1186/2197-425X-1-7.

Radhakrishnan, D.M., and Goyal, V. (2018). Parkinson's disease: A review. *Neurol India* 66(Supplement)**,** S26-S35. doi: 10.4103/0028-3886.226451.

Ramakrishnan, M., Jensen, P.H., and Marsh, D. (2006). Association of alpha-synuclein and mutants with lipid membranes: spin-label ESR and polarized IR. *Biochemistry* 45(10)**,** 3386-3395. doi: 10.1021/bi052344d.

Ransohoff, R.M. (2016). A polarizing question: do M1 and M2 microglia exist? *Nat Neurosci* 19(8)**,** 987-991. doi: 10.1038/nn.4338.

Raza, C., Anjum, R., and Shakeel, N.U.A. (2019). Parkinson's disease: Mechanisms, translational models and management strategies. *Life Sci* 226**,** 77-90. doi: 10.1016/j.lfs.2019.03.057.

Reu, P., Khosravi, A., Bernard, S., Mold, J.E., Salehpour, M., Alkass, K., et al. (2017). The Lifespan and Turnover of Microglia in the Human Brain. *Cell Rep* 20(4)**,** 779-784. doi: 10.1016/j.celrep.2017.07.004.

Rey, N.L., George, S., Steiner, J.A., Madaj, Z., Luk, K.C., Trojanowski, J.Q., et al. (2018). Spread of aggregates after olfactory bulb injection of alpha-synuclein fibrils is associated with early neuronal loss and is reduced long term. *Acta Neuropathol* 135(1)**,** 65-83. doi: 10.1007/s00401-017-1792-9.

Rey, N.L., Steiner, J.A., Maroof, N., Luk, K.C., Madaj, Z., Trojanowski, J.Q., et al. (2016). Widespread transneuronal propagation of alpha-synucleinopathy triggered in olfactory bulb mimics prodromal Parkinson's disease. *J Exp Med* 213(9)**,** 1759-1778. doi: 10.1084/jem.20160368.

Richardson, J.R., Caudle, W.M., Wang, M., Dean, E.D., Pennell, K.D., and Miller, G.W. (2006). Developmental exposure to the pesticide dieldrin alters the dopamine system and increases neurotoxicity in an animal model of Parkinson's disease. *FASEB J* 20(10)**,** 1695-1697. doi: 10.1096/fj.06-5864fje.

Riederer, P., Berg, D., Casadei, N., Cheng, F., Classen, J., Dresel, C., et al. (2019). alpha-Synuclein in Parkinson's disease: causal or bystander? *J Neural Transm (Vienna)* 126(7)**,** 815-840. doi: 10.1007/s00702-019-02025-9.

Robinson, P.A. (2008). Protein stability and aggregation in Parkinson's disease. *Biochem J* 413(1)**,** 1-13. doi: 10.1042/BJ20080295.

Rocha, E.M., De Miranda, B., and Sanders, L.H. (2018). Alpha-synuclein: Pathology, mitochondrial dysfunction and neuroinflammation in Parkinson's disease. *Neurobiol Dis* 109(Pt B)**,** 249-257. doi: 10.1016/j.nbd.2017.04.004.

Rocha, S.M., Bantle, C.M., Aboellail, T., Chatterjee, D., Smeyne, R.J., and Tjalkens, R.B. (2022a). Rotenone induces regionally distinct alpha-synuclein protein aggregation and activation of glia prior to loss of dopaminergic neurons in C57Bl/6 mice. *Neurobiol Dis* 167**,** 105685. doi: 10.1016/j.nbd.2022.105685.

Rocha, S.M., Kirkley, K.S., Chatterjee, D., Aboellail, T., Smeyne, R.J., and Tjalkens, R. (2022b). Microglia-specific NF-kB/IKK2 knock-out increases accumulation of misfolded alpha-synuclein through inhibition of p62/SQSTM-1-dependent autophagy in the rotenone model of Parkinson’s Disease. *Submitted*

Rocha, S.M., Kirkley, K.S., Chatterjee, D., Aboellail, T., Smeyne, R.J., and Tjalkens, R.B. (2022c). Microglia-specific NF-kB/IKK2 knock-out increases accumulation of misfolded alpha-synuclein through inhibition of p62/SQSTM-1-dependent autophagy in the rotenone model of Parkinson’s Disease. *Submitted*

Roels, H.A., Bowler, R.M., Kim, Y., Claus Henn, B., Mergler, D., Hoet, P., et al. (2012). Manganese exposure and cognitive deficits: a growing concern for manganese neurotoxicity. *Neurotoxicology* 33(4)**,** 872-880. doi: 10.1016/j.neuro.2012.03.009.

Rojo, A.I., Cavada, C., de Sagarra, M.R., and Cuadrado, A. (2007). Chronic inhalation of rotenone or paraquat does not induce Parkinson's disease symptoms in mice or rats. *Exp Neurol* 208(1)**,** 120-126. doi: 10.1016/j.expneurol.2007.07.022.

Roth, J.A. (2006). Homeostatic and toxic mechanisms regulating manganese uptake, retention, and elimination. *Biol Res* 39(1)**,** 45-57. doi: 10.4067/s0716-97602006000100006.

Sadasivan, S., Zanin, M., O'Brien, K., Schultz-Cherry, S., and Smeyne, R.J. (2015). Induction of microglia activation after infection with the non-neurotropic A/CA/04/2009 H1N1 influenza virus. *PLoS One* 10(4)**,** e0124047. doi: 10.1371/journal.pone.0124047.

Salvi, V., Sozio, F., Sozzani, S., and Del Prete, A. (2017). Role of Atypical Chemokine Receptors in Microglial Activation and Polarization. *Front Aging Neurosci* 9**,** 148. doi: 10.3389/fnagi.2017.00148.

Samii, A., Nutt, J.G., and Ransom, B.R. (2004). Parkinson's disease. *Lancet* 363(9423)**,** 1783-1793. doi: 10.1016/S0140-6736(04)16305-8.

Sarkar, S., Rokad, D., Malovic, E., Luo, J., Harischandra, D.S., Jin, H., et al. (2019). Manganese activates NLRP3 inflammasome signaling and propagates exosomal release of ASC in microglial cells. *Sci Signal* 12(563). doi: 10.1126/scisignal.aat9900.

Sasco, A.J., and Paffenbarger, R.S., Jr. (1985). Measles infection and Parkinson's disease. *Am J Epidemiol* 122(6)**,** 1017-1031. doi: 10.1093/oxfordjournals.aje.a114183.

Schapira, A.H., and Jenner, P. (2011). Etiology and pathogenesis of Parkinson's disease. *Mov Disord* 26(6)**,** 1049-1055. doi: 10.1002/mds.23732.

Scheiblich, H., Dansokho, C., Mercan, D., Schmidt, S.V., Bousset, L., Wischhof, L., et al. (2021). Microglia jointly degrade fibrillar alpha-synuclein cargo by distribution through tunneling nanotubes. *Cell* 184(20)**,** 5089-5106 e5021. doi: 10.1016/j.cell.2021.09.007.

Schetters, S.T.T., Gomez-Nicola, D., Garcia-Vallejo, J.J., and Van Kooyk, Y. (2017). Neuroinflammation: Microglia and T Cells Get Ready to Tango. *Front Immunol* 8**,** 1905. doi: 10.3389/fimmu.2017.01905.

Schober, A. (2004). Classic toxin-induced animal models of Parkinson's disease: 6-OHDA and MPTP. *Cell Tissue Res* 318(1)**,** 215-224. doi: 10.1007/s00441-004-0938-y.

Schrag, A., and Taddei, R.N. (2017). Depression and Anxiety in Parkinson's Disease. *Int Rev Neurobiol* 133**,** 623-655. doi: 10.1016/bs.irn.2017.05.024.

Schullehner, J., Thygesen, M., Kristiansen, S.M., Hansen, B., Pedersen, C.B., and Dalsgaard, S. (2020). Exposure to Manganese in Drinking Water during Childhood and Association with Attention-Deficit Hyperactivity Disorder: A Nationwide Cohort Study. *Environ Health Perspect* 128(9)**,** 97004. doi: 10.1289/EHP6391.

Schwab, R.S. (1961). Symptomatology and medical treatment of Parkinson's disease. *Int J Neurol* 2**,** 61-75.

Sekine, S., and Youle, R.J. (2018). PINK1 import regulation; a fine system to convey mitochondrial stress to the cytosol. *BMC Biol* 16(1)**,** 2. doi: 10.1186/s12915-017-0470-7.

Serdar, M., Kempe, K., Herrmann, R., Picard, D., Remke, M., Herz, J., et al. (2020). Involvement of CXCL1/CXCR2 During Microglia Activation Following Inflammation-Sensitized Hypoxic-Ischemic Brain Injury in Neonatal Rats. *Front Neurol* 11**,** 540878. doi: 10.3389/fneur.2020.540878.

Shahnawaz, M., Mukherjee, A., Pritzkow, S., Mendez, N., Rabadia, P., Liu, X., et al. (2020). Discriminating alpha-synuclein strains in Parkinson's disease and multiple system atrophy. *Nature* 578(7794)**,** 273-277. doi: 10.1038/s41586-020-1984-7.

Sherer, T.B., Kim, J.H., Betarbet, R., and Greenamyre, J.T. (2003). Subcutaneous rotenone exposure causes highly selective dopaminergic degeneration and alpha-synuclein aggregation. *Exp Neurol* 179(1)**,** 9-16. doi: 10.1006/exnr.2002.8072.

Shiba, M., Bower, J.H., Maraganore, D.M., McDonnell, S.K., Peterson, B.J., Ahlskog, J.E., et al. (2000). Anxiety disorders and depressive disorders preceding Parkinson's disease: a case-control study. *Mov Disord* 15(4)**,** 669-677. doi: 10.1002/1531-8257(200007)15:4<669::aid-mds1011>3.0.co;2-5.

Shin, H.W., and Chung, S.J. (2012). Drug-induced parkinsonism. *J Clin Neurol* 8(1)**,** 15-21. doi: 10.3988/jcn.2012.8.1.15.

Shou, J., Peng, J., Zhao, Z., Huang, X., Li, H., Li, L., et al. (2019). CCL26 and CCR3 are associated with the acute inflammatory response in the CNS in experimental autoimmune encephalomyelitis. *J Neuroimmunol* 333**,** 576967. doi: 10.1016/j.jneuroim.2019.576967.

Sidransky, E., and Lopez, G. (2012). The link between the GBA gene and parkinsonism. *Lancet Neurol* 11(11)**,** 986-998. doi: 10.1016/S1474-4422(12)70190-4.

Smeyne, R.J., Breckenridge, C.B., Beck, M., Jiao, Y., Butt, M.T., Wolf, J.C., et al. (2016). Assessment of the Effects of MPTP and Paraquat on Dopaminergic Neurons and Microglia in the Substantia Nigra Pars Compacta of C57BL/6 Mice. *PLoS One* 11(10)**,** e0164094. doi: 10.1371/journal.pone.0164094.

Smeyne, R.J., Noyce, A.J., Byrne, M., Savica, R., and Marras, C. (2021). Infection and Risk of Parkinson's Disease. *J Parkinsons Dis* 11(1)**,** 31-43. doi: 10.3233/JPD-202279.

Smith, W.W., Margolis, R.L., Li, X., Troncoso, J.C., Lee, M.K., Dawson, V.L., et al. (2005). Alpha-synuclein phosphorylation enhances eosinophilic cytoplasmic inclusion formation in SH-SY5Y cells. *J Neurosci* 25(23)**,** 5544-5552. doi: 10.1523/JNEUROSCI.0482-05.2005.

Sofroniew, M.V. (2020). Astrocyte Reactivity: Subtypes, States, and Functions in CNS Innate Immunity. *Trends Immunol* 41(9)**,** 758-770. doi: 10.1016/j.it.2020.07.004.

Sofroniew, M.V., and Vinters, H.V. (2010). Astrocytes: biology and pathology. *Acta Neuropathol* 119(1)**,** 7-35. doi: 10.1007/s00401-009-0619-8.

Sotnikova, T.D., Beaulieu, J.M., Espinoza, S., Masri, B., Zhang, X., Salahpour, A., et al. (2010). The dopamine metabolite 3-methoxytyramine is a neuromodulator. *PLoS One* 5(10)**,** e13452. doi: 10.1371/journal.pone.0013452.

Soto, C. (2001). Protein misfolding and disease; protein refolding and therapy. *FEBS Lett* 498(2-3)**,** 204-207. doi: 10.1016/s0014-5793(01)02486-3.

Soto, C. (2012). Transmissible proteins: expanding the prion heresy. *Cell* 149(5)**,** 968-977. doi: 10.1016/j.cell.2012.05.007.

Soto, C., and Pritzkow, S. (2018). Protein misfolding, aggregation, and conformational strains in neurodegenerative diseases. *Nat Neurosci* 21(10)**,** 1332-1340. doi: 10.1038/s41593-018-0235-9.

Spillantini, M.G., Schmidt, M.L., Lee, V.M., Trojanowski, J.Q., Jakes, R., and Goedert, M. (1997). Alpha-synuclein in Lewy bodies. *Nature* 388(6645)**,** 839-840. doi: 10.1038/42166.

Stephen, T.L., Cacciottolo, M., Balu, D., Morgan, T.E., LaDu, M.J., Finch, C.E., et al. (2019). APOE genotype and sex affect microglial interactions with plaques in Alzheimer's disease mice. *Acta Neuropathol Commun* 7(1)**,** 82. doi: 10.1186/s40478-019-0729-z.

Stopschinski, B.E., and Diamond, M.I. (2017). The prion model for progression and diversity of neurodegenerative diseases. *Lancet Neurol* 16(4)**,** 323-332. doi: 10.1016/S1474-4422(17)30037-6.

Subbarayan, M.S., Hudson, C., Moss, L.D., Nash, K.R., and Bickford, P.C. (2020). T cell infiltration and upregulation of MHCII in microglia leads to accelerated neuronal loss in an alpha-synuclein rat model of Parkinson's disease. *J Neuroinflammation* 17(1)**,** 242. doi: 10.1186/s12974-020-01911-4.

Subramaniam, S.R., and Federoff, H.J. (2017). Targeting Microglial Activation States as a Therapeutic Avenue in Parkinson's Disease. *Front Aging Neurosci* 9**,** 176. doi: 10.3389/fnagi.2017.00176.

Sulzer, D., Alcalay, R.N., Garretti, F., Cote, L., Kanter, E., Agin-Liebes, J., et al. (2017). T cells from patients with Parkinson's disease recognize alpha-synuclein peptides. *Nature* 546(7660)**,** 656-661. doi: 10.1038/nature22815.

Sulzer, D., and Edwards, R.H. (2019). The physiological role of alpha-synuclein and its relationship to Parkinson's Disease. *J Neurochem* 150(5)**,** 475-486. doi: 10.1111/jnc.14810.

Sveinbjornsdottir, S. (2016). The clinical symptoms of Parkinson's disease. *J Neurochem* 139 Suppl 1**,** 318-324. doi: 10.1111/jnc.13691.

Svensson, E., Horvath-Puho, E., Thomsen, R.W., Djurhuus, J.C., Pedersen, L., Borghammer, P., et al. (2015). Vagotomy and subsequent risk of Parkinson's disease. *Ann Neurol* 78(4)**,** 522-529. doi: 10.1002/ana.24448.

Szklarczyk, D., Gable, A.L., Nastou, K.C., Lyon, D., Kirsch, R., Pyysalo, S., et al. (2021). The STRING database in 2021: customizable protein-protein networks, and functional characterization of user-uploaded gene/measurement sets. *Nucleic Acids Res* 49(D1)**,** D605-D612. doi: 10.1093/nar/gkaa1074.

Takeda, A. (2003). Manganese action in brain function. *Brain Res Brain Res Rev* 41(1)**,** 79-87. doi: 10.1016/s0165-0173(02)00234-5.

Tan, J.S.Y., Chao, Y.X., Rotzschke, O., and Tan, E.K. (2020). New Insights into Immune-Mediated Mechanisms in Parkinson's Disease. *Int J Mol Sci* 21(23). doi: 10.3390/ijms21239302.

Tanaka, H., Park, C.H., Ninomiya, A., Ozaki, H., Takada, A., Umemura, T., et al. (2003). Neurotropism of the 1997 Hong Kong H5N1 influenza virus in mice. *Vet Microbiol* 95(1-2)**,** 1-13. doi: 10.1016/s0378-1135(03)00132-9.

Tanner, C.M., Kamel, F., Ross, G.W., Hoppin, J.A., Goldman, S.M., Korell, M., et al. (2011). Rotenone, paraquat, and Parkinson's disease. *Environ Health Perspect* 119(6)**,** 866-872. doi: 10.1289/ehp.1002839.

Tapias, V., and Greenamyre, J.T. (2014). A rapid and sensitive automated image-based approach for in vitro and in vivo characterization of cell morphology and quantification of cell number and neurite architecture. *Curr Protoc Cytom* 68**,** 12 33 11-22. doi: 10.1002/0471142956.cy1233s68.

Tapias, V., Greenamyre, J.T., and Watkins, S.C. (2013). Automated imaging system for fast quantitation of neurons, cell morphology and neurite morphometry in vivo and in vitro. *Neurobiol Dis* 54**,** 158-168. doi: 10.1016/j.nbd.2012.11.018.

Tarakad, A., and Jankovic, J. (2017). Anosmia and Ageusia in Parkinson's Disease. *Int Rev Neurobiol* 133**,** 541-556. doi: 10.1016/bs.irn.2017.05.028.

Tartaglia, G.G., Pawar, A.P., Campioni, S., Dobson, C.M., Chiti, F., and Vendruscolo, M. (2008). Prediction of aggregation-prone regions in structured proteins. *J Mol Biol* 380(2)**,** 425-436. doi: 10.1016/j.jmb.2008.05.013.

Tay, T.L., Mai, D., Dautzenberg, J., Fernandez-Klett, F., Lin, G., Sagar, et al. (2017). A new fate mapping system reveals context-dependent random or clonal expansion of microglia. *Nat Neurosci* 20(6)**,** 793-803. doi: 10.1038/nn.4547.

Taylor, C.A., Hutchens, S., Liu, C., Jursa, T., Shawlot, W., Aschner, M., et al. (2019). SLC30A10 transporter in the digestive system regulates brain manganese under basal conditions while brain SLC30A10 protects against neurotoxicity. *J Biol Chem* 294(6)**,** 1860-1876. doi: 10.1074/jbc.RA118.005628.

Teismann, P., Tieu, K., Choi, D.K., Wu, D.C., Naini, A., Hunot, S., et al. (2003). Cyclooxygenase-2 is instrumental in Parkinson's disease neurodegeneration. *Proc Natl Acad Sci U S A* 100(9)**,** 5473-5478. doi: 10.1073/pnas.0837397100.

Thibaudeau, T.A., Anderson, R.T., and Smith, D.M. (2018). A common mechanism of proteasome impairment by neurodegenerative disease-associated oligomers. *Nat Commun* 9(1)**,** 1097. doi: 10.1038/s41467-018-03509-0.

Tjalkens, R.B., Zoran, M.J., Mohl, B., and Barhoumi, R. (2006). Manganese suppresses ATP-dependent intercellular calcium waves in astrocyte networks through alteration of mitochondrial and endoplasmic reticulum calcium dynamics. *Brain Res* 1113(1)**,** 210-219. doi: 10.1016/j.brainres.2006.07.053.

Town, T., Nikolic, V., and Tan, J. (2005). The microglial "activation" continuum: from innate to adaptive responses. *J Neuroinflammation* 2**,** 24. doi: 10.1186/1742-2094-2-24.

Troncoso-Escudero, P., Parra, A., Nassif, M., and Vidal, R.L. (2018). Outside in: Unraveling the Role of Neuroinflammation in the Progression of Parkinson's Disease. *Front Neurol* 9**,** 860. doi: 10.3389/fneur.2018.00860.

Tuschl, K., Mills, P.B., and Clayton, P.T. (2013). Manganese and the brain. *Int Rev Neurobiol* 110**,** 277-312. doi: 10.1016/B978-0-12-410502-7.00013-2.

Tysnes, O.B., and Storstein, A. (2017). Epidemiology of Parkinson's disease. *J Neural Transm (Vienna)* 124(8)**,** 901-905. doi: 10.1007/s00702-017-1686-y.

Ullman, O., Fisher, C.K., and Stultz, C.M. (2011). Explaining the structural plasticity of alpha-synuclein. *J Am Chem Soc* 133(48)**,** 19536-19546. doi: 10.1021/ja208657z.

Ulmer, T.S., Bax, A., Cole, N.B., and Nussbaum, R.L. (2005). Structure and dynamics of micelle-bound human alpha-synuclein. *J Biol Chem* 280(10)**,** 9595-9603. doi: 10.1074/jbc.M411805200.

Vehovszky, A., Szabo, H., Hiripi, L., Elliott, C.J., and Hernadi, L. (2007). Behavioural and neural deficits induced by rotenone in the pond snail Lymnaea stagnalis. A possible model for Parkinson's disease in an invertebrate. *Eur J Neurosci* 25(7)**,** 2123-2130. doi: 10.1111/j.1460-9568.2007.05467.x.

Wakabayashi, K., Hayashi, S., Yoshimoto, M., Kudo, H., and Takahashi, H. (2000). NACP/alpha-synuclein-positive filamentous inclusions in astrocytes and oligodendrocytes of Parkinson's disease brains. *Acta Neuropathol* 99(1)**,** 14-20. doi: 10.1007/pl00007400.

Wakabayashi, K., Tanji, K., Mori, F., and Takahashi, H. (2007). The Lewy body in Parkinson's disease: molecules implicated in the formation and degradation of alpha-synuclein aggregates. *Neuropathology* 27(5)**,** 494-506. doi: 10.1111/j.1440-1789.2007.00803.x.

Wakabayashi, K., Tanji, K., Odagiri, S., Miki, Y., Mori, F., and Takahashi, H. (2013). The Lewy body in Parkinson's disease and related neurodegenerative disorders. *Mol Neurobiol* 47(2)**,** 495-508. doi: 10.1007/s12035-012-8280-y.

Walker, L.C., and Jucker, M. (2015). Neurodegenerative diseases: expanding the prion concept. *Annu Rev Neurosci* 38**,** 87-103. doi: 10.1146/annurev-neuro-071714-033828.

Wang, C., Fan, L., Khawaja, R.R., Liu, B., Zhan, L., Kodama, L., et al. (2022). Microglial NF-kappaB drives tau spreading and toxicity in a mouse model of tauopathy. *Nat Commun* 13(1)**,** 1969. doi: 10.1038/s41467-022-29552-6.

Wang, D.X., Chen, A.D., Wang, Q.J., Xin, Y.Y., Yin, J., and Jing, Y.H. (2020a). Protective effect of metformin against rotenone-induced parkinsonism in mice. *Toxicol Mech Methods* 30(5)**,** 350-357. doi: 10.1080/15376516.2020.1741053.

Wang, J., Wang, C.E., Orr, A., Tydlacka, S., Li, S.H., and Li, X.J. (2008). Impaired ubiquitin-proteasome system activity in the synapses of Huntington's disease mice. *J Cell Biol* 180(6)**,** 1177-1189. doi: 10.1083/jcb.200709080.

Wang, M., Ye, X., Hu, J., Zhao, Q., Lv, B., Ma, W., et al. (2020b). NOD1/RIP2 signalling enhances the microglia-driven inflammatory response and undergoes crosstalk with inflammatory cytokines to exacerbate brain damage following intracerebral haemorrhage in mice. *J Neuroinflammation* 17(1)**,** 364. doi: 10.1186/s12974-020-02015-9.

Watts, J.C., Condello, C., Stohr, J., Oehler, A., Lee, J., DeArmond, S.J., et al. (2014). Serial propagation of distinct strains of Abeta prions from Alzheimer's disease patients. *Proc Natl Acad Sci U S A* 111(28)**,** 10323-10328. doi: 10.1073/pnas.1408900111.

Wei, Y., Chen, T., Bosco, D.B., Xie, M., Zheng, J., Dheer, A., et al. (2021). The complement C3-C3aR pathway mediates microglia-astrocyte interaction following status epilepticus. *Glia* 69(5)**,** 1155-1169. doi: 10.1002/glia.23955.

Westermark, G.T., and Westermark, P. (2010). Prion-like aggregates: infectious agents in human disease. *Trends Mol Med* 16(11)**,** 501-507. doi: 10.1016/j.molmed.2010.08.004.

Wilhelmsson, U., Bushong, E.A., Price, D.L., Smarr, B.L., Phung, V., Terada, M., et al. (2006). Redefining the concept of reactive astrocytes as cells that remain within their unique domains upon reaction to injury. *Proc Natl Acad Sci U S A* 103(46)**,** 17513-17518. doi: 10.1073/pnas.0602841103.

Winner, B., Jappelli, R., Maji, S.K., Desplats, P.A., Boyer, L., Aigner, S., et al. (2011). In vivo demonstration that alpha-synuclein oligomers are toxic. *Proc Natl Acad Sci U S A* 108(10)**,** 4194-4199. doi: 10.1073/pnas.1100976108.

Woulfe, J., Hoogendoorn, H., Tarnopolsky, M., and Munoz, D.G. (2000). Monoclonal antibodies against Epstein-Barr virus cross-react with alpha-synuclein in human brain. *Neurology* 55(9)**,** 1398-1401. doi: 10.1212/wnl.55.9.1398.

Xie, W., Wan, O.W., and Chung, K.K. (2010). New insights into the role of mitochondrial dysfunction and protein aggregation in Parkinson's disease. *Biochim Biophys Acta* 1802(11)**,** 935-941. doi: 10.1016/j.bbadis.2010.07.014.

Yanguas-Casas, N. (2020). Physiological sex differences in microglia and their relavence in neurological disorders *Neuroimmunology and Neuroinflammation* 7.

Yao, L., Wu, J., Koc, S., and Lu, G. (2021). Genetic Imaging of Neuroinflammation in Parkinson's Disease: Recent Advancements. *Front Cell Dev Biol* 9**,** 655819. doi: 10.3389/fcell.2021.655819.

Yen, S.S. (2011). Proteasome degradation of brain cytosolic tau in Alzheimer's disease. *Int J Clin Exp Pathol* 4(4)**,** 385-402.

Zanardi, A.P.J., da Silva, E.S., Costa, R.R., Passos-Monteiro, E., Dos Santos, I.O., Kruel, L.F.M., et al. (2021). Gait parameters of Parkinson's disease compared with healthy controls: a systematic review and meta-analysis. *Sci Rep* 11(1)**,** 752. doi: 10.1038/s41598-020-80768-2.

Zeng, X.S., Geng, W.S., and Jia, J.J. (2018). Neurotoxin-Induced Animal Models of Parkinson Disease: Pathogenic Mechanism and Assessment. *ASN Neuro* 10**,** 1759091418777438. doi: 10.1177/1759091418777438.

Zengeler, K.E., and Lukens, J.R. (2021). Innate immunity at the crossroads of healthy brain maturation and neurodevelopmental disorders. *Nat Rev Immunol* 21(7)**,** 454-468. doi: 10.1038/s41577-020-00487-7.

Zhang, L., Zhou, L., Bao, L., Liu, J., Zhu, H., Lv, Q., et al. (2021). SARS-CoV-2 crosses the blood-brain barrier accompanied with basement membrane disruption without tight junctions alteration. *Signal Transduct Target Ther* 6(1)**,** 337. doi: 10.1038/s41392-021-00719-9.

Zhang, S., Zhou, Z., and Fu, J. (2003). Effect of manganese chloride exposure on liver and brain mitochondria function in rats. *Environ Res* 93(2)**,** 149-157. doi: 10.1016/s0013-9351(03)00109-9.

Zhang, X., Kracht, L., Lerario, A.M., Dubbelaar, M.L., Brouwer, N., Wesseling, E.M., et al. (2022). Epigenetic regulation of innate immune memory in microglia. *J Neuroinflammation* 19(1)**,** 111. doi: 10.1186/s12974-022-02463-5.

Zheng, T., and Zhang, Z. (2021). Activated microglia facilitate the transmission of alpha-synuclein in Parkinson's disease. *Neurochem Int* 148**,** 105094. doi: 10.1016/j.neuint.2021.105094.

Zhernakova, A., Kurilshikov, A., Bonder, M.J., Tigchelaar, E.F., Schirmer, M., Vatanen, T., et al. (2016). Population-based metagenomics analysis reveals markers for gut microbiome composition and diversity. *Science* 352(6285)**,** 565-569. doi: 10.1126/science.aad3369.

Zhong, N., Kim, C.Y., Rizzu, P., Geula, C., Porter, D.R., Pothos, E.N., et al. (2006). DJ-1 transcriptionally up-regulates the human tyrosine hydroxylase by inhibiting the sumoylation of pyrimidine tract-binding protein-associated splicing factor. *J Biol Chem* 281(30)**,** 20940-20948. doi: 10.1074/jbc.M601935200.

Zhou, B., Zuo, Y.X., and Jiang, R.T. (2019). Astrocyte morphology: Diversity, plasticity, and role in neurological diseases. *CNS Neurosci Ther* 25(6)**,** 665-673. doi: 10.1111/cns.13123.

Zong, X., Li, Y., Liu, C., Qi, W., Han, D., Tucker, L., et al. (2020). Theta-burst transcranial magnetic stimulation promotes stroke recovery by vascular protection and neovascularization. *Theranostics* 10(26)**,** 12090-12110. doi: 10.7150/thno.51573.

Zoni, S., Albini, E., and Lucchini, R. (2007). Neuropsychological testing for the assessment of manganese neurotoxicity: a review and a proposal. *Am J Ind Med* 50(11)**,** 812-830. doi: 10.1002/ajim.20518.

Zoroddu, M.A., Aaseth, J., Crisponi, G., Medici, S., Peana, M., and Nurchi, V.M. (2019). The essential metals for humans: a brief overview. *J Inorg Biochem* 195**,** 120-129. doi: 10.1016/j.jinorgbio.2019.03.013.

APPENDIX I
CHAPTER 2 SUPPLEMENTARY FIGURES

APPENDIX I

CHAPTER 2 SUPPLEMENTARY FIGURES

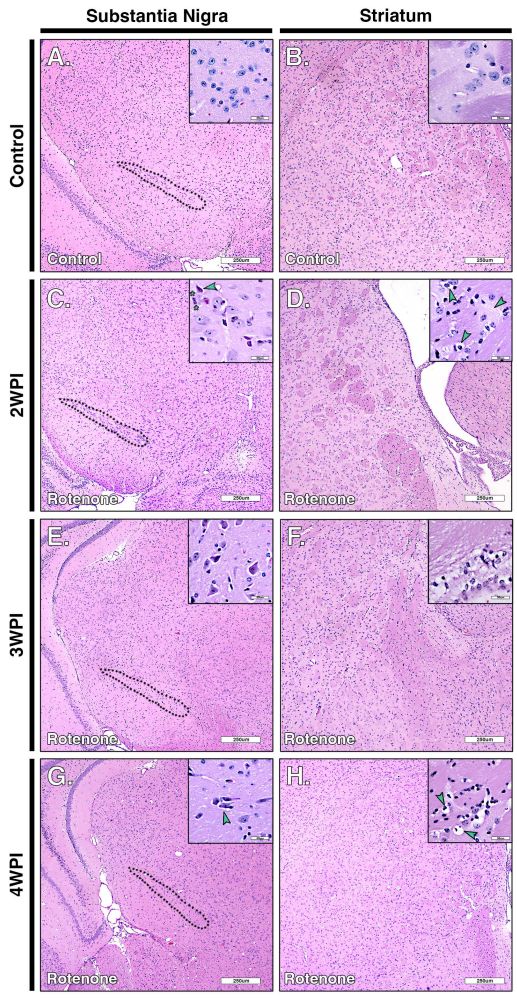

Supplemental Figure 1. Pathological analysis reveals time-dependent neuronal and glial changes within the nigro-striatal system following systemic administration of rotenone. (**A,B**) Control animals presented with normal cellular borders, with margins in the SN (**A**) and the ST (**B**) that were unremarkable in the cell populations present and had clear striosomes and axonal functionality. Pathological changes within the SN at 2WPI reveal hyper-eosinophilic cytoplasmic neurons (**C**, arrowheads) with focal neuronal apoptosis and presentation of Alzheimer Type II cells (**C**, asterisk). Cytotoxic edema is present surrounding glial cells within the ST and there is rare intramyelinic edema (**D**, arrowheads). (**E**) The SN at 3WPI had decreased numbers of neurons within the SN, with surviving neurons characterized by angular morphology, along with prolific spongiosis in the ST and persistent intramyelinic edema **(F)**. Marked loss of neuronal density was observed in the SN at 4WPI with the occurrence of angular bordered cells (**G**, arrowheads). Cytotoxic edema was present within the ST (**H**, arrowheads), and glial cell infiltration into striosomes.

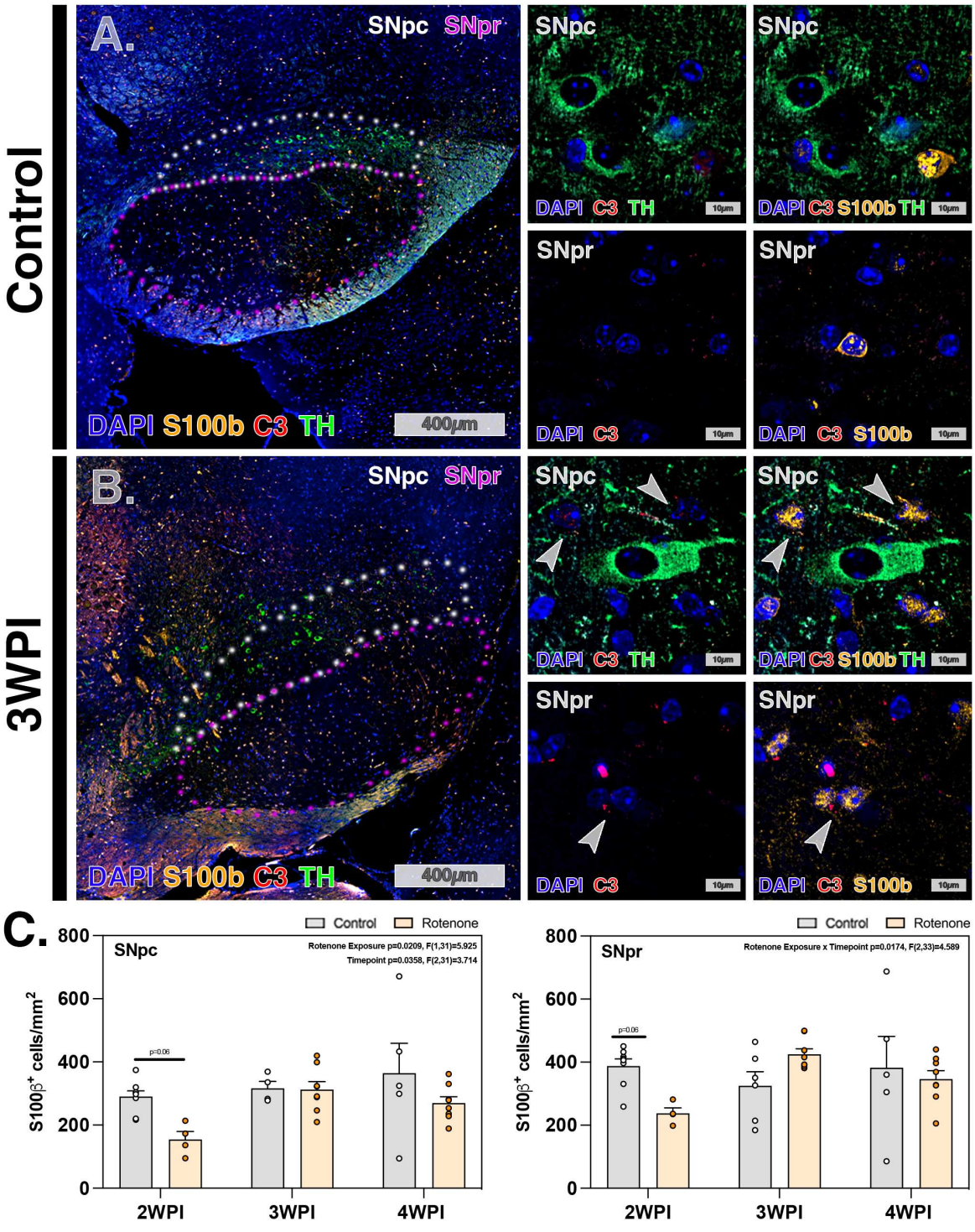

Supplemental Figure 2. S100β$^+$ populations' adaptation to rotenone exposure is time dependent. Montage images of control (**A**) and 3 WPI rotenone exposed (**B**) animals with high magnification inserts of TH$^+$ DAn (green), S100β$^+$ astrocytes (orange), and C3 (red) in the SNpc and SNpr. S100β$^+$ cell types correlating with positive C3 staining (arrowheads) (**A-B**, high magnification) and quantification of overall S100β$^+$ populations in the SNpc and SNpr (**C**).

APPENDIX II
CHAPTER 3 SUPPLEMENTARY FIGURES

APPENDIX II

CHAPTER 3 SUPPLEMENTARY FIGURES

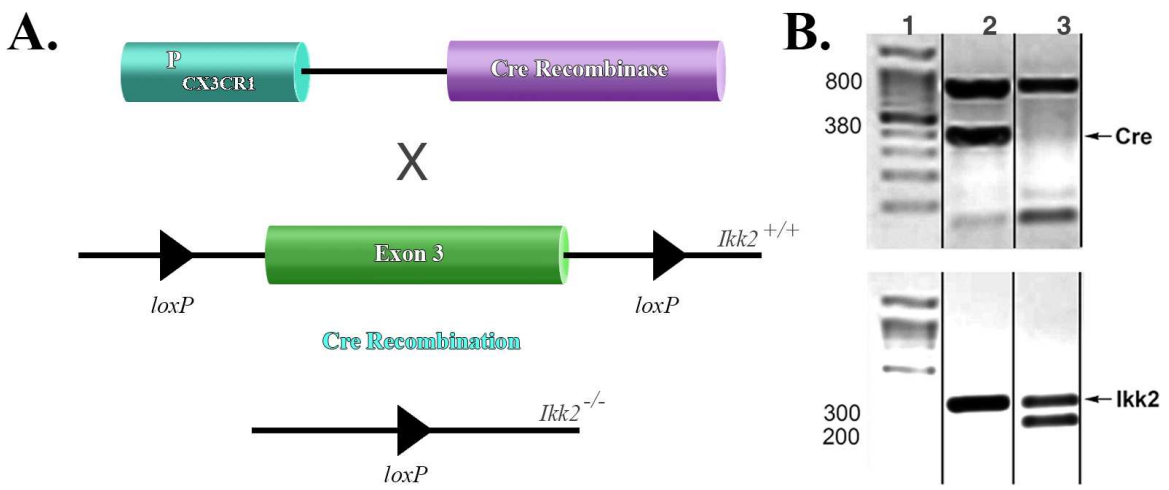

Supplemental Figure 3. Characterization and genotypic validation of CX3CR1-Cre::IKK2$^{fl/fl}$ transgenic mice. Schematic representation of CX3CR1 promotor driven Cre-recombinase in combination with IKK2 in-line orientation floxed sequences spanning exon 3 resulting in deletion of IKK2 (**A**). Ethidium bromide identification of Cre-recombinase in CX3CR1-Cre animals (lane 2) and IKK2 loxP sequences in IKK2$^{fl/fl}$ animals (lane 3) compared to sequence ladder (lane 1; **B**).

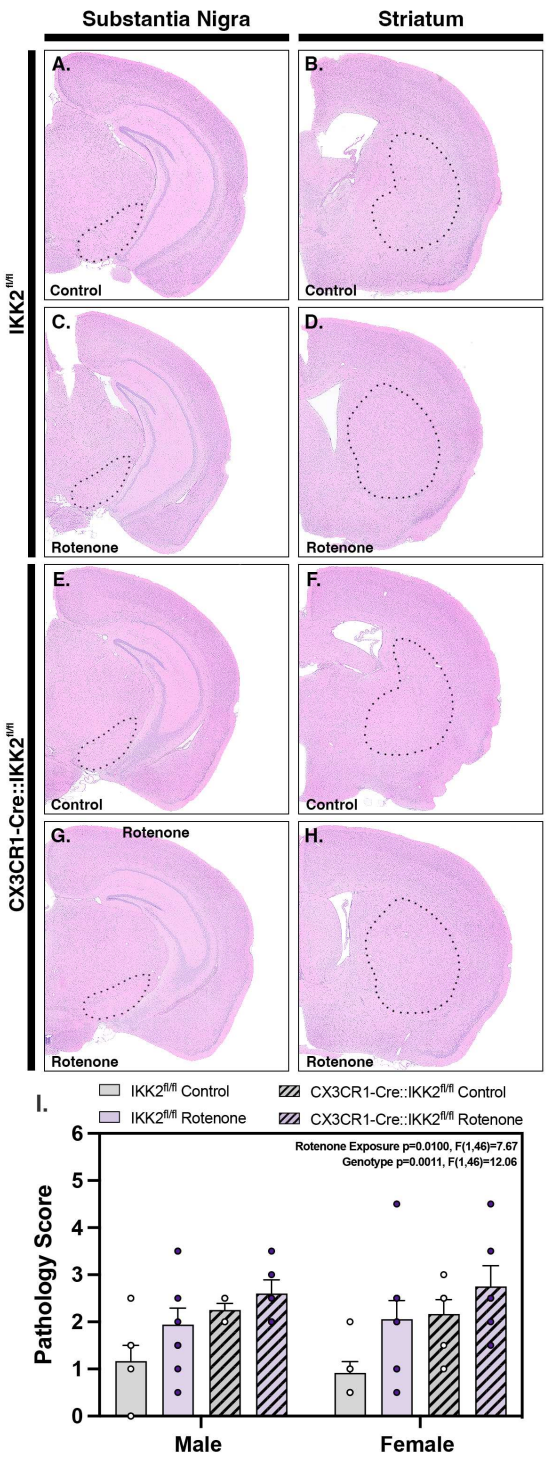

Supplemental Figure 4. Microglial NF-κB inhibition increases pathological scoring and cellular infiltrate into the substantia nigra and striatum. Full hemisphere montage images of the SN and ST for WT control (**A, B**), WT rotenone (**C, D**), KO control (**E, F**), and KO rotenone (**G, H**), respectively. Pathological scoring of cellular infiltration and neurodegeneration in the SN of animals (**I**).

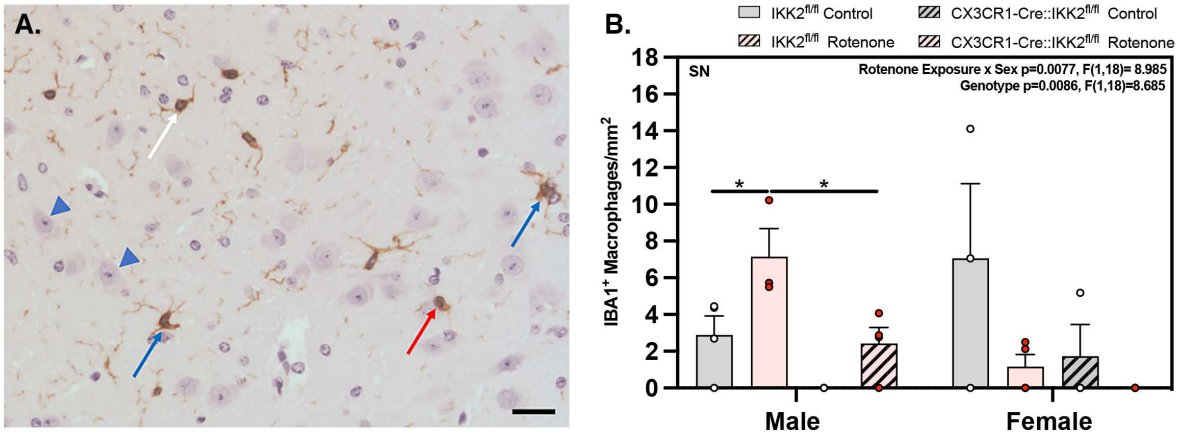

Supplemental Figure 5. Rotenone induces peripheral macrophage infiltration into the basal midbrain. Photomicrograph of rotenone-treated SN immunostained using antibodies directed against the microglia/macrophage-specific protein IBA-1 with DAB chromogen (brown). Macrophages (red arrows) are round and lack tendril-like processes. Resting microglia have a small nuclei and long thin processes (white arrow). Activated microglia have larger nuclei and shorter, thickened processes (blue arrows). Blue arrowheads mark Nissl-stained DAn in the SNpc. Scale bar, 30 microns (**A**). Quantification of peripheral macrophage populations in the SN (**B**). n=4 per group. *p<0.05.

APPENDIX III
CHAPTER 3 SUPPLEMENTARY TABLES

APPENDIX III

CHAPTER 3 SUPPLEMEMTARY TABLES

Supplemental Table 1. Additional Primer Sequences for Gene Expression in qRT-PCR Analysis

Gene	Forward Primer 5'-3'	Reverse Primer 5'-3'	Probe 5'-3'	Amplicon Length
B-actin	CTT TTC CAG CCT TCC TTC TTG	CAT AGA GGT CTT TAC GGA TGT CAA C	TGG CAT CCA TGA AAC TAC AT	103 bp
p62	TCC CCA CAG TTC CCC ATT G	AGG CTG TAT CCC GAT GTC AG	ACT GCT GAG TCA CGC TTG GC	125 bp
Snca	TTC AGA GGA AGG CTA CCA AGA C	CAT GAC TGG GCA CAT TGG AAC	GGC TGC TCT TCC ATG GCG TA	125 bp
Nr4a2	CAA GCA CGT CAA AGA ACT GGA	GTG AGG GCT AGG GGT CTA CA	CTG GTC ACA TGG GCA GAG AG	125 bp

APPENDIX IV
CHAPTER 4 SUPPLEMENTARY FIGURES

APPENDIX IV

CHAPTER 4 SUPPLEMENTARY FIGURES

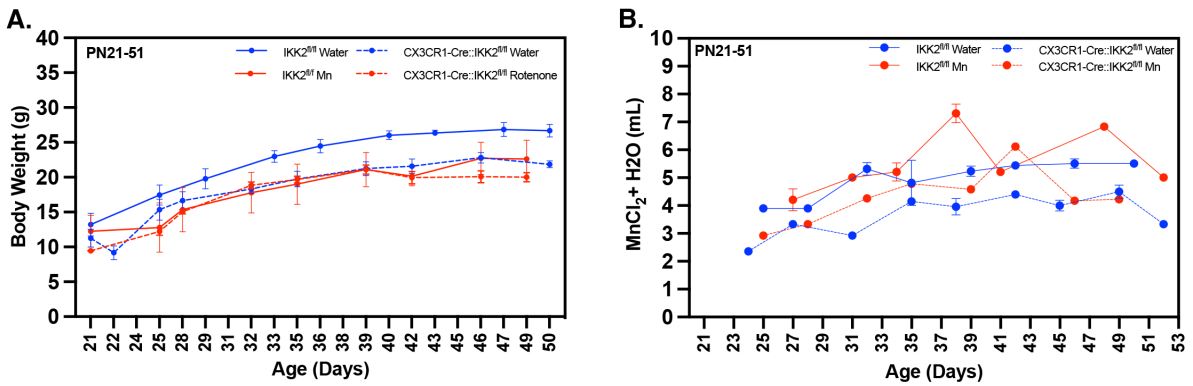

Supplemental Figure 6. Animal weight and water consumption during juvenile Mn exposure. Total body weight (g) of juvenile WT water (blue solid line), WT Mn (red solid line), KO water (blue dotted line), and KO (red dotted line) Mn during exposure (**A**). Daily averaged water consumption (mL) per animal during juvenile Mn exposure (**B**).

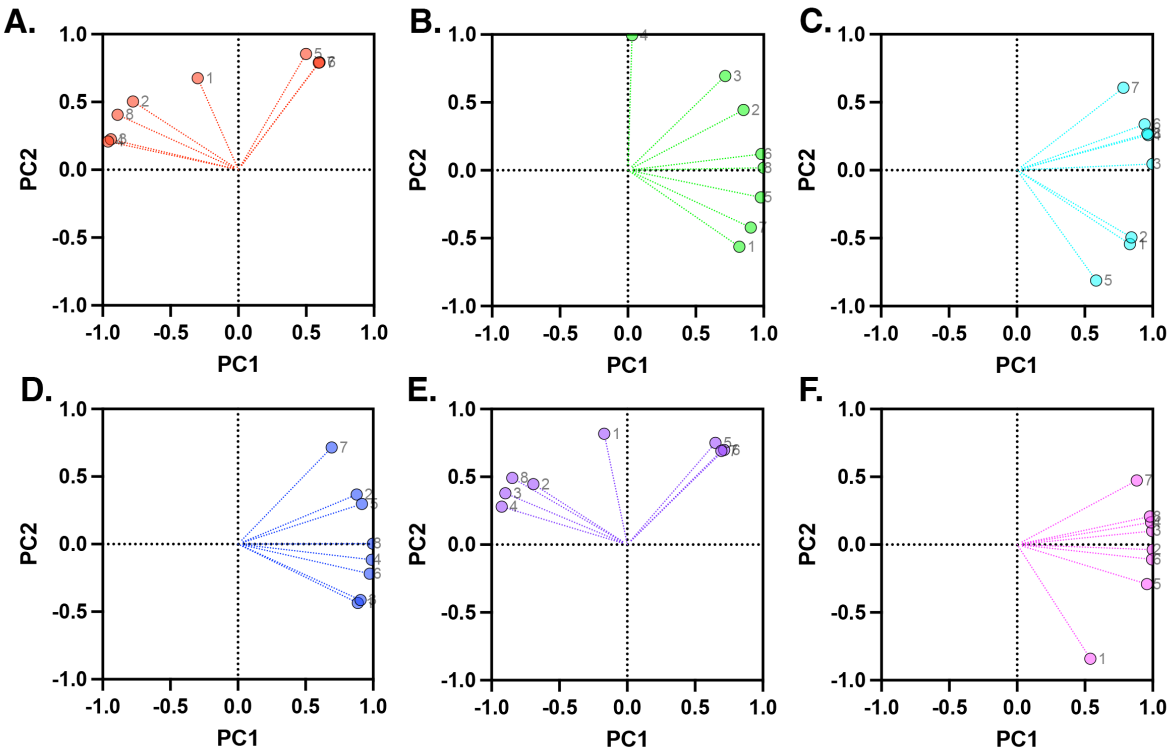

Supplemental Figure 7. Pro-inflammatory astrocyte and pan-inflammatory profiles account for variance observed between primed microglia and environmental exposures. PCA analysis of pro-inflammatory astrocyte (**A**), pro-inflammatory microglia (**B**), mitophagy associated (**C**), neuronal associated (**D**), pan-inflammatory (**E**), and glial mediated inflammatory (**F**) gene expression between 1) WT control, 2) WT rotenone, 3) WT Mn, 4) WT Mn and rotenone, 5) KO control, 6) KO rotenone, 7) KO Mn, and 8) KO Mn and rotenone exposed mice.

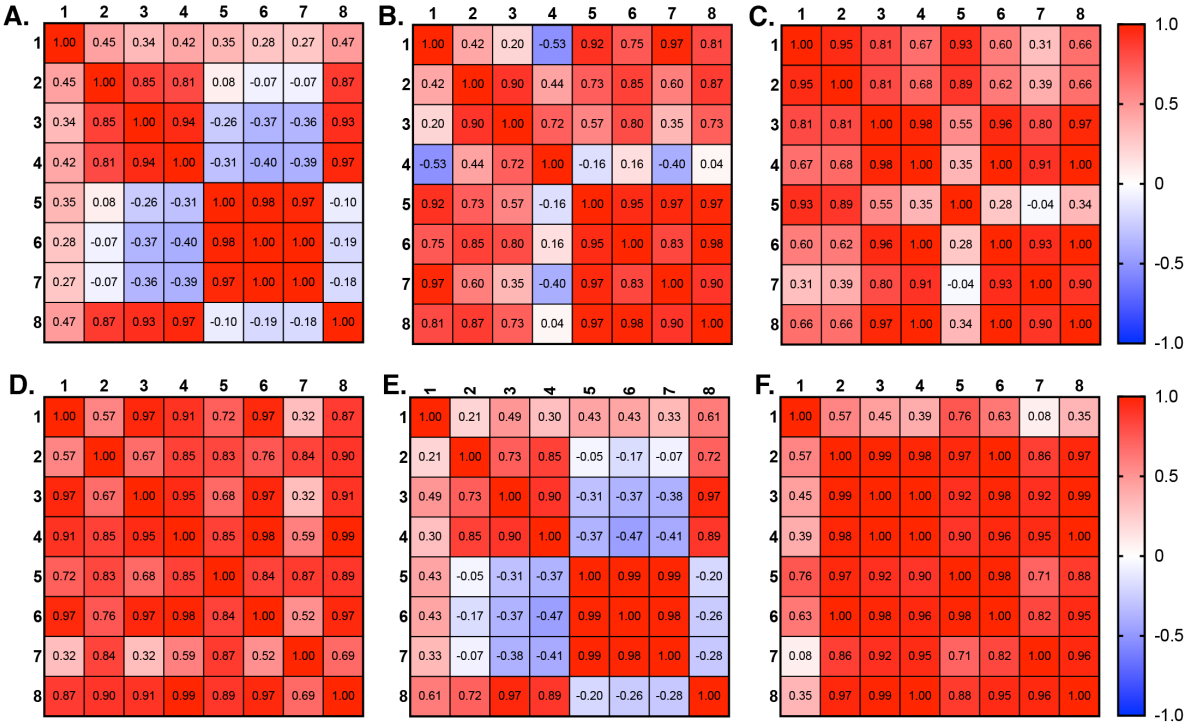

Supplemental Figure 8. Association of gene regulation imply pro-inflammatory astrocytes and pan-inflammatory signaling in overt disease. Pearson correlation coefficients between 1) WT control, 2) WT rotenone, 3) WT Mn, 4) WT Mn rotenone, 5) KO control, 6) KO rotenone, 7) KO Mn, 8) KO Mn rotenone for the combination of pro-inflammatory astrocytes (**A**), pro-inflammatory microglia (**B**), mitophagy associated (**C**), neuronal associated (**D**), pan-inflammatory (**E**), and glial mediated inflammatory genes (**F**).

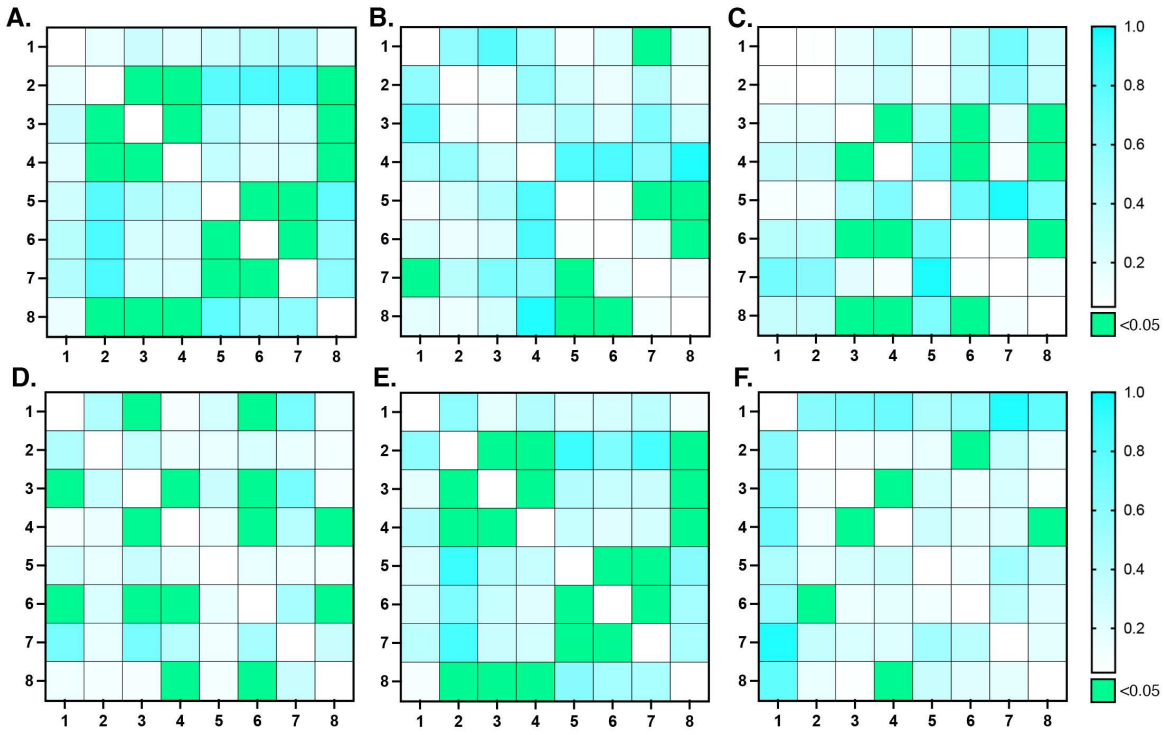

Supplemental Figure 9. Graphical representation of statistical significance between genotype:exposure correlation coefficient analysis. Statistical *p*-value of Pearson correlation coefficients between 1) WT control, 2) WT rotenone, 3) WT Mn, 4) WT Mn rotenone, 5) KO control, 6) KO rotenone, 7) KO Mn, 8) KO Mn rotenone for the combination of pro-inflammatory astrocytes (**A**), pro-inflammatory microglia (**B**), mitophagy associated (**C**), neuronal (**D**), pan-inflammatory (**E**), and glial mediated inflammation (**F**).

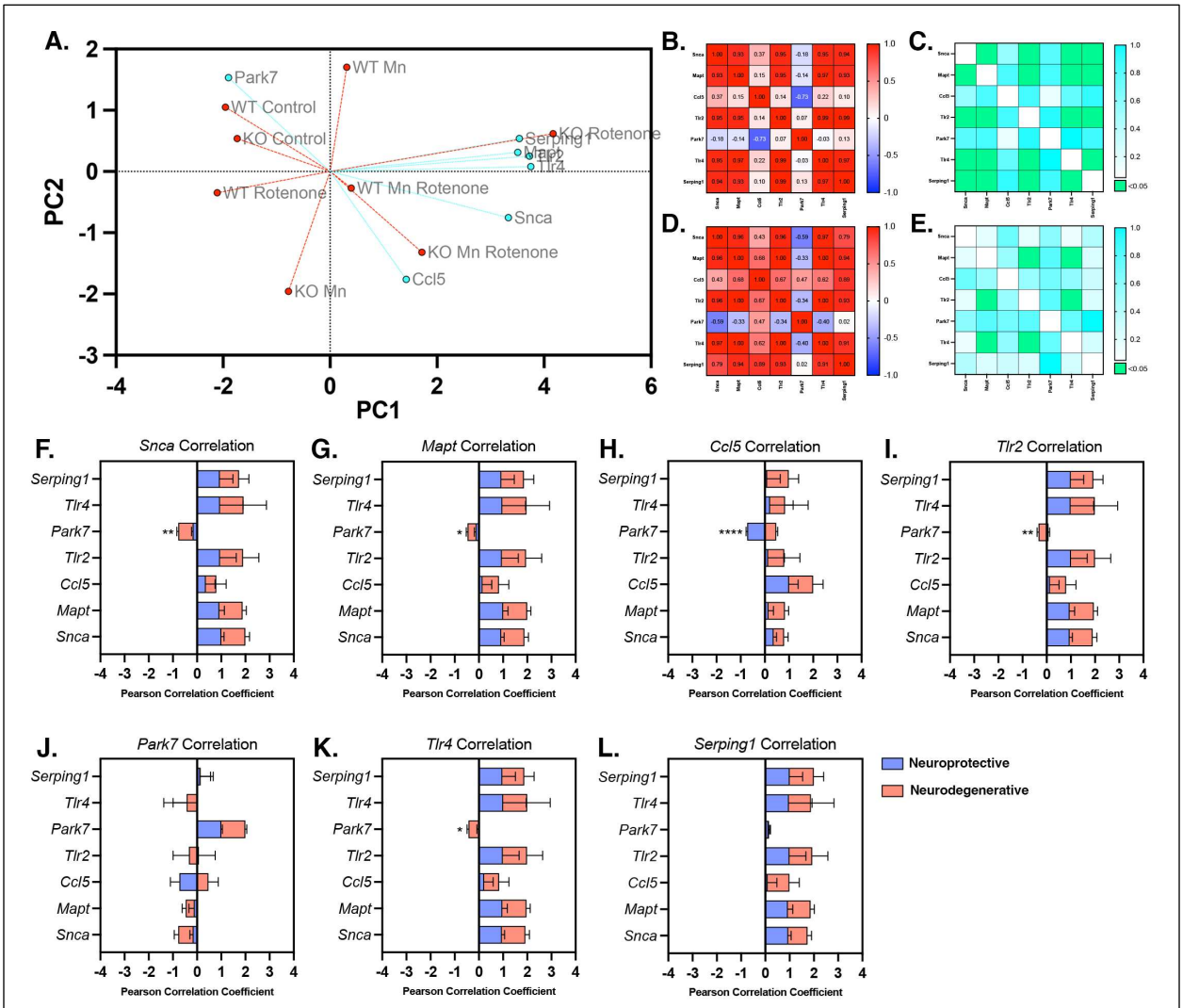

Supplemental Figure 10. Individual gene contribution analysis identifies astrocyte, oxidative stress, and α-synuclein as key signatures of neurodegeneration. Multiple-component PCA analysis of all gene investigated identified *Park7*, *Serping1*, *Mapt*, *Tlr2*, *Tlr4*, *Snca*, and *Ccl5* as driving factors that lead to the variability observed within single and dual environmental exposure models that lead to neurodegeneration (**A**). Pearson correlation coefficient analysis of these genes, along with *p*-value graphical representation of positively correlations in neuroprotective (**B, C**) and neurotoxic (**D, E**) outcomes. Individual gene transcript correlational coefficient differences between neuroprotective (blue) and neurotoxic (red) associations (**F-L**). *n*=6 per group. **p*<0.05, ***p*<0.001, *****p*<0.0001.

APPENDIX V
CHAPTER 4 SUPPLEMENTARY TABLES

APPENDIX V

CHAPTER 4 SUPPLEMENTARY TABLES

Supplemental Table 2. One-step focus panel qRT-PCR primer and probe sequences

Gene Name	Sequence (5'-3') F-Forward, R-Reverse, P-Probe	Amplicon Size (bp)	Accession Number
β-Actin	F: CTTTTCCAGCCTTCCTTCTTG R: CATAGAGGTCTTTACGGATGTCAAC P: TGGCATCCATGAAACTACAT	103	11461
C1qa	F: CGAAAAGGACCCCGCAAAG R: CGCAGGAGATGGCAGGAT P: TTCCTCATTTTCCCCTCGGC	125	12259
C3	F: GCAACAAACGACACTCAGGA R: ACCACATCCCAGATCTTGCT P: GGCTGTGGACAAGGGAGTGT	126	12266
Ccl2	F: GCCAGCTCTCTCTTCCTCCA R: CAGGTGAGTGGGGCGTTAAC P: GGTCCCTGTCATGCTTCTGG	126	20296
Ccl5	F: TGCTGCTTTGCCTACCTCTC R: GCACACACTTGGCGGTTC P: GTGCCCACGTCAAGGAGTATT	125	20304
Cd14	F: CTGCCCTCTCCACCTTAGAC R: TCTCCATCCCCGCGTTAC P: AGCCCTCTGTCCCCTCAAGT	126	12475
Csf1	F: GTGACAGGGCTCTCATTTGC R: AGCTTACAGACCACTCTCCT P: GCTGAGTCCCCCTTTCCTGC	125	12977
Gfap	F: GAAGCCCAAGGACACAGATG R: AAACCAAACCCCACCCTCA P: AAGCAGCAACAGCCTCCTCC	125	14580
Il1a	F: CCGTACATTCCTGCACTTGG R: GAATACCCAGACAGCTTTAAGGAC P: TGAGTCAGTCTTTCTCCCTCCC	125	16175
Il1β	F: GCTTTCAGGAATGGAGGGCTA R: GGTTGGGCTTGGGAGTGAAG P: TTCAGAGGCCAGAGAGTCCC	125	16176
Il6	F: TCTTGGGACTGATGCTGGT R: AATTAAGCCTCCGACTTGTGA P: ACAACCACGGCCTTCCCTAC	125	16193

Mapt	F: TCCACGAATCCAACCAGTGT R: CAGAGGTCCAAGGTCATCCC P: GAACTGGTGTGTGCCTGCCT	123	17762
Myd88	F: GCTCCCAAGGATAGCTGAGT R: ACCTCCCAAATGCTGAAACT P: TGGACAAAAGTGGGGTGCCT	125	17874
Nlrp3	F: TGCACCCGGACTGTAAACTA R: GTTGCCCAGGTTCAGCTTC P: TGACCCACAACCACAGCCTT	125	216799
Nos2	F: CCCAAGCCCCTCATGTCATT R: GGAGTGGAGAAGAAGGGAGGA P: CCTCCTCCACCCTACCAAGT	125	18126
Nr4a2/Nurr1	F: CAAGCACGTCAAAGAACTGGA R: GTGAGGGCTAGGGGTCTACA P: CTGGTCACATGGGCAGAGAG	125	18227
P2ry12	F: TCAACACCACCTCAGCCAATA R: GATGAGCCCAGCAAAGAACAG P: ACCCAGGTTCTCTTCCCATTGC	125	70839
P62/Sqstm1	F: TCCCCACAGTTCCCCATTG R: AGGCTGTATCCCGATGTCAG P: ACTGCTGAGTCACGCTTGGC	125	18412
Park7/Dj1	F: TTATCTGAGTCGCCTATGGT R: ACCTTGCATCCAAAACCTACT P: TGCAGGTCCTACGGCTCTGT	125	57320
Park2/Prkn	F: GAGAGTATGCCTGACCCCTT R: GTGTGTGTATTGCCCTGTCTG P: TCTGCTCCC/ZEN/TCCTCTGCTGT	125	50873
Pink1	F: GGACTCCCCTCCATCTCATG R: GCCACCACGCTCTACACT P: TGGCTGTCCCTGGCTAGTGA	125	68943
S100a10	F: GGGGAAGAAGTAGGCCAACTG R: TGCACATTTCCTAAGGGTCCTG P: GAATCTGCC/TAO/CCACTGCTTCT	125	20194
Serping1	F: GTACCCGTGTTCCCAAAGC R: TGAGGCATCGTCAGGTAAGT P: ACCCCACTGTCTTCAAGGCC	125	12258
Slc6a3	F: CGTCCCACTTGCTTTGTCTC R: GTCTCCCCAGTTCTCCCTTC P: CAAGGGAGCAGGGTCGGAGA	124	13162
Snca	F: TTCAGAGGAAGGCTACCAAGAC R: CATGACTGGGCACATTGGAAC P: GGCTGCTCTTCCATGGCGTA	125	20617
Sting1	F: GAGCCAAGACTCCTCATCAGT R: GAAGGAAGGCTCAGTCAGGA P: CCTCTCCCACTCCGCACTGA	125	72512
Tlr2	F: ACCACTGCCCGTAGATGAAG	125	24088

	R: CCTCCGACAGTTCCAAGATGT P: TCACCGATGAAGAAGCTGGC		
Tlr4	F: GTCACTGGAACCTCATGCTTT R: GCTCAACACCAAGGAAGCAAA P: TTGGGAGACTGGGGAGCCAT	124	21898
Tlr9	F: TCTGCCCAAACTCCACACTC R: AAGGCCCACTGATGCGATT P: TCATCAACCAGGCACAGCTC	125	81897
Tnf	F: TGTACCTTGTCTACTCCCAGGT R: GACGGCAGAGAGGAGGTTG P: TCTTCAAGGGACAAGGCTGC	125	21926

LIST OF ABBREVIATIONS

Abbreviations	Meaning	Page Number
2 WPI	Two weeks post initial injection	35
3-MT	3-Methoxytyramine	78
3D	Three dimensional	35
3 WPI	Three weeks post initial injection	35
4 WPI	Four weeks post initial injection	34
5-HIAA	5-Hydroxyindoleacetic acid	78
5-HT	Serotonin	78
6-OHDA	6-hydroxy-dopamine	26
α-syn	α-Synuclein	2
AAV	Adeno-associated virus	15
AD	Alzheimer's Disease	22
ADHD	Attention Deficit Hyperactivity Disorder	15
AI	Artificial Intelligence	46
ALS	Amyotrophic Lateral Sclerosis	22
APC	Antigen presenting cell	7
ATP	Adenosine-triphosphate	43
BBB	Blood-brain barrier	23
C1qA	Complement C1q A-chain	19
C3	Complement component 3	4
CCL2	Chemokine C-C motif ligand 2	10
CCL5	Chemokine C-C motif ligand 5	27
CCR2	C-C chemokine receptor type 2	38
CD4	Cluster of differentiation molecule 4	20
CD40	Cluster of differentiation molecule 40	26
CD40L	Cluster of differentiation molecule 40 ligand	20
CD8	Cluster of differentiation molecule 8	20
CNII	Cranial nerve II-Optic Nerve	20
CNS	Central nervous system	7
CNX	Cranial Nerve X-Vaugs Nerve	10
COMT	Catechol-O-methyltransferase	2
COX2	Cyclooxygenase 2	28
CSF	Cerebral spinal fluid	13
CXCL1	Chemokine ligand 1	66
CXCR7	Atypical chemokine receptor 7	17

DA	Dopamine	2
DAB	3,3'-Diaminobenzadine	82
DAMP	Damage associated molecular pattern	74
DAn	Dopaminergic neuron	1
DAPI	6-Diamidino-2-phenylindole	38
DMSO	Dimethyl sulfoxide	35
DMT-1	Divalent metal transporter 1	7
DOPAC	3,4-Dihydroxphenylacetic acid	78
EBV	Epstein Barr Virus	12
EL	Encephalitis Lethargica	85
ELISA	Enzyme Linked Immunosorbent Assay	76
EtBr	Ethidium Bromide	76
ETC	Electron transport chain	9
EtOH	Ethanol	36
GFAP	Glial fibrillary acidic protein	15
GP	Globus pallidus	40
GPER1	G protein-coupled estrogen receptor 1	118
GWAS	Genome wide association study	3
HIV	Human Immunodeficiency Virus	12
HLA-DR	Human leukocyte antigen-DR isotype	27
HPLC	High pressure liquid chromatography	78
HRP	Horse-radish peroxidase	85
HSP60	Heat shock protein 60	129
HVA	Homovanillic acid	78
IACUC	Institutional Animal Care and Use Committee	35
IBA1	Ionized calcium binding adaptor molecule 1	38
IDT	Integrated DNA technologies	76
IKK2	IκB kinase 2	27
IL-10	Interleukin 10	17
IL-12	Interleukin 12	66
IL-1α	Interleukin 1 α	27
IL-1β	Interleukin 1 β	26
IL-2	Interleukin 2	26
IL-6	Interleukin 6	17
INF-γ	Interferon γ	26
IQ	Intelligence quotient	7
KO	Knockout	76
L-Dopa	Leva DOPA	2

LPS	Lipopolysaccharide	10
LRKK2	Leucine-rich repeat kinase 2	3
MAC-1	Macrophage antigen 1	27
MAO-B	Monoamine Oxidase B	2
MHCII	Major histocompatibility complex II	19
MMT	Methylcyclopentadienyl Mn tricarbonyl	7
Mn	Manganese	5
MPP^+	1-Methyl-4-phenylpyridium	8
MPTP	1-Methyl-4-phenyl-1,2,3,6-tetrahyrdopyridine	8
mRNA	Messenger RNA	21
mtDNA	Mitochondrial DNA	123
NADH	Nicotinamide adenine dinucleotide-dehydrogenase	9
NBF	Neutral buffered formalin	38
NE	Norepinephrine	78
NeuN	Neuronal nuclei	38
NF-κB	Nuclear factor κ B	19
NIH	National Institutes of Health	35
NLRP3	NLR Family Pyrin Domain Containing 3	66
NMDA	N-methyl-D-aspartate	2
NOS2	Inducible nitric oxide synthase	26
OMM	Outer mitochondrial membrane	5
p129	Phosphorylation at serine 129 on α-synuclein	38
PAMP	Pathogen associated molecular pattern	18
PARK2	Parkin	3
PARK7	DJ-1	3
PBS	Phosphate buffered-saline	38
PCA	Principal component analysis	87
PD	Parkinson's Disease	1
PEP	Post-encephalitic Parkinson's disease	12
PGE2	Prostaglandin E2	17
pK	Proteinase K	44
pS65	Phosphorylation of serine 65 on PARK2	129
PTX3	Penatrexin 3	17
ROI	Region of Interest	36
ROS	Reactive oxygen species	5
S100a10	S100 calcium binding protein A10	17
S100β	S100 calcium binding protein β	38
SIPR3	Sphingosine 1-phosphate receptor 3	17

SN	Substantia nigra	49
SNpc	Substantia nigra pars compacta	2
SNpr	Substantia nigra pars reticulata	40
SQSTM1/p62	Sequestosome 1	73
ST	Striatum	36
STAT3	Signal transducer and activator of transcription 3	17
STING	Stimulator of interferon genes	123
TBI	Traumatic brain injury	23
TBS	Tris buffered-saline	38
TGFβ	Transforming growth factor β	17
TH	Tyrosine hydroxylase	38
TLR	Toll-like receptor	18
TNF	Tumor necrosis factor	17
TOM	Translocase of the outer membrane	5
TWEAK	Tumor necrosis factor related weak inducer of apoptosis	17
UPS	Ubiquitin proteosome system	21
VEGF	Vascular endothelial growth factor	17
VZV	Varicella Zoster Virus	12
WEEV	Western Equine Encephalitis Virus	12
WT	Wildtype	76
ZIP8	Zinc transporter 8 ZIP8	122